Contribution to the DC-AC conversion in photovoltaic systems : Module oriented converters

Oswaldo Lopez Santos

▶ **To cite this version:**

Oswaldo Lopez Santos. Contribution to the DC-AC conversion in photovoltaic systems : Module oriented converters. Electric power. INSA de Toulouse, 2015. English. NNT : 2015ISAT0001 . tel-01146805

HAL Id: tel-01146805

https://theses.hal.science/tel-01146805v1

Submitted on 29 Apr 2015

HAL is a multi-disciplinary open access archive for the deposit and dissemination of scientific research documents, whether they are published or not. The documents may come from teaching and research institutions in France or abroad, or from public or private research centers.

L'archive ouverte pluridisciplinaire **HAL**, est destinée au dépôt et à la diffusion de documents scientifiques de niveau recherche, publiés ou non, émanant des établissements d'enseignement et de recherche français ou étrangers, des laboratoires publics ou privés.

THÈSE

En vue de l'obtention du

DOCTORAT DE L'UNIVERSITÉ DE TOULOUSE

Délivré par :
Institut National des Sciences Appliquées de Toulouse (INSA de Toulouse)

Discipline ou spécialité :
Automatique

Présentée et soutenue par
Oswaldo LOPEZ SANTOS
Le *06 février 2015*

Titre :
CONTRIBUTION TO THE DC-AC CONVERSION IN PHOTOVOLTAIC SYSTEMS: MODULE ORIENTED CONVERTERS

JURY
M. Francesc GUINJOAN-GISPERT, Rapporteur
M. Bruno ROBERT, Rapporteur
Mme, Corinne ALONSO, Examinateur
M. Maurice FADEL, Examinateur
M. Hugo VALDERRAMA-BLAVI, Examinateur

Ecole doctorale : *École Doctorale Systèmes (EDSYS)*
Unité de recherche : *Laboratoire d'Analyse et d'Architecture des Systèmes (LAAS-CNRS)*
Directeurs de Thèse : *Germain GARCIA et Luis MARTINEZ SALAMERO*

They worked all the life without spared efforts or sacrifice to put each day a new stone in our home thinking always in other following stone. This goal is dedicated to my parents, José and Doris.

She is today the coauthor of my achievements and weaknesses, and in this case, it is her love, patience and constancy, the pillars of this building. This goal is dedicated to my wife Viviam.

The highest cost I paid for this trip has been to be far away from his hugs, his cries, his voice and his life. This goal is especially dedicated to my son Nicolás.

Acknowledgements

I wish to express my immense gratitude and my deepest admiration to professors Germain Garcia and Luis Martinez Salamero whose are the promoters of this project. It is really nostalgic for me remembering all the moments shared with them which have meant that this achievement is a reality today. Among the things that I have learned, beyond of the knowledge, there are many lessons of these two admirable people that have inspired me to be better.

I want to offer my acknowledgements to the institutions in Colombia which have participated to the funding of this project through the program of doctoral formation "Metas 2019": ASCUN (Asociación Colombiana de Facultades de Ingeniería), COLFUTURO (Fundación para el future de Colombia), Embassy of France in Colombia, Ministerio de Educación de Colombia and Universidad de Ibagué.

I wish to express my gratefulness to the Universidad de Ibagué, particularly to William Alexander Londoño Marín, Gloria Piedad Barreto Bonilla, Luis Alfonso Muñoz Hernández and Helga Patricia Bermeo Andrade, who believed in my abilities and appreciated my work promoting the initiative that has brought me here. I am grateful for the constant support, the aid and the encouragement words to realize this thesis.

I want to express my gratitude to the Laboratoire d'Analyse et d'Architecture des Systèmes (LAAS-CNRS), the Université de Toulouse, the Institute National des Sciences Appliquées (INSA), the Ecole Doctorale de Systèmes (EDSYS) and to the Equipe MAC, for the place and opportunity given to me in France, the support to realize this dissertation and the divulgation of the associated results, and especially by integrate me as an student member of the group.

I wish to express my appreciation to the Group GAEI of the Universitat Rovira i Virgili for open the doors receiving me in their laboratory, giving me the space and support to obtain experimental results, contributing with ideas, discussions, experience and critics during the development of this thesis.

I express my thanks to the Group ISGE in LAAS, especially to professor Corine Alonso, Youseff ElBasri and Lionel Seguier, to support with patience my presence in the laboratory during the experimental tests and providing me all the required equipment, aid and support.

I offer my thanks to the students of the "research hotbed SICEP" of the Electronics Engineering Program in the Universidad de Ibagué, specially to Tomás E. Sierra, David F. González, Juan C. Ávila, David F. Zambrano and Yamel A. Moreno.

I wish to thank to my colleague and friend Tomás Urrego to offer to me his collaboration to make more easy and familiar my stay in Toulouse, reviving the camaraderie and friendship of those times when the table was brimming of MOSFET corpses in the Universidad Distrital Francisco José de Caldas.

I offer my thanks to my friends in LAAS, especially to Carlos Quintero, Josu Doncel, Maialen Larranaga, Carlos Bartual, Aloña Berasategui, Isidre Mateu, Marti Bassas, and Youssef ElBasri, to share the coffee breaks, weekly dinners, birthdays and several conversations.

Table of contents

Abstract

These last years, a growing interest in power electronic systems has been motivated by the emergence of distributed renewable energy resources and their interconnection with the grid. In this context, the need of low power topologies fed by a few photovoltaic modules avoiding the use of transformers opens the study of special converters and the associated control strategies ensuring stability, reliability and high efficiency. A resulted generic device known in the commercial and scientific literature as “microinverter” or “module integrated converter” performs a plug and play product together with the PV module called an “AC module”.

This work is devoted to the study of a transformer-less single-phase double-stage grid-connected microinverter. The proposed topology has a non-isolated high-gain boost type DC-DC converter and a non-isolated buck type DC-AC converter connected in cascade through a DC bus. The DC-DC converter permanently extracts the maximum power of the PV module ensuring at the same time a good performance coping with power changes introduced by the change in the environmental conditions. The DC-AC stage injects the power extracted by the DC-DC stage into the grid ensuring a high level of power quality. The research efforts focus on the involved control functions based on the sliding mode control theory, which leads to a simple implementation with a comprehensive theoretical description validated through simulation and experimental results.

After giving the state-of-the-art in the first chapter, the manuscript is divided into four chapters, which are dedicated to the Maximum Power Point Tracking (MPPT), the DC-DC stage and its control, the DC-AC stage and its control and the complete microinverter. A new Extremum Seeking Control (ESC) MPPT algorithm is proposed.

The single-switch quadratic boost converter is studied operating as a Loss-Free-Resistor (LFR) obtaining a high DC output voltage level with a safe operation. The full-bridge converter is controlled as a Power Source Inverter (PSI) using a simple sliding-mode based tracking law, regulating the voltage of the DC bus and then ensuring a high power quality level in the grid connection. Finally, the three building blocks are merged to obtain a sliding mode controlled microinverter constituting the main result and contribution of the work.

Résumé

Ces dernières années, un intérêt croissant pour les systèmes électroniques de puissance a été motivé par l'émergence de sources d'énergie distribuées et renouvelables raccordées aux réseaux électriques. Dans ce contexte, la nécessité de topologies de faibles puissances alimentées par quelques modules photovoltaïques, en évitant l'utilisation de transformateurs, a ouvert l'étude de convertisseurs spéciaux et l'étude des stratégies de commande associées afin d'assurer la stabilité, la fiabilité et un rendement élevé du dispositif. Une possible solution est d'utiliser un dispositif générique connu dans la littérature scientifique et commerciale comme « micro-onduleur » ou «convertisseur intégré au module » qui avec le module photovoltaïque définit un produit « plug and play » appelé "module AC".

Ce travail est consacré à l'étude d'un micro-onduleur monophasé avec deux étapes sans transformateur raccordée au réseau. La topologie proposée est composé d'un convertisseur DC-DC non isolé élévateur avec un gain quadratique et un onduleur réducteur lié au réseau connectés en cascade. Le convertisseur DC-DC extrait en permanence la puissance maximale du module photovoltaïque malgré les changements dans les conditions environnementales. L'étape DC-AC injecte la puissance extraite par l'étape DC-DC dans le réseau et assure un niveau élevé de qualité de l'énergie. Les efforts de recherche de ce travail sont concentrés sur la mise au point de commandes utilisant comment base, la théorie de contrôle par mode de glissement, qui conduit à une mise en œuvre simple avec une description théorique complète validée á partir de simulations et expérimentations.

Après avoir décrit l'état de l'art dans le premier chapitre, le manuscrit est divisé en quatre chapitres, qui sont dédiés respectivement à l'algorithme de recherche du point de puissance maximale (MPPT), á l'étape de conversion DC-DC, á l'étape de conversion

DC-AC et finalement au micro-onduleur complet. Un nouvel algorithme de recherche extrémal du point de puissance maximale est développé (SM-ESC). Pour la étape DC-DC, le convertisseur élévateur quadratique avec seulement un interrupteur contrôlé est étudié utilisant le concept de résistance sans perte par mode de glissement (de l'acronyme anglais : Sliding-Mode Loss-Free-Resistor – SM-LFR) afin d'obtenir un gain de tension élevé avec un fonctionnement sûr et compatible avec l'algorithme MPPT. Pour la étape DC-AC, le convertisseur de pont complet est contrôlé comme un onduleur de source de puissance (de l'acronyme anglais : Power Source Inverter - PSI) en utilisant une commande par mode de glissement qui poursuit une référence sinusoïdale de courant de sortie. Cette commande est complétée par une boucle de régulation de la tension du bus DC qui assure une haute qualité d'énergie injectée dans le réseau. Enfin, les trois étapes constitutives sont fusionnées pour obtenir un micro-onduleur complètement contrôlé par la technique de mode de glissement, ce qui constitue le principal résultat et contribution de cette thèse.

Résumé long

Ces dernières années, un intérêt croissant pour les systèmes de conversion d'énergie a été motivé en part pour l'émergence du concept de génération distribue, le quel consiste en l'intégration des sources renouvelables d'énergie avec le réseau électrique. D'entre eux, les générateurs photovoltaïques peuvent être composés d'une grande quantité de panneaux solaires et un seul convertisseur centralisé de haute puissance ou d'un arrangement de quelques panneaux solaires utilisant une chaine avec diffèrent convertisseurs combines. Une solution plus récente consiste d'utiliser un dispositif générique connu dans la littérature scientifique et commercial comme « micro-onduleur » ou «convertisseur intégré au module » qui rejoint avec le module photovoltaïque assemblent le produit appelé « module AC ». Ce dispositif est développé pour travailler avec faibles niveaux de puissance et également avec faibles niveaux de tension d'entrée. Par conséquence, il y a diffèrent défis liés avec le développement des micro-onduleurs qui justifient la recherche pour assurer la stabilité, la robustesse, la fiabilité, la qualité d'énergie, la performance dynamique et le rendement élevé. D'entre le plusieurs objectives possibles à proposer, c'est importante trouver des configurations du dispositif en évitant l'utilisation de transformateurs car elles peuvent réduire les couts et augmenter la densité de puissance sans augmenter la complexité. Ainsi c'est importante à définir un schéma de control pour fournir une performance adéquate de toutes les fonctionnes de contrôle sans s'introduire en solutionnes qui peuvent être inutilement complexes.

Pour ce que concerne l'électronique de puissance, cette thèse est consacrée à l'étude du micro-onduleur monophasé sans transformateur à deux étapes de conversion. La topologie proposée est composé par un convertisseur DC-DC non isolé avec un gain

d'élévation quadratique et un convertisseur DC-AC réducteur, lesquels sont connectés en cascade. Le convertisseur DC-DC extrait en permanence la puissance maximale du panneau photovoltaïque pour générer le niveau de tension DC nécessaire pour alimenter l'onduleur. L'étape DC-AC injecte le pourcentage le plus élevé possible de la puissance délivrée par l'étape DC-DC dans le réseau.

D'un point de vue de l'automatique et le commande appliquée, cette thèse est dédié à l'étude des fonctionnes de contrôle nécessaires pour l'opération des étapes constitutifs du micro-onduleur. Le contrôle par mode de glissement a été choisi comme le fondement théorique des travaux afin d'obtenir une mise en œuvre simple, un fonctionnement robuste, et une justification mathématique claire. Chacun des fonctions de commande est étudiée de façon indépendante et postérieurement le micro-onduleur est analysé comme un système unique.

Le manuscrit est divisé en cinq chapitres, qui sont dédiés respectivement à l'introduction général de l'application, l'algorithme de recherche du point de puissance maximal, l'étape de conversion DC-DC et son commande, l'étape de conversion DC-AC et son commande et finalement au micro-onduleur complet. Toutes les hypothèses théoriques qui sont présentées dans cette thèse sont aussi validées utilisant des résultats de simulation et expérimentation.

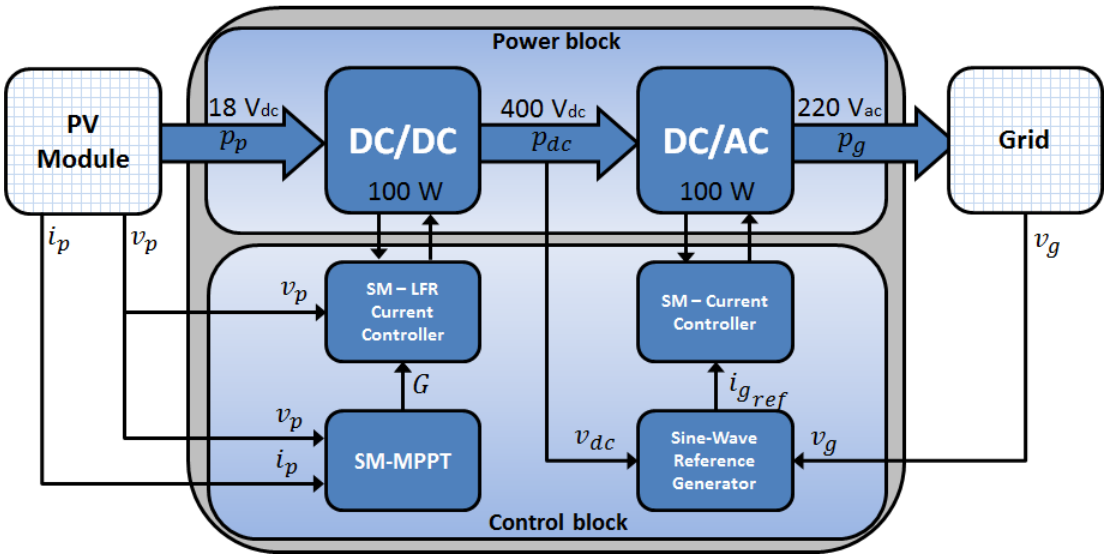

Figure 1. Schéma du micro-onduleur identifiant les étapes de conversion d'énergie et les différentes fonctionnent de commande

Le premier chapitre de la thèse est dédié à l'état de l'art des générateurs photovoltaïques raccordées au réseau électrique, lequel est présenté utilisant diverses

classifications basées sur les dimensionnés de l'installation photovoltaïque, le nombre de étapes du convertisseur de puissance, la configuration utilise dans le bus de DC, l'isolation galvanique présente dans le système et le type de puissance générée. Postérieurement, cette classification est complémentée pour une description des micro-onduleurs commerciaux, dans laquelle se montre et compare les caractéristiques les plus importantes comme les rendements, la densité de puissance, le facteur de puissance et les caractéristiques nominales d'entrée et sortie. De cette façon, ayant déjà décrit l'application du micro-onduleur et son contexte réel, les tendances de recherche qui sont identifiés dans la littérature sont présentées pour finalement montrer et préciser la structure de micro-onduleur à utiliser et les fonctionnes de commande qui seront étudiées à travers la thèse. Dans cette chapitre il est déclaré que l'étude va être consacre au commande par mode de glissement d'un micro-onduleur de deux étapes sans transformateur raccordé au réseau suivant le schéma montré dans la figure 1.

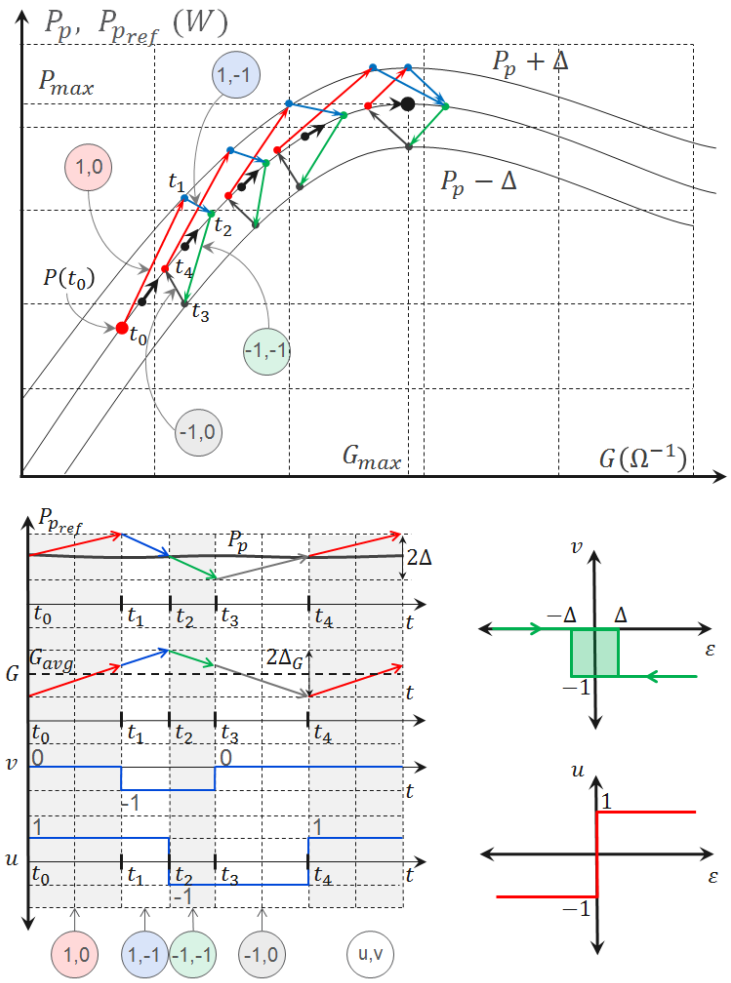

Figure 2. Trajectoire non linéaire de la puissance vers le maximum et représentation graphique dans le temps des variables de l'algorithme MPPT dans un régime établi

Dans le deuxième chapitre, un nouvel algorithme de recherche extrémal du point de puissance maximal d'un panneau photovoltaïque est proposé et justifié. Au début du chapitre, une classification des algorithmes MPPT (sigle en anglais de : « Maximum Power Point Tracking ») est présenté pour introduire les particularités du algorithme proposée et pour établir le point de partie dans l'état de l'art correspondant. L'algorithme proposé utilise la commande par mode de glissement pour obtenir la valeur de la conductance que permettre piloter le système permanentent vers le point de puissance maximum indépendamment des changements d'irradiation solaire. Comme cela est illustré dans la figure 2, l'algorithme utilise deux fonctionnes non linéaires de deux niveaux (u and v) pour produire les quatre possibles structures du système lesquelles sont obtenu dans une séquence spécial et évoluent en fonction de l'erreur de puissance obtenu de la comparaison entre la mesure instantanée de la puissance du panneau (Pp) et le référence auto-généré pour l'algorithme (Pp_{ref}). L'algorithme assure au même temps une bonne performance dynamique pour répondre aux changements provoqués par les conditions environnementales.

Compte tenu que l'algorithme transforme le problème de recherche du point de puissance maximum en un problème d'optimisation et que la variable à manipuler est la conductance, une transformation de variables est appliquée pour obtenir la courbe de puissance du panneau solaire comme une fonction de la conductance. De cette manière, est illustre l'obtention de la valeur de la dérive maximum de cette fonction, laquelle est utilisé pour le réglage des paramètres de l'algorithme. L'étude théorique de l'algorithme a permis d'obtenir les relations entre les paramètres qui garantirent la stabilité de et la convergence permanent vers le point de puissance maximal. A la fin du chapitre, le fonctionnement de l'algorithme a été validé utilisant des résultats obtenus par simulation et résultats expérimentaux montrant sa robustesse.

Le troisième chapitre est dédié à l'étape de conversion DC-DC laquelle utilise un convertisseur élévateur quadratique avec seulement un commutateur contrôlé. Initialement, le choix du convertisseur élévateur quadratique est justifié utilisant une introduction qui décrit les différentes topologies de convertisseurs utilises pour obtenir grandes gains de tension et explique les avantages du convertisseur proposée. Le circuit du convertisseur élévateur quadratique est montré dans la figure 3.

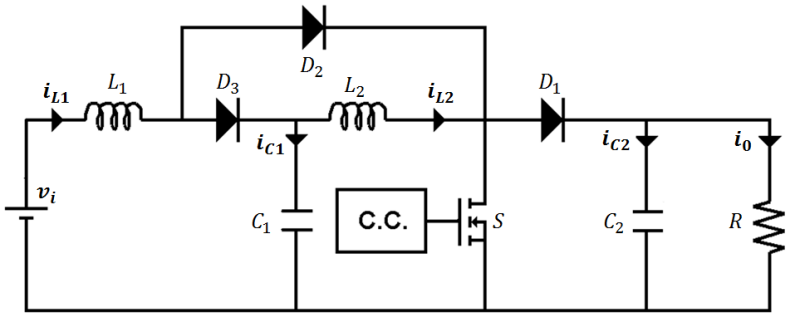

Figure 3. Convertisseur élévateur quadratique

Après cela, le régime établi du convertisseur est étudié pour révéler les différentes modes de conduction qui peuvent être obtenus montrant l'existence d'un mode de conduction continu et de quatre modes de conduction discontinus. L'analyse est adressée considérant toutes les possibles structures du convertisseur et les transitions probables entre eux. Un diagramme d'états est montré dans la figure 4 en décrivant tous les modes de conduction possibles.

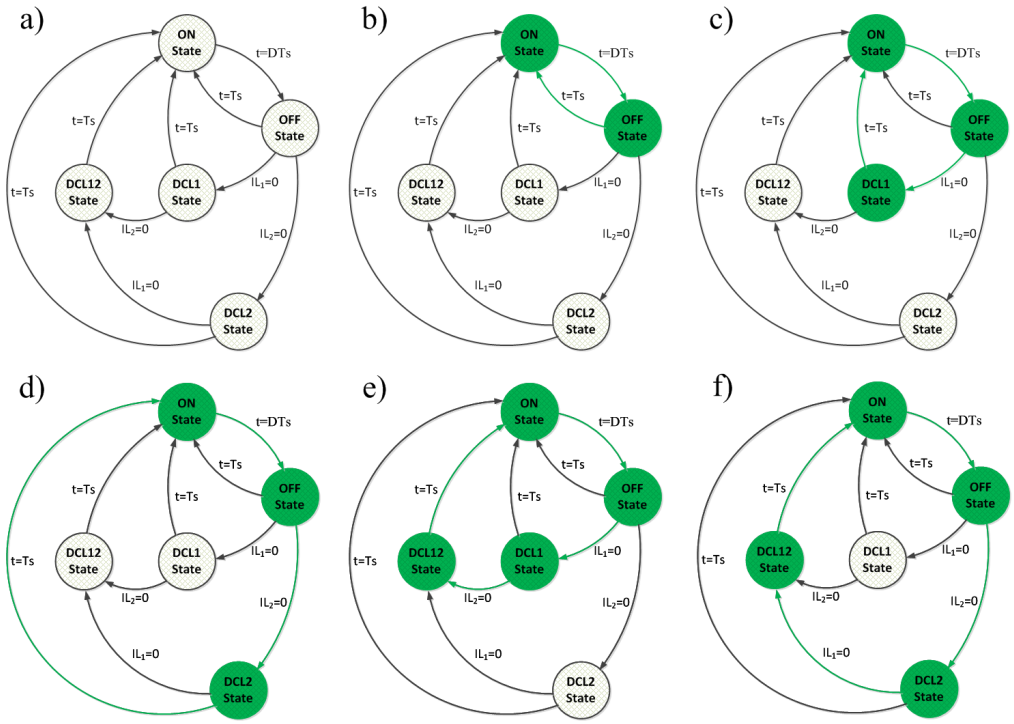

Figure 4. Diagramme d'évènements des modes de conduction du convertisseur élévateur quadratique : a) Représentation générale ; b) Mode de conduction continue ; c) Mode de condition discontinu dans l'inductance L1 ; d) Mode de conduction discontinue dans l'inductance L2 ; e) et f) Modes de conduction discontinue dans les deux inductances.

A partir de cette représentation, le fonctionnement du convertisseur utilisant un modulateur de largueur de pulse, et dans autre cas, un comparateur d'hystérésis est distingué en raison des restrictions que son imposées pour chaque méthode de commutation.

Finalement, le convertisseur est commandé en mode de conduction continu, utilisant une loi de commande par mode glissante laquelle est implémenté utilisant un comparateur d'hystérésis.

Le commande proposé consiste en suivre une référence de courant laquelle est traite initialement comme une valeur constante mais qui va être imposé finalement pour la boucle de commande externe constitué pour l'algorithme « MPPT ». La stabilité du convertisseur avec ce loi de contrôle est démontré à travers d'une fonction de Lyapunov. Postérieurement, la surface de glissement est modifié de façon que la référence de courant est obtenu à partir du concept du LFR (en anglais: Loss Free Resistor) lequel calcule la référence de courant à partir de la valeur de la tension mesuré dans l'entrée du convertisseur et une valeur donnée de conductance. Cette problème de control est traite considérant uniquement une source de tension d'entrée et un charge de sortie composé par une résistance et une source de courant. La stabilité du convertisseur est montrée utilisant la méthode du contrôle équivalent pour obtenir une représentation linéaire du système opérant autour un point d'équilibre. Ensuite, le rendement du convertisseur est estimé considérant les particularités du convertisseur élévateur quadratique et la variation de fréquence introduit par l'implémentation utilisant un comparateur d'hystérésis. A la fin du chapitre, le fonctionnement de l'algorithme est validé utilisant des résultats obtenus par simulation et résultats expérimentaux qui montrent la validité des résultats théoriques.

Pour la étape DC-AC, dans le quatrième chapitre, l'onduleur de pont complet de caractéristique réductrice est traite considérant une source de puissance à l'entrée et le réseau électrique a la sortie comme charge. L'entrée du convertisseur est étudié comme une source de puissance considérant la caractéristique donnée à l'étape DC-DC à travers la loi de commande de LFR et pris en compte que la tension de entrée minimum pour l'onduleur doit être plus grande que l'amplitude de la tension de la réseau. La dénomination d'onduleur de source de puissance est utilisée pour surligner les particularités de ce mode d'opération de l'onduleur. Le diagramme du circuit correspondant est montré dans la figure 6.

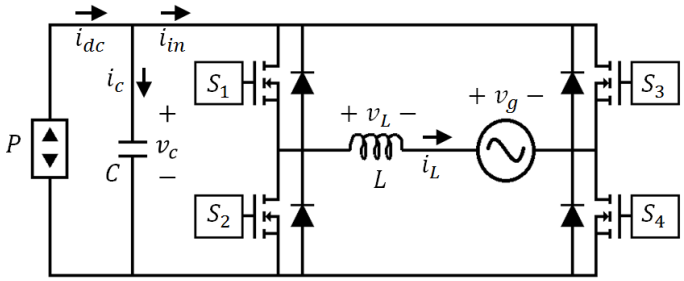

Figure 6. Diagramme du circuit de l'onduleur de source de puissance de pont complet raccordée au réseau.

L'onduleur est contrôlé utilisant la commande par mode de glissement pour suivre une référence sinusoïdale dans le courant de sortie. La forme d'onde de la courant est obtenu à partir d'un system de synchronisation basée en un PLL (en anglais : Phase-Locked-Loop) lequel donne un signal sinusoïdale d'amplitude normalisé synchronisé en fréquence et phase avec le réseau. L'amplitude de la référence est donnée pour une boucle externe de régulation de la tension du bus CC qui maintient la balance de puissance dans la chaine de conversion. Au même temps, la boucle de régulation assure une haute qualité d'énergie dans le raccordement au réseau évitant l'influence de l'ondulation naturelle de la tension du bus CC dans la référence de courant. Le schéma fonctionnel du control de l'onduleur est montré dans la figure 7.

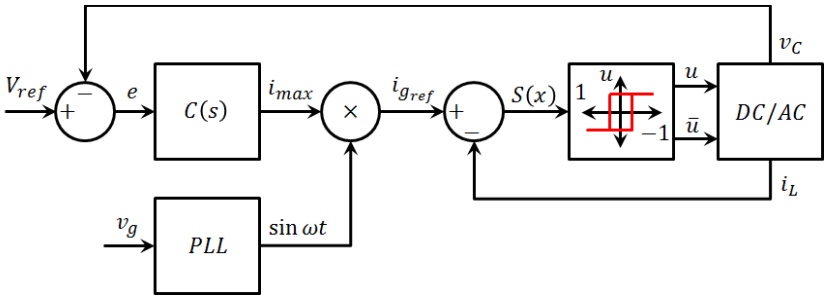

Figure 7. Schéma fonctionnel du control du l'onduleur raccordée au réseau

Dans le cinquième et dernier chapitre, les trois éléments constitutifs décris dans les chapitres précédents sont fusionnés pour obtenir un micro-onduleur complètement contrôlée utilisant le mode de glissement. Le modelé traite dans le chapitre quatre pour le convertisseur CC-CC est complété considérant le panneau solaire comme une source de courant et incluant le condensateur connecte en parallèle avec le panneau solaire. Ainsi, un modèle linéaire pour le convertisseur est obtenu considérant la valeur de la conductance, l'amplitude de la source de courant qui représente le panneau solaire et une source de courant qui représente l'onduleur comme une charge connectée à la sortie du convertisseur.

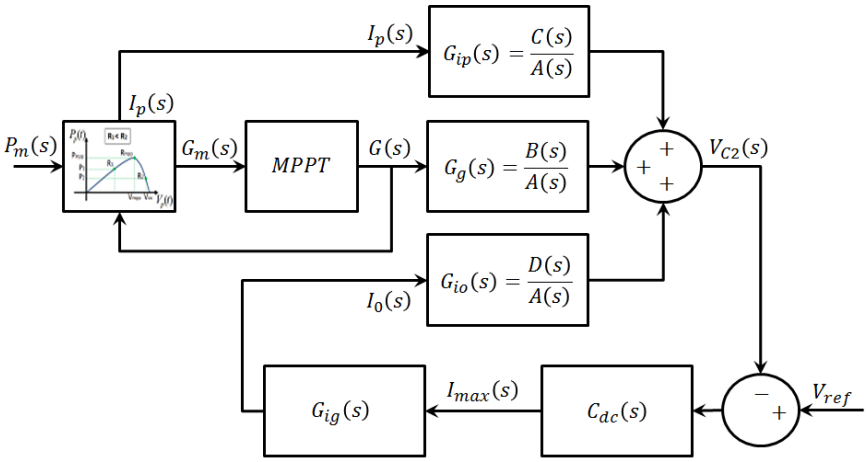

Figure 7. Représentation du system de control montrant l'interaction entre l'étape CC-CC et l'étape DC-AC à travers de ses fonctionnes transfert

Ce model représente d'une manière convenaient le micro-onduleur comme un système complète et permettre d'étudier la stabilité de l'ensemble laquelle est montrée dans le chapitre utilisant le polynôme caractéristique. Afin du chapitre, il est montré le montage expérimental complet qui a permis d'obtenir les résultats expérimentaux pour valider toutes les étages de contrôle étudies dans la thèse. Ce montage est reproduit dans la figure 9 pour illustrer la réalisation pratique qui a été requis.

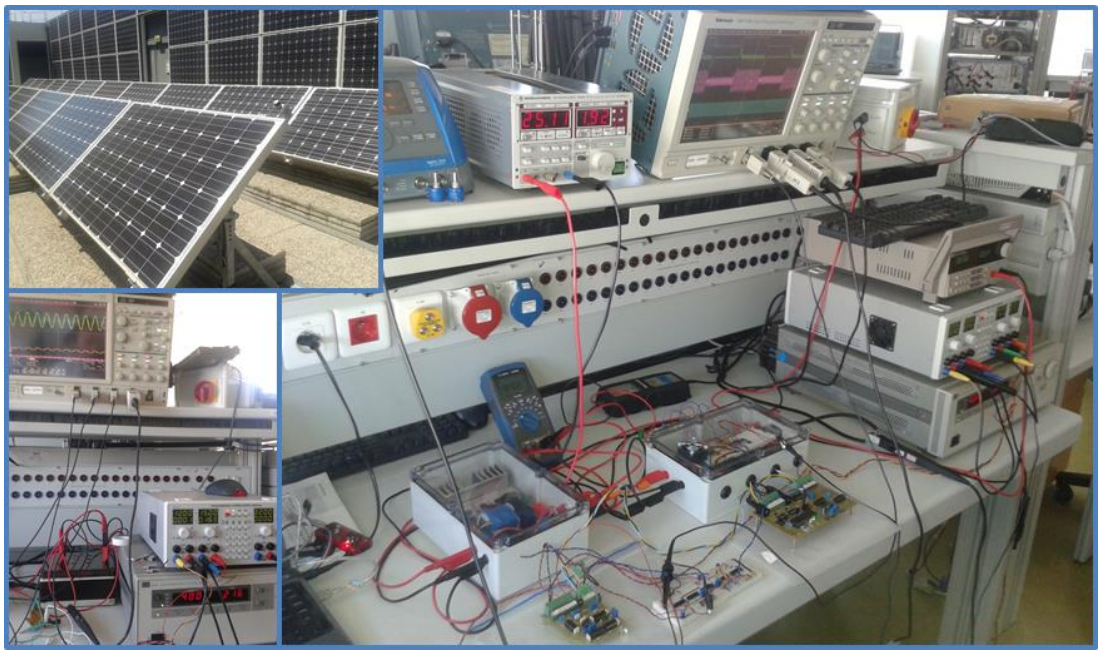

Figure 9. Montage expérimental du micro-onduleur complet

La thèse montre dans les chapitres deux, trois et quatre, les résultats de simulation et les résultats expérimentaux correspondants à chaque fonction de commande dans le micro-onduleur. Le chapitre 5 montre des résultats les plus importantes en relation avec

l’application du micro-onduleur car correspondent au système complète. Deux captures s’oscilloscope montrant les comportements statiques et dynamiques dans les variables du micro-onduleur sont montrés dans la figure 10.

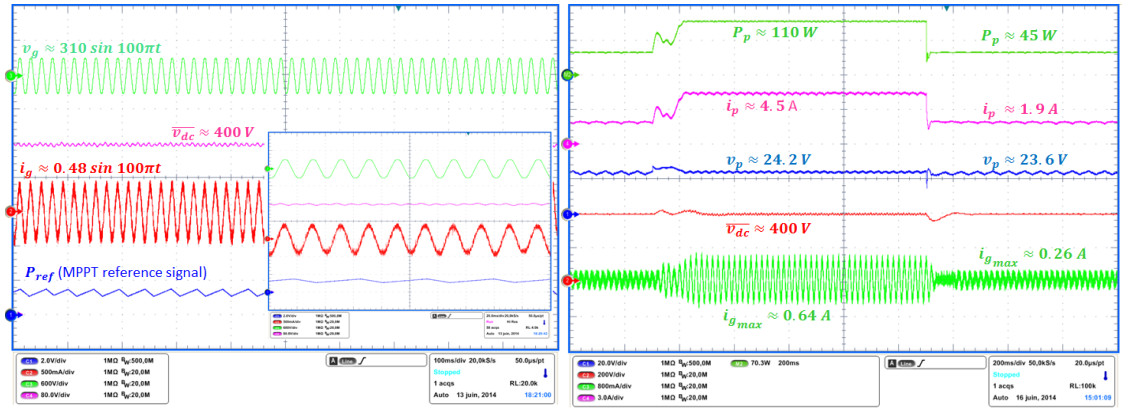

Figure 10. Mesures expérimentaux du régime établi et de la réponse dynamique du system complet

Key-words

Photovoltaic generator

Photovoltaic solar energy

Power Electronics Converter

High-gain DC-DC converter

Sliding-mode Control

Loss-Free-Resistor

Maximum Power Point Tracking

Extremum Seeking Control

Power Sourced Inverters

Modelling of Power Converters

Grid-connected Inverter

Micro-inverter

Mots-clés

Générateur photovoltaïque

Energie solaire photovoltaïque

Convertisseur électronique de puissance

Convertisseur continu-continu á grand gain

Commande par mode de glissement

Résistance libre de pertes

Recherche du point de puissance maximale

Régulation extrémal

Modélisation des convertisseurs de puissance

Onduleur raccordée au réseau

Micro-onduleur

Chapter 1

Introduction

1.1 DISTRIBUTED PHOTOVOLTAIC GENERATION

The distributed generation (DG) of energy can be associated with a decentralized way to process electrical power from energy resources such as photovoltaic (PV), wind, fuel-cells, geothermal, hydroelectric, waste-to-energy turbines and others [1]-[5]. These generators allow covering the user's consumption leading to economic savings and slowly replacing the centralized sources that threaten the environmental integrity of the planet. The DG is intimately related with the micro-grid [6]-[7] and the smart-grid concepts [8]-[9] present in many of the current developments of the energy systems. Among the available alternative energy resources involved in a distributed generation, the photovoltaic solar energy (PSE) together with hydro and wind power have an important role , they motivating an intensive research work in recent years [10]-[14].

The photovoltaic generators can be introduced in many applications depending on particular situations which induce associated constraints. For example, a photovoltaic generator used in a place where other energy sources are absent must have the ability to provide the required power with the specific voltage characteristics such as frequency and amplitude. In other cases, the photovoltaic generator must work in a cooperative way with other generators connected to a grid system providing only a portion of the required power. It is then possible to classify the photovoltaic generators in "stand-alone" or "grid-connected" (GC) systems. The "stand-alone generators" are used in isolated applications and are in general complemented by a storage system like battery arrays. Thus, these systems can feed a load while a portion of the energy is accumulated

in batteries in order to guarantee an autonomy level during the absence of solar radiation [15]-[16]. The “GC generators” are used in interconnected applications which work with a power grid. This type of generators can produce and inject true power into the grid reducing the consumption from the main power source [17]-[20]. Commercially, these devices are also presented as self-consumption generators. A third possibility appears when the properties of both systems are combined. This type of “hybrid” or “universal” generator must have the capability to permanently inject the power into the grid and also to operate eventually in an isolated mode [21]-[23]. It goes without saying that the control of this last type of generators is more complex because of the need of islanding control and power flow configuration algorithms [24]-[27]. This dissertation focuses on a kind of “GC generators” and hence, the literature review is concentrated on this family of power converters.

1.2 CLASSIFICATION OF THE PV GC GENERATORS

Some different ways can be used to classify the PV GC generators, in particular, taking into account the advantages, drawbacks, application possibilities and limitations. A detailed classification, presented below, is used to introduce the main motivations of our research work.

1.2.1 According to the installation size

The size of the installation differentiates three kinds of PV GC generators [17]. Commonly, in this classification, it is possible to give to a generator the attribute of “oriented to” complemented with a description of the installation size using the words “central”, “array” or “module”. Then, in the first group, one finds the “central inverters” or “centralized inverters” working with many photovoltaic modules connected in series-parallel arrays in order to have high levels of DC voltage and hundreds of kilowatts or even of megawatts. This type of installation uses a centralized inverter which can cover the whole system power requirement [28]-[30]. In a second group, we have the “array oriented generators” or “string oriented generators” working with series connected arrays of some photovoltaic modules covering only the requirement to have a high DC voltage level working with amounts of power in the order of dozens of kilowatts. This

kind of installation can use two different configurations of power converters which have been denominated in the literature as “string inverters” [31]-[34] or “multi-string inverters” [35]-[37]. The multi-string inverters are a generalization of the string inverters which uses an output connection of DC-DC converters whose inputs are independently connected to a separate array of PV modules centralizing the power in only one inverter. Finally, in the third group, we have “module oriented converters” which work with the low voltage level of one or two PV modules generating powers of only a few hundreds of watts. This same concept has been developed using the denomination “module integrated converter (MIC)” [38]-[40], “microinverter” [41]-[44] or “AC module” [45]-[47], which consists on connecting a low power converter to each photovoltaic module. The figure 1.1 shows the different generator topologies classified according to the installation size.

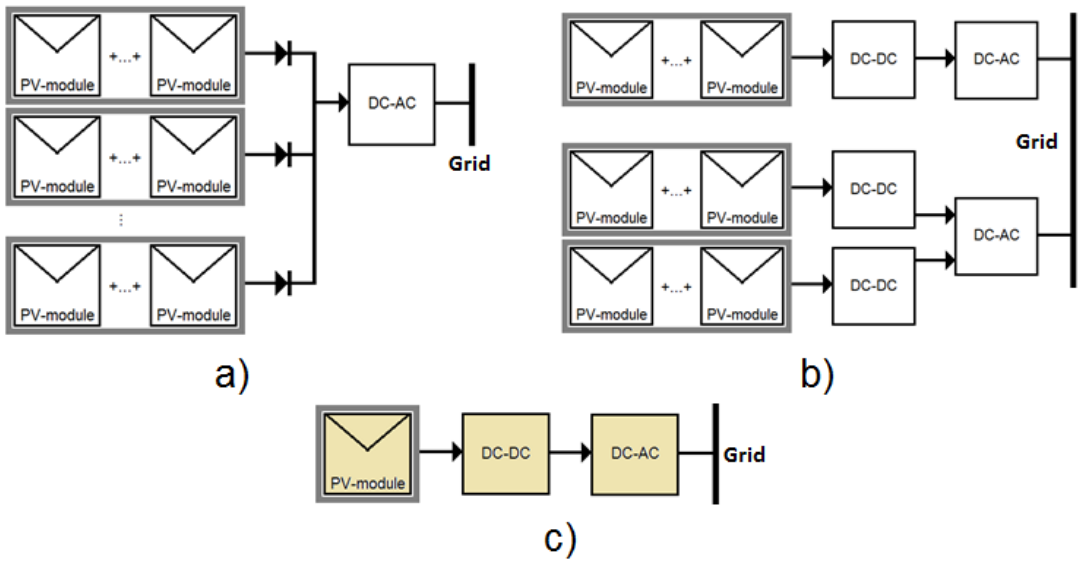

Fig. 1.1. Different types of photovoltaic installation: a) centralized inverters, b) string and multi-string inverters, c) module oriented inverters.

1.2.2 According to the number of stages

The photovoltaic generators are in general a type of DC-AC converters. These converters can be composed by one, two or more stages. Then, we can have either a single-stage topology or a dual-stage topology or a multi-stage topology [3], [48]-[49]. The single stage topology has only a DC-AC stage which is directly connected to the PV module at the DC side and connected to the grid at the AC side [50]. The dual stage

topology is performed using a DC-DC stage and a DC-AC stage connected in cascade obtaining a conversion chain of the type DC-DC-AC [51]. In this case, the DC-DC converter is connected to the PV module and the DC-AC converter is connected to the grid. The point of connection of both converters commonly defines a DC bus. An alternative way to constitute a dual stage topology can be obtained using a series output connection of DC-DC converters , each one being fed by a PV module [52]-[54]. Then, the DC voltage obtained as the sum of the output voltage of each converter feeds an inverter connected to the grid. Finally, a multi-stage topology can be obtained from the connection of multiple converters preserving a DC side at the input port and an AC side at the output port. For example, it is possible to have a three -stage topology in such a way that the conversion chain is defined as DC-AC-DC-AC. In this case, we have a DC-AC stage, an AC-DC stage and a DC-AC stage. The first stage (an inverter) is connected to the PV module at the input port and connected to the second stage (a rectifier) at the output port. The second stage is connected to the first stage at the input port and to the third one (an inverter) at the output port. The third stage is connected to the second stage at the input port and connected to the grid at the output port. Using this configuration it is possible to configure a resonant converter in the first stage allowing galvanic isolation through a high-frequency transformer feeding a high-frequency rectifier which in turn feeds the output inverter [3].

Some authors have discussed the topology which can offer the best performance. However, the selection of a topology depends on both power and voltage levels. In this context, the dual stage topology (figure 1.1c) is advantageous in terms of control because the control functions can be distributed between both stages [2]-[4], [48].

1.2.3 According to the DC-link configuration

In [55], the MIC topologies are classified in either converters with DC link, converters with a pseudo DC link and converters without DC link. Converters with DC link produce a DC voltage level higher than the peak of the grid voltage, this ensuring the correct operation of a buck type inverter stage. Converters with a pseudo DC-link produce a rectified current from a first DC-DC stage to unfold subsequently this signal using a low frequency bridge inverter. Converters without DC link use a high frequency AC conversion involving transformers or coupled inductors using forced-commutated cycloconverters [56].

1.2.4 According to the isolation

The galvanic isolation of a grid-connected inverter can be determinant in high power applications. In fact, in many industrial applications, a low frequency transformer is used because it gives robustness and an inherent protection to the system. However, in low power applications the existence of this type of transformer is increasingly less acceptable because of the size and weight of the final solution. Therefore, if isolation is needed a converter topology with a high frequency transformer can be used obtaining a reduced size at the expense of some complexity. But, if isolation is not required, many topologies can be used and better performances can be attained. Then, we can differentiate either transformer-based [57]-[58] or transformer-less topologies [59]-[60]. The more typical configurations of transformer-based topologies employ the fly-back topology [61]-[62] or the interleaved fly-back topology in more recent works [63]-[64]. The transformer-less topologies use existing topologies of DC-DC converters or interconnection of them to look for a solution satisfying a DC-gain requirement [65]-[72]. Moreover, multilevel topologies have been proposed in order to improve the power quality of the microinverters, avoiding at the same time, the use of transformers [73]-[75].

In microinverter applications using a double-stage topology, a high-gain DC-DC converter is needed because of the low voltage levels at the input port. This is a real challenge when no transformer-based topology is used.

1.2.5 According to the type of the generated power

A power converter connected to the grid can generate either “active power”, “reactive power” or a combination of them. In this context, there are power conditioners or generator-conditioners. The control of the first group consists in enforcing the inverter to inject all of the available active power into the grid preserving a unitary power factor with a reduced harmonic content. The control of the power conditioners is more complex because the system must compensate the displacement of power factor giving reactive power or compensating a portion of the harmonic content generated by a load increasing the power factor and reducing the harmonic distortion to admissible levels [76]-[77]. Moreover, the control of active power is also necessary in power conditioners because of the power losses of the converter. An attractive solution can be the

implementation of a system with two modes, having a first mode to inject the maximum power produced by the PV module into the grid and a second mode to operate as a conditioner when the solar radiation is lower.

1.3 REVIEW OF COMMERCIAL MICROINVERTERS

1.3.1 Technical characteristics

The name "microinverter" is given commercially to inverters which work with low power levels (less than 500 W) [78]. However, a really important difference exists between this generic product and a photovoltaic microinverter because the photovoltaic application requires both the extraction of the maximum power from the DC side and a grid connection. The industrial development of this technology offers a wide availability of that device as a product. Some manufacturers have gained popularity because of the presence of their microinverters in the market. The main electrical characteristics of a few commercial microinverters are listed in table 1.1 and table 1.2.

Table 1.1. Summary of commercial microinverter characteristics

Characteristics / Manufacturer	Input voltage	MPPT Efficiency	Maximum Efficiency	Weighted Efficiency	Nominal Power	Power Factor	Current THD
Aurora [79]	25-60 V	*NS	95.5%	95%	300 W	>0.95	*NS
Direct-grid [80]	53-75 V	99%	*NS	92%	460 W	>0.99	*NS
Emphase [81]	27-39 V	99.4%	96.5%	96.5%	215 W	>0.95	*NS
Enecsys [82]	27-54 V	*NS	94%	91%	200 W	>0.95	<5%
iEnergy [83]	25-58 V	99.3%	94%	93%	240 W	>0.95	<3%
Involar [84]	24-40 V	*NS	95%	94%	250 W	>0.99	<3%
SolarBridge [85]	28-36 V	99.6%	95.5%	94.5%	240 W	>0.99	<5%
SolarEuropa [86]	24-50 V	*NS	95%	94%	250 W	>0.99	<3%
Sparq [87]	32-50 V	*NS	95%	93.4%	190 W	>0.99	<2%
SunSine [88]	*NS	*NS	*NS	*NS	200 W	>0.98	<5%
ReneSola [89]	22-55 V	99.5%	96.3%	95%	250 W	>0.99	*NS
APS [90]	22-45 V	*NS	95.5%	*NS	250 W	>0.99	<3%
Siemens [91]	16-36 V	99.6%	96.3%	96%	215 W	>0.95	*NS
ABB [92]	25-60 V	*NS	96.5%	96%	250 W	>0.95	*NS
AE Conversion [93]	18-45 V	99.8%	93.5%	91.4%	250 W	>0.99	*NS

*NS: No Specified

As it can be noted in table 1.1, only the microinverters of the manufacturers "Siemens" [91] and "AE Conversion" [93] work with the voltage levels corresponding to a 24 VDC PV module while the others work with voltage levels corresponding to a series connection of two or three PV modules. Further, efficiency levels are around 95% being the microinverter of the manufacturer "Emphase" [81] the device with the best performance. The MPPT efficiencies are reported always higher than 99%. The power factor is always higher than 0.95, but it is not clear if all manufacturers report the power factor or the displacement power factor. The best lower THD (2%) is offered by the manufacturer "Sparq" [87] besides the better MPPT efficiency.

As it is observed in table 1.2, the majority of the microinverter manufacturers offer warranties of more than 20 years. This fact implies that converter topologies do not use electrolytic capacitors since they suffer degradation in less than 10 years. The best trade-off power-weight is found for the microinverter of the manufacturer "Aurora" [79].

Table 1.2. Summary of commercial microinverter characteristics

Characteristics / **Manufacturer**	**Warranty Years**	**Nominal Power**	**Maximum Efficiency**	**Weight [kg]**	**Size**			**Power Density**
					W [cm]	H [cm]	D [cm]	
Aurora [79]	*NS	300 W	95.5%	1.50	21.00	16.00	5.00	0.18 W/cm^3
Direct-grid [80]	20	460 W	*NS	2.17	22.53	22.76	3.05	0.29 W/cm^3
Emphase [81]	25	215 W	96.5%	1.60	16.30	17.30	2.50	0.30 W/cm^3
Enecsys [82]	20	200 W	94%	1.80	26.20	16.00	3.50	0.14 W/cm^3
iEnergy [83]	25	240 W	94%	1.60	23.20	21.10	4.31	0.11 W/cm^3
Involar [84]	15	250 W	95%	2.90	23.50	14.40	5.30	0.14 W/cm^3
SolarBridge [85]	25	240 W	95.5%	2.41	20.32	16.51	3.17	0.22 W/cm^3
SolarEuropa [86]	15	250 W	95%	2.40	23.00	13.80	3.50	0.22 W/cm^3
Sparq [87]	25	190 W	95%	1.45	19.05	12.70	3.04	0.26 W/cm^3
SunSine [88]	20	200 W	*NS	*NS	*NS	*NS	*NS	*NS
ReneSola [89]	25	250 W	96.3%	2.00	23.00	13.80	3.50	0.22 W/cm^3
APS [90]	25	250 W	95.5%	1.50	16.00	15.00	2.90	0.36 W/cm^3
Siemens [91]	25	215 W	96.3%	1.60	17.30	16.40	2.50	0.30 W/cm^3
ABB [92]	10	250 W	96.5%	1.65	26.60	24.60	3.50	0.11 W/cm^3
AE Conversion [93]	*NS	250 W	93.5%	2.50	31.4	26.7	6.65	0.04 W/cm^3

*NS: No Specified

In general, it is possible to identify a trend to increase the lifetime of the microinverters in order to ensure warranty times around 25 years. It is possible to

observe that the best maximum efficiency of 96.5% is offered by the manufacturers "Emphase" and "ABB" with very different power densities: 0.3 and 0.11 W/cm^3 respectively. However, only the price can be determinant because a low difference in size or weight is acceptable considering the dimension of the PV modules. The AC module offered by "SunSine" [88] does not exhibit much information because it considers the microinverter and the PV module as an integrated product.

It is possible to conclude that the microinverter is an interesting commercial device which leads to wide developments in future years in order to adapt these technologies to the specific conditions and electrical standards of many countries around the world. For instance, it is common to find microinverters covering the standards of 110 V at 60 Hz and consisting in an adaptation of a microinverter developed to work at 220 V with an autotransformer to obtain the required voltage levels. Naturally, this solution increases the price and reduces the performance. Moreover, in several microinverters, because the converter topology is not known, it is not possible to conclude on the reliability or the stability of them, so that they can be categorized as a black box technology. Hence, it is necessary to develop a technology providing the most appropriate answers to well-posed technical problems of control, stability, assessment and reliability.

1.3.2 Standards and regulations

Some standards and regulations related to microinverters are listed below:

- Electromagnetic Compatibility (EMC)-Part 3-2: Limits for Harmonic Current Emissions (Equipment Input Current Under 16 A per Phase) [94].
- IEEE 1547.1-2005 IEEE Standard Conformance Test Procedures for Equipment Interconnecting Distributed Resources with Electric Power Systems [95].
- UL 1741. Standard for Safety Inverters, Converters, Controllers and Interconnection System Equipment for Use with Distributed Energy Resources [96].
- IEEE 929-2000. Recommended Practice for Utility Interface of Photovoltaic (PV) Systems [97].
- IEC 61727 (1995-06) Photovoltaic Systems – Characteristics of the Utility Interface [98].
- DS/EN 61000-3-2 (2001) EMC, Limits for harmonic emissions (equipment input current up to and including 16 A per phase) [99].

1.3.3 Challenges and opportunities

The microinverter concept appears as an interesting solution to many present challenges in PV systems. We can highlight that PV installations were not popular in the past for the reasons listed below:

- *Short lifetime of the converters:*

The need of high capacitances to reduce the voltage and current ripples in the PV modules forces the use of electrolytic capacitors which are very sensitive to the temperature and have a reduced lifetime in comparison with the PV module and other electronic components.

- *Need of storage elements:*

The grid-connected concept was only applied in large- size installations while little installations with a few PV modules were only used in isolated stand-alone applications requiring storage of energy. The use of batteries increases the cost of the system and reduces the reliability in general. Moreover, the supervision or maintenance increases the cost to sustain the operation of the system.

- *Difficult reproducibility:*

The need of different elements or devices to constitute a PV installation and their size leads to a difficult industrial production process because of the prohibitive assembly times and the required infrastructures.

- *Problems with partial shadowing:*

Depending on the size of the PV installation, the effect of the partial shadowing can have more or less impact on the general performance of the system. This is mainly due to the series connection of modules and the utilization of a MPPT algorithm per each series array.

- *Limited scalability:*

The cost of the PV system including PV modules and power converters increases with the number of PV modules in the system. Then, the initial investment for the realization of a PV system is important and requires a long amortization period (years or decades).

Considering the reduced life time of the converters, the system requires a replacement before the amortization of the initial investment. For all the previous reasons, many users considered other type of electric generators.

Taking into account all the points mentioned above, it is necessary to think in a low power solution in which the power converter can be integrated directly with the PV modules constituting a single device which permanently operates maximizing the power harvesting. Since each PV module has its own converter, the effect of partial shadowing is reduced. In addition, the resulting power device can be more easily assembled and reproduced leading to a flexible plug-and-play product. Users can built their own installations in non-used surfaces in their homes, using a step by step planning while enjoying this technology in the consumption but also contributing to the utilization of clean energies. In the future, roofs and windows can be used as areas for installing AC modules generating improvements in the developments of the photovoltaic cells. Figure 1.2 shows an example in which the microinverter concept is explained together with complementary products assembling a complete self-consumption solution.

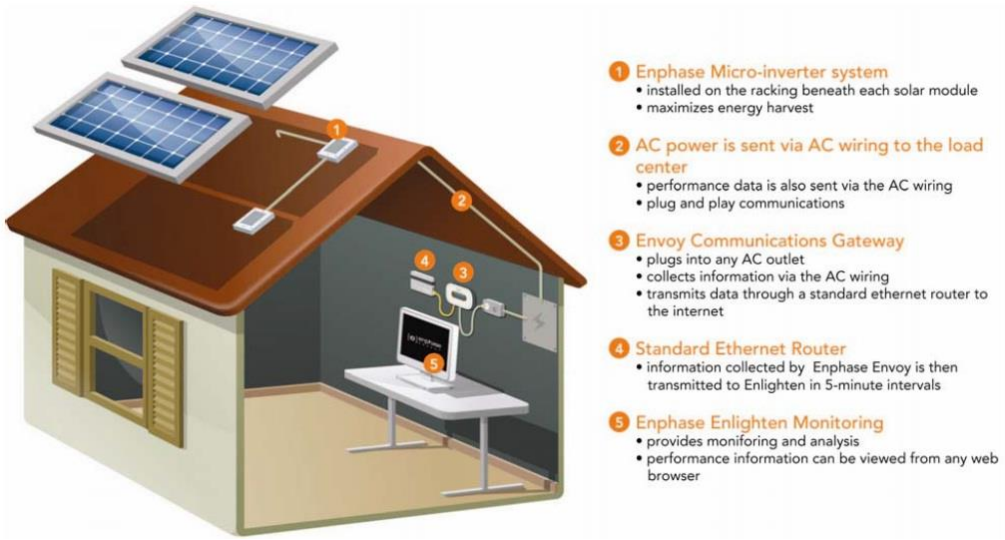

Fig. 1.2. Photovoltaic system based on “microinverters”. [Source: www.emphase.com]

The current interest in microinverters has prompted some manufacturers of digital devices to develop specific applications in the microinverter field [99]-[101]. The competition in the development of digital devices generates intensive works which give prospectively a central role to the microinverter in the next generation of photovoltaic installation around the world, this satisfying all the conditions needed in the context of electrical grids [102].

1.4 RESEARCH TRENDS IN MICROINVERTERS

As it was introduced in the state-of-the-art of the grid-connected PV generators, a trend to work with low power levels and distributed generators can be easily identified. Many research groups around the world consider the "microinverter" as an attractive subject in the fields of power electronics and control. The motivations of that research have been reported in [102]-[105] and are summarized in the following paragraphs.

1.4.1 Efficiency

Although the efficiency of some topologies have reached levels higher than 95% (see table 1.1), looking for improvements in the efficiency of other topologies can offer other advantages and change the current industrial preferences [106]. Because of the reduced efficiency of the commercial PV modules, any additional watt potentially exploitable is a significant contribution in the context of the microinverter-based distributed generation technology. However, it is worth noting that the reported efficiencies correspond to the peak efficiencies which are not the efficiencies in all operational points. Hence, the weighted efficiency (expression 1.1) is a more accurate measure of the global efficiency.

$$\eta_{eu} = 0.03\eta_{5\%} + 0.06\eta_{10\%} + 0.13\eta_{20\%} + 0.1\eta_{30\%} + 0.48\eta_{50\%} + 0.48\eta_{100\%} \qquad (1.1)$$

1.4.2 Semiconductor devices advances

The development of the technologies for power semiconductor devices has led to an increment of the power density in several power electronics applications. The use of SiC or GaN in fast recovery diodes and MOSFETs has increased the efficiency levels and reduced many undesired phenomena [107]. Moreover, it has been possible to increase the break-down voltages of the semiconductor devices improving their potentialities.

1.4.3 Diagnosis and fault detection

The reliability is another key aspect in the development of the microinverter system. It can be improved from the design of more stable systems providing robustness through the control. However, the diagnosis and fault detection of the device become necessary because the fault probability increases as the number of connected microinverters increases [108]. In the same direction as the anti-islanding algorithms which prevents erroneous operation of the system in the absence of the grid, the supervision of variables such as temperature, the injected DC current could be desirable to prevent faults in the system.

1.4.4 Life-time and reliability

The life-time of the microinverters is also a key factor in the development of the photovoltaic technology. In fact, one of the more relevant problems in photovoltaic systems in the last decades is the reduced life-time of the power converters in comparison with the PV modules [109]. The main problem is caused by the required large capacitance to decouple the PV modules, which can be only solved using electrolytic capacitors. In this context, the reduced life-time of these elements, mainly due to the temperature, voltage level and current ripple affect the microinverter. The advances in the improvement of capacitors less sensitive and more efficient allow replacement of the electrolytic capacitors by thin film capacitors [110]-[111], increasing the life-time of the photovoltaic inverters. It is apparent that this technology imposes to work with lower capacitances implying high voltages and low powers.

1.4.5 Leakage and ground currents

Another important task is related to the compatibility between the grid and the PV modules which depends on the isolation of the inverter. In transformer-less topologies, the leakage and ground currents are more important because there is no isolation element which can decouple them [112]-[113]. These currents are caused by oscillatory voltage components produced between the PV modules and the grid. They circulate through the parasitic capacitances introduced by the PV modules and the length of the

interconnection cables. As it can be expected, this problem is proportionally accentuated with a high number of PV modules.

1.4.6 Communications

The intensive work in the smart-grid and micro-grid fields introduces some special constraints for involved devices. Because of the need of centralized supervision of power converters, power meters and protection systems, some interactivity is necessary and then the role of communications in these systems is central [114]. They offer some opportunities of monitoring and supervision which have been extended for example to even smart phone applications (apps) [115] (see figure 1.3).

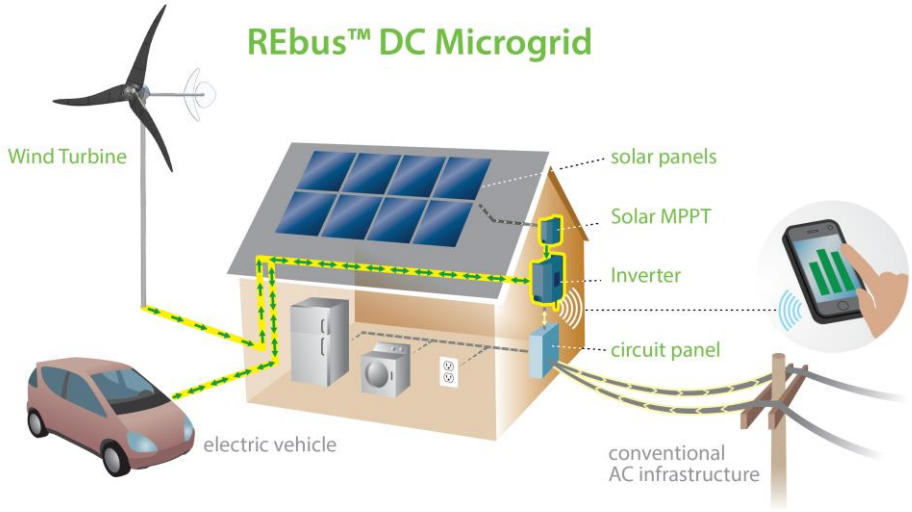

Fig. 1.3. Technology of interconnection of micro-grid including micro-inverters and smart-phone apps

1.4.7 Modeling and control

The system modeling and control theories also play a fundamental role in power electronics. It is well known that the majority of the applications requires at least of a feed-back control system. Many efforts have been made in the last decades to improve control techniques applicable to power conversion. Controllers for high frequency DC-DC, DC-AC and AC-DC converters have been involved in the associated basic control problems. However, complex structures with more than one conversion stage or special functionalities require a special attention to solve the related control problems. In the case of the photovoltaic generators these problems remain as an important challenge [116]-[121].

1.5 THE PROPOSED MICROINVERTER

1.5.1 General description

A possible way to contribute to the development of the low power DC-AC conversion for photovoltaic generation is to work on the development of a microinverter whose control problems are studied and solved by means of specific techniques. In our case, the selected technique is the sliding-mode control because of its inherent robustness and simple implementation [122]-[124].

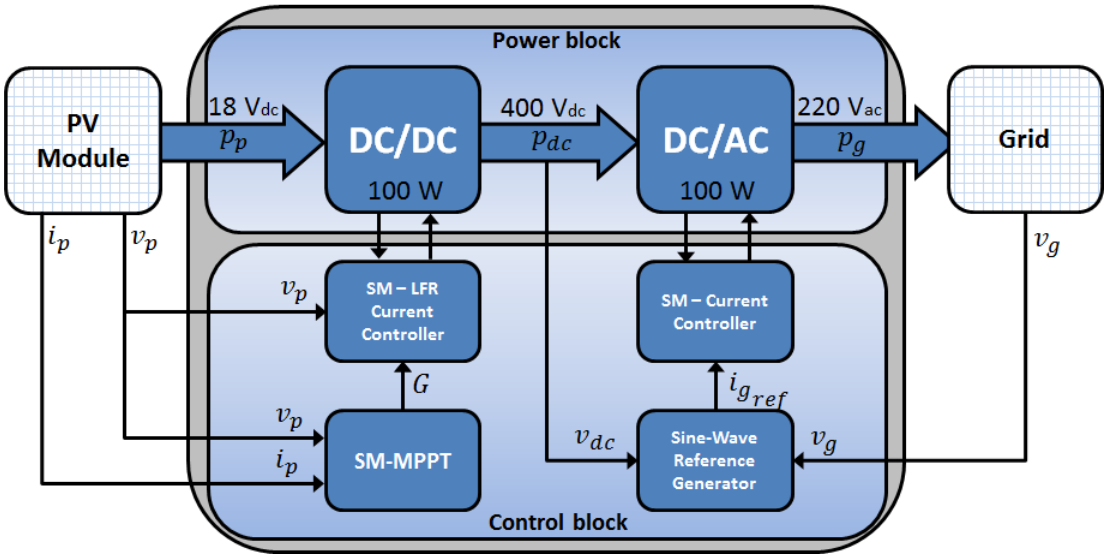

Fig. 1.4. General scheme of the sliding-mode controlled microinverter

As it is shown in figure 1.4, our proposed microinverter can be divided into a power and a control blocks. The power block is composed by both a DC-DC and DC-AC converters, which are respectively a “quadratic boost converter” and a “full-bridge converter”. The control block is composed by a MPPT algorithm (SM-MMPT), an impedance matching control for the DC-DC converter (SM-LFR Current Controller), a sine-wave current reference generator and a tracking reference control for the inverter (SM Current Controller). The control of the DC-Link is addressed through the box of the sine-wave generator which defines the amplitude of the injected current using a measurement of the voltage of the DC-link.

1.5.2 Proposed research and contributions

As mentioned above, the sliding-mode control technique is central in our work. First, we develop a new sliding-mode based MPPT algorithm that can be classified within the family of the sliding-mode Extremum Seeking Control MPPTs [125]-[129]. This algorithm does not employ the duty cycle as the manipulated variable but it uses instead the conductance to obtain impedance matching for maximum power transference. This constitutes a first contribution which in fact is not limited to our microinverter application.

The use of a high DC voltage (400 VDC) reduces the coupling capacitance allowing the use of thin film capacitors increasing the lifetime of our device. Then, considering the need to have a transformer-less converter topology with a high DC gain, we select the quadratic boost converter. This converter has been recently proposed in the literature and hence some important aspects such as discontinuous conduction modes, efficiency, dynamic performance together with stability and control have still to be investigated in detail [130]-[134]. The need of a simple control law orients our choice to a Sliding-Mode Loss-Free-Resistor (SM-LFR) design , this providing simultaneously the impedance matching with the PV module and the input voltage step-up to the required levels [135]-[136].

The DC-AC conversion stage is focused on the traditional H-bridge as grid-connected inverter. Using the SM-LFR properties allows considering together the PV module and the quadratic boost converter as a power source. Therefore, by using this kind of source to feed the inverter, we extended the group of the grid-connected inverters adding the class of "Power Source Inverter (PSI)" to the well-known Voltage Source Inverter (VSI) and Current Source Inverter (CSI). The sliding-mode control is applied to the inverter which tracks the current reference when both unipolar and bipolar commutation techniques are employed [137]-[139]. A deep study is done for the bipolar commutation applying the harmonic balance technique to the ideal sliding dynamic of the converter. Moreover, a linear controller is designed to regulate the voltage in the DC bus obtaining an appropriate equilibrium for the power [140]-[142]. The influence of the controller in the power quality is studied in the controller design. A feed-forward compensation technique is also proposed as an alternative to maximize the power quality in the grid connection.

By assembling all the above described building-blocks, we show that the sliding-mode control theory is a good candidate for the control requirements of a grid connected photovoltaic applications [143].

1.6 CONCLUSION

In this chapter, the state-of-the-art of module integrated converters, a review of commercial microinverters and AC modules and the main objectives of our work have been presented. The study of an entirely sliding-mode controlled single-phase transformer-less dual-stage grid-connected microinverter has been proposed by describing its main components, namely, a MPPT algorithm, a DC-DC converter and a DC-AC converter.

1.7 REFERENCES

Distributed generation

[1] L. Philipson, "Distributed and dispersed generation: addressing the spectrum of consumer needs," *in Proc. IEEE Power Engineering Society Summer Meeting*, vol. 3, pp. 1663-1665, 2000.

[2] F. Blaabjerg, Z. Chen, S.B. Kjaer, "Power electronics as efficient interface in dispersed power generation systems," *IEEE Trans. Power Electron.*, vol. 19, no. 5, pp. 1184-1194, Sep. 2004.

[3] Y. Xue, L. Chang; S.B. Kjaer, J. Bordonau, T. Shimizu, "Topologies of single-phase inverters for small distributed power generators: an overview," *IEEE Trans. Power Electron.*, vol. 19, no. 5, pp. 1305-1314, Sep. 2004.

[4] J.M. Carrasco, L.G. Franquelo, J.T. Bialasiewicz, E. Galvan, R.C.P. Guisado, Ma.A.M Prats, J.I. Leon, N. Moreno-Alfonso, "Power-Electronic Systems for the Grid Integration of Renewable Energy Sources: A Survey," *IEEE Trans. Ind. Electron.*, vol. 53, no. 4, pp. 1002-1016, Jun. 2006.

[5] J. M- Carrasco, L. Garcia Franquelo, J. T. Bialasiewicz, E. Galván, R. C. Portillo Guisado, Ma. Á. Martín Prats, J. I. León, N. Moreno-Alfonso, "Power-Electronic Systems for the Grid Integration of Renewable Energy Sources: A Survey," *IEEE Trans. Industry Appl.*, vol. 53, no. 4, pp. 1002-1016, Aug. 2006.

Microgrid-Distributed generation

[6] F. Katiraei, M.R. Iravani, "Power Management Strategies for a Microgrid With Multiple Distributed Generation Units," *IEEE Trans. Power Syst.*, vol. 21, no. 4, pp. 1821-1831, Nov. 2006.

[7] K.T. Tan, P.L. So, Y.C. Chu, M.Z.Q. Chen, "Coordinated Control and Energy Management of Distributed Generation Inverters in a Microgrid," *IEEE Trans. Power Delivery*, vol. 28, no. 2, pp.704-713, Apr. 2013.

Smartgrid-Distributed generation

[8] M. Vaziri, S. Vadhva, T. Oneal, M. Johnson, "Smart grid, Distributed Generation, and standards," *in Proc. IEEE Power and Energy Society General Meeting*, 2011, pp. 1-8.

[9] R. Hidalgo, C. Abbey, G. Joos, "Integrating distributed generation with Smart Grid enabling technologies," *in Proc. IEEE PES Conf. Innovative Smart Grid Technologies (ISGT Latin America)*, pp. 1-7, Oct. 2011.

Distributed generation-Photovoltaics

[10] M.M. Begovic, I. Kim, D. Novosel, J.R. Aguero, A. Rohatgi, "Integration of Photovoltaic Distributed Generation in the Power Distribution Grid," *in. Proc. 45th Hawaii Int. Conf. System Science (HICSS)*, 2012, pp.1977-1986.

[11] S. Teleke, F. Jahanbakhsh, F. Katiraei, J. Romero Aguero, "Analysis of interconnection of photovoltaic distributed generation," *in Proc. IEEE Industry Appl. Society Annu. Meeting (IAS)*, 2011, pp.1-6.

[12] J.R. Agüero, S.J. Steffel, "Integration challenges of photovoltaic distributed generation on power distribution systems," *in Proc. IEEE Power and Energy Society General Meeting*, 2011, pp.1-6.

[13] D.O. Akinyele, R.K. Rayudu, "Distributed photovoltaic power generation for energy-poor households: The Nigerian perspective," *in Proc. IEEE PES Asia-Pacific Power and Energy Engineering Conf. (APPEEC)*, 2013, pp. 1-6.

[14] M.M. Begovic, I. Kim; D. Novosel, J.R. Aguero, A. Rohatgi, "Integration of Photovoltaic Distributed Generation in the Power Distribution Grid," *in Proc. 45th Hawaii Int. Conf. System Science (HICSS)*, 2012, pp. 1977-1986.

Photovoltaic Stand-alone

[15] M. Kolhe, "Techno-Economic Optimum Sizing of a Stand-Alone Solar Photovoltaic System," *IEEE Trans. Energy Convers.*, vol. 24, no. 2, pp. 511-519, Jun. 2009.

[16] P.G. Nikhil, D. Subhakar, "Sizing and Parametric Analysis of a Stand-Alone Photovoltaic Power Plant," *IEEE Trans. Photovoltaics*, vol. 3, no. 2, pp. 776-784, Apr. 2013.

Photovoltaic Grid-Connected

[17] S.B. Kjaer, J.K. Pedersen, F. Blaabjerg, "A review of single-phase grid-connected inverters for photovoltaic modules," *IEEE Trans. Industry Appl.*, vol. 41, no. 5, pp. 1292-1306, Sep.-Oct. 2005.

[18] M. A. Eltawil, Z. Zhao, "Grid-Connected Photovoltaic Power Systems: Technical and Potential Problems—A review," *Renewable and Sustainable Energy Reviews*, Vol. 14, pp 112-129, Jan. 2010.

[19] B. Yang, W. Li, Y. Zhao, X. He, "Design and Analysis of a Grid-Connected Photovoltaic Power System," *IEEE Trans. Power Electron.*, vol. 25, no. 4, pp. 992-1000, Apr. 2010.

[20] M. Calais, J. Myrzik, T. Spoone, V. G. Agelidis, "Inverters for Single-phase Grid Connected Photovoltaic Systems - An Overview," *IEEE Trans. Ind. Appl.*,vol.41, no.5, pp.1292,1306, Sept.-Oct. 2005.

Photovoltaic Universal

[21] B. S. Prasad, S. Jain, and V. Agarwal, "Universal Single-Stage Grid-Connected Inverter," *IEEE Trans. Energy Convers.*, vol. 23, no. 1, pp. 128-137, Mar. 2008.

[22] A. Nagliero, R.A. Mastromauro, V.G. Monopoli, M. Liserre, A. Dell'Aquila, "Analysis of a universal inverter working in grid-connected, stand-alone and micro-grid," *in Proc. IEEE Int. Symp. Ind. Electron. (ISIE)*, 2010, pp. 650-657.

[23] J. M.A. Myrzlk, "Novel Inverter Topologies for Single-phase Stand-Alone or Grid-Connected Photovoltaic Systems," *in Proc. 4th IEEE Int. Conf. on Power Electron. Drive Syst.*, 2001, vol. 1, pp. 103-108.

Islanding detection and anti-islanding algorithms

[24] E.J. Estébanez, V.M. Moreno, A. Pigazo, M. Liserre, A. Dell'Aquila, "Performance Evaluation of Active Islanding-Detection Algorithms in Distributed-Generation Photovoltaic Systems: Two Inverters Case," *IEEE Trans. Ind. Electron.*, vol. 58, no. 4, pp. 1185-1193, Apr. 2011.

[25] S. Syamsuddin, N.A. Rahim, Krismadinata, J. Selvaraj, "Implementation of TMS320F2812 in Islanding Detection for Photovoltaic Grid Connected Inverter," *in Proc. Int. Conf. for Technical Postgraduates (TECHPOS)*, Dec. 2009, pp.1-5.

[26] I.V. Banu, M. Istrate, D. Machidon, R. Pantelimon, "A study on anti-islanding detection algorithms for grid-tied photovoltaic systems," *in Proc. Int. Conf. on Optimization of Electrical and Electronic Equipment (OPTIM)*, 2014, pp. 655-660.

[27] E.J. Estebanez, V.M. Moreno, A. Pigazo, M. Liserre, "An overview of anti-islanding detection algorithms in photovoltaic systems in case of multiple current-controlled inverters," *in Proc. 35th Annu. IEEE Conf. Ind. Electron. (IECON)*, 2009, pp. 4555-4560, Nov. 2009.

Photovoltaic central inverters

[28] B. Dhakal, F. Mancilla-David, E. Muljadi, "Centralized and modular architectures for photovoltaic panels with improved efficiency," *in Proc. North American Power Symp. (NAPS)*, 2012, pp. 1-6.

[29] S.K. Chattopadhyay, C. Chakraborty, B.C. Pal, "A hybrid multilevel inverter topology with third harmonic injection for grid connected photovoltaic central inverters," *in Proc. IEEE Int. Symp. Ind. Electron. (ISIE)*, 2012, pp. 1736-1741.

[30] J.A. Villarejo, A. Molina-Garcia, E. De Jodar, "Comparison of central vs distributed inverters: application to photovoltaic systems," *IEEE Int. Symp. Ind. Electron. (ISIE)*, 2011, pp. 1741-1746.

Photovoltaic string inverters

[31] L. Xiaoyan, D. Zhang, Y. Li, Y. Xu, "Multi-String Photovoltaic Grid-Connected Inverter Based on Alternate Single-Phase PWM Control," *in Proc. Asia-Pacific Power and Energy Engineering Conference (APPEEC)*, 2012, pp. 1-4.

[32] V.F. Pires, J.F. Martins, O.P. Dias, A.J. Pires, C. Hao, "A photovoltaic string architecture with multiple single-phase inverter modules," *in Proc. 13th Biennial Baltic Electron. Conf. (BEC)*, 2012, pp. 211-214.

[33] K.D. Papastergiou, P. Bakas, S. Norrga, "Photovoltaic string configuration for optimal inverter performance," *in Proc. IEEE 8th Int. Conf. on Power Electron. & ECCE Asia (ICPE & ECCE)*, 2011, pp. 1632-1636.

[34] J. M. A. Myrzik, M. Calais, "String and Module Integrated Inverters for Single-phase Grid Connected Photovoltaic Systems - A Review," *in Proc. IEEE Power Tech Conf.*, 2003.

Photovoltaic multi-string inverters

[35] H. Keyhani, H.A. Toliyat, W.C. Alexander, "A single-stage multi-string quasi-resonant inverter for grid-tied photovoltaic systems," *in Proc. IEEE Energy Convers. Congr. Expo. (ECCE)*, 2013, pp.1925-1932.

[36] Y.-M. Chen, K.-Y. Lo, Y.-R. Chang, "Multi-string single-stage grid-connected inverter for PV system," *in Proc. IEEE Energy Conversion Congr. Expo. (ECCE)*, 2011 pp. 2751-2756.

[37] D. Amorndechaphon, S. Premrudeepreechacharn, K. Higuchi, "Modified grid-connected current source inverter for multi-string PV system," *in Proc. IEEE PES Innovative Smart Grid Technologies (ISGT)*, 2012, pp. 1-8.

Module Integrated Converter

[38] Y. Zhou, L. Liu, H. Li, "A High-Performance Photovoltaic Module-Integrated Converter (MIC) Based on Cascaded Quasi-Z-Source Inverters (qZSI) Using eGaN FETs," *IEEE Trans. Ind. Electron.*, vol. 28, no. 6, pp. 2727-2738, Jun. 2013.

[39] F.F. Edwin, X. Weidong, V. Khadkikar, "Dynamic Modeling and Control of Interleaved Flyback Module-Integrated Converter for PV Power Applications," *IEEE Trans. Ind. Electron.,* vol. 61, no. 3, pp. 1377-1388, Mar. 2014.
[40] B. Sahan, A.N. Vergara, N. Henze, A. Engler, P. Zacharias, "A Single-Stage PV Module Integrated Converter Based on a Low-Power Current-Source Inverter," *IEEE Trans. Ind. Electron.,* vol. 55, no. 7, pp. 2602-2609, Jul. 2008.

Microinverters

[41] C.L. Trujillo, D. Velasco, E. Figueres, G. Garcerá, R. Ortega, "Modeling and control of a push–pull converter for photovoltaic microinverters operating in island mode," *Applied Energy*, vol. 88, pp. 2824-2834, Aug. 2011.
[42] R. W. Erickson and A. P. Rogers, "A Microinverter for Building-Integrated Photovoltaics," *in Proc. Applied Power Electron. Conf. Expo. (APEC)*, Feb. 2009, pp.911-917.
[43] A. Amirahmadi, L. Chen, U. Somani, H. Hu, N. Kutkut, I. Bartarseh, "High Efficiency Dual-Mode Current Modulation Method for Low-Power DC/AC Inverters," *IEEE Trans. Power Electron.,* vol. 29, no. 6, pp. 2638-2642, Jun. 2014.
[44] W.-F. Lai, S.-M. Chen, T.-J. Liang, K.-W. Lee, A. Ioinovici, "Design and Implementation of Grid Connection Photovoltaic Micro Inverter," *in Proc. Energy Conversion Congr. Expo. (ECCE)*, 2012, pp.2426-2432.

AC module

[45] R. Carbone, A. Tomaselli, "Recent Advances on AC PV-Modules for Grid-Connected Plants," *in Proc. Int. Conf. Clean Electrical Power (ICCEP)*, 2011, pp.124-129.
[46] H. Oldenkamp, I. de Jong, "Next Generation of AC-Module Inverters," in 2nd World Conf. and Exhibition on Photovoltaic *Solar Energy Conversion*, Vienna, 1998.
[47] R. H. Wills, S. Krauthamer, A. Bulawka, J. P. Posbic, "The AC Photovoltaic Module Concept," *in Proc. 32nd Intersociety Energy Convers. Engineering Conf. (IECEC)*, 1997, vol. 3, pp. 1562-1563.

Classification by number of stages

[48] S. B. Kjaer, J. K. Pedersen and F. Blaabjerg, "Power Inverter Topologies for Photovoltaic Modules – A Review," *in Proc. Conf. Record of the 37th Annu. Meeting Industry Applicat. Conf. (IAS)*, Oct. 2002, vol.2, pp. 782-788.
[49] B. K. Bose, P. M. Szczesny, R. L. Steigerwald, "Microcomputer control of a residential photovoltaic power conditioning system," *IEEE Trans. Ind. Applications,* vol. IA-21, pp. 1182–1191, Sep. 1985.

One-stage inverter

[50] L.-M. Wu, Y.-M. Yeh, "A Novel Single Stage Photovoltaic Energy Converter," *in Proc. Int. Conf. on Power Electron. Drive Syst. (PEDS)*, Nov. 2009, pp.482-487.

Two-Stage inverter

[51] D. Cruz Martins, R. Demonti, "Grid Connected PV System Using Two Energy Processing Stages," *in Conf. Record of the 29th IEEE Photovoltaic Specialists Conf.*, May 2002, pp.1649-1652.

Cascaded DC-DC

[52] G.R. Walker, P.C. Sernia, "Cascaded DC-DC converter connection of photovoltaic modules," *IEEE Trans. Power Electron.,* vol. 19, no. 4, pp. 1130-1139, Jul. 2004.
[53] E.I. Roman, P. Ibanez, S. Elorduizapatarietxe, R. Alonso, D. Goitia, I. Martinez de Alegria, "Intelligent PV Module for Grid-connected PV Systems," *in Proc. 30th Annu. Conf. of the IEEE Ind. Electron. Soc.,* November 2004, pp. 3082-3087.
[54] T. Shimizu, O. Hashimoto and G. Kimura, "A Novel High-Performance Utility-Interactive Photovoltaic Inverter System," *IEEE Trans. Power Electron.,* vol. 18, no. 2, pp. 704-711, Mar.2003.

Classification by DC-link

[55] Q. Li; P. Wolfs, "A Review of the Single Phase Photovoltaic Module Integrated Converter Topologies With Three Different DC Link Configurations," *IEEE Trans. Power Electron.,* vol. 23, no. 3, pp. 1320-1333, May. 2008.

Cyclonverter-based microinverter

[56] D.R. Nayanasiri, D.M. Vilathgamuwa, D.L. Maskell, "Half-Wave Cycloconverter-Based Photovoltaic Microinverter Topology With Phase-Shift Power Modulation," *IEEE Trans. Power Electron.,* vol. 28, no. 6, pp. 2700-2710, Jun. 2013.

Transformer-based

[57] S. B. Kjær, F. Blaabjerg, "Design Optimization of a Single Phase Inverter for Photovoltaic Applications," *in Proc. IEEE 34th Annu. Power Electron. Specialist Conf. (PESC*), June 2003, vol.3, pp. 1183-1190.
[58] T. Shimizu, M. Hirakata, T. Kamezawa, H. Watanabe, "Generation Control Circuit for Photovoltaic Modules," *IEEE Trans. Power Electron.*, vol. 16, no. 3, pp. 293-300, May 2001.

Transformer-less general

[59] D. Meneses, F. Blaabjerg, O. García, J.A. Cobos, "Review and Comparison of Step-Up Transformerless Topologies for Photovoltaic AC-Module Application," *IEEE Trans. Power Electron.,* vol. 28, no. 6, pp. 2649-2663, Jun. 2013.
[60] F. Schimpf, L. E. Norum, "Grid connected Converters for Photovoltaic, State of the Art, Ideas for Improvement of Transformerless Inverters," *in Proc. Nordic Workshop on Power and Ind. Electron.,* 2008.

Fly-back based

[61] N. Sukesh, M. Pahlevaninezhad, P.K. Jain, "Analysis and Implementation of a Single-Stage Flyback PV Microinverter With Soft Switching," *IEEE Trans. Ind. Electron.,* vol. 61, no. 4, pp. 1819-1833, Apr. 2014.

[62] A.C. Nanakos, E.C. Tatakis, N.P. Papanikolaou, "A Weighted-Efficiency-Oriented Design Methodology of Flyback Inverter for AC Photovoltaic Modules," *IEEE Trans. Power Electron.,* vol. 27, no. 7, pp. 3221-3233, Jul. 2012.

Interleaved Fly-back based

[63] L. Garcia-Rodriguez, E. Williams, J.C. Balda, J. Gonzalez-Llorente, E. Lindstrom, A. Oliva, "Dual-stage microinverter design with a GaN-based interleaved flyback converter stage," *in Proc. IEEE Energy Convers. Congr. Expo. (ECCE),* 2013, pp. 4496-4502.

[64] Z. Zhang; X.-F. He; Y.-F. Liu, "An Optimal Control Method for Photovoltaic Grid-Tied-Interleaved Flyback Microinverters to Achieve High Efficiency in Wide Load Range," *IEEE Trans. Power Electron.,* vol. 28, no. 11, pp. 5074-5087, Nov. 2013.

Transformer-less specific

[65] T. Kerekes, R. Teodorescu, P. Rodriguez, G. Vazquez, E. Aldabas, "A New High-Efficiency Single-Phase Transformerless PV Inverter Topology," *IEEE Trans. Ind. Electron.,* vol. 58, no. 1, pp. 184-191, Jan. 2011.

[66] M. Calaisa, V. G. Agelidisb, M. S. Dymondc, "A cascaded inverter for transformer-less single-phase grid-connected photovoltaic systems," *Renewable Energy*, vol. 22, pp 255-262, Jan/Mar 2001.

[67] T. Kerekes, R. Teodorescu, U. Borup, "Transformerless Photovoltaic Inverters Connected to the Grid," *in Proc. 22nd Annual IEEE Applied Power Electron. Conf. (APEC),* Mar. 2007, pp.1733-1737.

[68] S. Vasconcelos Araújo, P. Zacharias, R. Mallwitz, "Highly Efficient Single-Phase Transformerless Inverters for Grid-Connected Photovoltaic Systems," *IEEE Trans. Ind. Electron.,* vol. 57, no. 9, pp. 3118-3128, Sept. 2010.

[69] H. Xiao, S. Xie, Y. Chen, and R. Huang, "An Optimized Transformerless Photovoltaic Grid-Connected Inverter," *IEEE Trans. Ind. Electron.,* vol. 58, no. 5, pp. 1887-1895, May 2011.

[70] M. Kusakawa, H. Nagayoshi, K. Kamisako, K. Kurokawa, "Further Improvement of a Transformerless, Voltage-Boosting Inverter for AC Modules," *Solar Energy Materials and Solar Cells*, Volume 67, Mar. 2001, Pages 379-387.

[71] H. Zhang, L. Shan, J. Ren, B. Cheng, H. Zhang, "Study on Photovoltaic Grid-connected Inverter Control System," *in Proc. Int. Conf. Power Electron. Drive Syst. (PEDS),* Nov. 2009, pp.210-212.

[72] Y. Fang, X. Ma, Y. Xing, "Study on PV Micro-inverter with Coupled Inductors and Double Boost Topology," *in Proc. 7th IEEE Conf. Ind. Electron. Appl. (ICIEA)*, 2012, pp. 2054-2058.

Transformer-less multilevel

[73] O. Lopez, Remus Teodorescu, J. Doval-Gandoy, "Multilevel transformer-less topologies for single-phase grid-connected converters," *in 32nd IEEE Annu. Conf. on Industrial Electronics (IECON),* Nov. 2006, pp.5191-5196.

[74] M. Calais, V. G. Agelidis, L.J. Borle, M.S. Dymond, "A Transformerless Five Level Cascaded Inverter Based Single Phase Photovoltaic System," *in Proc. IEEE 31st Annu. Power Electronics Specialists Conf. (PESC),* vol.3, 2000, pp.1173-1178.

[75] E. Beser, B. Arifoglu, S. Camur, E.K. Beser, "A grid-connected photovoltaic power conversion system with single-phase multilevel inverter," *Solar Energy*, vol. 84, pp. 2056-2067, Dec. 2010.

Power conditioning

[76] Y. Nishida, N. Aikawa, S. Sumiyosm, H. Yamashita, H. Omon, "A Novel Type of Utility-Interactive Inverter for Photovoltaic System*," in Proc. 4th Int. Power Electron. Motion Control Conf. (IPEMC),* vol.3, Aug. 2004, pp. 1785-1790.

[77] J.-M. Kwon, B.-H. Kwon, K.-H. Nam, "High-efficiency module-integrated photovoltaic power conditioning system," *IET Power Electron.,* vol.2, no.4, pp. 410-420, July 2009.

Micro and mini inverter

[78] "Micro and Mini Inverter," Baldor Electric Company, [Online] Available: www.baldor.com

Commercial review

[79] "AURORA MICRO-0.3-I. Especificaciones generales modelos de exterior," Power –one, [Online] Available: www.power-one.com

[80] "DGM-460 Utility grade grid tie micro-inverter," Direct Grid Technologies, [Online] Available: www.directgrid.com

[81] "Emphase M215 Microinverter," Emphase, [Online] Available: www.emphase.com

[82] "SMI-S200W-72, SMI-S240W-72 Enecsys Micro Inverters," Enecsys, [Online] Available: www.enecsys.com

[83] "i-Microinverter GT-260," iEnergy, [Online] Available: www.i-energy.com.tw

[84] "INVOLAR MAC250 Photovoltaic Micro-Inverter, Installation and Operation Manual," INVOLAR Microinverters, [Online] Available: www.involar.net/involarWeb/

[85] ""Solarbridge phanteon" microinverter," SolarBringe Technologies, [Online] Available: www.solarbridgetech.com

[86] "Solar Europa's Micro-inverter Model EURO250," Solar Europa, [Online] Available: www.solareuropainternational.com

[87] "SPARQ's 190-Watt Microinverters," Sparq Systems Inc., [Online] www.sparksys.com

[88] "SunSine 200 AC Module: The ultimate All-in-One Solar Solution," GreenRAY, [Online] Available: www.greenraysolar.com

[89] "Replus-250 User Manual," ReneSola., [Online] Available: www.renesola.com

[90] "APS M1A-SAA Grid-connected Microinverter," Altenergy Power System Inc., [Online] Available: www.APSmicroinverter.com

[91] "Siemens Microinverter System," Siemens Industry Inc., [Online] Available : www.usa.siemens.com/microsolar

[92] “ABB micro inverter system MICRO-0.25/0.3/0.3HV-I-OUTD 0.25kW to 0.3kW,” ABB Solar Inverters, [Online] Available: www.abb.com/solarinverters
[93] “AEconversion Micro-Inverter Product Overview,” AE Conversion GmbH & Co. KG, [Online] Available: www.aeconversion.de

Normativity and standards

[94] Electromagnetic Compatibility (EMC)-Part 3-2: Limits-Limits for Harmonic Current Emissions (Equipment Input Current Under 16 A per Phase), EN 61000-3-2:2006, 2006.
[95] IEEE Std 1547.1-2005. IEEE Standard Conformance Test Procedures for Equipment Interconnecting Distributed Resources with Electric Power Systems.
[96] UL 1741. Standard for Safety Inverters, Converters, Controllers and Interconnection System Equipment for Use with Distributed Energy Resources.
[97] IEEE 929-2000. Recommended Practice for Utility Interface of Photovoltaic (PV) Systems.
[98] IEC 61727; "Characteristics of the utility interface for photovoltaic (PV) systems"; International Electrotechnical Commission, IEC 61727, 2002.

Application notes

[99] Microchip Technology Inc., Application Note 1338 - Grid-Connected Solar Microinverter Reference Design Using a dsPIC Digital Signal Controller, 2010.
[100] J. Tao, V. Xue. Application Report SPRABT0 – Grid-Connected Solar Inverter Implemented Using a C2000 MCU, Texas Instruments, 2013.
[101] LM5046, SM72295. Application Note 2116 - SolarMagic ICs in Micro-Inverter Applications, Literature Number: SNVA471A, National Semiconductor, 2011.

Motivations

[102] H. A. Sher, K.E. Addoweesh, “Micro-inverters - Promising Solutions in Solar Photovoltaics,” *Energy for Sustainable Development*, vol. 16, pp. 389-400, Dec. 2012.
[103] G. Spagnuolo, G. Petrone, S. V.Araujo, C. Cecati, E. Friis-Madsen, E. Gubia, D. Hissel, M. Jasinski, W. Knapp, M. Liserre, P. Rodriguez, R. Teodorescu, P. Zacharias, “Renewable Energy Operation and Conversion Schemes: A Summary of Discussions During the Seminar on Renewable Energy Systems,” *IEEE Trans. Ind. Electron*, vol. 4, no. 1, pp. 38-51, Mar. 2010.
[104] S. Fritzand, L.E. Norum, “Grid connected Converters for Photovoltaic, State of the Art, Ideas for Improvement of Transformerless Inverters,” *in Proc. Nordic Workshop on Power and Ind. Electron.* (NORPIE), Jun. 2008.
[105] P. P. Barker and James M. Bing, “Advances in Solar Photovoltaic Technology: An Applications Perspective,” *in Proc. IEEE Power Engineering Soc. General Meeting*, 2005, vol. 2, pp. 1955-1960.

Efficiency and global performance

[106] C. Prapanavarat, M. Barnes, N. Jenkins, “Investigation of the performance of a photovoltaic AC module,” *in Proc. IEEE Generation, Transmission and Distribution*, vol.149, no.4, pp.472-478, Jul 2002.

Use of novel semiconductor devices

[107] B. Burger, D. Kranzer, “Extreme High Efficiency PV-Power Converters,” *in Proc. 13th Eur. Conf. Power Electron. Appl. (EPE)*, 2009, pp.1-13.

Fault tolerance or diagnosis

[108] K.-H. Chao, C.-J. Li, S.-H. Ho, “Modeling and Fault Simulation of Photovoltaic Generation Systems Using Circuit-Based Model,” *in Proc. IEEE Int. Conf. Sustainable Energy Technologies (ICSET)*, Nov. 2008. pp. 290-294.

Long life-time

[109] C. Rodriguez, G.A.J. Amaratunga, “Energy control for long lifetime photovoltaic ac module inverter,” *in Proc. 37th IEEE Power Electron. Specialists Conf. (PESC)*, 2006, pp.1-6.

Thin-film Capacitors

[110] H. Haibing, S. Harb, N.H. Kutkut, Z.J. Shen, I. Batarseh, “A Single-Stage Microinverter Without Using Eletrolytic Capacitors,” *IEEE Trans. Power Electron.*, vol. 28, no. 6, pp. 2677-2687, Jun. 2013.
[111] G.Frattini, G.Petrone, G.Spagnuolo, M.Vitelli, “AC Module Design Employing Low Capacitance Values,” *in Proc. IEEE Int. Symp. Ind. Electron. (ISIE)*, July 2010, pp.3444-3449.

Leakage and ground currents

[112] O. López, F.D. Freijedo, A. G. Yepes, Pablo Fernández-Comesaña, J. Malvar, R. Teodorescu, J. Doval-Gandoy, “Eliminating Ground Current in a Transformerless Photovoltaic Application,” *IEEE Trans. Energy Convers.*, vol. 25, no. 1, Mar. 2010
[113] O. Lopez, R. Teodorescu, F. Freijedo, J. Doval-Gandoy, “Leakage current evaluation of a single phase transformer-less PV inverter connected to the grid,” *in Proc. 22nd Annual IEEE Applied Power Electron. Conf. (APEC)*, 2007, pp. 907-912.

Communications and smart-grid

[114] W.-Y. Choi, J.-S. Lai, “High-efficiency grid-connected photovoltaic module integrated converter system with high-speed communication interfaces for small-scale distribution power generation,” *Solar Energy*, vol. 84, April 2010, pp. 636-649.
[115] “REbus DC Microgrid, PV Link,” [Online] Available: www.pika-energy.com/company/our-technology

Modeling and control issues

[116] S. Jiang, D. Cao, F. Z. Peng, Yuan Li, “Grid-Connected Boost-Half-Bridge Photovoltaic Micro Inverter System Using Repetitive Current Control and Maximum Power Point Tracking*,” in Proc. 27th Annu. IEEE Applied Power Electron. Conf. Expo. (APEC)*, Feb. 2012, pp.590-597.

[117] L. Sujuan, J. Qiufeng, Y. Hai-zhu "Study of Control Strategy on Small Power Photovoltaic Grid-connected Generation System," *in Proc. Int. Conf. on Intelligent Computing and Cognitive Informatics*, 2010, pp. 271-274.
[118] A. Andreotti, G.Langella, C. Noviello, "Influence of inverter control logics on energetic performances of PV modules – inverter systems," *in Proc. Int. Conf. on Clean Electrical Power*, 2009, pp.178-181.
[119] M. Makhlouf, F. Messai, H. Benalla, "Modeling and Control of a Single-Phase Grid Connected Photovoltaic System," *Journal of Theoretical and Applied Information Technology*, vol. 37, no.2, Mar. 2012.
[120] Y. Chen, F. Liu, "Research on Design and Control of a Grid Connected Photovoltaic Inverter," *in Proc. 6th IEEE Int. Power Electron. Motion Control Conf. (IPEMC)*, May 2009, pp. 2165-2169.
[121] B.M.T. Ho, H.S.-H. Chung, "An Integrated Inverter With Maximum Power Tracking for Grid-Connected PV Systems," *IEEE Trans. Power Electron.*, vol. 20, no. 4, pp. 953-962, Jul. 2005.

Sliding-mode control

[122] V.I. Utkin, J. Guldner and J. Shi, Sliding mode control in electromechanical systems, CRC Press, 2th. Edition, Taylor and Francis Group, 2009.
[123] H. Sira-Ramirez and R. Silva-Ortigoza, Control Design Techniques in Power Electronic Devices, 1th. Edition. Germany: Springer, 2006.
[124] H. Sira-Ramirez, "Sliding motions in bilinear switched networks," *IEEE Trans. Circuits and Systems*, vol. 34, no. 8, pp. 919-933, Aug. 1987.

Sliding-mode MPPT

[125] Y. Levron, D. Shmilovitz, "Maximum Power Point Tracking Employing Sliding Mode Control," *IEEE Trans. Circuits and Syst. I: Regular Papers*, vol. 60, no. 3, pp. 724-732, Mar. 2013.
[126] I.-S. Kim, "Robust maximum power point tracker using sliding mode controller for the three-phase grid-connected photovoltaic system," *Solar Energy*, vol. 81, pp. 405-414, 2007.
[127] C.-C. Chu, C.-L. Chen, "Robust maximum power point tracking method for photovoltaic cells: A sliding mode control approach," *Solar Energy*, vol. 83, pp. 1370-1378, 2009.
[128] V.I. Utkin, Sliding Modes in Control and Optimization, Ed. Springer-Verlag, 1981.
[129] A.H. Alqahtani, V.I. Utkin, "Self-optimization of photovoltaic system power generation based on sliding mode control," *in Proc. 38th Annual Conf. on IEEE Ind. Electron. Society (IECON)*, 2012, pp. 3468-3474.

Quadratic boost converter

[130] J. Leyva-Ramos, M.G. Ortiz-Lopez, L.H. Diaz-Saldierna and J.A. Morales-Sandaña, "Switching regulator using a quadratic boost converter for wide DC conversion ratios", *IET Power Electron.*, vol. 2, no. 5, pp. 605-613, 2009.
[131] J.A. Morales-Saldaña, R. Loera-Palomo, E. Palacios-Hernández, J.L. González-Martínez, "Modelling and control of a DC-DC quadratic boost converter with R2P2," *IET Power Electron.*, vol. 7, no. 1, pp. 11-22, 2014.
[132] P. Yang, J. Xu, G. Zhou, F. Zhang, "Analysis of sensorless peak current mode controlled quadratic boost converter," *in proc. of the IEEE Int. Symposium on Ind. Electron. (ISIE)*, pp. 200-204, 2012.
[133] O. Lopez-Santos, L. Martinez-Salamero, G. Garcia, H. Valderrama-Blavi, T. Sierra-Polanco, "Robust Sliding-Mode Control Design for a Voltage Regulated Quadratic Boost Converter," *IEEE Trans. Power Electron.*, vol. PP, no. 99, pp. 1-15, 2015.
[134] O. Lopez-Santos, L. Martinez-Salamero, G. Garcia, H. Valderrama-Blavi and D.O. Mercuri, "Efficiency analysis of a sliding-mode controlled quadratic boost converter," *IET Power Electron.*, vol. 6, no. 2, pp. 364-373, 2013.

LFR-Concept

[135] S. Singer, "Realization of loss-free resistive elements," *IEEE Trans. Circuits and Systems*, vol. 37, no. 1, pp. 54-60, 1990.
[136] A. Cid-Pastor, L. Martinez-Salamero, A. El Aroudi, R. Giral, J. Calvente, R. Leyva, "Synthesis of loss-free-resistors based on sliding-mode control and its applications in power processing," *Control Engineering Practice*, vol. 21 no. 5 pp. 689-699. 2013.

Sliding-mode grid-connected inverter

[137] V. Fernao Pires, D.M. Sousa, J.F. Martins, "Controlling a grid-connected T-type three level inverter system using a sliding mode approach," *in proc. IEEE Int. Symposium on Industrial Electron.*, pp. 2002-2007, 2014.
[138] H. Jiabing, Z.Q. Zhu, H. Nian, L. Shang, Y. He, "Sliding mode current control of grid-connected voltage source converter," *in proc. of the IEEE Energy Conversion Congress and Exposition (ECCE)*, pp. 912-919, 2010.
[139] I.-S. Kim, "Sliding mode controller for the single-phase grid-connected photovoltaic system," *Applied Energy*, vol. 83, pp. 1101-1115, 2006.

Control of the DC-bus

[140] L. Zhang, K. Sun, Y. Xing, L. Feng, H. Ge, "A Modular Grid-Connected Photovoltaic Generation System Based on DC bus," IEEE Trans. Power Electron., vol. 26, no. 2, pp. 523-531, Feb. 2011.
[141] C. Meza, J.J. Negroni, D. Biel, F. Guinjoan, "Energy-Balance Modeling and Discrete Control for Single-Phase Grid-Connected PV Central Inverters," IEEE Trans. Ind. Electron., vol. 55, no. 7, pp. 2734-2743, Jul. 2008.
[142] M. Karimi-Ghartemani, S.A. Khajehoddin, P. Jain, A. Bakhshai, "A Systematic Approach to DC-Bus Control Design in Single-Phase Grid-Connected Renewable Converters," *IEEE Trans. Power Electron.*, vol. 28, no. 7, pp. 3158-3166, 2013.

Our proposal

[143] O. Lopez-Santos, L. Martinez-Salamero, G. Garcia, H. Valderrama-Blavi, "Sliding-mode control of a transformer-less dual-stage grid-connected photovoltaic micro-inverter," *in Proc. 10th Int. Multi-Conf. on Systems, Signals & Devices (SSD)*, 2013, pp. 1-6.

Chapter 2

MPPT Algorithm: Sliding-Mode Extremum Seeking Control

2.1 INTRODUCTION

Among the different control functions that integrate the photovoltaic generators, the controller which defines the instantaneous power extracted from the PV modules can be considered as one of the most influential in the overall performance of the system. Therefore, the proper operation of this controller consists in enforcing the system to always work at the maximum power. To solve this important problem, the controller must have the ability not only to find a maximum power point but also to permanently track the maximum power point when unpredictably changes appear in the power as a consequence of changes in the environmental variables (irradiance and temperature). Hence, a solution of the problem can be obtained using tracking algorithms or optimization methods. In the control community, the problem has been largely investigated and is known as the "Maximum Seeking Control". In the context of energy conversion, the problem is the well-known "Maximum Power Point Tracking" (MPPT) and it has been extensively studied in the literature [1]-[9]. Among the existing methods, some of them use the characteristic of the power source. Also, there can be either parametric-based or heuristic-based algorithms. The first group uses a parametrical model and works with direct or indirect measurements of the power source [10]-[12]. The second group is composed of methods that use measurements of the electrical variables in order to determine whether the system is at the maximum power point or not. Recently, an interesting MPPT integrating both parametric and heuristic methods has been proposed [13].

From a widespread and historically point of view, the heuristic MPPT algorithms can be classified as part of the Extremum Seeking Control (ESC) techniques which have been studied since the 1950s. A first group involves algorithms which apply an additive disturbance or introduce an oscillation in one or more variables of the system observing the evolution of some variables in order to determine the appropriate action of the control. The perturbation can be introduced in either the electric variables (current and voltage) or in the control variables such as frequency [14]-[16] or duty cycle [17]-[21]. Some of these methods are named Perturb and Observe (P&O) algorithms which are widely used in academic studies and commercial products because of its simplicity and low cost implementation [22]-[28]. However, despite of the volume of latest works in P&O algorithms, this research field still retains the attention of researchers who try to improve their performances [29]-[34]. A second group involves algorithms which apply slope regulation, because a necessary condition to reach the maximum of a function consists in having a null derivative. These methods also introduce a disturbance in the system to evaluate the derivative of the power for determining the action of the control. In the context of photovoltaic applications with this philosophy, we can cite the Incremental Conductance (INC) [35]-[42] and the Incremental Resistance [43]-[44]. These methods are also the source of constant research focused on the improvement of their performances [45]-[47]. A third group considers the algorithms which define an error signal between the maximum or a fictitious maximum and the actual operational point in order to ensure a trajectory toward the real maximum of the function. These are named peak-holding, peak-searching or peak-detection algorithms and are widely involved in many engineering areas. This group includes the fuzzy-logic [48]-[52], the predictive [53] and the random search approaches [54]. Other methods such as Ripple Correlation Control (RPC) can be considered as an ESC method [55], because they use a natural oscillatory component and the knowledge of its behavior around the optimum of the function to drive the system to a single desired operational point [56]-[59]. Many different proposals are named and grouped specifically under ESC [60]-[70].

Regarding the tracking of the maximum power point as an optimization problem, some methods use a sliding-mode strategy as the way to ensure that the maximum is reached. These MPPT techniques are known in the literature as the Sliding-Mode Extremum Seeking Control (SM-ESC) methods [71]-[75], and can be combined in some cases with a perturb and observe algorithm [76]. An interesting approach to solve the problem applying sliding-modes is presented as "*one-dimensional self-optimization*"

by professor V. Utkin in [77] (published in 1981). Recently, an attempt to describe and analyze this algorithm working in a PV system has been presented in [78]. It has to be pointed out that this preliminary work, introducing the Utkin's algorithm into photovoltaics applications has captured our interest and motivated the work presented in this chapter. The main characteristics of the proposed method can be summarized as follows:

- The implementation is easy.
- The performances of the method can be justified theoretically.
- The knowledge of an upper bound of the panel characteristics derivative and the measurement of the extracted power are the only needed information.
- Four tuning parameters have to be selected. They must satisfy simple inequality constraints and, because their impacts on the performance of the method are clearly identified, they can be easily determined.

The MPPT algorithm must be compatible with the proposed control in the DC-DC stage (SM-LFR). In that sense, the current control loop requires a conductance reference which must be given by the MPPT algorithm. This constitutes a first difference with the other sliding-mode methods: the output variable of the MPPT is the conductance not the duty cycle. The first part of this chapter describes an asymptotic approximation of the I-V and P-V characteristics in order to extract a P-G characteristic where *G* represents the equivalent conductance of the DC-DC converter determining the limits of the slopes, and thus avoiding a complex modelling of the PV module

Then, the new algorithm is studied in detail in terms of sliding-mode techniques, namely, attraction and transversal conditions of the sliding surface using the equivalent control method are developed. The dynamic responses of the algorithm produced by a sudden positive or negative change due to variations in irradiance are also studied. Simulation and experimental results illustrate the potentialities of the new algorithm.

2.2 ASYMPTOTIC MODELING OF THE PV MODULE

The Current-Voltage (I-V) and Power-Voltage (P-V) characteristics of the solar panel are crucial in the MPPT problem [79]. Because of the complexity of the mathematical models which define these characteristics, some methods work with approximations in

order to reduce the complexity of the controller synthesis [80]. In this paragraph, the objective is to asymptotically approximate the I-V and the P-V characteristics of a PV module in order to determine a P-G characteristic curve.

As shown in figure 2.1a, the I-V characteristic curve of a PV module can be approximated by two asymptotes. They are defined using the short circuit current (I_{sc}), the open circuit voltage (V_{oc}) and the voltage corresponding to the maximum power (V_{mp}).

Using this approximation, the I-V characteristic is defined by:

$$i_p(v_p) = \begin{cases} I_{sc} & 0 < v_p < V_{mp} \\ -G_0(v_p - V_{oc}) & V_{mp} < v_p < V_{oc} \end{cases} \quad (2.1)$$

where $G_0 = I_{sc}/(V_{oc} - V_{mp})$. The P-V characteristic can be deduced multiplying the previous approximation by v_p. The two asymptotes are transformed into the curves depicted in figure 2.1b. In order to improve the approximation, a third asymptote corresponding to the maximum attainable power (P_{mp}) is introduced (in red in figure 2). An analytical expression for the derived approximation follows and is given by:

$$p_p(v_p) = \begin{cases} I_{sc}v_p & 0 < v_p < V_1 \\ P_{mp} & V_1 < v_p < V_2 \\ -G_0({v_p}^2 - V_{oc}v_p) & V_2 < v_p < V_{oc} \end{cases} \quad (2.2)$$

where $V_1 = P_{mp}/I_{sc}$. V_2 is the positive root of the following second order polynomial:

$${V_2}^2 - V_{oc}V_2 + \frac{P_{mp}}{G_0} = 0$$

and can be expressed as:

$$V_2 = 0.5V_{oc} + \sqrt{0.25{V_{oc}}^2 - P_{mp}(V_{oc} - V_{mp})/I_{sc}}$$

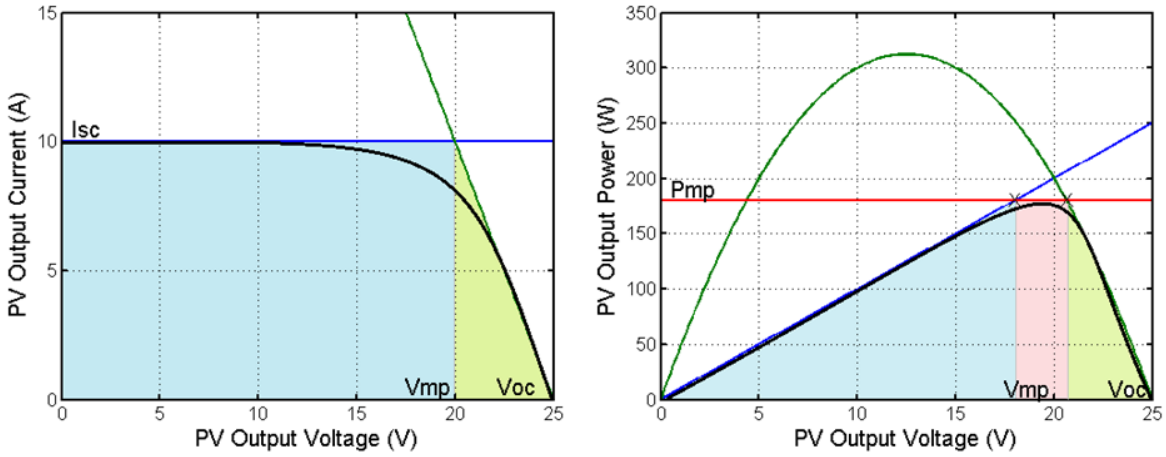

Fig. 2.1. Asymptotic approach of the characteristic curves of the PV module: a) I-V; b) P-V.

In order to obtain the P-G characteristic, the variable G, which is defined as $G = i_p/v_p$ is introduced in the previous approximation. Remarking that ${v_p}^2 = p_p/G$ and replacing in the previous approximation leads to:

$$p_p(G) = \begin{cases} {G_0}^2 {V_{oc}}^2 \dfrac{G}{(G+G_0)^2} & 0 < G < G_1 \\ P_{mp} & G_1 < G < G_2 \\ \dfrac{{I_{sc}}^2}{G} & G_2 < G < \infty \end{cases} \tag{2.3}$$

where $G_2 = {I_{sc}}^2/P_{mp}$ and $G_1 = \left({G_0}^2 {V_{oc}}^2 \left[1 - \sqrt{1 - 4P_{mp}/\left({V_{oc}}^2 G_0\right)}\right] - 2G_0 P_{mp}\right)/2P_{mp}$.

The resulting characteristic is depicted in figure 2.2.

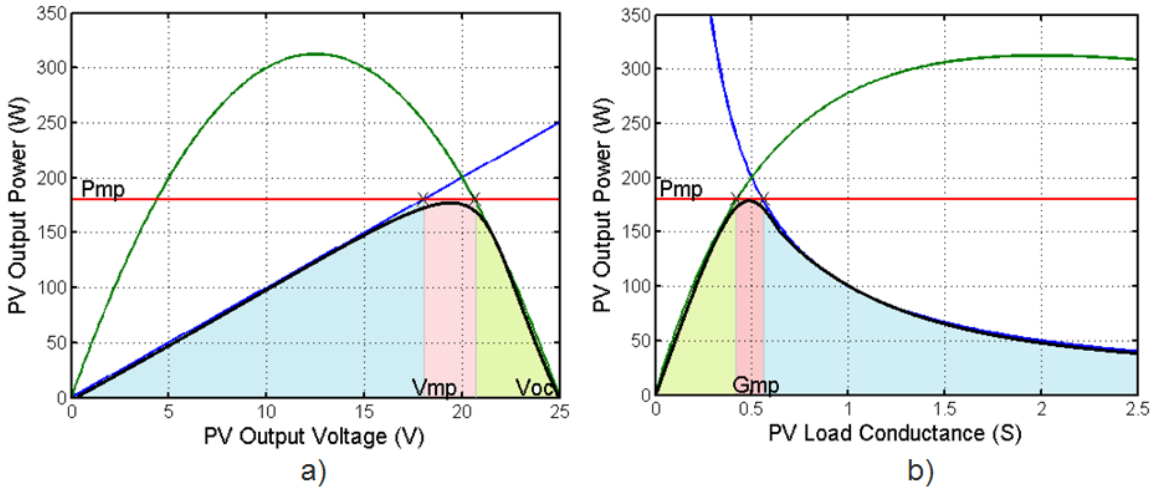

Fig. 2.2. Asymptotic approach of the characteristic curves of the PV module: a) P-V; b) P-G.

The maximum derivatives of the two asymptotes representing the curve $p_p(G)$ are evaluated for $G = G_1$ and $G = G_2$, obtaining:

$$\frac{dP_p}{dG}(G_1) = \frac{{G_0}^2 {V_{oc}}^2 (G_0 - G_1)}{(G_1 + G_0)^3} \tag{2.3}$$

$$\frac{dP_p}{dG}(G_2) = -\frac{{I_{sc}}^2}{{G_2}^2} \tag{2.4}$$

where the maximum computed value using (2.3) and 2.4 is always above that the maximum real derivative.

Usually, in a MPPT algorithm, the power versus duty cycle characteristic is used. Here, because the high-gain of the converter, the duty cycle could also be high (greater than 0.75). Then, the conditioning of the P-G characteristic is better than the one of power versus duty cycle. The main reason, as the previous analysis revealed, is that the high duty cycles are located between small values of conductance and the values of conductance around the maximum power P_{mp}. Also, it is worth noting that this transformation allows an objective function which has a domain of conductance from zero to infinite solving the problem that is present in the P-V characteristic when the domain is defined between zero and the open circuit voltage. These facts explain why the P-G characteristic is preferred. In addition, the DC-DC converter will be controlled through its input conductance to extract the maximum power of a PV module.

2.3 A NEW SLIDING-MODE MPPT METHOD

2.3.1 Fundamentals of the method

The proposed method for tracking the MPPT is summarized in figure 2.3. The main idea is to define a sliding surface $S\left(P_{p_{ref}}, P_p\right) = \varepsilon(t) = P_{p_{ref}}(t) - P_p(t)$ and at each instant t, to extract a power $P_p(t)$ from the solar panel equal to the average value of a given power reference $P_{p_{ref}}(t)$. This is possible, acting appropriately on the conductance $G(t)$. The algorithm ensures that the reference $P_{p_{ref}}(t)$ increases automatically until it reaches the maximal power P_{mp} where it is maintained. When an abrupt change in irradiance occurs, a discontinuous change in $P_p(t)$ can be observed, but due to the sliding mode control strategy, the algorithm is able to redefine an

appropriate reference $P_{p_{ref}}(t)$ which in turn converges to the new admissible maximal power.

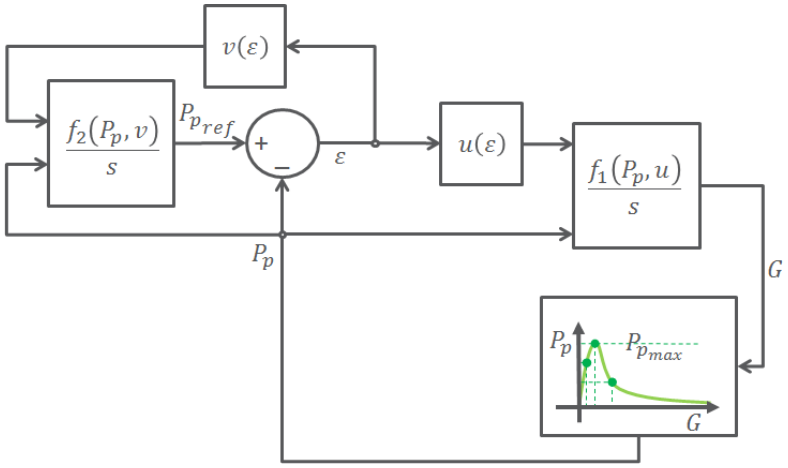

Fig. 2.3. Block diagram of the new self-optimized MPPT algorithm

The equations associated with the flow-chart represented in figure 2.3 are given by:

$$\frac{dG}{dt} = f_1(P_p, u) \tag{2.6}$$

$$\frac{dP_{p_{ref}}}{dt} = f_2(P_p, v) \tag{2.7}$$

$$f_1(P_p, u) = K_1 P_p u, \quad K_1 > 0 \tag{2.8}$$

$$f_2(P_p, v) = K_2 P_p + M P_p v, \quad K_2 > 0, \quad M > 0 \tag{2.9}$$

$$\varepsilon(t) = P_{p_{ref}}(t) - P_p(t) \tag{2.10}$$

$$u = sign(\varepsilon) \tag{2.11}$$

$$v = -\frac{1}{2} - \frac{1}{2}\, sign(\varepsilon) \tag{2.12}$$

The signals u and v are represented in figure 2.4.

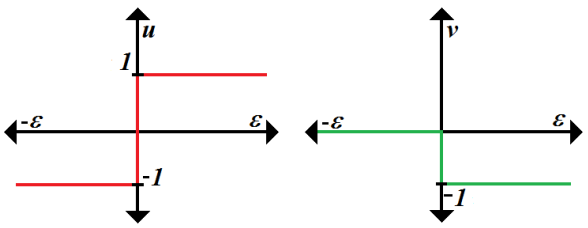

Fig. 2.4. Ideal switching functions of the proposed sliding-mode MPPT.

2.3.2 Reachability conditions

First, the conditions of reachability to the sliding surface are analyzed. This analysis allows the determination of constraints on constants M, K_1 and K_2 guaranteeing that the sliding surface is always reachable. Consider the Lyapunov function:

$$\boldsymbol{V}(\varepsilon) = \frac{1}{2}\varepsilon^2 \tag{2.13}$$

Reachability is ensured if $\varepsilon\dot{\varepsilon} < 0$. We have:

$$\varepsilon\dot{\varepsilon} = \varepsilon P_p\left[-\frac{1}{2}M - \frac{1}{2}Msign(\varepsilon) + K_2 - \frac{dP_p}{dG}K_1 sign(\varepsilon)\right] \tag{2.14}$$

But $\varepsilon = |\varepsilon| sign(\varepsilon)$ and $|\varepsilon| = \varepsilon \cdot sign(\varepsilon)$. Then:

$$\begin{aligned}\varepsilon\dot{\varepsilon} &= P_p\left[-\frac{1}{2}M\varepsilon - \frac{1}{2}M|\varepsilon| + K_2\varepsilon - \frac{dP_p}{dG}K_1|\varepsilon|\right] \\ &= |\varepsilon|P_p\left[-\frac{1}{2}Msign(\varepsilon) - \frac{1}{2}M + K_2 sign(\varepsilon) - \frac{dP_p}{dG}K_1\right]\end{aligned} \tag{2.15}$$

1) If $\varepsilon > 0$:

$$\varepsilon\dot{\varepsilon} = |\varepsilon|P_p\left[-M + K_2 - \frac{dP}{dG}K_1\right] \tag{2.16}$$

$$\text{If } M > K_2 + \left|\frac{dP_p}{dG}\right|_{max} K_1 \text{ then } M > K_2 - \frac{dP_p}{dG}K_1 \text{ and } \varepsilon\dot{\varepsilon} < 0 \tag{2.17}$$

2) If $\varepsilon < 0$

$$\varepsilon\dot{\varepsilon} = |\varepsilon|\left[-K_2P_p - \frac{dP}{dG}K_1P_p\right] = |\varepsilon|P_p\left[-K_2 - \frac{dP}{dG}K_1\right] \tag{2.18}$$

$$\text{If } K_2 > \left|\frac{dP_p}{dG}\right|_{max} K_1 \text{ then } K_2 > -\frac{dP_p}{dG}K_1 and\ \varepsilon\dot{\varepsilon} < 0 \tag{2.19}$$

In conclusion, the conditions for guaranteeing $\varepsilon\dot{\varepsilon} < 0$ are:

$$M > K_2 + \left|\frac{dP_p}{dG}\right|_{max} K_1 \text{ and } K_2 > \left|\frac{dP_p}{dG}\right|_{max} K_1 \tag{2.20}$$

The above conditions show that the algorithm attains the sliding surface at least asymptotically. In practice, it is necessary to attain the sliding-surface in a finite time. The appropriate stability concept in such a situation is the "finite time stability concept" whose definition can be found, for example, in [81]. Let us define:

$$C_1 = \left[M - K_2 + K_1 \left|\frac{dP_p}{dG}\right|_{max}\right] P_p(0^+) > 0$$

$$C_2 = \left[K_2 - K_1 \left|\frac{dP_p}{dG}\right|_{max}\right] P_p(0^+) > 0$$

and $C = \min\{C_1, C_2\}$. From (2.16) and (2.18), we can deduce, remarking that $|\varepsilon| = \sqrt{2}C[\boldsymbol{V}(\varepsilon)]^{\frac{1}{2}}$:

$$\dot{\boldsymbol{V}}(\varepsilon) + \sqrt{2}C[\boldsymbol{V}(\varepsilon)]^{\frac{1}{2}} \leq 0 \qquad \forall \quad \varepsilon$$

From theorem 4.2 in [81] (p. 760), we can conclude that the error $\varepsilon(t)$ is finite-time stable, meaning that $\varepsilon(t)$ attains the sliding-surface in a finite time T_ε satisfying (see [80]):

$$T_\varepsilon \leq \frac{|\varepsilon(0^+)|}{C}$$

Another remarkable point is that the previous conditions only depend on the knowledge of $\left|\frac{dP_p}{dG}\right|_{max}$. From the panel characteristic curve and in particular from the approximation developed in paragraph 2, it is possible to easily evaluate $\left|\frac{dP_p}{dG}\right|_{max}$. In the sequel, we consider that the different constants in the algorithm are selected according to the above reachability conditions.

2.3.3 Equivalent control

If we suppose that the algorithm has reached the sliding surface, we have $\varepsilon(t) = 0$ and $P_p(t) = P_{Pref}(t)$. The equivalent controls are defined equating the derivative of ε to zero. Then, denoting equivalent controls by u_{eq} and v_{eq}, they must satisfy:

$$\frac{d\varepsilon}{dt} = MP_p v_{eq} + K_2 P_p - \frac{dP_p}{dG} K_1 P_p u_{eq} = 0 \text{ with } -1 < v_{eq} < 0 \text{ and } -1 < u_{eq} < 1 \qquad (2.21)$$

If $P_{Pref}(t)$ changes and if the reachability conditions are satisfied, $P_p(t)$ tracks the reference $P_{Pref}(t)$. Now it is necessary to determine under what conditions, the algorithm increases $P_{Pref}(t)$ until it reaches P_{mp}.

2.3.4 Trajectory towards the maximum power point

To analyze the evolution of $P_{Pref}(t)$, it has to be remarked first that nonlinearities u and v are practically implemented as shown in figure 2.5. As reported in sliding mode control approaches, a hysteresis band Δ is introduced in the switching functions. Here only v is modified accordingly while u is maintained ideal. The resulting waveforms are presented in figure 2.6.

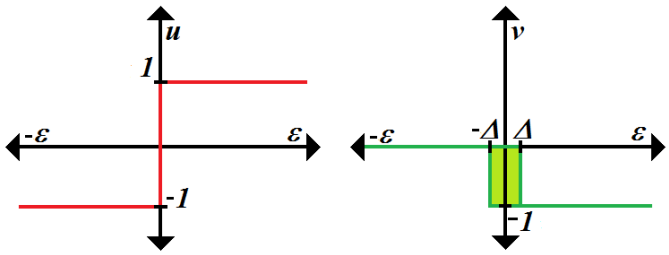

Fig. 2.5. Switching functions of the proposed sliding-mode MPPT.

They can be explained from the following analysis. At time t_0, $v = 0$ and $u = 1$. The error increases until it reaches the value Δ at time t_1 $(i.e.\ \varepsilon(t_1) = \Delta)$. At ${t_1}^+, v = -1$ and $u = 1$ and the error decreases from Δ to $-\Delta$, reached at time t_3 $(i.e.\ \varepsilon(t_3) = -\Delta)$. But at time t_2 (between instants t_1 and t_3), the error crosses zero and at instant ${t_2}^+, u = -1\ and\ v = -1$ as shown in figure 6. At time ${t_3}^+, v = 0$ and $u = -1$. The error then increases until it reaches the value Δ, but at time ${t_4}^+$, the error is crossing zero inducing a change of value in u $(u = 1)$, v remaining equal to zero. Then the

system returns to the initial configuration $v = 0$ and $u = 1$ and so on. Summarizing the previous analysis, the waveform associated to ε exhibits a behavior resulting from the repeated sequence presented below with the associated time intervals.

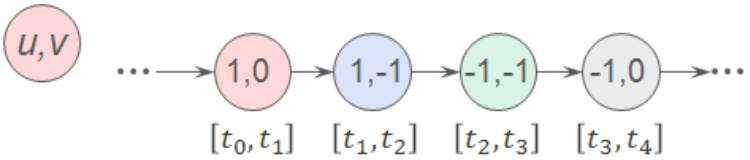

The trajectory induced by the repeated sequences in power characteristic is shown in figure 2.6. If $P_{p_{ref}}(t_4) > P_{p_{ref}}(t_0)$, after each sequence, $P_{p_{ref}}(t)$ is growing up as shown in figure 2.6. Now, we will try to find the conditions under which the previous assertion is true.

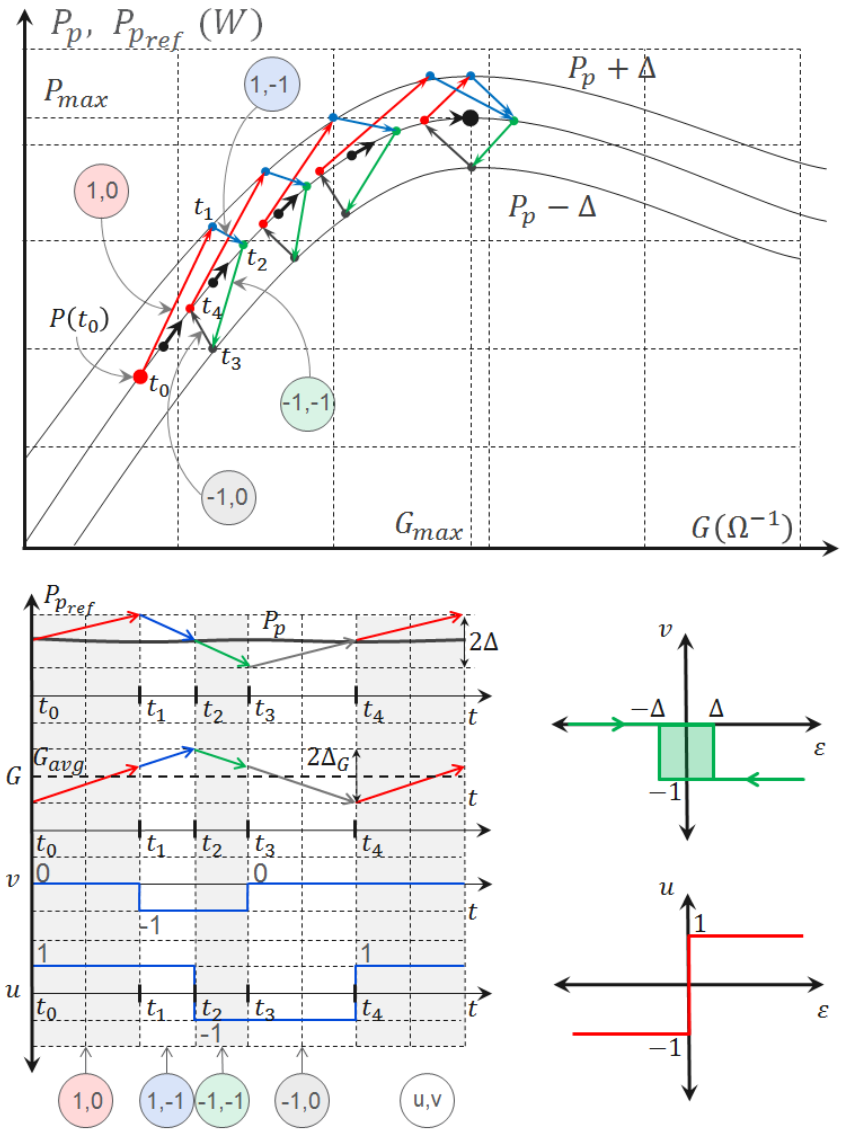

Figure 2.6. Implemented nonlinearities, waveforms and trajectory on the power characteristic

The dynamical equations describing the motion of $P_{p_{ref}}(t)$ and $G(t)$ for each time interval can be easily calculated, recalling that:

$$\frac{dP_{p_{ref}}}{dt} = K_2 P_p + M P_p v \tag{2.22}$$

$$\frac{dG}{dt} = K_1 P_p u \tag{2.23}$$

They are summarized in the following table.

Table 2.1. Modeling of the four MPPT structures in the plane P-G

u,v	Differential equations describing the dynamic behavior of $P_{p_{ref}}$ and G	
1,0	$\left.\frac{dP_{p_{ref}}}{dt}\right\|_{(1,0)} = K_2 P_p$ $\left.\frac{dG}{dt}\right\|_{(1,0)} = K_1 P_p$	$\left.\frac{dP_{p_{ref}}}{dG}\right\|_{(1,0)} = \frac{K_2}{K_1}$
1,-1	$\left.\frac{dP_{p_{ref}}}{dt}\right\|_{(1,-1)} = [K_2 - M] P_p$ $\left.\frac{dG}{dt}\right\|_{(1,-1)} = K_1 P_p$	$\left.\frac{dP_{p_{ref}}}{dG}\right\|_{(1,-1)} = \frac{K_2 - M}{K_1}$
-1,-1	$\left.\frac{dP_{p_{ref}}}{dt}\right\|_{(-1,-1)} = [K_2 - M] P_p$ $\left.\frac{dG}{dt}\right\|_{(-1,-1)} = -K_1 P_p$	$\left.\frac{dP_{p_{ref}}}{dG}\right\|_{(-1,-1)} = \frac{M - K_2}{K_1}$
-1,0	$\left.\frac{dP_{p_{ref}}}{dt}\right\|_{(-1,0)} = K_2 P_p$ $\left.\frac{dG}{dt}\right\|_{(-1,0)} = -K_1 P_p$	$\left.\frac{dP_{p_{ref}}}{dG}\right\|_{(-1,0)} = -\frac{K_2}{K_1}$

Remarking that:

$$\varepsilon = P_{p_{ref}} - P_p \text{ and } \frac{d\varepsilon}{dt} = \frac{dP_{p_{ref}}}{dt} - \frac{dP_p}{dt} = \left[\frac{dP_{p_{ref}}}{dG} - \frac{dP_p}{dG}\right]\frac{dG}{dt} \tag{2.24}$$

The associated differential equations describing the motion of the error for each time interval can also be easily determined. They are listed in the following table.

Table 2.2. Modeling of the MPPT power error

u,v	Differential equations describing the dynamic behavior of ε
1,0	$\left.\frac{d\varepsilon}{dt}\right\|_{(1,0)} = \left[\frac{K_2}{K_1} - \frac{dP_p}{dG}\right] K_1 P_p = \left[K_2 - K_1 \frac{dP_p}{dG}\right] P_p$
1,-1	$\left.\frac{d\varepsilon}{dt}\right\|_{(1,-1)} = \left[\frac{K_2 - M}{K_1} - \frac{dP_p}{dG}\right] K_1 P_p = \left[K_2 - M - K_1 \frac{dP_p}{dG}\right] P_p$
-1,-1	$\left.\frac{d\varepsilon}{dt}\right\|_{(-1,-1)} = \left[\frac{M - K_2}{K_1} - \frac{dP_p}{dG}\right] (-K_1 P_p) = \left[K_2 - M + K_1 \frac{dP_p}{dG}\right] P_p$
-1,0	$\left.\frac{d\varepsilon}{dt}\right\|_{(-1,0)} = \left[-\frac{K_2}{K_1} - \frac{dP_p}{dG}\right] (-K_1 P_p) = \left[K_2 + K_1 \frac{dP_p}{dG}\right] P_p$

From the conditions of reachability reproduced below

$$K_2 > \left|\frac{dP_p}{dG}\right|_{max} K_1 \text{ and } M > K_2 + \left|\frac{dP_p}{dG}\right|_{max} K_1 \tag{2.25}$$

It can be derived

$$\left.\frac{d\varepsilon}{dt}\right|_{(1,0)} > 0, \quad \left.\frac{d\varepsilon}{dt}\right|_{(1,-1)} < 0, \quad \left.\frac{d\varepsilon}{dt}\right|_{(-1,-1)} < 0, \quad \left.\frac{d\varepsilon}{dt}\right|_{(-1,0)} > 0 \tag{2.26}$$

This is in accordance with the waveform of figure 2.6. In practical applications, Δ is usually small and then, P_p and $\frac{dP_p}{dG}$ do not significantly vary inside intervals of lengths Δ. Consequently, we can consider that they are practically constant in such intervals. Taking into account the equations describing the motion of ε, we deduce that:

$$t_1 - t_0 \cong \frac{\Delta}{\left[K_2 - K_1 \frac{dP_p}{dG}\right] P_p}, \qquad t_2 - t_1 \cong \frac{\Delta}{\left[M - K_2 + K_1 \frac{dP_p}{dG}\right] P_p} \tag{2.27}$$

$$t_3 - t_2 \cong \frac{\Delta}{\left[M - K_2 - K_1 \frac{dP_p}{dG}\right] P_p}, \qquad t_4 - t_3 \cong \frac{\Delta}{\left[K_2 + K_1 \frac{dP_p}{dG}\right] P_p}$$

Having in mind, the differential equations describing the error motion (see table 2.2), the variation of P_{Pref} can be easily evaluated in the interval $[t_0, t_4]$ expressed as:

$$\begin{aligned} P_{Pref}(t_4) &\cong P_{Pref}(t_0) + K_2 P_p(t_1 - t_0) + (K_2 - M) P_p(t_2 - t_1) \\ &\quad + (K_2 - M) P_p(t_3 - t_2) + K_2 P_p(t_4 - t_3) \\ &= P_{Pref}(t_0) + K_2 P_p(t_4 - t_0) - M P_p(t_3 - t_1) \end{aligned} \tag{2.28}$$

After some simple algebraic calculations, we obtain:

$$\begin{aligned} &K_2 P_p(t_4 - t_0) - M P_p(t_3 - t_1) \\ &\quad = \Delta \left[\frac{2{K_2}^2}{{K_2}^2 - {K_1}^2 \left(\frac{dP_p}{dG}\right)^2} - \frac{2(M - K_2)^2}{(M - K_2)^2 - {K_1}^2 \left(\frac{dP_p}{dG}\right)^2} \right] \\ &\quad = \Delta [f(K_2) - f(M - K_2)] \end{aligned} \tag{2.29}$$

where $f(x)$ is defined by:

$$f(x) = \frac{2x^2}{x^2 - a^2} \;\; with\; a = \; K_1 \frac{dP_p}{dG} \tag{2.30}$$

The derivative of $f(x)$is given by:

$$\frac{df(x)}{dx} = \frac{4x(x^2 - a^2) - 2x^2(2x)}{(x^2 - a^2)^2} = \frac{-4a^2 x}{(x^2 - a^2)^2} < 0 \; if \; x > 0 \; and \; x \neq a \tag{2.31}$$

If $f(K_2) - f(M - K_2) > 0$, this implies $P_{p_{ref}}(t_4) > P_{p_{ref}}(t_0)$. Since the derivative of f is negative, K_2 and $M - K_2 \neq K_1 \frac{dP_p}{dG}$ from reachability conditions, it can be concluded that $f(K_2) - f(M - K_2) > 0$ if and only if $M - K_2 > K_2$, which can also be written as $M > 2K_2$. Adding this last condition to the reachability ones, we obtain all the constraints the parameters $M, K_1 \; and \; K_2$ must satisfy. Note the important fact that

only the knowledge of $\left|\frac{dP_p}{dG}\right|_{max}$ is needed, but as pointed out before, $\left|\frac{dP_p}{dG}\right|_{max}$ can be evaluated from the panel power characteristic curve. To summarize, the expected properties of the algorithm will be guaranteed if the parameters $M, K_1 \; and \; K_2$ are selected in order to satisfy the following constraints:

$$M > 2K_2 \; and \; K_2 > \left|\frac{dP_p}{dG}\right|_{max} K_1 \tag{2.32}$$

From the above analysis, $P_{Pref}(t)$ increases until it reaches P_{mp} and remains in its vicinity where it imposes the condition $P_p \cong P_{mp}$. Then:

$$\frac{d\,P_{Pref}}{dt} \cong \frac{d\,P_p}{dt} \cong \frac{dG}{dt} \cong 0 \tag{2.33}$$

Invoking now the expression of the derivative of the error on the sliding surface, we can deduce the equivalent controls defined by:

$$v_{eq} = -\frac{K_2}{M} > -1 \text{ and } u_{eq} = 0 \tag{2.34}$$

2.3.5 Influence of parameters Δ, M, K_1 and K_2

This paragraph discusses the performance of the proposed algorithm evaluating the influence of the parameters Δ, M, K_1 and K_2. The period T_p of the oscillation around the power P_p is equal to $t_4 - t_0$. Then it can be expressed as:

$$T_p = \frac{2K_2\Delta/P_p}{{K_2}^2 - {K_1}^2\left(\frac{dP_p}{dG}\right)^2} + \frac{2(M-K_2)\Delta/P_p}{(M-K_2)^2 - {K_1}^2\left(\frac{dP_p}{dG}\right)^2} \tag{2.35}$$

When the algorithm attains P_{mp}, we have $\frac{dP_p}{dG} \cong \frac{dP_{p_{ref}}}{dG} \cong 0$. We can also remark that in the interval $[t_0, t_4]$, we have:

$$\left.\frac{dP_{p_{ref}}}{dG}\right|_{(1,0)} + \left.\frac{dP_{p_{ref}}}{dG}\right|_{(1,-1)} + \left.\frac{dP_{p_{ref}}}{dG}\right|_{(-1,-1)} + \left.\frac{dP_{p_{ref}}}{dG}\right|_{(-1,0)} = \frac{K_2}{K_1} + \frac{K_2 - M}{K_1} + \frac{M - K_2}{K_1} - \frac{K_2}{K_1} = 0 \tag{2.36}$$

Then, when the algorithm attains the maximum, we have:

$$T_p = T_{mp} = \frac{2\Delta M}{K_2(M - K_2)P_{mp}} \tag{2.37}$$

The associated frequency is given by:

$$f_{mp} = \frac{K_2(M - K_2)P_{mp}}{2\Delta M} \tag{2.38}$$

where Δ and K_2 are fixed, considering the constraints $2K_2 < M < \infty$, $f_{mp} \in \left]\frac{K_2 P_{mp}}{4\Delta}, \frac{K_2 P_{mp}}{2\Delta}\right[$. Hence, it is possible to control the frequency f_{mp} by an appropriate selection of the free parameters Δ, M and K_2. Now, the amplitude of the fluctuations of the power reference around the maximum point P_{mp} is evaluated. Its determination is illustrated in figure 2.7.

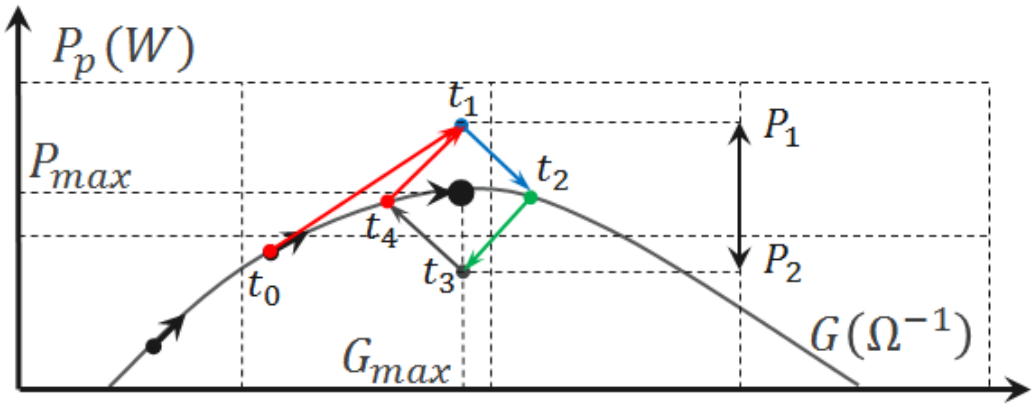

Figure 2.7. Determination of the amplitude of power reference and conductance at the maximum power point.

As shown in figure 2.7, the amplitude of the oscillation in the power reference is given by:

$$\begin{aligned}\Delta P_{Pref} &= P_{Pref}(t_1) - P_{Pref}(t_3) \\ &= -(K_2 - M)P_p(t_2 - t_1) - (K_2 - M)P_p(t_3 - t_2) \\ &= (M - K_2)P_p(t_3 - t_1) = \frac{2(M - K_2)^2\Delta}{(M - K_2)^2 - {K_1}^2\left(\frac{dP_p}{dG}\right)^2}\end{aligned} \tag{2.39}$$

At the maximum, we recover that $\frac{dP_p}{dG} \cong 0$ and as expected $\Delta P = 2\Delta$. The parameter Δ is the only parameter involved in the expression of power fluctuations amplitude. Now, the conductance is constrained to lie in a band of width $\Delta G = G(t_2) - G(t_4)$ given by:

$$\Delta G = K_1 \frac{\Delta M}{\left[M - K_2 - K_1 \frac{dP_p}{dG}\right]\left[K_2 + K_1 \frac{dP_p}{dG}\right]} \tag{2.40}$$

At the maximum point, because $\frac{dP_p}{dG} \cong 0$, we have:

$$\Delta G = \frac{K_1 \Delta M}{(M - K_2)K_2} \tag{2.41}$$

considering the constraints $2K_2 < M < \infty$, $\Delta G \in \left]\frac{K_1\Delta}{K_2}, \frac{2\,K_1\Delta}{K_2}\right[$.

We can conclude that the value of Δ controls the amplitude of the power fluctuations around P_{mp} and that we have three parameters, namely, M, K_1 and K_2, for controlling the frequency and the conductance fluctuations around the maximum. These constants have to satisfy some constraints recalled here

$$M > 2K_2 \; and \; K_2 > \left|\frac{dP_p}{dG}\right|_{max} K_1 \tag{2.42}$$

Analyzing the last inequality, we can remark that the smaller K_1 is , more insensitive the algorithm is to $\left|\frac{dP_p}{dG}\right|_{max}$, but the weaker the action on $G(t)$ is. This action has to be sufficient to guarantee a good behavior of the algorithm.

2.3.6 Behavior working with irradiance variations

When irradiance is constant, the behavior of the power of a PV module is represented by a single curve corresponding to the characteristics of the PV module, which is described here as a function of the conductance (P-G). When a sudden change in irradiance occurs, we can consider two cases:

- ***Case a:*** it corresponds to an increasing of irradiance. Before the change, $P_{Pref}(t)$ is at the admissible maximum power, for example P_{mp2} (see figure 2.8). Due to this sudden change at t_{mp2}, $P_p(t)$ suffers a discontinuity and the panel characteristic suddenly changes. It corresponds to a new characteristic whose powers are higher (see figure 2.8).

In that case, we have $\varepsilon({t_{mp2}}^+) = P_{p_{ref}}({t_{mp2}}^+) - P_p({t_{mp2}}^+) < 0$. For $t > t_{mp2} + \delta$, δ being positive, we have:

$$\frac{dP_{Pref}(t)}{dt} = K_2 P_p(t) > 0 \text{ and } \frac{dG(t)}{dt} = -K_1 P_p(t) < 0 \tag{2.43}$$

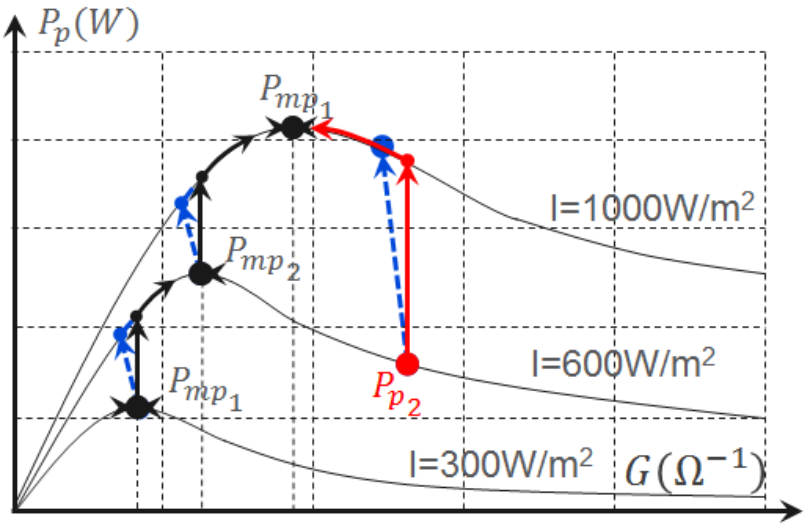

Fig. 2.8. Power point after sudden irradiance changes from a lower to a higher irradiance.

Two cases must be considered on the new power characteristic curve:

- If $\frac{dP_P({t_{mp2}}^+)}{dG}$ >0, $P_{Pref}(t)$ is increasing and $P_p(t)$ is decreasing until they will be equal. From the analysis developed in paragraphs 2.3.1 to 2.3.5, $P_{p_{ref}}(t)$ will move towards the new maximum.

- If $\frac{dP_P(t_{mp2}{}^+)}{dG}$ <0, $P_{Pref}(t)$ and $P_p(t)$ are increasing. But from reachability conditions we have:

$$\frac{dP_{Pref}(t)}{dG} = -\frac{K_2}{K_1} < \frac{dP_p(t)}{dG} \Rightarrow \frac{dP_{Pref}(t)}{dt} > \frac{dP_p(t)}{dt} \tag{2.44}$$

$P_{Pref}(t)$ is growing up faster than $P_P(t)$, at a moment they will be equal and then we can deduce that $P_{p_{ref}}(t)$ will move toward the new maximum from the analysis developed in paragraph 2.3.1 to 2.3.5.

- ***Case b:*** it corresponds to a decreasing of irradiance. With the same notations as before, we have $\varepsilon(t_{mp2}{}^+) = P_{p_{ref}}(t_{mp2}{}^+) - P_p(t_{mp2}{}^+) > 0$ (see figure 2.9). For $t > t_{mp2} + \delta$, δ positive, we have:

$$\frac{dP_{Pref}(t)}{dt} = (K_2 - M)P_p(t) < 0 \text{ and } \frac{dG(t)}{dt} = K_1 P_p(t) > 0 \tag{2.45}$$

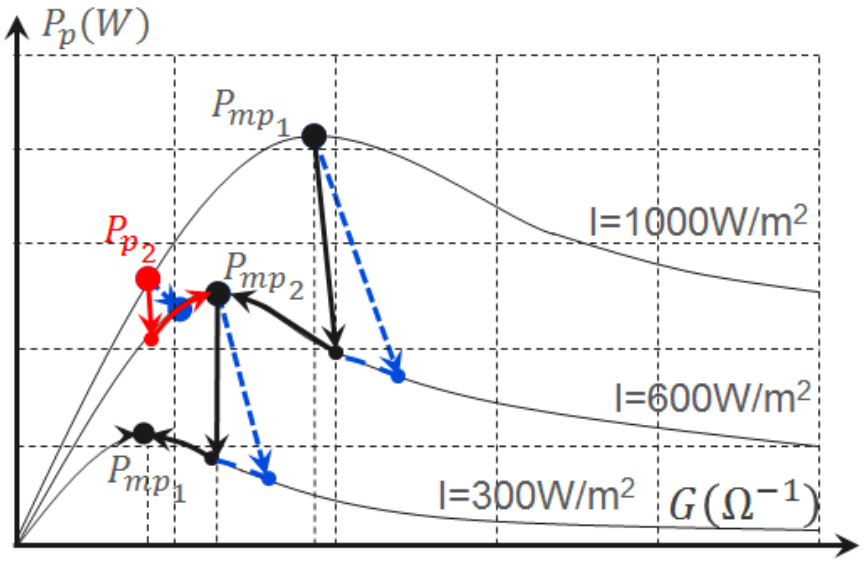

Fig. 2.9. Power point after sudden irradiance changes from a higher to a lower irradiance

Two cases must be considered on the new power characteristic curve:

- If $\frac{dP_P(t_{mp2}{}^+)}{dG}$ >0, $P_{Pref}(t)$ is decreasing and $P_p(t)$ is increasing until they will be equal. From the analysis developed in paragraph 2.3.1 to 2.3.5, $P_{p_{ref}}(t)$ will move toward the new maximum.
- If $\frac{dP_P(t_{mp2}{}^+)}{dG}$ <0, $P_{Pref}(t)$ and $P_p(t)$ are decreasing. But from reachability conditions we have:
-

$$\frac{dP_{Pref}(t)}{dG} = \frac{K_2 - M}{K_1} < \frac{dP_p(t)}{dG} \Rightarrow \frac{dP_{Pref}(t)}{dt} < \frac{dP_p(t)}{dt} \tag{2.46}$$

$P_{Pref}(t)$ is falling down faster than $P_P(t)$, at a moment they will be equal and then we can deduce that $P_{p_{ref}}(t)$ will move toward the new maximum from the analysis developed in paragraph 2.3.1 to 2.3.5.

The analysis of the algorithm is now complete. Even if sudden changes of irradiance occur, the proposed algorithm will allow extracting the maximum power of the PV module, provided $\left|\frac{dP_p}{dG}\right|_{max}$ is evaluated appropriately. Recall that the analysis developed in paragraph 2.2 can be used to evaluate the value of $\left|\frac{dP_p}{dG}\right|_{max}$ and to select the constants Δ, M, K_1 and K_2.

2.4 ASSESSMENT OF THE ALGORITHM

In order to show how the algorithm practically works and to illustrate the theory presented in the previous paragraphs, we consider three characteristics defined in the plane f-u as follow:

$f_1 = 800 - 20(u-2)^2$

$f_2 = 200 - 10(u-6)^2$

$f_3 = 600 - 25(u-3)^2$

The derivatives for each characteristic are given by:

$f_1' = -40(u - 2)$

$f_2' = -20(u - 6)$

$f_3' = -50(u - 3)$

The maximal value of derivatives can be determined from the above expressions. To cover all cases the maximum value is equal to 50. The constants of the algorithm must verify $K_2 > \left|\frac{dP_p}{dG}\right|_{max} K_1$ and $M > K_2 + \left|\frac{dP_p}{dG}\right|_{max} K_1$.

A set of constants satisfying all the constraints are given by $M = 100$, $K_1 = 0.1, K_2 = 40$ and $\Delta = 20$. To test the algorithm, two commutations among the previous f-u characteristics are made as depicted in the figure 2.10. For the first commutation occurring at $u = 4$, the algorithm jumps from the curve f_1 (maximum of 800) to the curve f_2 (maximum of 200). The second commutation occurs at $u = 8$, and the algorithm jumps from the curve f_2 (maximum of 200) to the curve f_3 (maximum of 600).

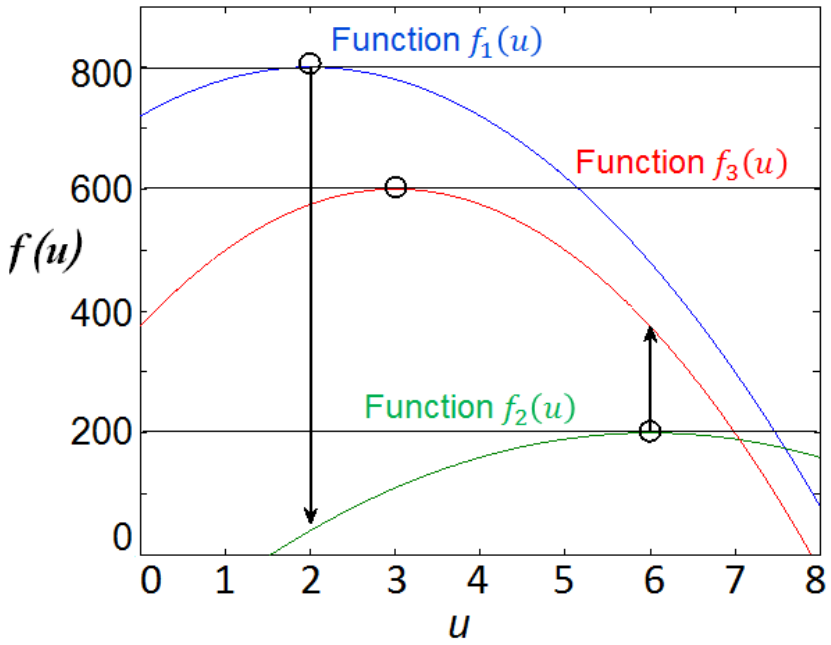

Fig. 2.10. Simulated commutations

As shown in figure 2.11, the algorithm leads the function *f* towards the instantaneous maximum value having a fictitious reference f_{ref} varying around the maximum value. The behavior of the variable *u* shows the smooth convergence to the maximum points.

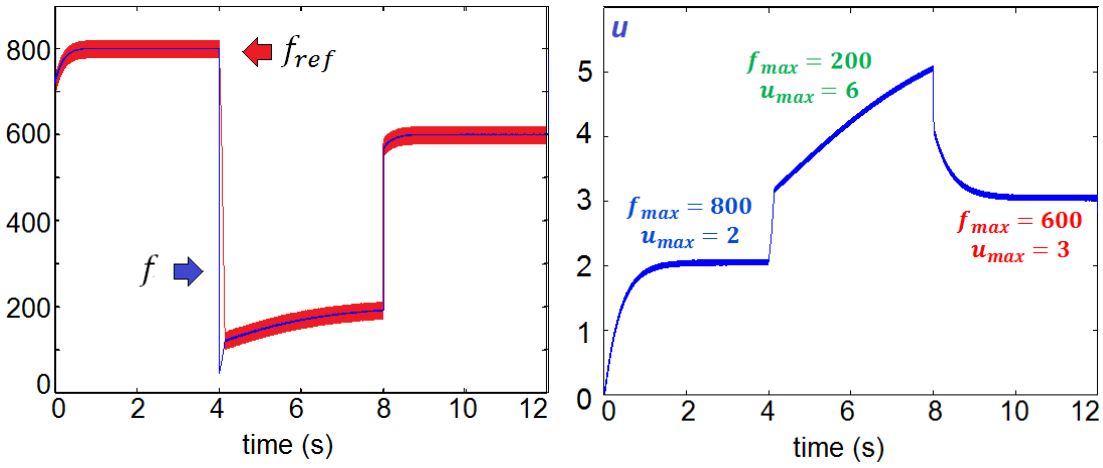

Fig. 2.11. a)Evolution of *fref* and *f* versus time; b) evolution of the variable *u* versus time

Despite the commutations from one characteristic to another, we can remark that the algorithm converges to the corresponding maxima. Figure 2.12 represents the trajectory of f_{ref} as function of u in the f-u plane. Note that the second commutation occurs before the algorithm attains the maximum.

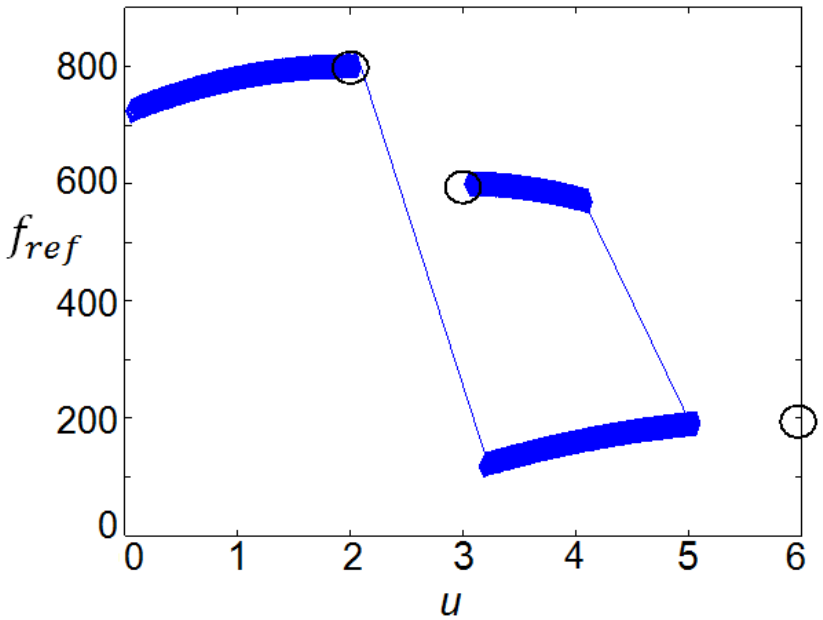

Fig. 2.12. Trajectory in the plane f_{ref} versus u.

A zoom on the trajectory when the algorithm is growing up to the first maximum is represented in Figure 2.13. The reference is behaving exactly as the theory predicts. The original characteristic is represented in black and the reference is moving around it.

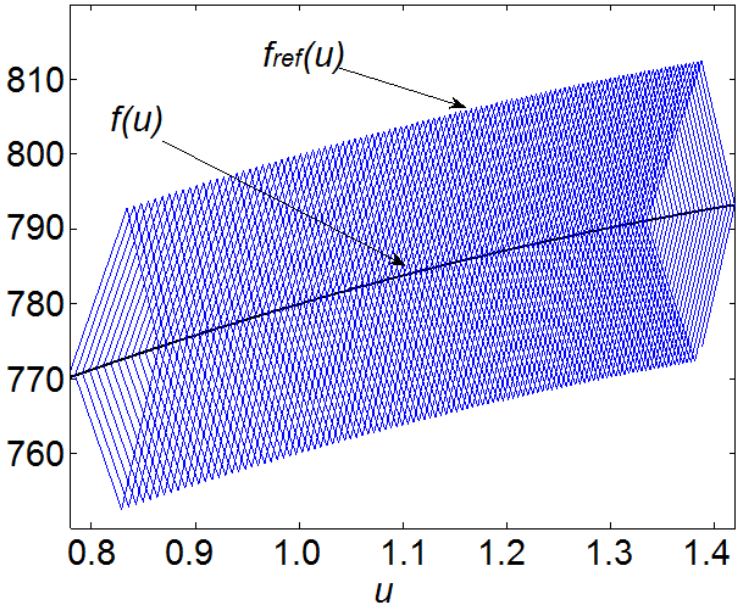

Fig. 2.13. Zoom of the trajectories in the f-u plane.

To verify the analysis of paragraph 2.3.5, a zoom of the trajectories of f_{ref} and u at maximum 800 is represented below.

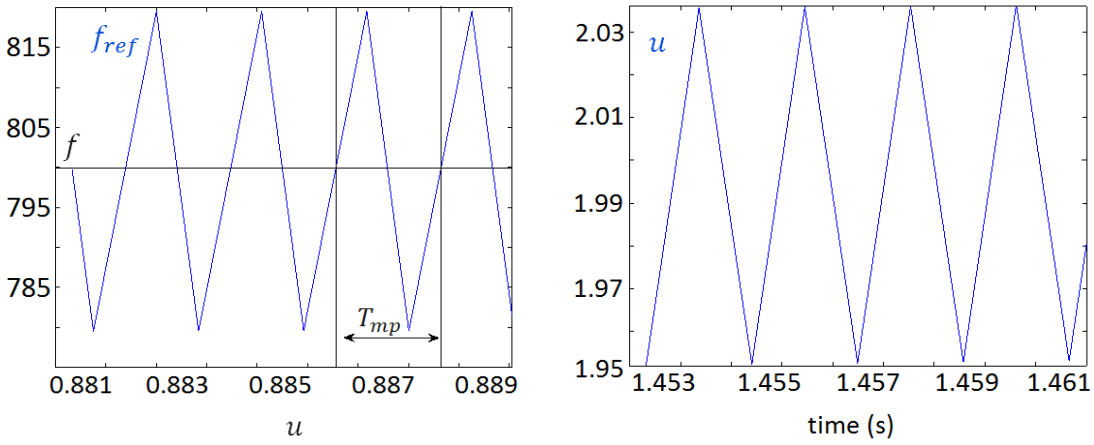

Fig. 2.14. Zoom on trajectories of f_{ref} and u versus time for the maximum 800.

With the selected constants, we have:

$$T_{mp} = \frac{2\Delta M}{K_2(M-K_2)P_{mp}} = \frac{1}{480} = 2.1 \times 10^{-3} s$$

$$\Delta G = \frac{K_1 \Delta M}{(M-K_2)K_2} = \frac{1}{12} = 8.3 \times 10^{-2} S$$

The above theoretical values coincide exactly with the ones extracted from the curves of figure 2.14, this validating the developed theory.

2.5 SIMULATION RESULTS

In order to verify the theoretical prediction about the behavior of the MPPT algorithm, a set of simulation has been implemented in PSIM using the model of the panel available in that software [82]. The general block diagram of the implemented model is depicted in figure 2.15 while the PV module parameters are shown in figure 2.16. Note that a block representing the DC-DC converter (quadratic boost converter) and a block representing the solar panel has been included to evaluate the relation between the MPPT variables and the system variables.

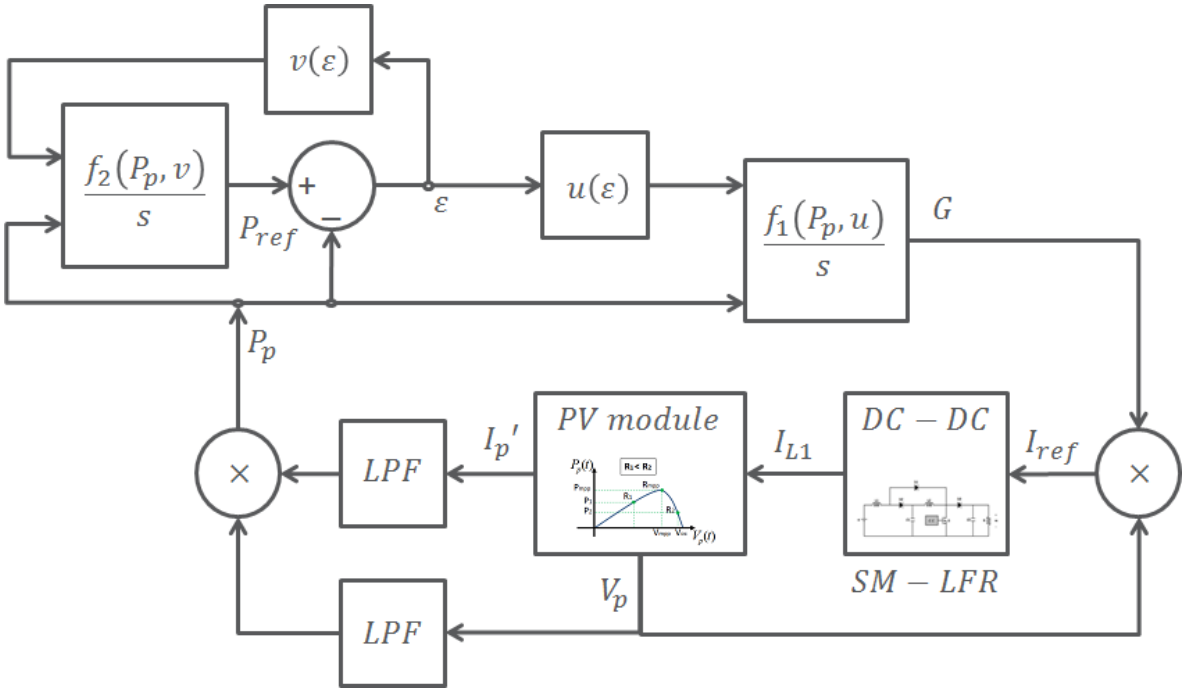

Fig. 2.15. Block diagram of the power stage connected to the PV module and the MPPT (LPF: Low Pass Filter; SM-LFR: Sliding-Mode Loss-Free-Resistor)

As observed in figure 2.16, a PV module with normalized values of 5 V in the open circuit voltage and 5 A in the short circuit current has been selected. The DC-DC stage has been replaced by a controlled current source whose value is defined by the product of the conductance given by the MPPT and the measured voltage of the PV module. A capacitor of 10 µF has been connected in parallel with the module. This simulated model allows an easy validation of the theoretical predictions with results close to the real application. The maximum derivative using the asymptotic model of the PV model and equations (4.3) and (4.4) is $\left|\frac{dP_p}{dG}\right|_{max} = 17$. Then, the parameters of the algorithm are defined as $K_1 = 0.2$, $K_2 = 10$, $M = 40$, $\Delta = 2$.

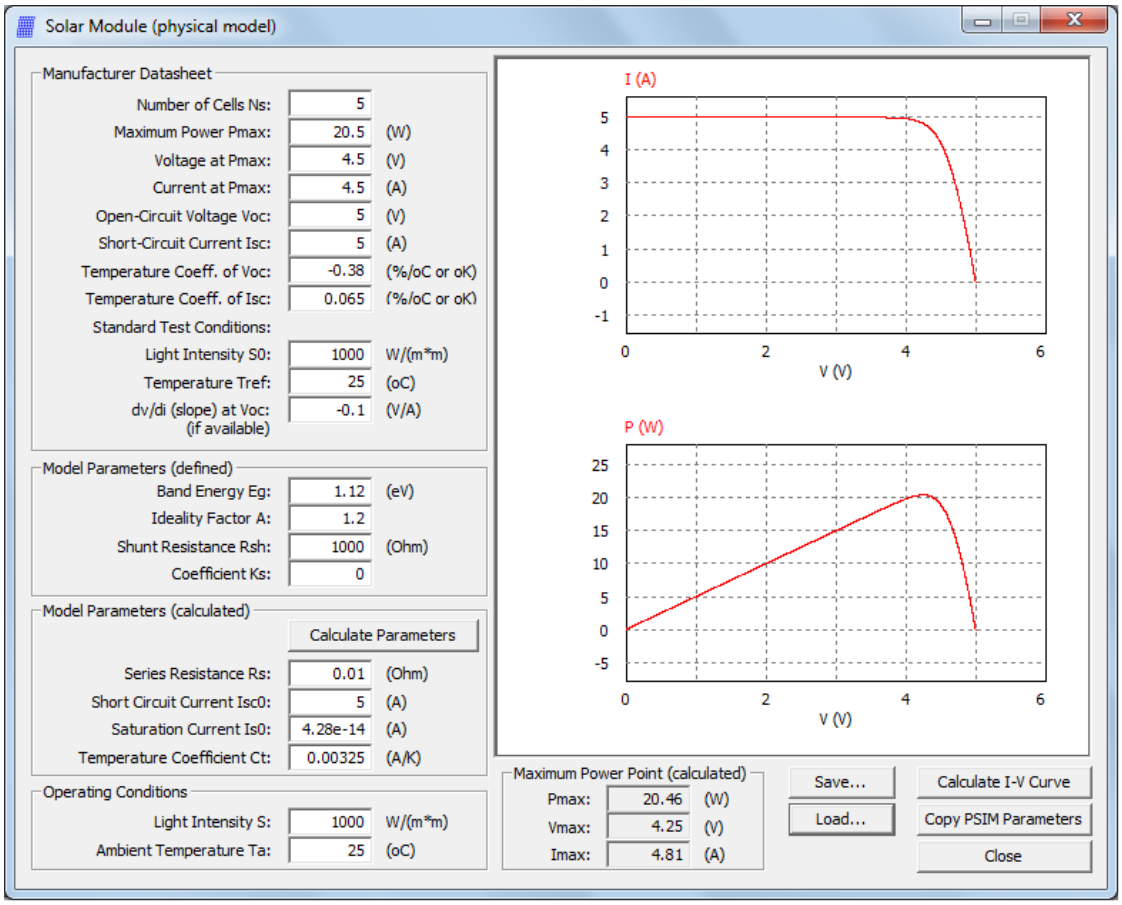

Fig. 2.16. Graphic interface defining the parameters of the Solar Module in PSIM

2.5.1 Steady-state of the PV module variables

The figure 2.17 shows the steady-state waveforms when an average power of 19.36 W is supplied by the PV module. The operation at the maximum power point is confirmed because of the double frequency of the power function. The efficiency of the MPPT is computed as 99.8% at this condition. The oscillatory components of the PV module variables have amplitudes of 100 mA (3.4%), 170 mV (4%) and 0.062 W (0.5%).

2.5.2 Steady-state and motion of the MPPT variables

Figure 2.18 shows the trajectory of the system in the P-G plane towards the maximum power point. The power reference shows a limit cycle when the system yields the maximum whereas the output power is shown invariant. Moreover, it is possible to observe the motion of the system towards the maximum power point. Complementarily, the figure 2.19 depicts the stationary state of the MPPT variables showing the relation between the time response and the P-G plane representation.

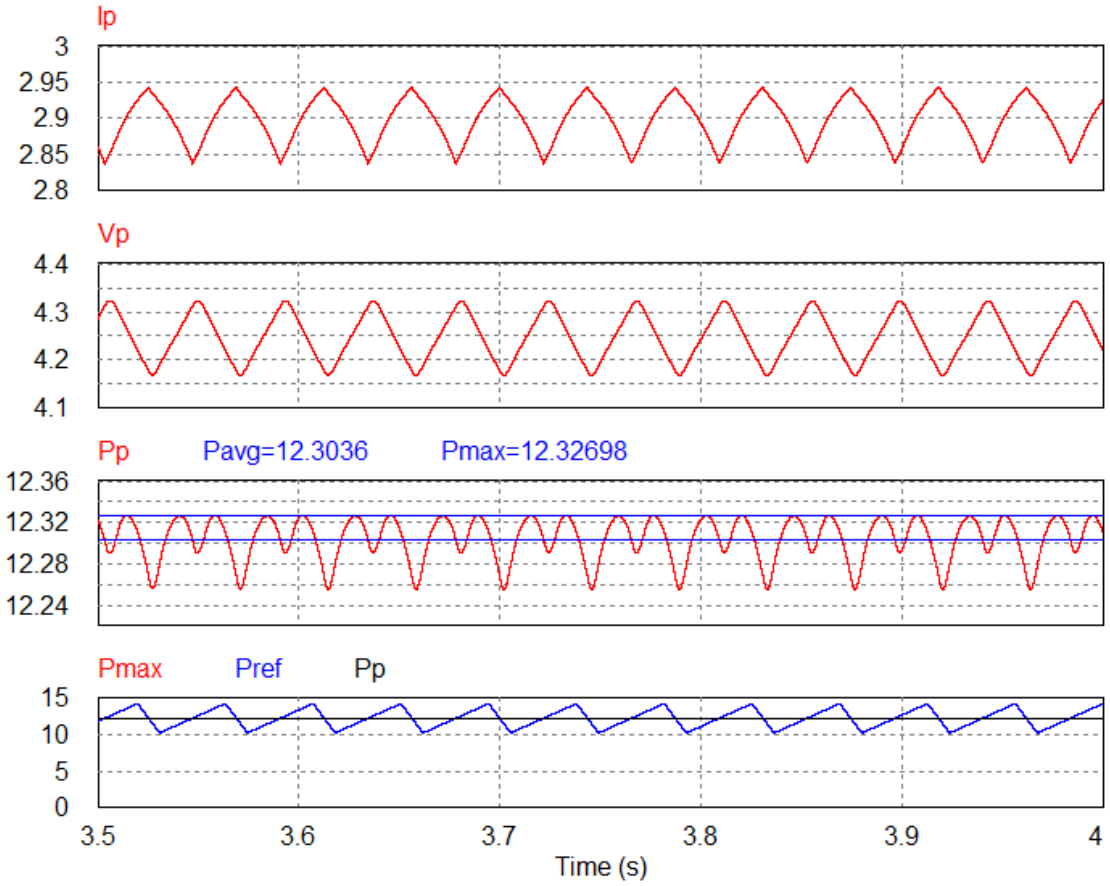

Fig. 2.17. Detail of the simulated oscillatory components of current, voltage and powers.

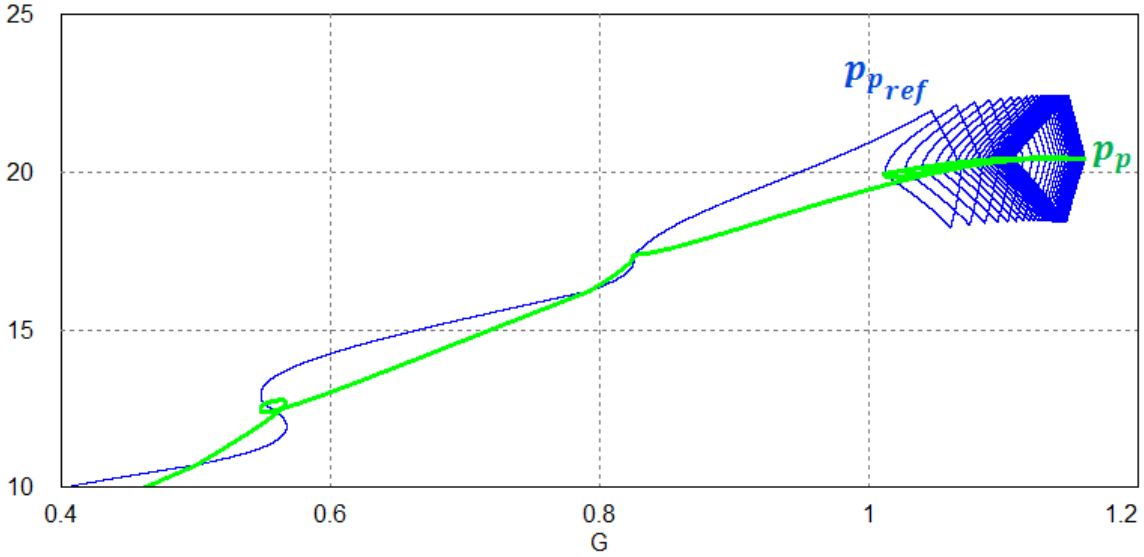

Fig. 2.18. Steady-state behavior of the proposed MPPT algorithm

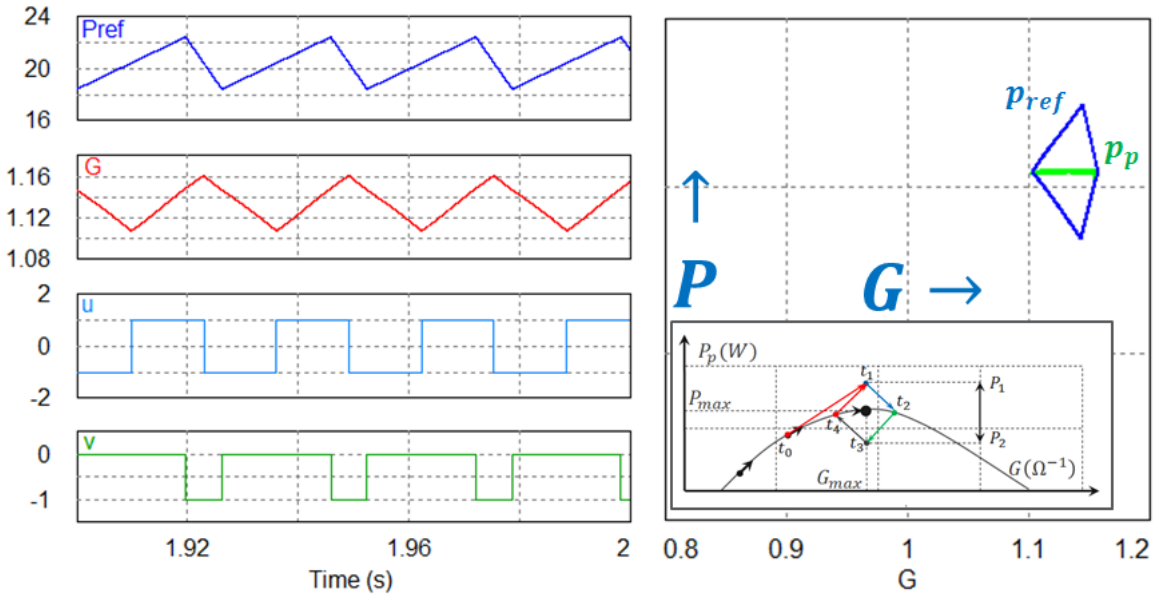

Fig. 2.19. Steady-state behavior of the proposed MPPT algorithm

2.5.3 Detail of the sliding motion

When the parameter K_1 is reduced, a slower variation is produced in the conductance. This condition increases the frequency of the reference and the movement towards the maximum becomes slow. Figure 2.20 shows the motion at this condition ($K_1 = 0.1$, $K_2 = 10$ and $M = 40$). The corresponding behavior in the P-G plane is illustrated in figure 2.21. As it can be noted, the trajectory of the power reference guides the output power towards the maximum with a slow rate, which can be considered as an inconvenient for the global performance of the system.

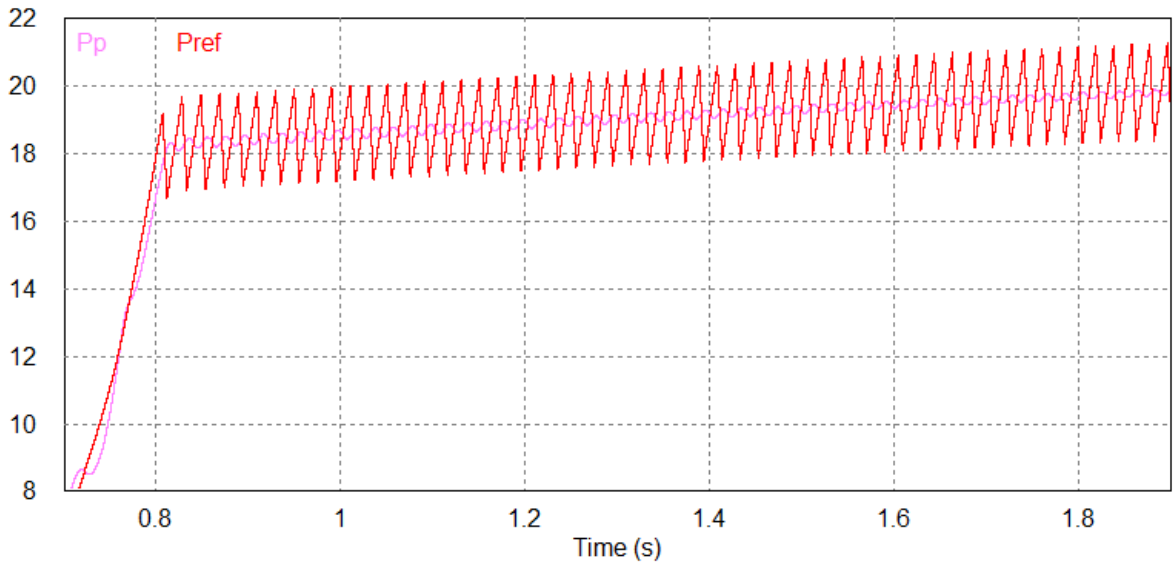

Fig. 2.20. Evolution of the power towards the maximum power point after the system's start-up

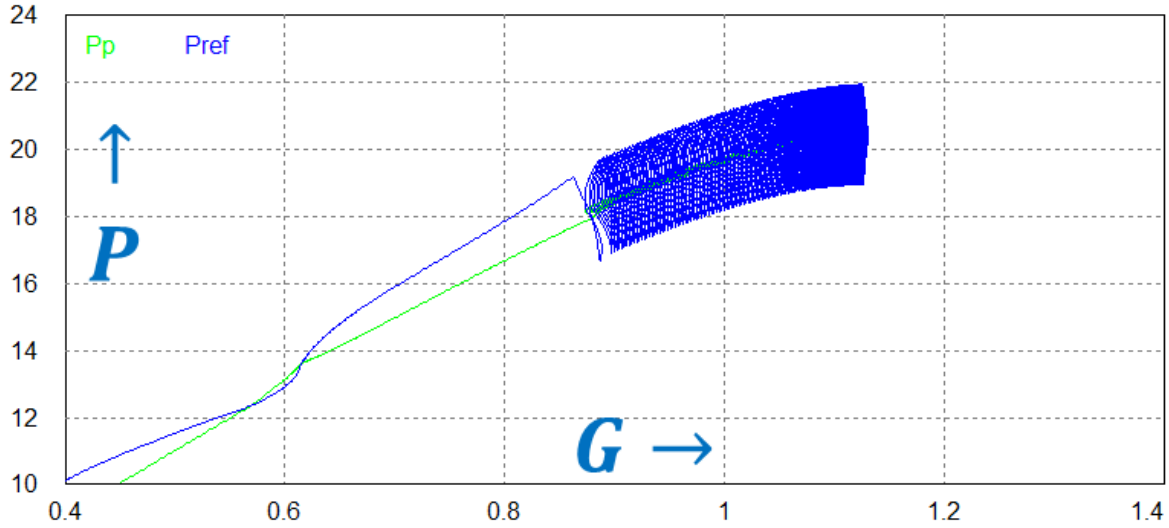

Fig. 2.21. Trajectory of the power towards the maximum power point in the P-G plane showing the variable structure behavior while approaching the maximum power point

Maximizing the response in the P-G plane leads to a more accurate definition of the limit cycle of the power reference. As shown in figure 2.22, the motion of the power reference holds the power at the maximum power point. No important change can be observed since the power remains almost constant taking the same value of the reference in the horizontal line passing through the vertices of the rhombus. It is also possible to measure the amplitude of the both variations of conductance (0.05 S) and power reference (2 W).

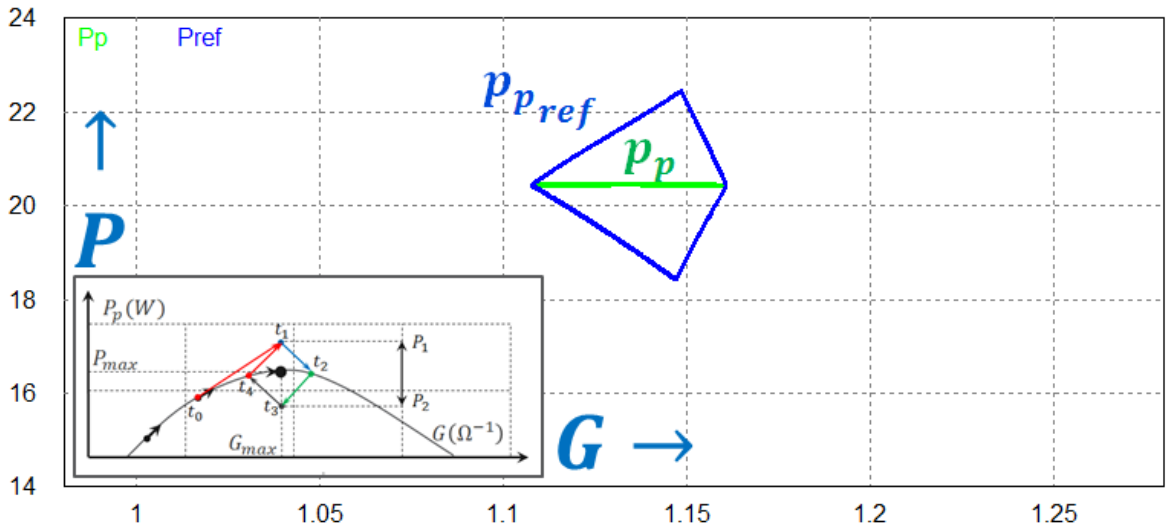

Fig. 2.22. Zoom of the simulated steady state of power and conductance in the P-G plane.

2.5.4 Start-up of the algorithm

A simulation of the start-up of the algorithm has been developed in order to observe the transient behavior from the starting point (zero current) to an equilibrium point corresponding to the maximum power. As observed in figure 2.23, the steady-state is reached in around 300 ms. Note that the power quickly arrives to values in the neighborhood of the maximum power point ensuring an appropriate behavior for the algorithm.

It is important to note that during the start-up, both power reference and measured power show an important proximity, induced by the sliding-mode control. Although it is not possible to identify the same hysteretic behavior for the maximum power point, the power of the panel remains oscillating around the power reference while the maximum power point is reached.

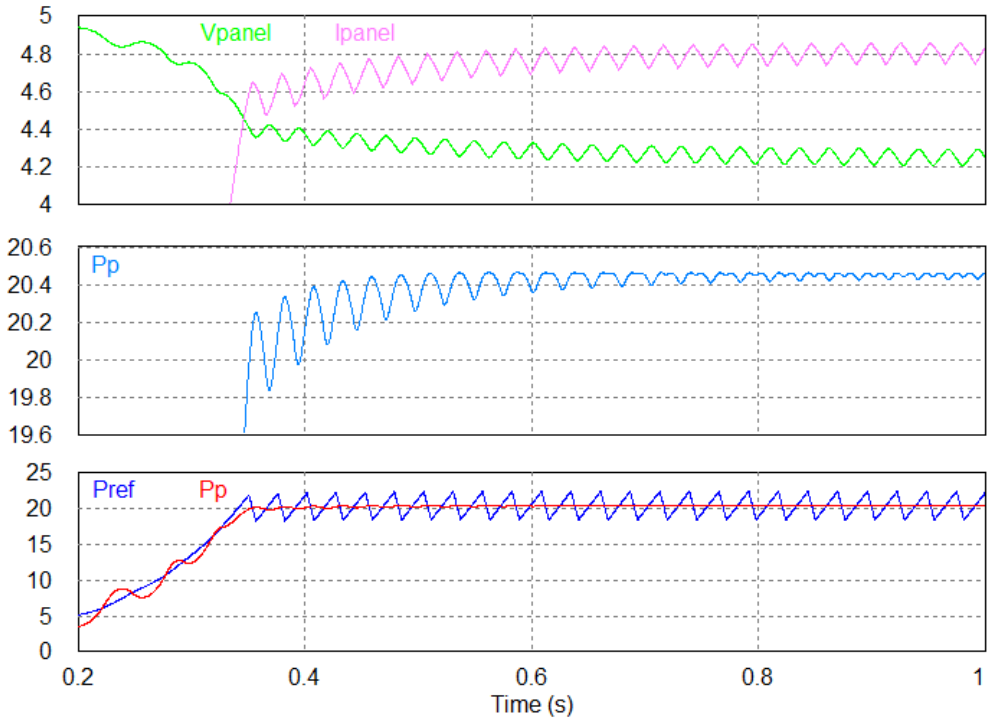

Fig. 2.23. Response of voltage, current and power during the system's start-up ($K_1 = 0.2$, $K_2 = 10$ and $M = 40$)

2.5.5 Sliding motion of the MPPT algorithm

A series of positive and negative step-type stimuli has been defined to give the irradiance to the Solar Module in PSIM. Each step has introduced an irradiance jump of 400 W/m^2 starting from an irradiance of 1000 W/m^2 and returning to the same value

after two negative and to positive changes. Each irradiance value remains during 2 s. Figure 2.24 shows the power signals obtained from the above test where it is possible to observe that the power of the panel takes values near the average value of the power reference. Moreover, it is possible to observe that the efficiency of the algorithm with high powers is higher because of the reduction of the amplitude of the oscillatory component. The system has a stable behavior and a smooth transition in the changes of equilibrium points. Figure 2.24 also shows a zoom of both increasing and decreasing transitions to give an approach of the waveform during the transient response.

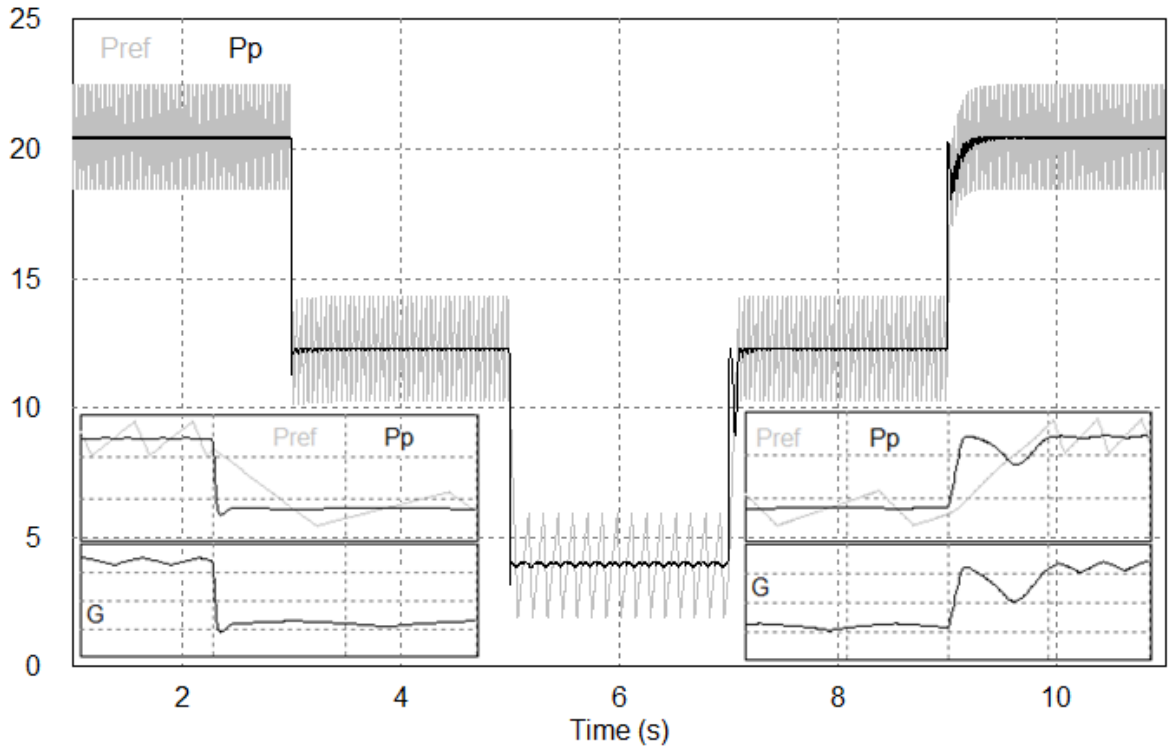

Fig. 2.24. Simulated time response of the algorithm to irradiance changes

2.5.6 Dynamic response in front of changes in the P-V characteristic

Finally, two simulations were performed in order to assess the dynamic response of the MPPT algorithm. The first one changes the irradiance of the Solar Module from 300 W/m^2 to 700 W/m^2 and vice versa remaining each value during 1 s. This simulation is also used to introduce changes between 200 W/m^2 to 1000 W/m^2 and vice versa using the same time intervals. The simulated results of the MPPT are shown in figures 2.25 and 2.26 respectively.

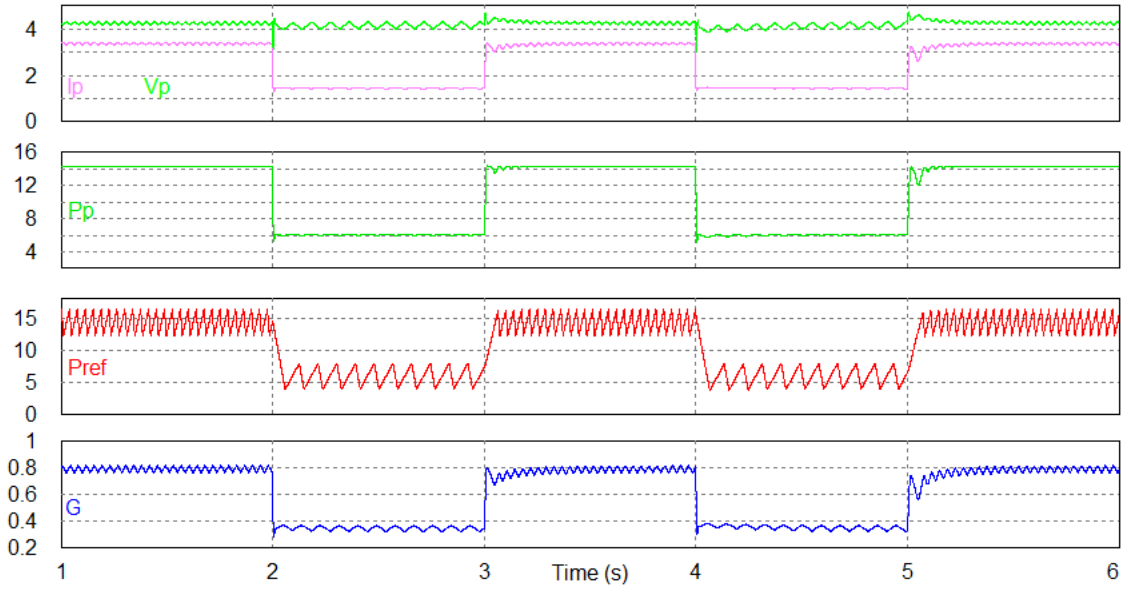

Fig. 2.25. Simulated results using sudden changes of 9 W in the maximum power P-V characteristic

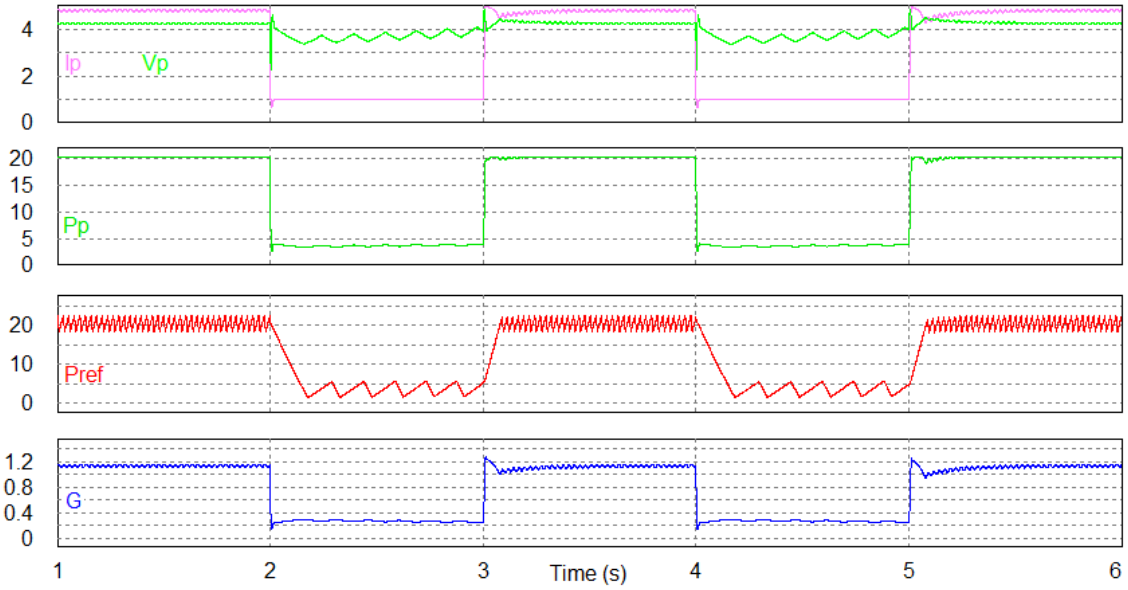

Fig. 2.26. Simulated results using sudden changes of 16 W in the maximum power P-V characteristic

As it can be noted in both tests, the algorithm quickly reaches the maximum power point, also exhibiting a smooth transient response when step disturbances are applied to the power. Further, it is worth to note that the system shows a similar behavior and in general, a good performance because the maximum power is almost reached instantaneously after a power disturbance. Then, although the power reference increases or decreases slower than the power of the module, it moves to the sliding surface and clearly exhibits a sliding motion at the maximum power points.

All of simulated results confirm the theoretical predictions and the expected efficiency of the proposed MPPT method. Now, the last important step in this chapter consists in demonstrating that this method can be physically implemented using simple electronics circuits and that it works in a real application.

2.6 EXPERIMENTAL RESULTS

In this paragraph, we report the experimental measurements validating the theoretical predictions and simulation results.

2.6.1 Prototype and experimental set-up

The MPPT control has been implemented using a microcontroller dsPIC30F4011 and some analogic electronic circuits. Both, current and voltage measurements have been conditioned with second order filters which have a cut-off frequency of 100 Hz and a damping factor of 0.7. The filters are used to mitigate the high frequency ripple component in the case of the current and the peaks induced in the voltage as effect of the commutation of the DC-DC converter. A constant sampling frequency of 50 kHz has been established in the microcontroller. The serial digital-to-analog (DAC) converter MCP4812 has been used in order to obtain the continuous signal G which used in the control of the DC-DC converter and the signal $P_{p_{ref}}$ (VOUTB) which is observed for analysis. Two digital pins of the micro-controller are used to reproduce the corresponding signals of the non-linear functions u and v for the experiments. Figure 2.27 illustrates the schematic diagram of the MPPT circuit.

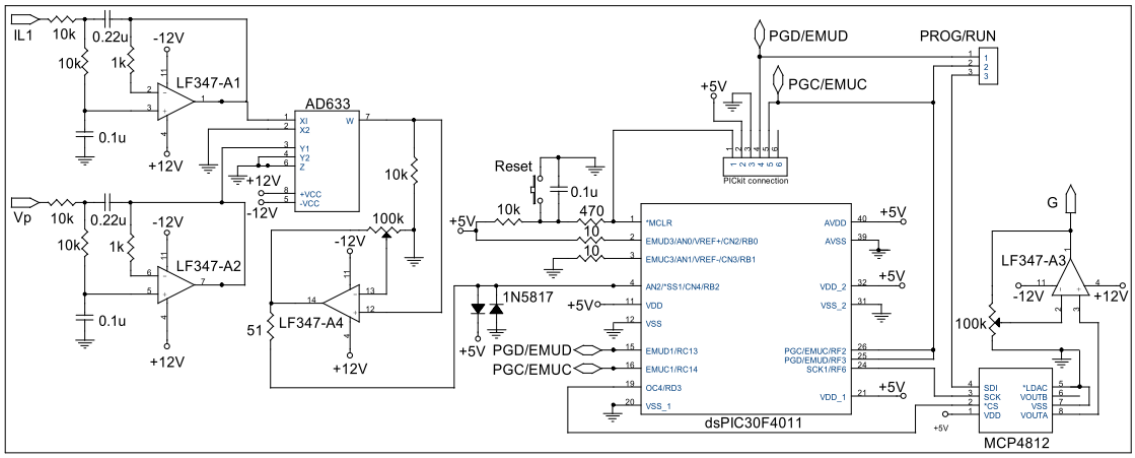

Fig. 2.27. Schematic electronic circuit for the MPPT algorithm

The set-up for measurements, photovoltaic modules, converter prototype and MPPT circuit are shown in figure 2.28. The experimental set-up is composed of a solar panel emulator E4360A from Agilent, an oscilloscope MSO3014 from Tektronix, current probes TCP202 and TCPA300 from Tektronix, a power supply Multimeteix XA3033, a multimeter HP34401A from Hewlett Packard, an electronics load IT8512B from ITEC, a I-V Curve Tracer MP-160 from EKO and a pyranometer SP LITE from KIPP & ZONEN.

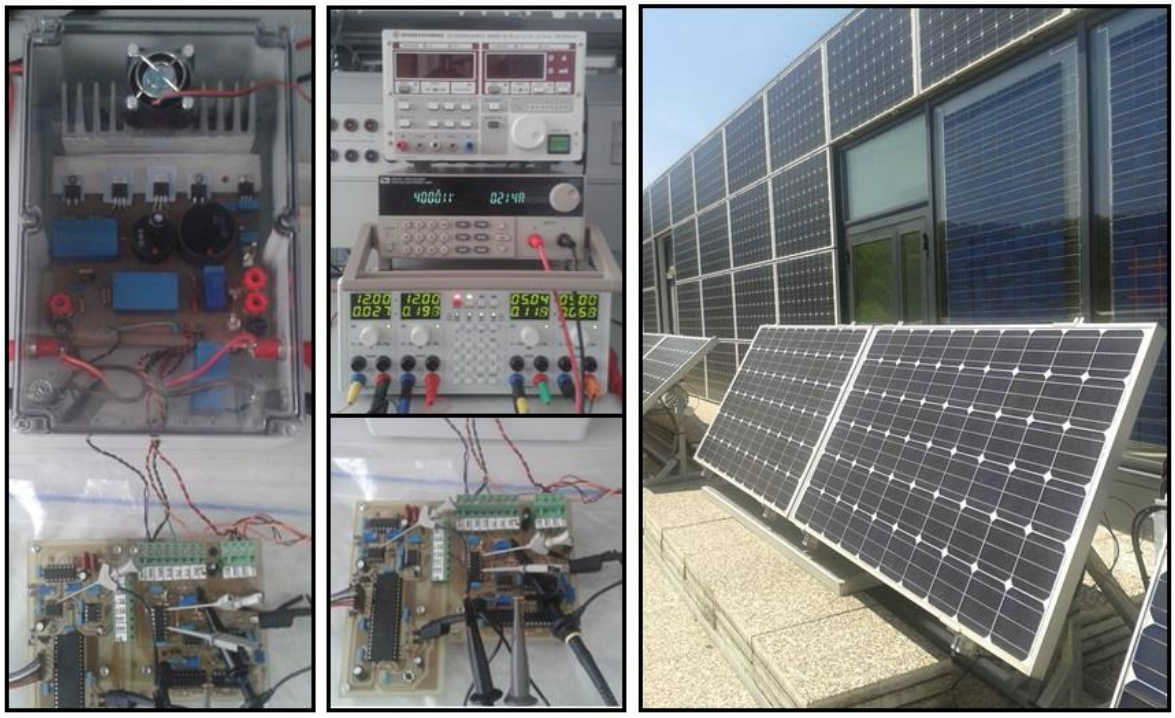

Fig. 2.28. Converter and MPPT prototypes ,and experimental set-up

	BP 585
Maximum power (P_{max})[2]	85W
Voltage at P_{max} (V_{mp})	18.0V
Current at P_{max} (I_{mp})	4.72A
Warranted minimum P_{max}	80.8W
Short-circuit current (I_{sc})	5.0A
Open-circuit voltage (V_{oc})	22.1V
Temperature coefficient of I_{sc}	(0.065±0.015)%/°C
Temperature coefficient of voltage	-(80±10)mV/°C
Temperature coefficient of power	-(0.5±0.05)%/°C
NOCT[3]	47±2°C
Maximum system voltage	600V (U.S. NEC rating) 1000V (TÜV Rheinland rating)
Maximum series fuse rating	20A (U, H versions) 15A (S, L versions)

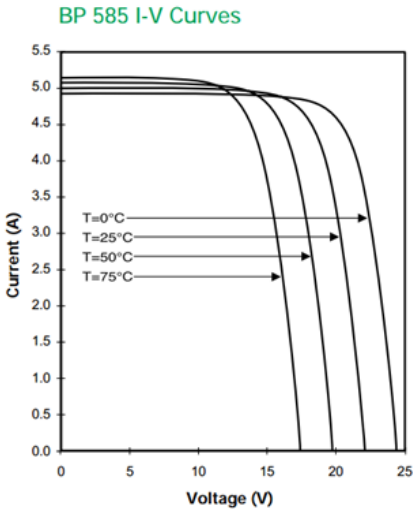

Fig. 2.29. Technical specifications of the PV module BP585

Two solar panels BP 585 from BP SOLAR have been used in the experimental test. The characteristics and parameters are listed in figure 2.29.

2.6.2 Steady-state of the PV module variables

Figure 2.30 shows the steady-state waveforms when an average power of 91.2 W is extracted from the PV emulator and injected in a voltage load of 400 V through a quadratic boost converter. The PV emulator has been configured with an *Isc* of 4 A and a *Voc* of 25 V. The maximum derivative for this module using the asymptotic model of the PV model and equations (4.3) and (4.4) is $\left|\frac{dP_p}{dG}\right|_{max} = 531$. Then, the parameters of the algorithm are defined as $K_1 = 0.015$, $K_2 = 20$, $M = 500$, $\Delta = 5$. The double frequency of the power waveform in comparison with the frequency of the voltage and current waveforms confirms that the system works at the maximum power point (considering a single maximum operational condition). Further, the oscilloscope capture shows the measured power computed from the product of the filtered and conditioned current and voltage, which is compared with the power reference.

The static performance of the MPPT algorithm operating in the steady state (one cycle) can be obtained using the expression $\boldsymbol{\eta = \overline{P_p}/P_{p_{max}}}$, when $\overline{P_p}$ is the average value of the power and $P_{p_{max}}$ is the maximum power. Using this definition, a 99.2% MPPT efficiency is obtained. The oscillating components of the PV module variables have amplitudes of 200 mA (5%), 1.6 V (6.6%) and 2.6 W (2.8%) respectively.

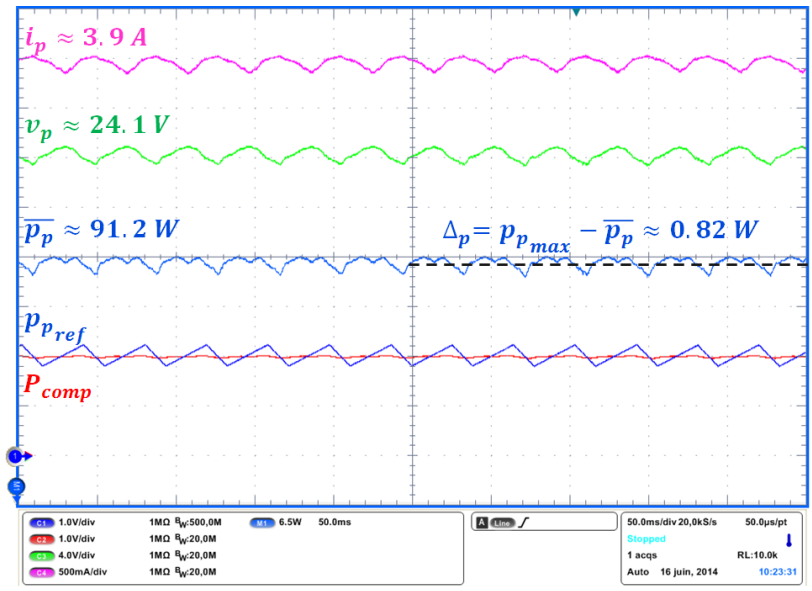

Fig. 2.30. Detail of the experimental oscillating components of the current, voltage and powers.

2.6.3 Steady-state and motion of the MPPT variables

As shown in figure 2.31, interesting experimental results can be obtained by a repetitive start-up of the converter without changes in the PV module characteristics. Because the maximum point is the same, the curve in the plane P-G shows the trajectory of the system towards the maximum power point. As expected the same limit cycle is obtained for the power reference when the system attains the maximum. It is possible to observe that the power of the panel is constrained more or less in the middle point between the maximum and minimum power reference. Further, it is possible to observe in the trace of the extracted power (p_p) the behavior representing the motion around the maximum power point.

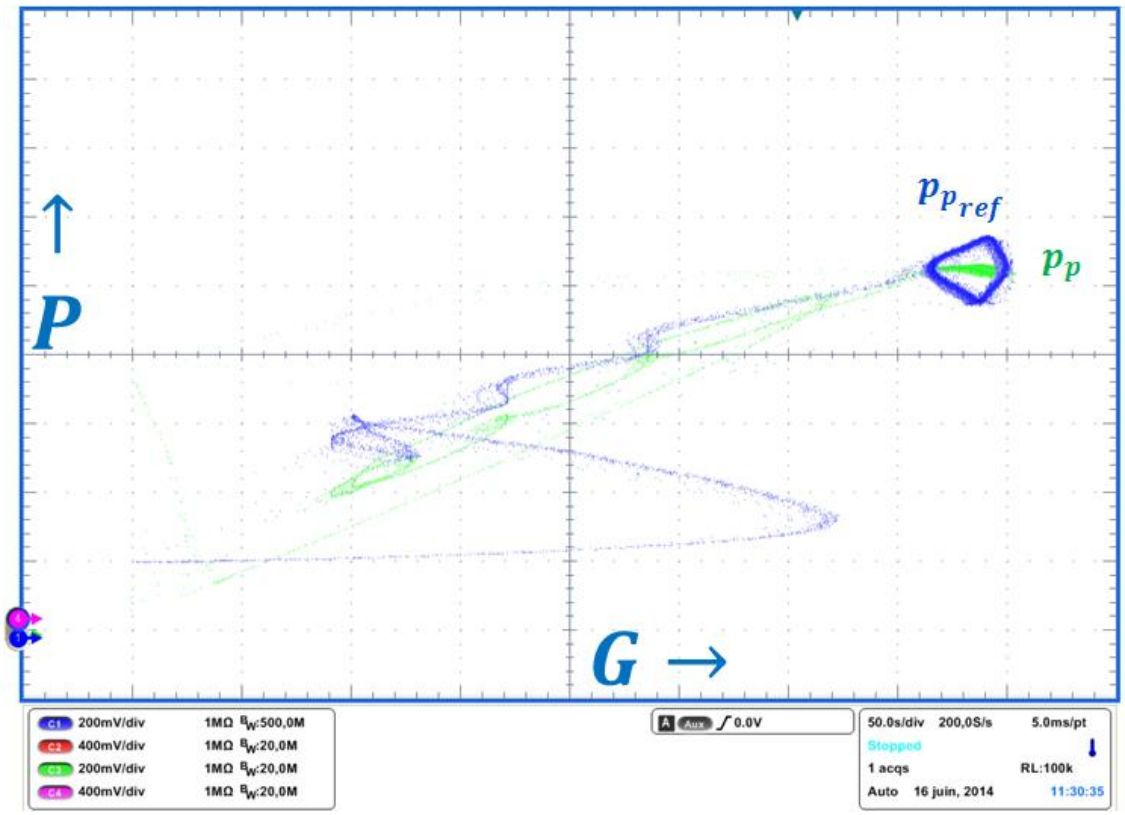

Fig. 2.31. Steady-state behavior of the proposed MPPT algorithm

To complete the result of figure 2.31 with the MPPT internal signals, figure 2.32 shows the steady-state behavior of the system working in the maximum power point by comparing the time -based representation with the P-G representation.

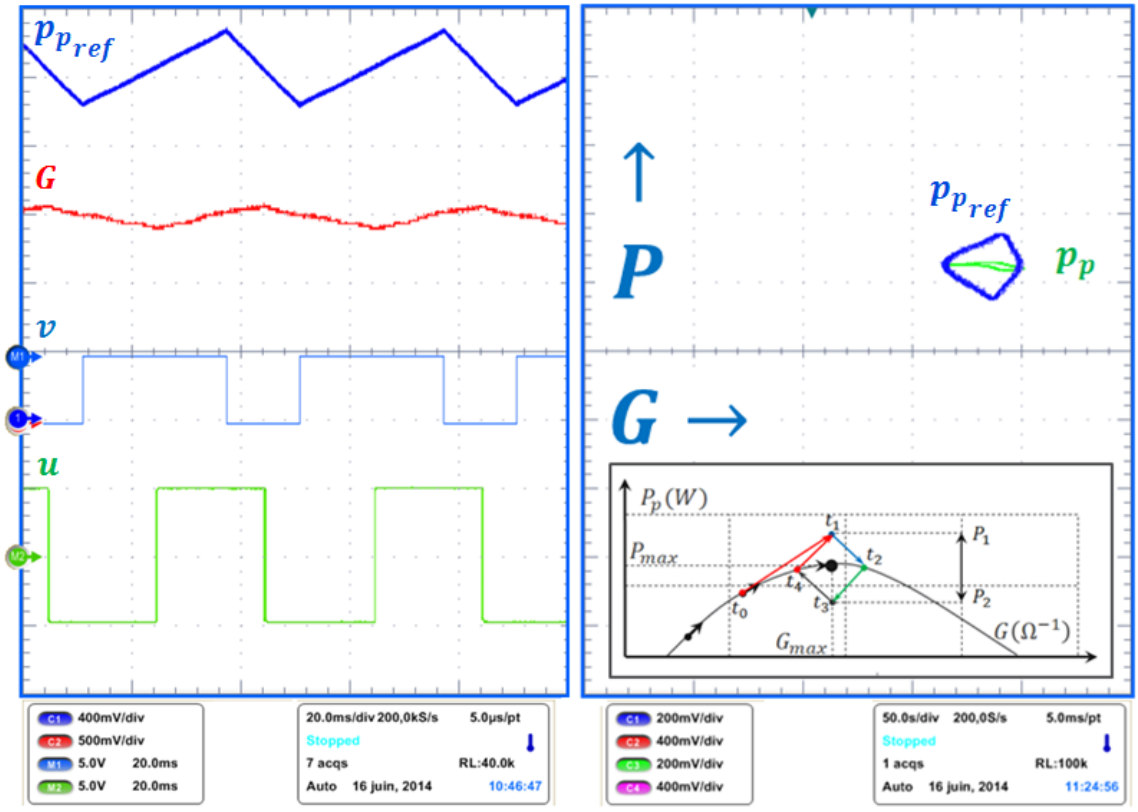

Fig. 2.32. Steady-state behavior of the proposed MPPT algorithm

The four trajectories corresponding to the four structures of the system are clearly differentiated in the capture at the right of figure 2.32. These four trajectories form a rhombus as depicted in the figure 2.7. Each trajectory consists in a simultaneous variation of the conductance and the power reference. The waveforms at the left of figure 2.32 allows to observe the increment or decrement of the conductance, the power reference and illustrates how the nonlinearities u and v induce the motion of the system.

2.6.4 Detail of the sliding motion towards the maximum

When the parameter K_2 is reduced close to the limit of stability, a quick variation is induced in the power reference. This condition increases the frequency of the reference and slows the motion towards the maximum as illustrated in figure 2.33.

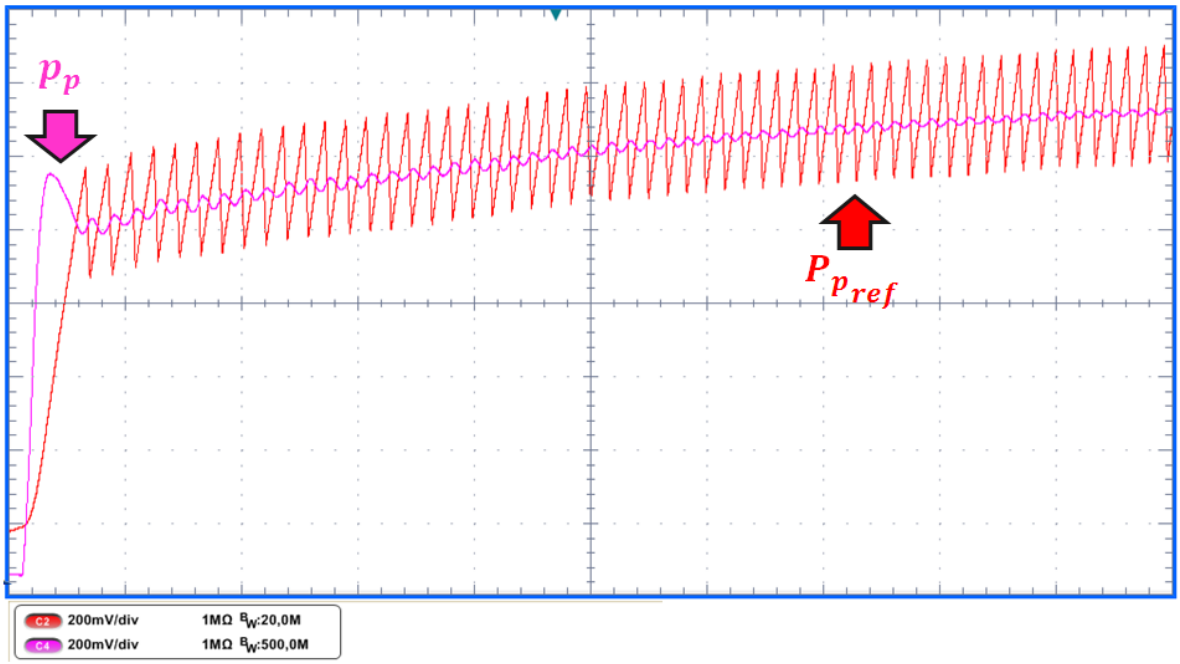

Fig. 2.33. Response of the power towards the maximum power point after the system's start-up

The corresponding behavior described in the plane P-G is shown in figure 2.34, where it can be observed that the motion of the power reference is constrained between two envelopes. It is also possible to observe the motion of the power inside the envelopes being very close to the average value of the power reference.

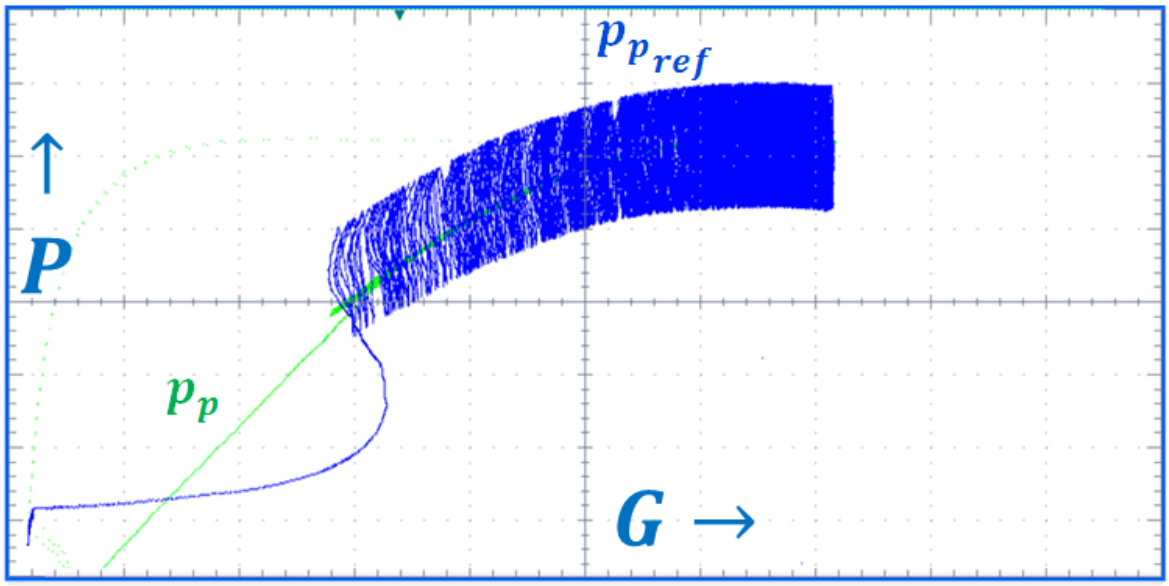

Fig. 2.34. Measured trajectory of the power towards the maximum power point in the P-G plane showing the variable structure behavior while approaching to the maximum power point

Making an important zoom in both variables (P and G) at the steady-state, the result in figure 2.35 is obtained. In this case, the motion of the power reference induces a very small variation of the real power (p_p) ensuring the maximum power point with reduced oscillations increasing the performance of the algorithm. However, as shown in figure 2.33, this improved performance can be obtained with a slower transient response.

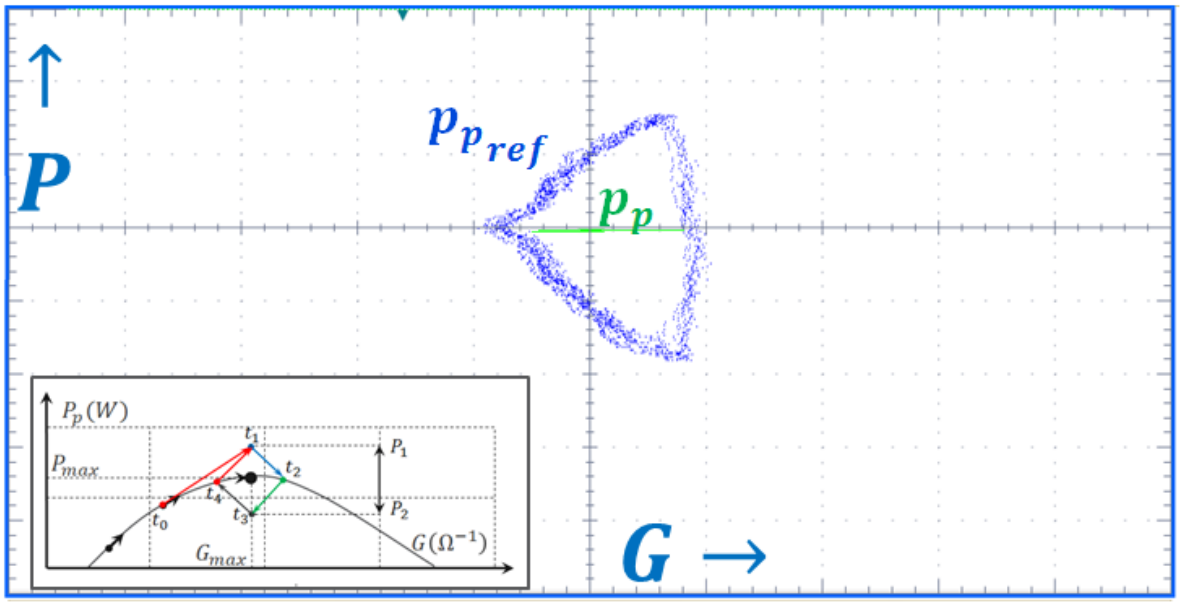

Fig. 2.35. Zoom of the experimental steady -state behavior of powers and conductance in the P-G plane.

2.6.5 Start-up of the algorithm

The start-up of the algorithm has been captured in order to evaluate the transient behavior from the open circuit condition to the maximum power point. As it can be observed in figure 2.36, the steady- state is reached in 300 ms approximately. Although the algorithm is able to have a faster start-up, the presence of the filters conditioning the current and voltage has an impact on the transient response of the measured power, introducing a deviation between the real power and the measured power. However, these filters reduce the presence of noise and eliminate the high frequency in the measurement of the inductor current.

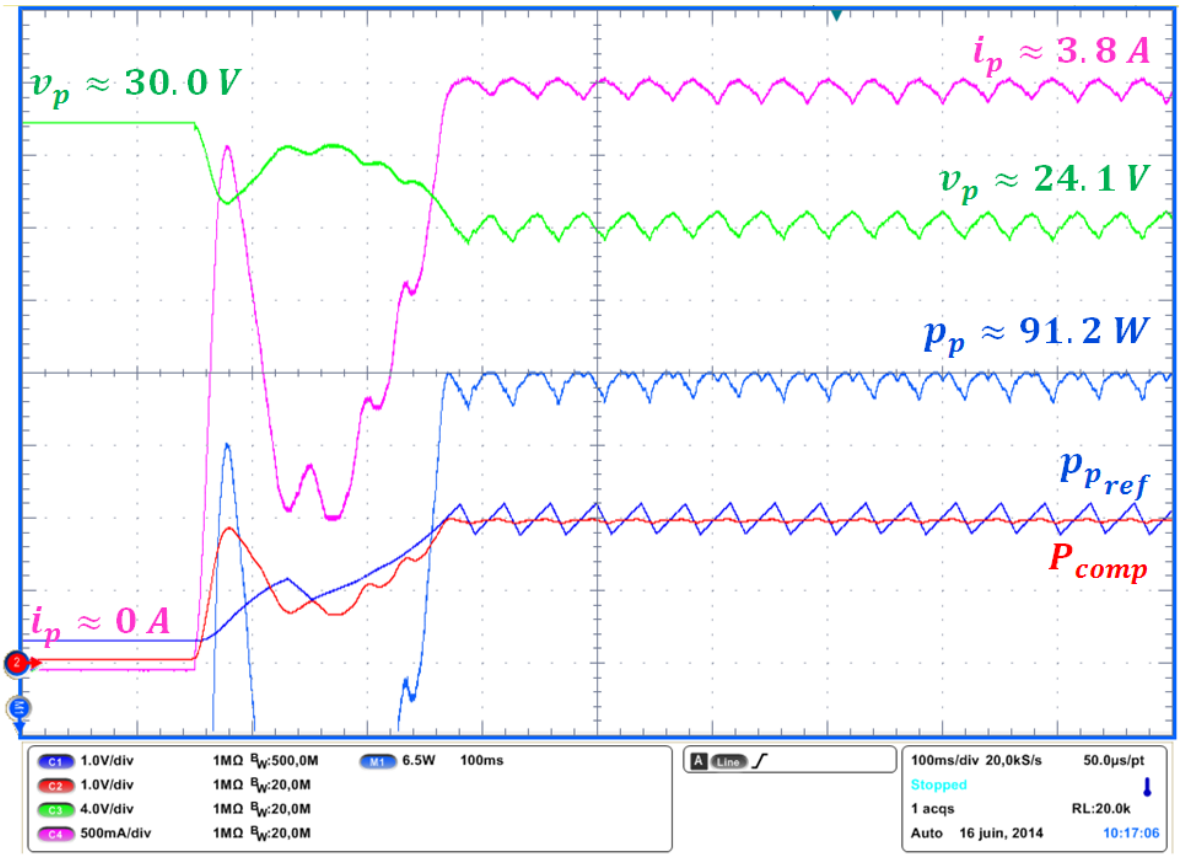

Fig. 2.36. Time response of the voltage, current and power of the system during a start-up

2.6.6 Sliding motion of the MPPT algorithm

A programed sequence of I-V characteristics has been introduced in the PV module emulator E4360A in order to have stepped increments and decrements with a holding time each one of 2 s. Figure 2.37 shows the power signals for the above test in the voltage levels of the control circuit. A power of 100 W corresponds to a voltage level of 1 V and a power level of 50 W corresponds to a voltage level of 500 mV. As it can be shown, the system shows a stable behavior and a smooth transition in the changes of equilibrium points. The power reference is constrained into the hysteresis band. However, the hysteresis is defined for the power error and not for the power reference leading to an extracted power of the panel in a neighborhood of the maximum power with a small variation. Figure 2.37 also shows a zoom in transitions to clearly show the behavior of both power reference and the real power.

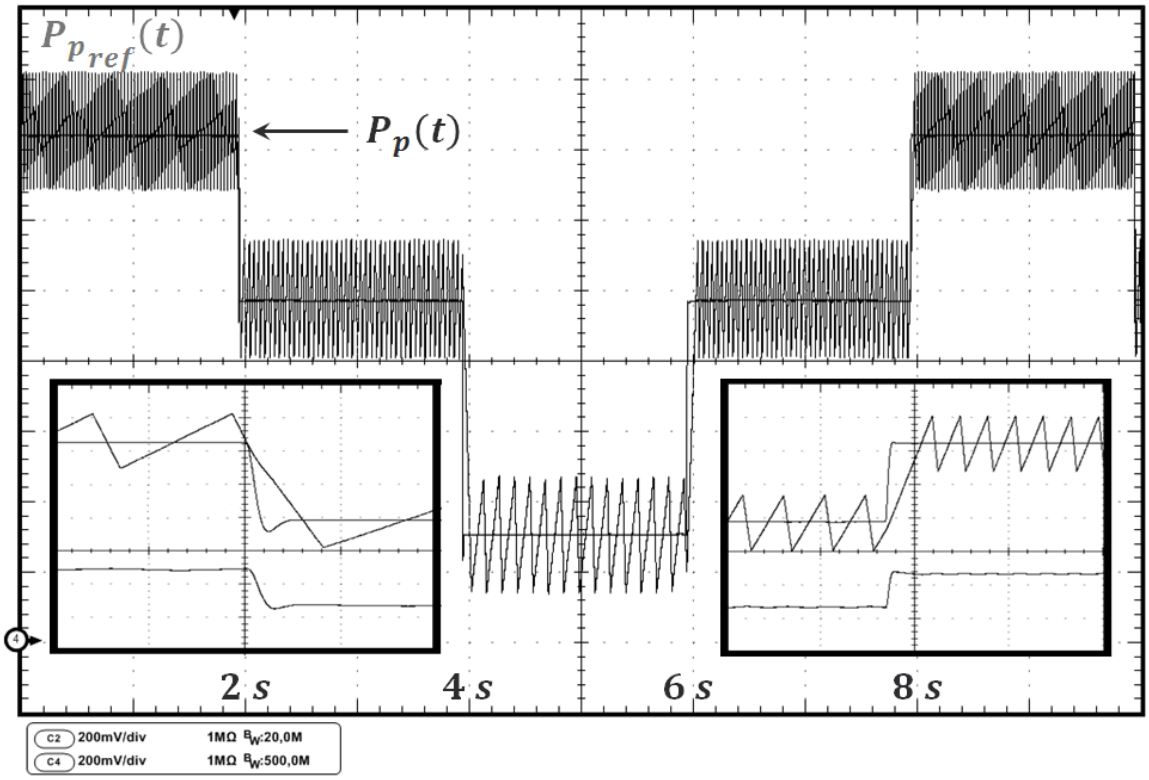

Fig. 2.37. Time response of the algorithm to irradiance changes

2.6.7 Dynamic response for changes in the P-V characteristic

Two tests are performed in order to assess the dynamic response of the algorithm. The first test consists in changing the I-V characteristic of the panel emulator from a first point with a maximum power value about 95 W to another one with a maximum power value of 65 W and vice versa. Each I-V characteristic is maintained during 500 ms. An oscilloscope capture with the experimental results is shown in figure 2.38. The second test consist in changing the I-V characteristic from a first point with a maximum power of about 110 W to another one with a maximum power value of 20 W and vice versa. An oscilloscope capture with the corresponding results is depicted in figure 2.39. As it can be observed in both tests, the algorithm has a significant rapid response. Furthermore, it is possible to observe that the real power reaches the maximum value before that the power reference reaches the steady- state increasing the general performance and the harvesting of the power.

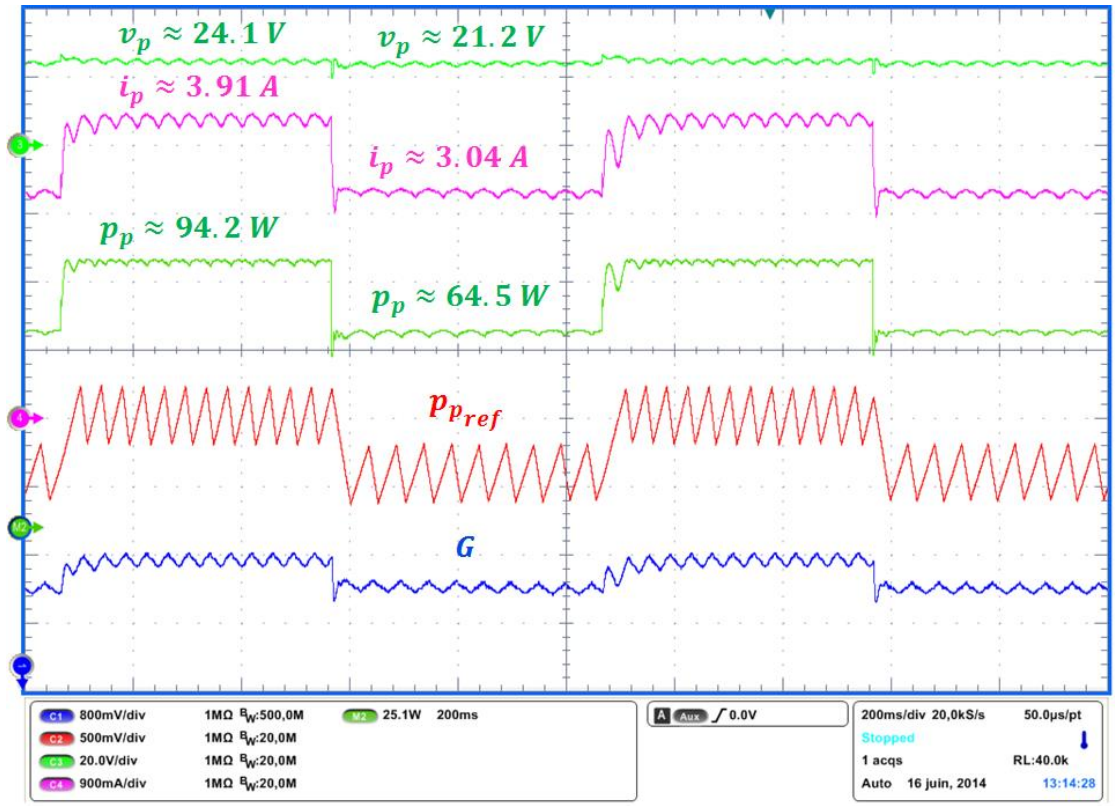

Fig. 2.38. Experimental results for 30 W sudden changes in the P-V characteristic curve.

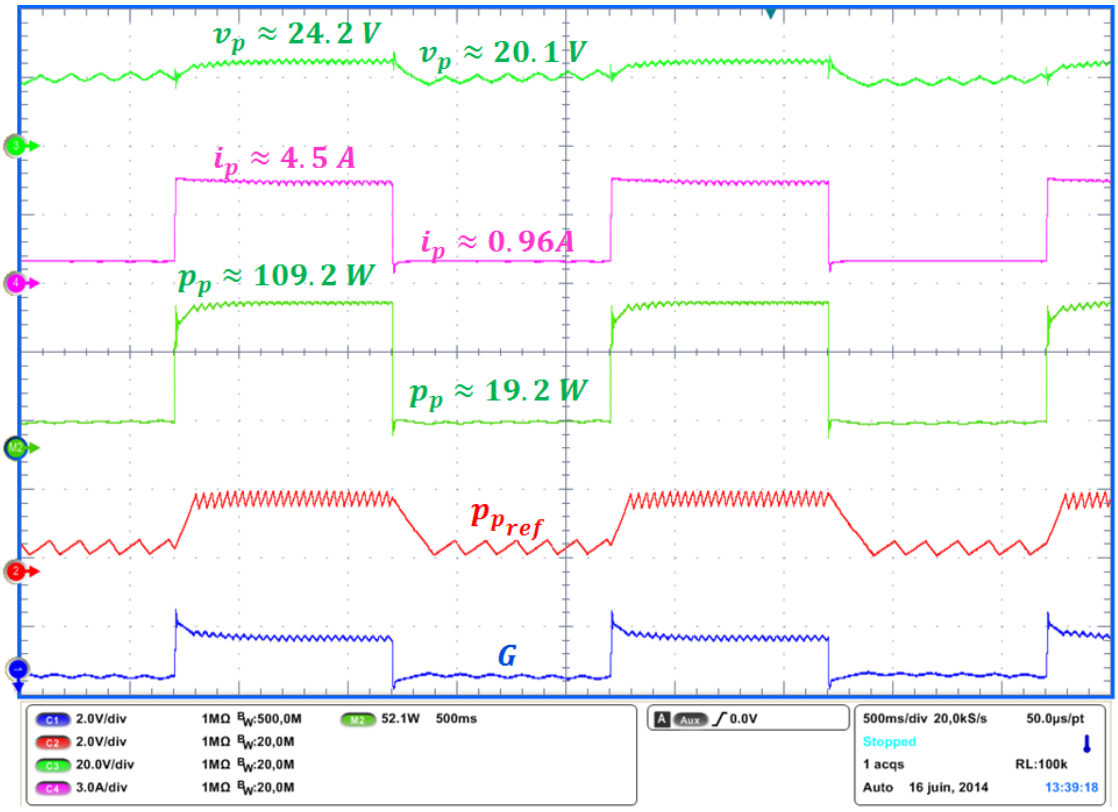

Fig. 2.39. Experimental results for 80 W sudden changes in the P-V characteristic curve.

2.6.8 General approach of the functionality and performance

The general functionality of the algorithm has been experimentally evaluated using the overall microinverter system connected to the grid and fed by a solar panel. As it can be observed in figure 2.40, in this test the P-V characteristic curve of the panel has been captured using the curve tracer , and the more representative waveforms have been captured. The maximum power measured with the tracer instrument is 82.4 W while the maximum power measured by the oscilloscope is 82.24 W. The average value of the power measured by the oscilloscope is 81.82 W and hence the MPPT efficiency is around 99.45%. In the oscilloscope capture, it is possible to observe the power waveform which exhibits the expected double frequency phenomenon at the maximum power point. The power reference and the voltage of the DC bus (400 V) are also measured. For this operational condition, the frequency of the power reference is 20 Hz.

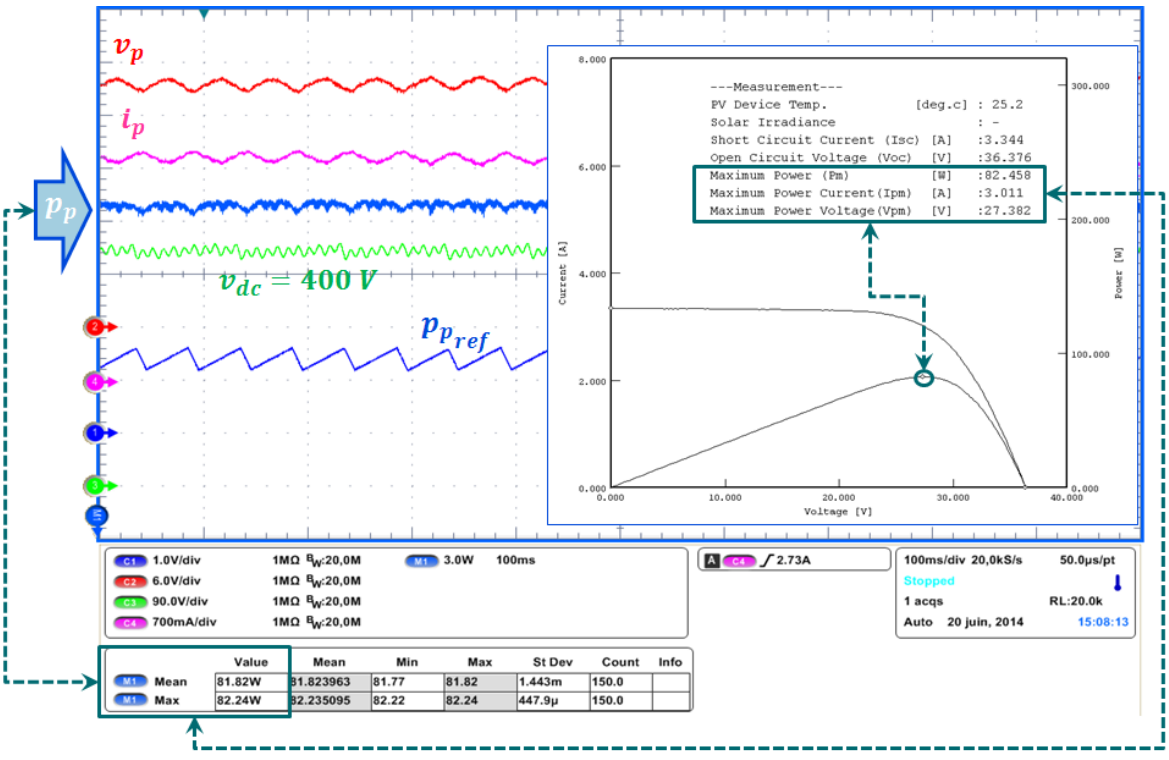

Fig. 2.40. General validation of the performance of the proposed MPPT algorithm.

These results are only presented to complete this chapter. An accurate description of the overall system will be presented in the chapter 5.

2.7 CONCLUSIONS

In this chapter a Sliding-Mode Extremum Seeking Control MPPT algorithm has been developed. A new proposal has been inspired from the self-optimized function based on sliding-mode proposed by Professor Vadim Utkin more than thirty years ago and revisited recently in the photovoltaic field [77]. Our algorithm shows several advantages to operate with high-gain converters because it does not work using the duty cycle as output signal since that approach introduces several limitations in the domain of the objective optimization function (P-D characteristic). By contrast, the conductance is used as output variable leading to a good compatibility with the proposed control law for the DC-DC conversion stage of the microinverter.

The basic idea is to generate a fictitious power reference compared with the instantaneous power measured at the output of the PV module. The resulted error defines the states of non-linear functions increasing or decreasing the output signal (conductance) and the internal reference (power reference). The dynamics of the algorithm correspond to a variable structure system with four structures since four motions are identified in the P-G plane. The attractivity of the sliding surface and also the trajectory towards the maximum point has been modeled, studied and validated. Only four tuning parameters are required in the algorithm: K_1, K_2, M and Δ, which only depends on the maximum derivative of the power with respect to the conductance. A particular way to evaluate the maximum derivative of a specific PV module has been also proposed using an asymptotic modelling of the PV module characteristics. As a consequence, the algorithm can be easily tuned ensuring a proper operation in a wide range of power.

The high performances of the algorithm have been verified using simulation and experimental results. The algorithm supports sudden changes on the irradiance and temperature levels demonstrating robustness and reliability. These results motivate the study of the functionalities of the algorithm in the context of other applications. The efficiency of the power extraction was evaluated around 99.6% which is comparable with the best reported performances in ESC MPPT algorithms which normally are above 99% [60]-[70]. Further, the trade-off between the performance and the robustness of the algorithm is very favorable in comparison with other methods that use derivatives or logical operator to find the maximum power point.

2.8 REFERENCES

Comparison of methods

[1] V. Salas, E. Olias, A Barrado, A. Lázaro, "Review of the Maximum Power Point Tracking Algorithms for Stand-Alone Photovoltaic Systems," *Solar Energy Materials & Solar Cells*, vol. 90, pp. 1555-1578, 2006.

[2] B. Subudhi, R. Pradhan, "A Comparative Study on Maximum Power Point Tracking Techniques for Photovoltaic Power Systems," *IEEE Trans. on Sustainable Energy*, vol. 4, no. 1, pp. 89-98, Jan. 2013.

[3] M.AG. de Brito, L. Galotto, L.P. Sampaio, G. de Azevedo e Melo, C.A. Canesin, "Evaluation of the Main MPPT Techniques for Photovoltaic Applications," *IEEE Trans. Industrial Electron.*, vol. 60, no. 3, pp. 1156-1167, Mar. 2013.

[4] D. Sera, L. Mathe, T. Kerekes, S.V. Spataru, R. Teodorescu, "On the Perturb-and-Observe and Incremental Conductance MPPT Methods for PV Systems," *IEEE J. of Photovoltaics*, vol. 3, no. 3, pp. 1070-1078, Jul. 2013.

[5] S.B. Kjaer, "Evaluation of the "Hill Climbing" and the "Incremental Conductance" Maximum Power Point Trackers for Photovoltaic Power Systems," *IEEE Trans. Energy Conversion*, vol. 27, no. 4, pp. 922-929, Dec. 2012.

[6] C.B. Salah, M. Ouali, "Comparison of Fuzzy Logic and Neural Network in Maximum Power Point Tracker for PV Systems," *Electric Power System Research*, vol. 81, pp. 43-50, 2011.

[7] T. Esram, P.L. Chapman, "Comparison of Photovoltaic Array Maximum Power Point Tracking Techniques," *IEEE Trans. Energy Conversion*, vol. 22, no. 2, pp. 439-449, Jun. 2007.

[8] S. Jain, V. Agarwal, "Comparison of the performance of maximum power point tracking schemes applied to single-stage grid-connected photovoltaic systems," *IET Electric Power Applications*, vol. 1, no. 5, pp. 753-762, Sep. 2007.

[9] M.A. Masoum, H. Dehbonei, E.F. Fuchs, "Theoretical and Experimental Analyses of Photovoltaic Systems with Voltage and Current-Based Maximum Power Point Tracking," *IEEE Power Engineering Review*, vol. 22, no. 8, pp. 62-62, Aug. 2002.

Model or Parameter based methods

[10] K.-J. Lee, R.-Y. Kim, "An Adaptive Maximum Power Point Tracking Scheme Based on a Variable Scaling Factor for Photovoltaic Systems," IEEE Trans. Energy Conversion, vol. 27, no. 4, pp. 1002-1008, Dec. 2012.

[11] D. Shmilovitz, "On the control of photovoltaic maximum power point tracker via output parameters," IEE Proceedings - Electric Power Applications, vol. 152, no. 2, pp. 239-248, Mar. 2005.

[12] V.V.R. Scarpa, G. Spiazzi, S. Buso, "Low complexity MPPT technique exploiting the effect of the PV cell series resistance," in Proc. Twenty-Third Annual IEEE Applied Power Electronics Conference and Exposition, 2008, pp. 1958-1964, Feb. 2008.

Model based and heuristic methods

[13] L.V. Hartmann, M.A. Vitorino, M.B.R. Correa, AM.N. Lima, "Combining Model-Based and Heuristic Techniques for Fast Tracking the Maximum-Power Point of Photovoltaic Systems," IEEE Trans. Power Electron., vol. 28, no. 6, pp. 2875-2885, Jun. 2013.

Frequency based methods

[14] K. K. Tse, M.T. Ho, H.S.-H. Chung, S.Y.R. Hui, "A novel maximum power point tracker for PV panels using switching frequency modulation," IEEE Trans. Power Electron., vol. 17, no. 6, pp. 980-989, Nov. 2002.

[15] K.K. Tse, B.M.T. Ho, H.S.-H. Chung, S.Y. Ron Hui, "A comparative Study of Maximum-Power-Point-Trackers for Photovoltaic Panels Using Switching-Frequency Modulation Scheme," IEEE Trans. Ind. Electron., vol. 51, no. 2, Apr. 2004.

[16] Y. Jiang; J.AA. Qahouq, T.A. Haskew, "Adaptive Step Size With Adaptive-Perturbation-Frequency Digital MPPT Controller for a Single-Sensor Photovoltaic Solar System," IEEE Trans. Power Electron., vol. 28, no. 7, pp. 3195-3205, Jul. 2013.

Duty Cycle Based

[17] H.S.-H. Chung, K.K. Tse, S.Y.R. Hui, C. M. Mok, M.T. Ho, "A novel maximum power point tracking technique for solar panels using a SEPIC or Cuk converter," IEEE Trans. Power Electron., vol. 18, no. 3, pp. 717-724, May. 2003.

[18] E. Koutroulis, K. Kalaitzakis, N.C. Voulgaris, "Development of a microcontroller-based, photovoltaic maximum power point tracking control system," IEEE Trans. Power Electron., vol. 16, no. 1, pp. 46-54, Jan. 2001.

[19] M. Veerachary, T. Senjyu, K. Uezato, "Voltage-based maximum power point tracking control of PV system," IEEE Trans. Aerospace and Electron. Syst., vol. 38, no. 1, pp. 262-270, Jan. 2002.

[20] H.-S. Bae, J.-H. Park, B.-H. Cho, G.-J. Yu, "New MPPT Control Strategy for Two-Stage Grid-Connected Photovoltaic Power Conditioning System," J. of Power Electron., vol. 7, no. 2, pp. 174-180, 2007.

[21] M. Veerachary, T. Senjyu, K. Uezato, "Maximum Power Point Tracking of Coupled Inductor Interleaved Boost Converter Supplied PV System," IEE Proc. Electric Power Applications, vol. 150, no. 1, pp. 71-80, Jan. 2003.

Perturb and Observe

[22] S.K. Kollimalla, M.K. Mishra, "A Novel Adaptive P&O MPPT Algorithm Considering Sudden Changes in the Irradiance," IEEE Trans. Energy Conversion, vol. 29, no. 3, pp. 602-610, Sep. 2014.

[23] S.K. Kollimalla, M.K. Mishra, "Variable Perturbation Size Adaptive P&O MPPT Algorithm for Sudden Changes in Irradiance," IEEE Trans. Sustainable Energy, vol. 5, no. 3, pp. 718-728, Jul. 2014.

[24] D.C. Jones, R.W. Erickson, “Probabilistic Analysis of a Generalized Perturb and Observe Algorithm Featuring Robust Operation in the Presence of Power Curve Traps,” IEEE Trans. Power Electron., vol. 28, no. 6, pp. 2912-2926, Jun. 2013.
[25] N. Fermia, G. Petrone, G. Spagnuolo, M. Vitelli, “A technique for Improving P&O MPPT Performances of Double-Stage Grid-Connected Photovoltaic Systems,” IEEE Trans. Ind. Electron., vol. 56, no. 11, Nov. 2009.
[26] Y. Yang, F.P. Zhao, “Adaptive Perturb and Observe MPPT Technique for Grid-Connected Photovoltaic Inverters,” Procedia Engineering, vol. 23, pp. 468-473, 2011.
[27] tracking method,” IEEE Trans. on Power Electron., vol. 20, no. 4, pp. 963-973, Jul. 2005.
[28] N. Femia, G. Petrone, G. Spagnuolo, M. Vitelli, “Perturb and observe MPPT technique robustness improved,” IEEE Int. Symposium on Ind. Electron., 2004, vol. 2, pp. 845-850.

Optimized Perturb and Observe

[29] A. El Khateb, N.A. Rahim, J. Selvaraj, M.N. Uddin, “Maximum power point tracking of single-ended primary-inductor converter employing a novel optimization technique for proportional-integral-derivative controller,” IET Power Electron., vol. 6, no. 6, pp. 1111-1121, Jul. 2013.
[30] G. Carannante, C. Fraddanno, M. Pagano, L. Piegari, “Experimental Performance of MPPT Algorithm for Photovoltaic Sources Subject to Inhomogeneous Insolation,” IEEE Trans. Ind. Electron., vol. 56, no. 11, pp. 4374-4380, Nov. 2009.
[31] K.L. Lian, J.H. Jhang, IS. Tian, “A Maximum Power Point Tracking Method Based on Perturb-and-Observe Combined With Particle Swarm Optimization,” IEEE J. of Photovoltaics, vol. 4, no. 2, pp. 626-633, Mar. 2014.
[32] D. Sera, R. Teodorescu, J. Hantschel, M. Knoll, “Optimized Maximum Power Point Tracker for Fast-Changing Environmental Conditions,” IEEE Trans. Ind. Electron., vol. 55, no. 7, pp. 2629-2637, Jul. 2008.
[33] D. Sera, T. Kerekes, R. Teodorescu, F. Blaabjerg, “Improved MPPT method for rapidly changing environmental conditions,” in Proc. IEEE Int. Symposium on Ind. Electron., vol. 2, pp. 1420-1425, Jul. 2006.
[34] N. Femia, G. Petrone, G. Spagnuolo, M. Vitelli, “Optimization of perturb and observe maximum power point tracking method," IEEE Trans. Power Electron., vol. 20, no. 4, pp. 963-973, Jul. 2005.

Incremental conductance

[35] K. Soon Tey, S. Mekhilef, “Modified Incremental Conductance Algorithm for Photovoltaic System under Partial Shading Conditions and Load Variation,” IEEE Trans. Ind. Electron., vol. 61, no. 10, pp. 5384-5392, Oct. 2014.
[36] R. Faraji, A. Rouholamini, H.R. Naji, R. Fadaeinedjad, M.R. Chavoshian, “FPGA-based real time incremental conductance maximum power point tracking controller for photovoltaic systems,” IET Power Electron., vol. 7, no. 5, pp. 1294-1304, May 2014.
[37] M.A. Elgendy, B. Zahawi, D.J. Atkinson, “Assessment of the Incremental Conductance Maximum Power Point Tracking Algorithm,” IEEE Trans. Sustainable Energy, vol. 4, no. 1, pp. 108-117, Jan. 2013.
[38] H. Guan-Chyun, H. Hung-I Hsieh, T. Cheng-Yuan, W. Chi-Hao, “Photovoltaic Power-Increment-Aided Incremental-Conductance MPPT With Two-Phased Tracking,” IEEE Trans. Power Electron., vol. 28, no. 6, pp. 2895-2911, Jun. 2013.
[39] G.J. Kish, J.J. Lee, P.W. Lehn, “Modelling and control of photovoltaic panels utilizing the incremental conductance method for maximum power point tracking,” IET Renewable Power Generation, vol. 6, no. 4, pp. 259-266, Jul. 2012.
[40] A. Safari, S. Mekhilef, “Simulation and Hardware Implementation of Incremental Conductance MPPT With Direct Control Method Using Cuk Converter,” IEEE Trans. Ind. Electron., vol. 58, no. 4, pp. 1154-1161, Apr. 2011.
[41] T. Kerekes, R. Teodorescu, M. Liserre, R. Mastromauro, A. Dell'Aquila, “MPPT algorithm for voltage controlled PV inverters,” in Proc. 11th Int. Conf. on Optimization of Electrical and Electronic Equipment, (OPTIM), 2008, pp. 427-432.
[42] Y.-C. Kuo; T.-J. Liang; J.-F. Chen, “Novel Maximum-Power-Point-Tracking Controller for Photovoltaic Energy Conversion System,” IEEE Trans. Ind. Electron., vol. 48, no. 3, pp. 594-601, Jun. 2001.

Incremental resistance

[43] Q. Mei, M. Shan; L. Liu, J.M. Guerrero, “A Novel Improved Variable Step-Size Incremental-Resistance MPPT Method for PV Systems,” IEEE Trans. Ind. Electron., vol. 58, no. 6, pp. 2427-2434, Jun. 2011.
[44] J.-H. Park, J.-Y. Ahn, B.-H. Cho, G.-J. Yu, “Dual-Module-Based Maximum Power Point Tracking Control of Photovoltaic Systems,” IEEE Trans. Ind. Electron., vol. 53, no. 4, pp. 1036-1047, Jun. 2006.

Modified Incremental conductance

[45] T. Kerekes, R. Teodorescu, M. Liserre, R. Mastromauro, A. Dell'Aquila, “MPPT Algorithm for Voltage Controlled PV Inverters," in Proc. 11th International Conference on Optimization of Electrical and Electronic Equipment (OPTIM), 2008. pp. 427-432, May. 2008.
[46] Y. Zou, Y. Yu, Y. Zhang, J. Lu, “MPPT Control for PV Generation System Based on an Improved Inccond Algorithm,” Procedia Engineering, vol. 20, pp. 105-109, 2012.
[47] E. Roman, R. Alonso, P. Ibanez, S. Elorduizapatarietxe, D. Goitia, “Intelligent PV Module for Grid-Connected PV Systems,” IEEE Trans. Ind. Electron., vol. 53, no. 4, pp. 1066-1073, Jun. 2006.

Fuzzy-logic Algorithms

[48] A. El Khateb, N. Abd Rahim, J. Selvaraj, M.N. Uddin, “Fuzzy-Logic-Controller-Based SEPIC Converter for Maximum Power Point Tracking,” IEEE Trans. Industry Applications, vol. 50, no. 4, pp. 2349-2358, Jul. 2014.

[49] M.AA. Mohd Zainuri, M.A. Mohd Radzi, AC. Soh, N.A. Rahim, "Development of adaptive perturb and observe-fuzzy control maximum power point tracking for photovoltaic boost dc-dc converter," IET Renewable Power Generation, vol. 8, no. 2, pp. 183-194, Mar. 2014.
[50] B.N. Alajmi, K.H. Ahmed, S.J. Finney, B.W. Williams, "Fuzzy-Logic-Control Approach of a Modified Hill-Climbing Method for Maximum Power Point in Microgrid Standalone Photovoltaic System," IEEE Trans. Power Electron., vol. 26, no. 4, pp. 1022-1030, Apr. 2011.
[51] M. Veerachary, T. Senjyu, K. Uezato, "Feedforward maximum power point tracking of PV systems using fuzzy controller," IEEE Trans. Aerospace and Electro. Syst., vol. 38, no. 3, pp. 969-981, Jul. 2002.
[52] F. Chekired, C. Larbes, D. Rekioua, F. Haddad, "Implementation of a MPPT Fuzzy Controller for Photovoltaic Synthesis on FPGA Circuit," Energy Procedia, vol. 6, pp. 541-549, 2011.

Predictive

[53] P.E. Kakosimos, AG. Kladas, S.N. Manias, "Fast Photovoltaic-System Voltage- or Current-Oriented MPPT Employing a Predictive Digital Current-Controlled Converter," IEEE Trans. Ind. Electron., vol. 60, no. 12, pp. 5673-5685, Dec. 2013.

Random search

[54] K. Sundareswaran, S. Peddapati, S. Palani, "Application of random search method for maximum power point tracking in partially shaded photovoltaic systems," IET Renewable Power Generation, vol. 8, no. 6, pp. 670-678, Aug. 2014.

RPC as Extermum Seeking Technique

[55] AM. Bazzi, P.T. Krein, "Ripple Correlation Control: An Extremum Seeking Control Perspective for Real-Time Optimization," IEEE Trans. Power Electron., vol. 29, no. 2, pp. 988-995, Feb. 2014.

Ripple Correlation Control

[56] J.-Y. Gu; G.-C. Chen, "A fast MPPT algorithm for single stage grid-connected PV inverter," in Proc. 7th IEEE Conf. on Ind. Electron. and Applications (ICIEA), 2012, pp. 960-965.
[57] J.W. Kimball, P.T. Krein, "Discrete-Time Ripple Correlation Control for Maximum Power Point Tracking," IEEE Trans. on Power Electron., vol. 23, no. 5, pp. 2353-2362, Sep. 2008.
[58] T. Esram, J.W. Kimball, P.T. Krein, P.L. Chapman, P. Midya, "Dynamic Maximum Power Point Tracking of Photovoltaic Arrays Using Ripple Correlation Control," IEEE Trans. Power Electron., vol. 21, no. 5, pp. 1282-1291, Sep. 2006.
[59] R. Stala, K. Koska, L. Stawiarski, "Realization of modified ripple-based MPPT in a single-phase single-stage grid-connected photovoltaic system," in Proc. IEEE International Symposium on Industrial Electronics (ISIE), 2011, pp. 1106-1111.

Extremum seeking control

[60] R. Leyva, C. Alonso, I. Queinnec, A. Cid-Pastor, D. Lagrange, L. Martinez-Salamero, "MPPT of photovoltaic systems using Extremum - seeking control," IEEE Trans. Aerospace and Electron. Syst., vol. 42, no. 1, pp. 249-258, Jan. 2006.
[61] H. Zazo, R. Leyva, E. del Castillo, "MPPT based on Newton-Like Extremum Seeking Control," in Proc. IEEE International Symposium on Industrial Electronics (ISIE), 2012, pp. 1040-1045.
[62] C. Zhang, Z. Zhang, M. Chen, Z. Qian, "An improved variable step-size maximum power point tracking (MPPT) based on Extremum seeking control (ESC) in gird-connected photovoltaic micro-converter system," 2012 IEEE Int. Symposium on Ind. Electron. (ISIE), 2012, pp. 1765-1770.
[63] X. Li; Y. Li; J.E. Seem, "Maximum Power Point Tracking for Photovoltaic System Using Adaptive Extremum Seeking Control," IEEE Trans. on Control Syst. Technology, vol. 21, no. 6, pp. 2315-2322, Nov. 2013.
[64] S.J. Moura, Y.A. Chang, "Asymptotic convergence through Lyapunov-based switching in Extremum seeking with application to photovoltaic systems," in Proc. American Control Conference (ACC), 2010, pp. 3542-3548.
[65] X. Li, L. Yaoyu, J.E. Seem, "Maximum Power Point Tracking for Photovoltaic System Using Adaptive Extremum Seeking Control," IEEE Trans. Control Syst. Technology, vol. 21, no. 6, pp. 2315-2322, Nov. 2013.
[66] AM. Bazzi, P.T. Krein, "Concerning Maximum Power Point Tracking for Photovoltaic Optimization Using Ripple-Based Extremum Seeking Control," IEEE Trans. Power Electron., vol. 26, no. 6, pp. 1611-1612, Jun. 2011.
[67] C. Olalla, M.I. Arteaga, R. Leyva, A. El Aroudi, "Analysis and Comparison of Extremum Seeking Control Techniques," in Proc. IEEE International Symposium on Industrial Electronics (ISIE), 2007, pp.72-76, Jun. 2007.
[68] S.L. Brunton, C.W. Rowley, S.R. Kulkarni, C. Clarkson, "Maximum Power Point Tracking for Photovoltaic Optimization Using Ripple-Based Extremum Seeking Control," IEEE Trans. Power Electron., vol. 25, no. 10, pp. 2531-2540, Oct. 2010.
[69] R. Leyva, H. Zazo, "Saturation effects in digital Extremum seeking control for photovoltaic applications," IEEE Energy Conversion Congress and Exposition (ECCE), 2013, pp. 4775-4779.
[70] C. Cabal, C. Alonso, C., A. Cid-Pastor, B. Estibals, L. Seguier, R. Leyva, G. Schweitz, J. Alzieu, "Adaptive digital MPPT control for photovoltaic applications," IEEE International Symposium on Industrial Electronics (ISIE), 2007, pp. 2414-2419.

Sliding-mode

[71] H.-T. Yau, C.-J. Lin, C.-H. Wu, "Sliding Mode Extremum Seeking Control Scheme Based on PSO for Maximum Power Point Tracking in Photovoltaic Systems," Int. J. of Photoenergy, vol. 2013, pp. 1-10, 2013.

[72] E. Bianconi, J. Calvente, R. Giral, E. Mamarelis, G. Petrone, C.A. Ramos-Paja, G. Spagnuolo, M. Vitelli, "A Fast Current-Based MPPT Technique Employing Sliding Mode Control," IEEE Trans. Ind. Electron., vol. 60, no. 3, pp. 1168-1178, Mar. 2013.
[73] Y. Levron, D. Shmilovitz, "Maximum Power Point Tracking Employing Sliding Mode Control," IEEE Trans. Circuits and Syst. I: Regular Papers, vol. 60, no. 3, pp. 724-732, Mar. 2013.
[74] I.-S. Kim, "Robust maximum power point tracker using sliding mode controller for the three-phase grid-connected photovoltaic system," Solar Energy, vol. 81, pp. 405-414, 2007.
[75] C.-C. Chu, C.-L. Chen, "Robust maximum power point tracking method for photovoltaic cells: A sliding mode control approach," Solar Energy, vol. 83, pp. 1370-1378, 2009.

Perturb and observe and sliding-mode

[76] C. Cabal, L. Martinez-Salamero, L. Seguier, C. Alonso ,F. Guinjoan " Maximum power point tracking based on sliding-mode control for output-series connected converters in photovoltaic systems" IET Power Electron., vol. 7, iss. 4 pp. 914-923, 2014.

Book of Utkin

[77] V.I. Utkin, Sliding Modes in Control and Optimization, Ed. Springer-Verlag, 1981.

Self-Optimized Sliding-Mode

[78] AH. Alqahtani, V.I. Utkin, "Self-optimization of photovoltaic system power generation based on sliding mode control," in Proc. 38th Annual Conf. on IEEE Ind. Electron. Society (IECON), 2012, pp. 3468-3474.

Approximations or analysis of the panel curves

[79] J.S.C.M. Raj, AE. Jeyakumar, "A Novel Maximum Power Point Tracking Technique for Photovoltaic Module Based on Power Plane Analysis of – Characteristics," IEEE Trans. Ind. Electron., vol. 61, no. 9, pp. 4734-4745, Sep. 2014.
[80] F.-S. Pai, R.-M. Chao, S.H. Ko, T.-S. Lee, "Performance Evaluation of Parabolic Prediction to Maximum Power Point Tracking for PV Array," IEEE Trans. Sustainable Energy, vol. 2, no. 1, pp. 60-68, Jan. 2011.

Finite time stability

[81] S.P. Bhat and D.S. Bernstein, "Finite-time stability of continuous autonomous systems". SIAM Journal of Control and Optimization, vol. 38, no. 3, pp. 751-766, 2000.

Simulation in PSIM

[82] PowerSim Inc. PSIM Tutorial. "How to Use Solar Module Physical Module." [Online] Available in: http://powersimtech.com/wp-content/uploads/2013/04/Tutorial-Solar-Module-physical-model.pdf

Chapter 3

DC-DC stage:
Quadratic Boost Converter

3.1 INTRODUCTION

A microinverter or module integrated converter (AC module) generally uses a transformer-based DC-DC converter with boost capability in order to avoid a bulky transformer operating at the grid frequency. Several topologies derived of the fly-back, push-pull and the full-bridge converter can be found in scientific and industrial literature. The use of this kind of converters can be justified by the galvanic isolation they provide reducing the common-mode noise interference and the grounding problems [1]-[12]. However, it is well know that the use of transformers in switching circuits introduces an important complexity beside an increment in the size, weight and cost of the circuits. Therefore, taking into account that the low power levels driven by a microinverter are below 250 W, a transformer-less topology can be preferred if a proper trade-off is achieved between efficiency and power density. Moreover, a transformer-less solution can be more attractive with a control system taking advantage of its key characteristics [13]. Hence, it is possible to evidence that this kind of converter becomes an important solution in the field of low power renewable energy applications [14]-[17].

Not all transformer-less converter topologies can be proposed to cover the requirements of the application because of the need of a high DC gain to boost the low voltage given by one or two solar panels (15 – 30 V) to a high voltage level around 400 V. Therefore, only a limited number of existing converters or some modifications of them can meet the main requirement of high DC gain without using a power transformer. These topologies are treated in the literature as high gain transformer-less topologies [18]-[20]. Among them, it is possible to identify topologies with coupled

inductors [21]-[29], switched capacitors [30]-[31], multiplier cells [32]-[33], additional resonant circuits [34], or other alternative ways which improve the efficiency at the expense of some additional complexity [35]-[37]. Further, recently studied topologies with floating output increase the possibilities to attain high gain with a reduced circuit complexity [38]-[39]. All of these topologies are not considered in this work because the study is concentrated in simpler topologies operating in hard switching, and its aim is searching for a competitive solution through the use of an adequate control strategy.

Among the classic DC-DC topologies used to boost a voltage level to another one several times higher, the boost converter is the most used because of its simplicity, high efficiency and the presence of the input inductor which guarantees the compatibility with the primary source and improves the global performance. However, many authors constrain the use of the boost converter to gains lower than 10 to prevent high values of the duty cycle which inhibit the proper operation of the regulation systems, increase the possibility to have irreversible damages and show risk of saturation in the modulator [40]-[41]. Therefore, the boost converter, in spite of being the basis of the converter which will be treated along the work, is not here considered because it should operate with gains always higher than 10.

The possibility to obtain high conversion ratios has been introduced over 40 years ago by Matsuo el al., with their work on the cascaded connection of the classic converter topologies [42]. After that, a family of DC-DC converters with only one controlled switch was presented by Maksimovic et al., over 20 years ago [43]. Recently, some works concentrate on the cascade connection of converters to obtain high DC gains in the field of the distributed power generation systems [44]-[48]. However, an interesting way for a cascade connection of the converters has been introduced by Ortiz-Lopez et al., giving a generalization for the cascade connection of buck and boost converters with multiple stages using only one controlled switch [49]. From that work, it is possible to differentiate the quadratic boost converter, the cubic boost converter and the nth boost converter with only one controlled switch motivating a research field around the quadratic boost converter in both power electronics and control communities. Several works have been inspired in the context of the quadratic boost converter covering dynamic modeling and control problems [50]-[58], the study of its efficiency [59], the use of soft switching techniques to improve the efficiency levels by means of resonant networks or soft switches [60]-[64], and its combination with another circuits in order to improve gain capability or efficiency [65]-[70]. Moreover, other authors have tried to

improve the performance of the quadratic boost converter by means of a structural change in its topology leading to two new topologies with the same quadratic gain characteristic. The first one reported by Lascu et al. was obtained by applying a rotation in the switching cells of the converter introducing a new converter in a power factor correction application [71]. The other one reported by Kadri et al. was obtained by means of a software algorithm searching in the entire possible configuration with the same elements of the basic traditional quadratic boost allowing an application in photovoltaic conversion [72].

Considering these two topologies, namely, the Rotated Cell Single Switch (RC$S^2 - QB$) and the Software Synthesized Single Switch ($S^4 - QB$), and adding the Cascaded Connected Double Switch ($C^2DS - QB$) and the Cascaded Connected Single Switch ($C^2S^2 - QB$), we report a comparative study of efficiency and performance based on simulation results which is also complemented with experimental results [73]. Figure 3.1 shows the aforementioned four quadratic boost converter topologies.

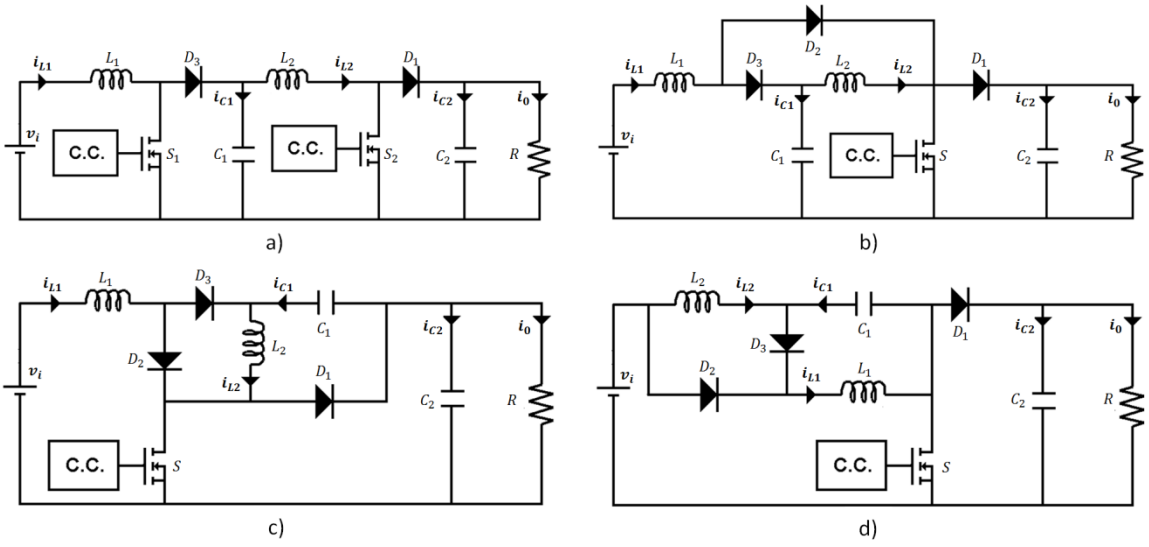

Fig. 3.1. Circuit diagram of the quadratic boost converter topologies: a) $C^2DS - QB$; b) $C^2S^2 - QB$: c) RC$S^2 - QB$; and, d) $S^4 - QB$.

Hitherto, from the results reported in [73], it is worth to point out the fact that the four quadratic boost converter topologies offer the possibility to work in a more safe area of the converter duty cycle without the need of a transformer or a complex additional circuit. Further, in the four topologies it is also possible to implement an input current control loop because all have an inductor connected to the input port. Additionally, the

three configurations with only one switch ($C^2S^2 - QB$, $S^4 - QB$ and $RCS^2 - QB$) require only a control system and the fact of replacing a MOSFET for a diode can be considered an advantage because only one driver circuit is needed. Assuming that this work is mainly devoted to control issues, we decided to study in deep the ($C^2S^2 - QB$) converter because our results can be posteriorly applied to the other topologies by exploring singular differences and by highlighting particular advantages or drawbacks.

Despite of its high gain capability and the absence of a power transformer, the modulation strategy used to control the quadratic boost converters plays a determinant role in its final reliability and performance. On the one hand, the use of Pulse Width Modulation (PWM) when the converter works with higher gains increases the risk of modulator saturation and hence increases the failure possibility. On the other hand, the use of a hysteretic modulator introduces a self-oscillating behavior with variable frequency which is constrained by the parameters of the modulator and some parameters of the converter [74]-[75]. Moreover, robust and reliable nonlinear control techniques such as sliding mode (SM) control can be easily implemented using hysteretic comparators , which has captured the interest of many authors to apply this kind of control in DC-DC power converter applications, including higher complexity structures such as the fourth order converters Cûk and SEPIC [76]-[78]. This control is highly suitable to control DC-DC converters given its variable structure nature which ensures robustness, reliability and simplicity [79]-[80].

Some authors have tried to generalize the approach of the use of the sliding-mode control applied in DC-DC power converters [81]-[85]. However, more and more works in different applications and methods or combinations of them permanently complement the state-of-the art of this research field. Despite of the large amount of works, there is always a challenge, for example, the use of a new converter or the study of an operational mode in a converter, the employ of other variables or sliding surfaces, the utilization of new implementation techniques and others. This is the case of applications in the context of the star-up in the converters [86]-[87], digital or hybrid (analogic-digital) control [88]-[89], interleaving or paralleled operation of converters [90]-[91], or the enforcing of desired behaviors [45]. In this work, the possibility for a converter to have a pure resistive behavior at the input port whereas its output port shows a power source characteristic is highly interesting. Ideally, this application can be classified into the Power Output Power Input (POPI) networks described by Singer et al. [92] and more specifically into the Loss Free Resistor concept (LFR) [93]-[96]. With the

synthesis of power processing stages using sliding mode control, it has been possible to define a Sliding Mode LFR (SM-LFR) [97]. Using this kind of approach, it is possible to cover the requirements of important applications such as Power Factor Correction (PFC) in switching rectifiers [98]-[99], driver of HB-LED lamps [100]-[102], or in our case, the impedance matching with photovoltaic modules [103]-[104]. In the case of the DC-DC stage of the microinverter, the sliding mode control allows attaining the SM-LFR behaviour with a relative simple electronic circuit implementation.

In the remainder of the chapter, the theoretical foundations of the steady-state operation of the quadratic boost converter are given for the continuous conduction mode (CCM) together with the analysis of three possible discontinuous conduction modes (DCM) which have been identified from this study. Then, studying the dynamics of the converter by means of the sliding mode control approach lead to the converter stabilization through a sliding surface defined for the input inductor current operating always in CCM. The stability of the converter operating with this control law is studied by means of a Lyapunov candidate function. After that, this control law is modified to impose a power source characteristic at the converter output port while the input port shows a pure resistive behavior. This subject is tackled treating the controlled converter as a SM-LFR, using the input conductance as the control variable. The effect of the proposed control on the converter efficiency is analyzed and discussed. The theoretical predictions of the analysis are first verified by means of MATLAB and PSIM- based simulations. Subsequently, experimental results validating the entire study are also given.

3.2 CONVERTER MODEL

3.2.1 Converter structures and conduction modes

As shown in figure 3.2, the quadratic boost converter has five possible structures (states) giving origin to a continuous conduction mode and three different discontinuous conduction modes. Two of these structures are attained when only one inductor current either L_1 or L_2 reaches zero before a switching period is finished, thus originating the DCL1 state (Discontinuous Conduction on inductor L_1) or the DCL2 state (Discontinuous Conduction on inductor L_2) respectively. The third structure is found

when the current of both inductors reach the value zero before a switching period is finished (DCL12 state).

Then, the quadratic boost converter can be modeled as a variable structure system which commutes between two, three or four structures (states) during a switching period ($T_s = 1/f_s$) originating one of its different conduction modes. The five possible conduction modes and the possible transitions between them are depicted in figure 3.3a.

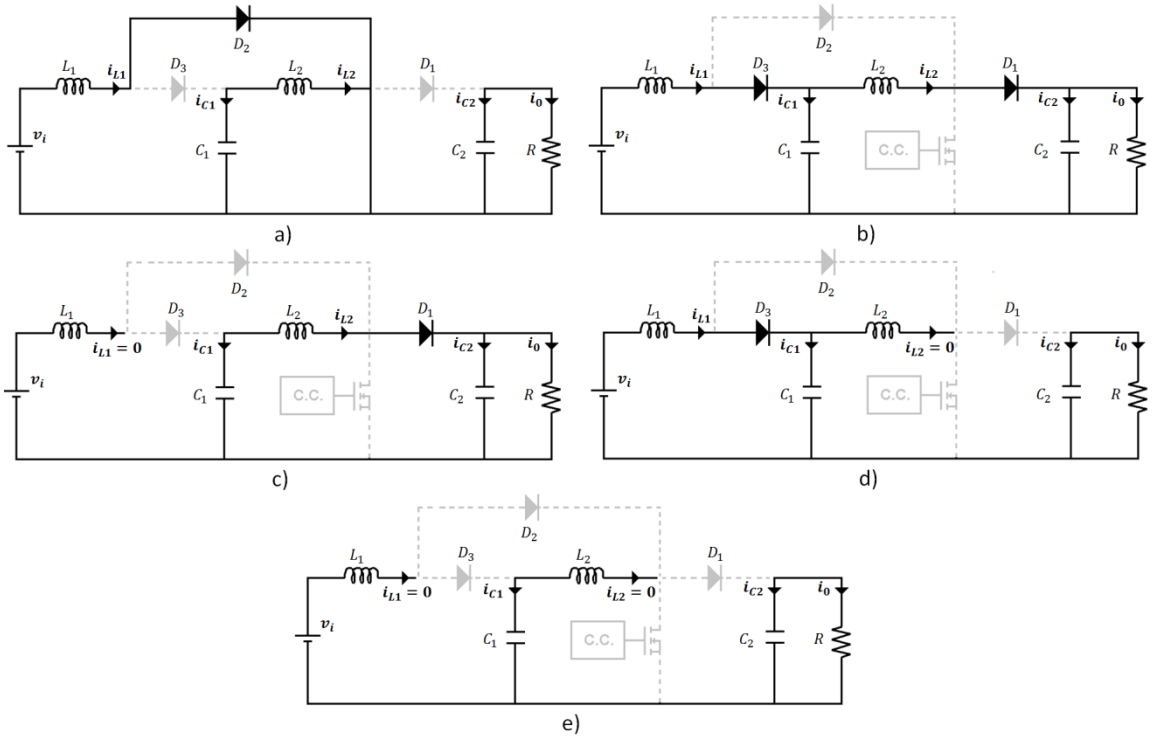

Fig. 3.2. Circuit diagrams of quadratic boost converter states: a) on-state; b) off-state: c) DCL1-state; d) DCL2-state; and, e) DCL12-state.

As shown in figure 3.3b, if the structure of the system changes from the off-state to the on-state at the start of the switching period and from the on-state to the off-state when the interval defined by the duty cycle of the control signal is finished, then, the converter operates in CCM. On the other hand, in the conduction modes DCL1 and DCL2, shown in figures 3.3c and 3.3d respectively, the converter changes from the off-state to either DCL1-state or DCL2-state and after that returns to the on-state at the beginning of a new switching period. Additionally, as shown in figures 3.3e and 3.3f, the converter can operate in either the mode DCL12 arriving to DCL12-state coming from DCL1-state or in the mode DCL21 arriving to DCL12-state coming from DCL2-state. The difference among these two consists in the state that is firstly attained after the off-state.

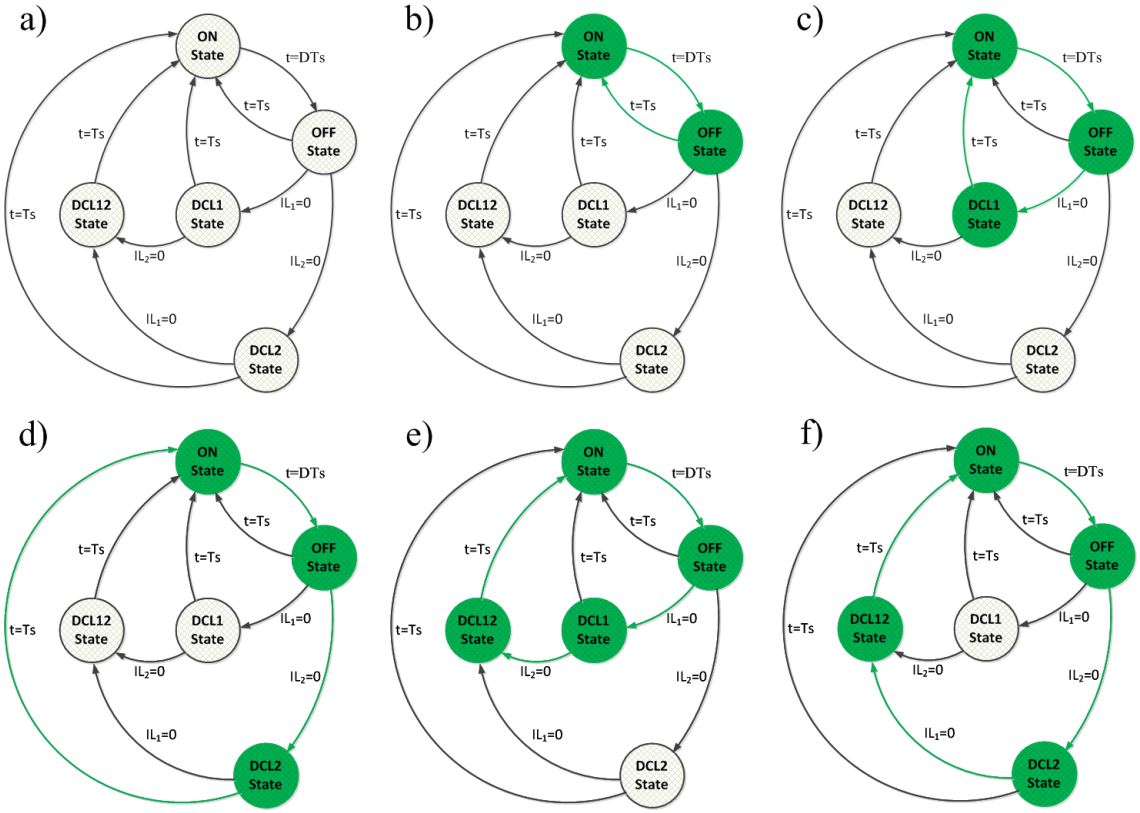

Fig. 3.3. Event diagram of the quadratic boost converter conduction modes: a) general representations of states and transitions, b) CCM mode, c) DCL1 mode, d) DCL2 mode, e) DCL12 mode, f) DCL21 mode.

However, if a hysteresis based controller is used to cope with the control objectives, then not all of the states will be reachable. The figure 3.4 shows the possible states and transitions for a quadratic boost converter controlled from the input inductor current using a hysteresis- based modulator considering a hysteresis band of 2Δ, with Δ defining a sliding behavior in the input current and constraining the switching frequency to finite values.

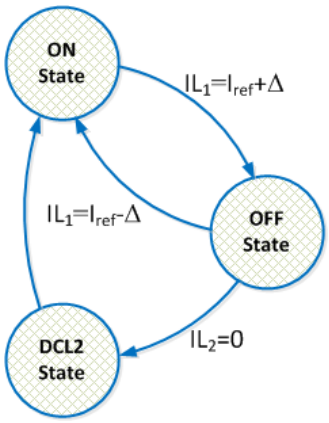

Fig. 3.4. Event diagram of the quadratic boost converter using a hysteresis comparator.

If the converter works in on-state, this changes to off-state depending of the instantaneous value of the input inductor current. Further, being in the off-state, the converter can change to either on-state or DCL2-state. Being in DCL2-state, the converter can only change to the on-state provided the input inductor is externally forced to remain in continuous conduction mode. This is mainly due to the need of ensure the validity of the control strategy and the existence of the hysteresis band.

3.2.2 Modeling of the converter dynamics

From the above analysis, four different conduction modes are defined: CCM, DCL1, DCL2 and DCL12 modes. To model their dynamic behavior, the set of differential equations corresponding to each circuit in figure 3.2 are summarized in table 3.1.

Table 3.1. Set of differential equations of the converter states

	ON-State	**OFF-State**	**DCL1-State**	**DCL2-State**	**DCL12-State**
$v_{L1} = L_1 \frac{di_{L1}}{dt}$	v_{in}	$v_{in} - v_{C1}$	0	$v_{in} - v_{C1}$	0
$v_{L2} = L_2 \frac{di_{L2}}{dt}$	v_{C1}	$v_{C1} - v_{C2}$	$v_{C1} - v_{C2}$	0	*0*
$i_{C1} = C_1 \frac{dv_{C1}}{dt}$	$-i_{L2}$	$i_{L1} - i_{L2}$	$-i_{L2}$	i_{L1}	*0*
$i_{C2} = C_2 \frac{dv_{C2}}{dt}$	$-\frac{v_{C2}}{R}$	$i_{L2} - \frac{v_{C2}}{R}$	$i_{L2} - \frac{v_{C2}}{R}$	$-\frac{v_{C2}}{R}$	$-\frac{v_{C2}}{R}$

From the equations in table 3.1, a compact representation can be obtained using the following multi-linear expression:

$$\begin{aligned}
\frac{di_{L1}}{dt} &= \frac{v_{in}}{L_1}(1-u_1) - \frac{v_{C1}}{L_1}(1-u-u_1) \\
\frac{di_{L2}}{dt} &= \frac{v_{C1}}{L_2}(1-u_2) - \frac{v_{C2}}{L_2}(1-u-u_2) \\
\frac{dv_{C1}}{dt} &= -\frac{i_{L2}}{C_1}(1-u_2) + \frac{i_{L1}}{C_1}(1-u-u_2) \\
\frac{dv_{C2}}{dt} &= \frac{i_{L2}}{C_2}(1-u-u_2) - \frac{v_{C2}}{RC_2}
\end{aligned} \tag{3.1}$$

where u is the control signal of the controlled switch, u_1 represents the existence of the discontinuous conduction mode DCL1 and u_2 represents the existence of the

discontinuous conduction mode DCL2. The variable u_1 takes the value 1 when the converter operates in the mode DCL1, and the variable u_2 takes the value 1 when the converter operates in the mode DCL2. In the mode DCL12, both u_1 and u_2 take the value 1. This model can be adopted to work with any kind of control irrespective of the employed modulator. Nevertheless, particular assumptions can be expected in order to cope with the analysis of discontinuous conduction modes with variable switching frequency.

3.2.3 Steady state of the converter

The steady state of the DC-DC converters is commonly analyzed using the current and voltage waveforms obtaining their mean values and the amplitude of their ripples. Working with a constant or variable frequency modulation methods does not affect the analysis of steady state since an equilibrium point is characterized by a constant switching frequency in both cases. Thus, from the steady state analysis can be deduced the gain of the converter as a function of either the duty cycle (CCM) or the duty cycle and the output load (DCL1, DCL2 and DCL12 modes). It is also possible to obtain the static relations between the average values of either the capacitor voltages and the input voltage or the inductor currents and the input and load currents. Further, a more complex relation is obtained when the converter enters in the mode DCL2 using a hysteresis modulator because of the interdependence among the switching frequency, the voltage gain and the steady state average value of the voltages. All of them are now discussed in detail.

The mean values of the converter variables in steady-state are represented by the notation $\langle\cdot\rangle$. The control variables are substituted by the variables U, U_1 and U_2 which represents the mean values of u, $1-u-u_1$ and $1-u-u_2$.

3.2.3.1 DC gain and average values of the converter variables

A. Converter operating in CCM

From the expressions listed in table 3.1, the balances are given by:

$$\langle v_{L1}\rangle = \frac{\langle v_i\rangle UT_s + (\langle v_i\rangle - \langle v_{C1}\rangle)(1-U)T_s}{T_s} = 0 \quad (3.2)$$

$$\langle v_{L2}\rangle = \frac{\langle v_{C1}\rangle UT_s + (\langle v_{C1}\rangle - \langle v_{C2}\rangle)(1-U)T_s}{T_s} = 0 \quad (3.3)$$

The charge balance in $C_1$and C_2 results in:

$$\langle i_{C1}\rangle = \frac{-\langle i_{L2}\rangle UT_s + (-\langle i_{L2}\rangle + \langle i_{L1}\rangle)(1-U)T_s}{T_s} = 0 \quad (3.4)$$

$$\langle i_{C2}\rangle = \frac{-\frac{\langle v_{C2}\rangle}{R}UT_s + \left(\langle i_{L2}\rangle - \frac{\langle v_{C2}\rangle}{R}\right)(1-U)T_s}{T_s} = 0 \quad (3.5)$$

Denoting $V_i = \langle v_i\rangle$, the mean values of the converter variables are given by:

$$\langle i_{L1}\rangle = I_{L1} = \frac{V_i}{R(1-U)^4} \quad (3.6)$$

$$\langle i_{L2}\rangle = I_{L2} = \frac{V_i}{R(1-U)^3} \quad (3.7)$$

$$\langle v_{C1}\rangle = V_{C1} = \frac{V_i}{(1-U)} \quad (3.8)$$

$$\langle v_{C2}\rangle = V_{C2} = \frac{V_i}{(1-U)^2} \quad (3.9)$$

from which it can be deduced the ideal static gain of the converter:

$$M_{CCM}(U) = \frac{V_{C2}}{V_i} = \frac{1}{(1-U)^2} \quad (3.10)$$

B. Converter operating in DCL1 mode

From the expressions listed in table 3.1, the balances in L_1 and L_2 can be characterized by:

$$\langle v_{L1}\rangle = \frac{\langle v_i\rangle UT_s + (\langle v_i\rangle - \langle v_{C1}\rangle)U_1T_s}{T_s} = 0 \quad (3.11)$$

$$\langle v_{L2}\rangle = \frac{\langle v_{C1}\rangle UT_s + (\langle v_{C1}\rangle - \langle v_{C2}\rangle)(1-U)T_s}{T_s} = 0 \quad (3.12)$$

The charge balance in C_2 is given by:

$$\langle i_{C2}\rangle = \frac{-\frac{\langle v_{C2}\rangle}{R}UT_s + \left(\langle i_{L2}\rangle - \frac{\langle v_{C2}\rangle}{R}\right)(1-U)T_s}{T_s} = 0 \tag{3.13}$$

By solving (3.11), (3.12) and (3.13), the steady-state expressions for v_{C1}, v_{C2} and i_{L2} are obtained.

$$\langle v_{C1}\rangle = V_{C1} = \frac{\langle v_i\rangle(U+U_1)}{U_1} \tag{3.14}$$

$$\langle v_{C2}\rangle = V_{C2} = \frac{\langle v_i\rangle(U+U_1)}{U_1(1-U)} \tag{3.15}$$

$$\langle i_{L2}\rangle = I_{L2} = \frac{\langle v_{C2}\rangle}{R(1-U)} \tag{3.16}$$

The average value of i_{L1} can be obtained from a geometrical analysis of the triangular area described by the current waveform shown in figure 3.5. The height of the triangle is defined by the maximum value of i_{L1}, which is denoted as I_{L1max} whereas the base is defined by the time interval $(U+U_1)T_s$.

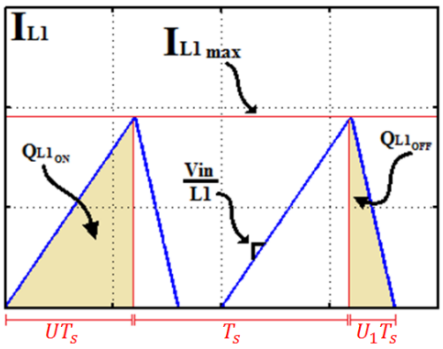

Fig. 3.5. Current waveform of the inductor L1 when the converter operates in DCL1 mode.

The value of I_{L1max} can be obtained using the slope of the inductor current in the on-state as follows:

$$I_{L1max} = \left(\frac{\langle v_i\rangle}{L_1}\right)UT_s \tag{3.17}$$

Then, we have:

$$\langle i_{L1}\rangle = \frac{1}{T_s}\left(\frac{1}{2} I_{L1_{max}}(U+U_1)T_s\right) = \frac{\langle v_i\rangle U(U+U_1)}{2L_1 f_s}$$

$$\langle i_{L1}\rangle = \frac{\langle v_i\rangle U(U+U_1)}{2L_1 f_s} \tag{3.18}$$

Note that in DCM operation it is not possible to use the low ripple approximation because of the presence of pulsating currents. Hence, it is necessary to analyze the charge balance with the charge given or extracted by the nearby elements. For instance, while the inductor L_2 is permanently connected to the capacitor C_1, the inductor L_1 is connected only during the off-state. Therefore, the charge balance in C_1 is given by

$$\langle i_{C1}\rangle = \frac{-\langle i_{L2}\rangle T_s + Q_{L1_{OFF}}}{T_s} = 0 \tag{3.19}$$

where $Q_{L1_{OFF}}$ represents the charge produced and given by inductor L_1 to capacitor C_1 across diode D_3. Its value can be determined as the area below the current waveform in figure 3.5.

$$Q_{L1_{OFF}} = \frac{\langle v_i\rangle U U_1 T_s}{2L_1 f_s} = \frac{U_1 T_s}{2} I_{L1_{max}} \tag{3.20}$$

Thus, by replacing (3.20) in (3.19), another steady-state expression for i_{L2} is obtained.

$$\langle i_{L2}\rangle = \frac{\langle v_i\rangle U U_1}{2L_1 f_s} \tag{3.21}$$

By equalizing the expressions (3.16) and (3.21), it is possible to obtain K_1, which is a standard parameter to analyze the discontinuous conduction mode [40].

$$K_1 = \frac{2L_1}{RT_s} = \frac{U(1-U)^2 {U_1}^2}{U+U_1} \tag{3.22}$$

After that, extracting $\langle v_i \rangle / \langle v_{C2} \rangle$ from (3.15) and replacing in (3.22), the value of U_1 is given by:

$$U_1 = K_1 \left(\frac{\langle v_{C2} \rangle}{\langle v_{in} \rangle} \right) \left(\frac{1}{U(1-U)} \right) = \frac{K_1}{2U(1-U)^2} \left(1 + \sqrt{1 + \frac{4U^2(1-U)^2}{K_1}} \right) \tag{3.23}$$

From the aforementioned expressions, the mean values of the converter variables are given by:

$$\langle i_{L1} \rangle = I_{L1} = \frac{V_i}{4R(1-U)^2} \left(1 + \sqrt{1 + \frac{4U^2(1-U)^2}{K_1}} \right)^2 \tag{3.24}$$

$$\langle i_{L2} \rangle = I_{L2} = \frac{V_i}{2R(1-U)^2} \left(1 + \sqrt{1 + \frac{4U^2(1-U)^2}{K_1}} \right) \tag{3.25}$$

$$\langle v_{C1} \rangle = V_{C1} = \frac{V_i}{2} \left(1 + \sqrt{1 + \frac{4U^2(1-U)^2}{K_1}} \right) \tag{3.26}$$

$$\langle v_{C2} \rangle = V_{C2} = \frac{V_i}{2(1-U)} \left(1 + \sqrt{1 + \frac{4U^2(1-U)^2}{K_1}} \right) \tag{3.27}$$

The voltage conversion ratio of the converter operating in DCL1 mode is

$$M_{DCM1}(U) = \frac{V_{C2}}{V_i} = \frac{1 + \sqrt{1 + \frac{4U^2(1-U)^2}{K_1}}}{2(1-U)} \tag{3.28}$$

C. Converter operating in DCL2 mode

From the expressions listed in table 3.1, the volts-second balances are given by

$$\langle v_{L1}\rangle = \frac{\langle v_i\rangle UT_s + (\langle v_i\rangle - \langle v_{C1}\rangle)(1-U)T_s}{T_s} = 0 \tag{3.29}$$

$$\langle v_{L2}\rangle = \frac{\langle v_{C1}\rangle UT_s + (\langle v_{C1}\rangle - \langle v_{C2}\rangle)U_2T_s}{T_s} = 0 \tag{3.30}$$

By solving (3.29) and (3.30), the steady-state expressions for v_{C1} and v_{C2} are obtained.

$$\langle v_{C1}\rangle = \frac{\langle v_i\rangle}{1-U} \tag{3.31}$$

$$\langle v_{C2}\rangle = \frac{\langle v_i\rangle(U+U_2)}{U_2(1-U)} \tag{3.32}$$

There are two charges involved in the charge balance of the capacitor C_1. A positive charge is given by the inductor L_1 during the interval $(1-U)T_s$ whereas a negative charge Q_{L2} is extracted for the inductor L_2 during the interval $(U+U_2)T_s$. Then, we have:

$$\langle i_{C1}\rangle = \frac{\langle i_{L1}\rangle(1-U)T_s - Q_{L2}}{T_s} = 0 \tag{3.33}$$

The value of Q_{L2} is obtained computing the area below the current waveform in figure 3.6 during the interval $(U+U_2)T_s$. The value of the charge Q_{L2} divided by the switching period is the same mean value of the inductor current i_{L2}. Hence, the following relation is obtained:

$$\langle i_{L1}\rangle = \langle i_{L2}\rangle \frac{1}{(1-U)} \tag{3.34}$$

The value of Q_{L2} is obtained as the area of the triangle below the current waveform of the inductor L_2 which is shown in figure 3.6b. The height of the triangle is defined by the maximum value of i_{L2}, denoted as $I_{L2_{max}}$, whereas the basis is the interval $(U+U_2)T_s$. The value of $I_{L2_{max}}$ is derived using the slope of the inductor current in the on state:

$$I_{L2_{max}} = \left(\frac{\langle v_{C1}\rangle}{L_2}\right)UT_s = \frac{1}{L_2}\left(\frac{\langle v_{in}\rangle}{1-U}\right)UT_s \tag{3.35}$$

and therefore , we obtain

$$Q_{L2} = \frac{\langle v_i \rangle}{2L_2 f_s} \frac{U(U+U_2)}{(1-U)} T_s \tag{3.36}$$

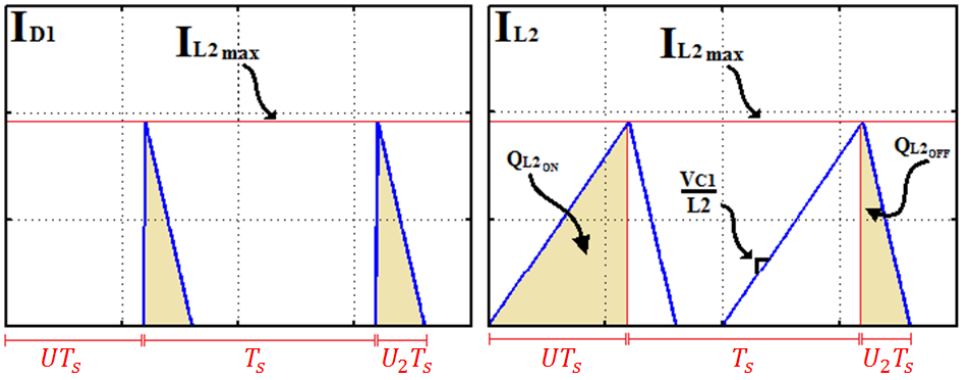

Fig. 3.6. Current waveforms when the converter operates in DCL2 mode: a) diode D1, b) inductor L2

On the other hand, the charge balance in capacitor C_2 is solved considering the relation between the load current and the current of the diode D_1 , which is shown in figure 3.6b. Hence, it is possible to derive equation (3.37) since the mean value of the output current is the same mean value of the current through diode D_1 (Q_{L2OFF}/T_s).

$$\frac{\langle v_{C2} \rangle}{R} = \langle i_{D1} \rangle = \frac{\langle v_i \rangle (U+U_2)}{RU_2(1-U)} \tag{3.37}$$

The mean value of the diode current is given by:

$$\langle i_{D1} \rangle = \frac{1}{T_s}\left(\frac{1}{2} I_{L2max} U_2 T_s\right) = \frac{\langle v_i \rangle U U_2}{2L_2 f_s (1-U)} \tag{3.38}$$

By equalizing expressions (3.37) and (3.38), it is obtained that:

$$K_2 = \frac{2L_2}{RT_s} = \frac{U{U_2}^2}{(U+U_2)} \tag{3.39}$$

By solving (3.32) for $\langle v_{C2} \rangle / \langle v_{in} \rangle$ and replacing in (3.39), the value of D_1 is deduced.

$$U_2 = K_2 \left(\frac{\langle v_{C2} \rangle}{\langle v_i \rangle} \right) \left(\frac{1-U}{U} \right) = \frac{K_2}{U} \left(1 + \sqrt{1 + \frac{4U^2}{K_2}} \right) \tag{3.40}$$

From the abovementioned expressions, the mean values of the converter variables are given by:

$$\langle i_{L1} \rangle = I_{L1} = \frac{V_i}{4R(1-U)^2} \left(1 + \sqrt{1 + \frac{4U^2}{K_2}} \right)^2 \tag{3.41}$$

$$\langle i_{L2} \rangle = I_{L2} = \frac{V_i}{4R(1-U)} \left(1 + \sqrt{1 + \frac{4U^2}{K_2}} \right)^2 \tag{3.42}$$

$$\langle v_{C1} \rangle = V_{C1} = \frac{V_i}{(1-U)} \tag{3.43}$$

$$\langle v_{C2} \rangle = V_{C2} = \frac{V_i}{2(1-U)} \left(1 + \sqrt{1 + \frac{4U^2}{K_2}} \right) \tag{3.44}$$

The voltage conversion ratio of the converter operating in DCL2 mode is:

$$M_{DCM2}(U) = \frac{V_{C2}}{V_i} = \frac{1 + \sqrt{1 + \frac{4U^2}{K_2}}}{2(1-U)} \tag{3.45}$$

D. Converter operating in DCL12, DCL21 modes

From the expressions listed in table 3.1, the balances in L_1 and L_2 are given by:

$$\langle v_{L1} \rangle = \frac{\langle v_i \rangle U T_s + (\langle v_i \rangle - \langle v_{C1} \rangle) U_1 T_s}{T_s} = 0 \tag{3.46}$$

$$\langle v_{L2}\rangle = \frac{\langle v_{C1}\rangle U T_s + (\langle v_{C1}\rangle - \langle v_{C2}\rangle) U_2 T_s}{T_s} = 0 \tag{3.47}$$

By solving (3.46) and (3.47), the steady-state expressions for v_{C1} and v_{C2} are obtained.

$$\langle v_{C1}\rangle = \frac{\langle v_i\rangle (U + U_1)}{U_1} \tag{3.48}$$

$$\langle v_{C2}\rangle = \frac{\langle v_{C1}\rangle (U + U_2)}{U_2} \tag{3.49}$$

The charge balances in both capacitors C_1 and C_2 can be obtained from the current waveforms shown in figure 3.7.

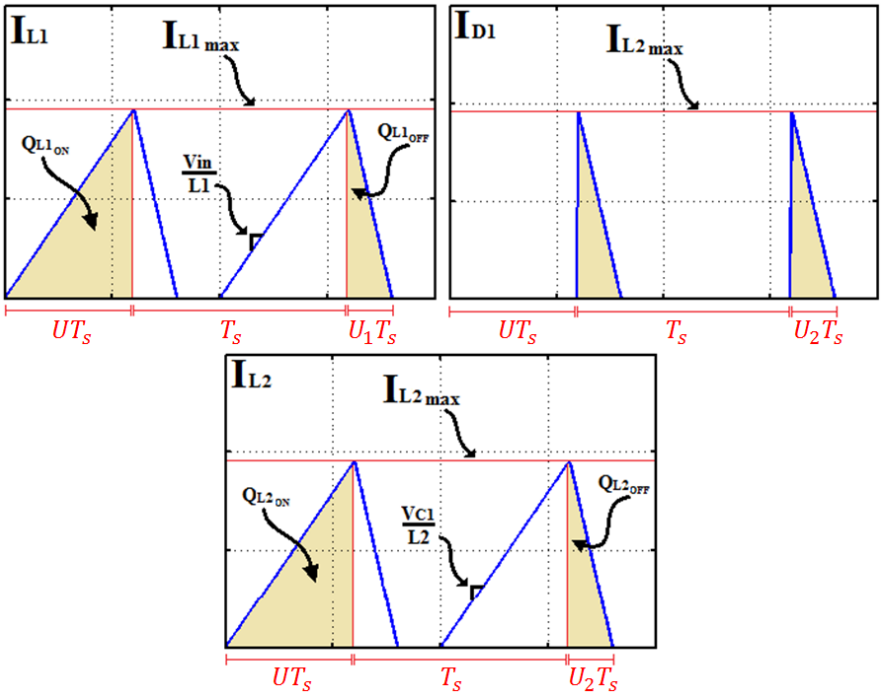

Fig. 3.7. Current waveforms when the converter operates in DCL12 mode: a) inductor L1, b) diode D1, c) inductor L2.

$$\langle i_{C1}\rangle = \frac{Q_{L1OFF} - Q_{L2}}{T_s} = \frac{1}{T_s}\left(\frac{I_{L1max} U_1 T_s}{2}\right) - \frac{1}{T_s}\left(\frac{I_{L2max}(U + U_2) T_s}{2}\right) = 0 \tag{3.50}$$

$$\langle i_{C2}\rangle = \frac{Q_{L2OFF}}{T_s} - \frac{\langle v_{C2}\rangle}{R} = \frac{1}{T_s}\left(\frac{I_{L2max} U_2 T_s}{2}\right) - \frac{\langle v_{C2}\rangle}{R} = 0 \tag{3.51}$$

where maximum values of the inductor currents are given by the expressions:

$$I_{L1max} = \left(\frac{\langle v_i \rangle}{L_1}\right) UT_s \tag{3.52}$$

$$I_{L2max} = \left(\frac{\langle v_{C1} \rangle}{L_2}\right) UT_s \tag{3.53}$$

By replacing (3.52) and (3.53) in (3.50) and solving for the relation $\langle v_{C1} \rangle / \langle v_{in} \rangle$, we obtain:

$$\frac{\langle v_{C1} \rangle}{\langle v_i \rangle} = \frac{L_2}{L_1}\left(\frac{U_1}{U + U_2}\right) \tag{3.54}$$

By defining the constants K_1 and K_2 with the expressions:

$$K_1 = \frac{2L_1}{RT_s} \tag{3.55}$$

$$K_2 = \frac{2L_2}{RT_s} \tag{3.56}$$

Then, from (3.54), (3.55) and (3.56), we have:

$$\frac{\langle v_{C1} \rangle}{\langle v_i \rangle} = \frac{K_2}{K_1}\left(\frac{U_1}{U + U_2}\right) \tag{3.57}$$

Then, by replacing (3.56) in (3.51), we have:

$$K_2 = \frac{U{U_2}^2}{U + U_2} = \frac{\langle v_{C1} \rangle}{\langle v_{C2} \rangle} U U_2 \tag{3.58}$$

By solving (3.58) for U_2 and replacing in (3.49), the following relation is obtained:

$$M_a(U) = \frac{\langle v_{C2} \rangle}{\langle v_{C1} \rangle} = \frac{1 + \sqrt{1 + \frac{4U^2}{K_2}}}{2} \tag{3.59}$$

On the other hand, by replacing (3.58) in (3.57), it is derived that:

$$\frac{\langle v_{C1}\rangle}{\langle v_i\rangle} = \left(\frac{1}{M_a(U)}\right)\frac{U_1 U U_2}{K_1(U+U_2)} \tag{3.60}$$

Then, solving (3.49) for $\langle v_{C1}\rangle/\langle v_{C2}\rangle$ and (3.48) for U_1, and replacing in (3.60), we deduce:

$$\frac{\langle v_{C1}\rangle}{\langle v_i\rangle} = \frac{U^2}{K_1}\frac{\left(\frac{1}{M_a(U)}\right)^2}{\left(\frac{\langle v_{C1}\rangle}{\langle v_i\rangle}-1\right)}$$

From which, it is obtained the voltage conversion ratio of the converter operating in DCL12 mode as:

$$\frac{\langle v_{C2}\rangle}{\langle v_i\rangle} = \frac{V_{C2}}{V_i} = \frac{M_a(U)+\sqrt{[M_a(U)]^2+\frac{4U^2}{K_1}}}{2} = \frac{1}{2}\left(\left(\frac{\langle v_{C2}\rangle}{\langle v_{C1}\rangle}\right)+\sqrt{\left(\frac{\langle v_{C2}\rangle}{\langle v_{C1}\rangle}\right)^2+\frac{4U^2}{K_1}}\right)$$

$$M_{DCM12}(U) = \frac{V_{C2}}{V_i} = \frac{1}{4}\left(1+\sqrt{1+\frac{4U^2}{K_2}}+\sqrt{\left(1+\sqrt{1+\frac{4U^2}{K_2}}\right)^2+\frac{16U^2}{K_1}}\right) \tag{3.61}$$

From the aforementioned expressions, the mean values of the converter variables are given by:

$$\langle v_{C1}\rangle = V_{C1} = V_i\frac{M_{DCM12}(U)}{M_a(U)} \tag{3.62}$$

$$\langle v_{C2}\rangle = V_{C2} = V_i[M_{DCM12}(U)] \tag{3.63}$$

From the input to output power balance, it is obtained that:

$$\langle i_{L1}\rangle = I_{L1} = \frac{V_i[M_{DCM12}(U)]^2}{R} \tag{3.64}$$

Since$\langle i_{L2} \rangle = I_{L2_{max}}(U + U_2)/2$, using (3.53) results in the following expression after some mathematical manipulation:

$$\langle i_{L2} \rangle = I_{L2} = \frac{V_i M_{DCM12}(U) M_a(U)}{R} \tag{3.65}$$

3.2.3.2 Boundaries of the conduction modes at constant frequency

The boundaries between the different discontinuous conduction modes are obtained considering the fact that an inductor current reaches the value of zero exactly at the end of the switching period. Then, it is possible to assert that the converter operates in a critical or boundary conduction mode. As expected, one or both parameters U_1 or U_2 are exactly equal to $1 - U$ allowing the use of this definition to obtain the mathematical conditions. The procedure consists in obtaining a critical value of K_1 or K_2 , wherein it is possible to distinguish the operational modes. The values will be denoted $K_{1_{crit}}$ or $K_{2_{crit}}$ respectively. Four different boundaries can be identified:

a) The converter operates in CCM and the current of inductor L1 reaches the critical conduction mode, which is the way to enter in DCL1 mode.

By replacing $U_1 = 1 - U$ in (3.22), the following expression is obtained:

$$K_{1_{crit}} = \frac{U(1-U)^2(1-U)^2}{U + (1-U)} = U(1-U)^4 \tag{3.66}$$

Then, it is possible to assert that when the converter operates in CCM, the boundary to enter into the DCL1 mode is defined by:

$$\frac{2L_1}{RT_s} < U(1-U)^4 \tag{3.67}$$

b) The converter operates in CCM and the current of inductor L_2 reaches the critical conduction mode, which is the way to enter into the DCL2 mode.

By replacing $U_2 = 1 - U$ in (3.39), it is obtained that:

$$K_{2_{crit}} = \frac{U(1-U)^2}{U + (1-U)} = U(1-U)^2 \tag{3.68}$$

Then, it is possible to assert that when the converter operates in CCM, the boundary to attain the DCL2 mode is defined by:

$$\frac{2L_2}{RT_s} < U(1-U)^2 \tag{3.69}$$

c) The converter operates in the DCL1 mode and the current of inductor L_2 reaches the critical conduction mode, which is the way to enter into the DCL12 mode.

By replacing $U_2 = 1 - U$ in (3.58), the expression (3.68) is anew obtained. Then, it is possible to assert that, being in the mode DCL1, the boundary to attain the DCL12 mode is also defined by expression (3.69)

d) The converter operates in the DCL2 mode and the current in inductor L_1 reaches the critical conduction mode, which is the way to enter into the DCL21 mode.

By replacing $U_1 = 1 - U$ in (3.48) and (3.57), and identifying the two expressions, we have:

$$K_1 = K_2 \frac{(1-U)^2}{U + U_2} \tag{3.70}$$

On the other hand, by using relation (3.59), expression (3.58) becomes:

$$K_2 = \frac{UU_2}{M_a(U)} \Rightarrow U_2 = \frac{M_a(U)K_2}{U} \tag{3.71}$$

Therefore (3.70) leads to:

$$K_{1_{crit}} = \frac{2K_2U(1-U)^2}{2U^2 + K_2\left(1+\sqrt{1+\frac{4U^2}{K_2}}\right)} \tag{3.72}$$

Then, it is possible to conclude that when the converter operates in the DCL2 mode, the boundary to attain the DCL12 mode is defined by:

$$\frac{2L_1}{RT_s} < \frac{2K_2U(1-U)^2}{2U^2 + K_2\left(1+\sqrt{1+\frac{4U^2}{K_2}}\right)} \tag{3.73}$$

Figure 3.8 shows the domains of the different conduction modes where it is possible to identify the regions for CCM, DCL1, DCL2 and DCL12 modes as a function of the duty cycle U and the DCM constants K_1 and K_2. As it can be observed, the discontinuous regions are concentrated around the low cycles and low values of K_1 and K_2, which correspond to low power levels. We can note that the converter cannot work in the region of high duty cycles because the existence of the discontinuous conduction modes requires always to satisfy the conditions $U_1 > 1-U$ or $U_2 > 1-U$ or both.

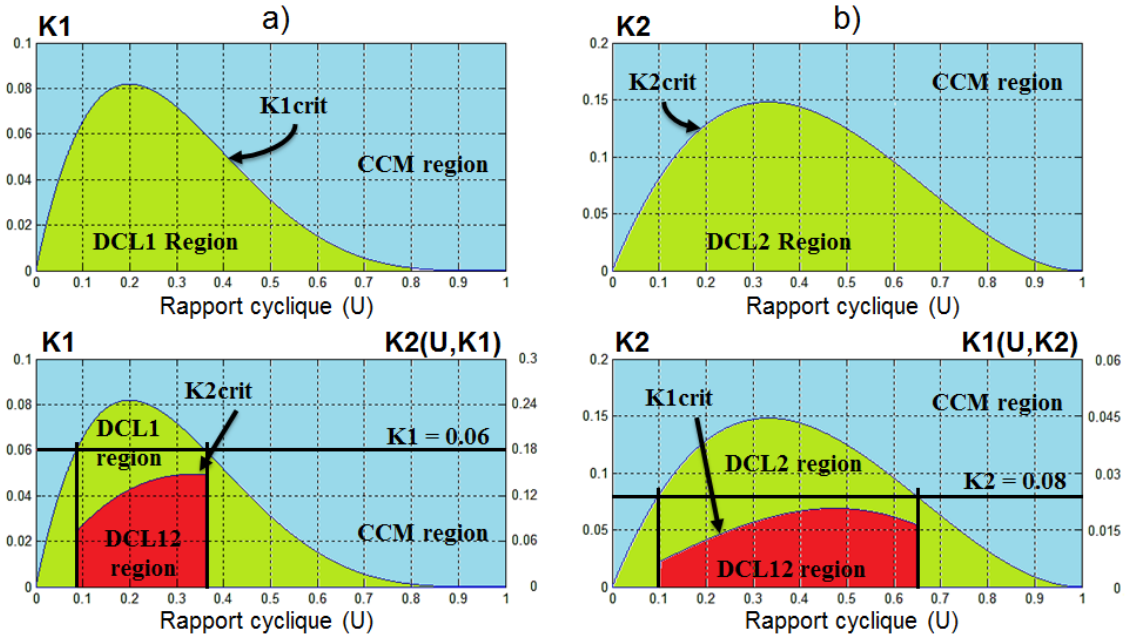

Fig. 3.8. Graphical representation of the critical values $K_{1_{crit}}$ and $K_{2_{crit}}$ as functions of the duty cycle U: a) CCM and DCL1 mode (K_1 vs. U), b) CCM and DCL2 mode (K_2 vs. U), c) CCM, DCL1 mode and DCL12 mode (K_2 vs. U, K_1); d) CCM, DCL2 mode and DCL21 mode (K_1 vs. U, K_2).

As shown in figure 3.8, the duty cycle and the critical values of K_1 and K_2 define the different limits between the conduction modes CCM, DCL1, DCL2 and DCL12. Figures 3.8a and 3.8b show the limits between CCM and the modes DCL1 and DCL2 respectively. It is interesting to observe that the limits of the regions are defined by the functions $K_1(U)$ and $K_2(U)$. Additionally, it is possible to observe that for a constant value of K_1(for example 0.06 in the figure 3.8c) or K_2 (for example 0.08 in the figure 3.8d), the modes DCL12 and DCL21 can only be attained for a delimited region of the duty cycle. Then, for these operating modes, it results that K_1 is a function of U and K_2, and K_2 is a function of U and K_1.

3.2.3.3 Conduction modes and DC gain in a specific converter

A quadratic boost converter can practically work in all of the different possible conduction modes depending of the values of duty cycle and output load. By using the equation derived in the paragraph 3.3.3, an interesting graphic representation can be obtained for the converter gain computed for the overall range of the duty cycle. In figure 3.9, for a set of converter parameters (L_1, L_2, C_1, C_2 and f_s) listed in the figure caption, the gain of the converter is represented for the different conduction modes as a function of the duty cycle and output load R showing their influence.

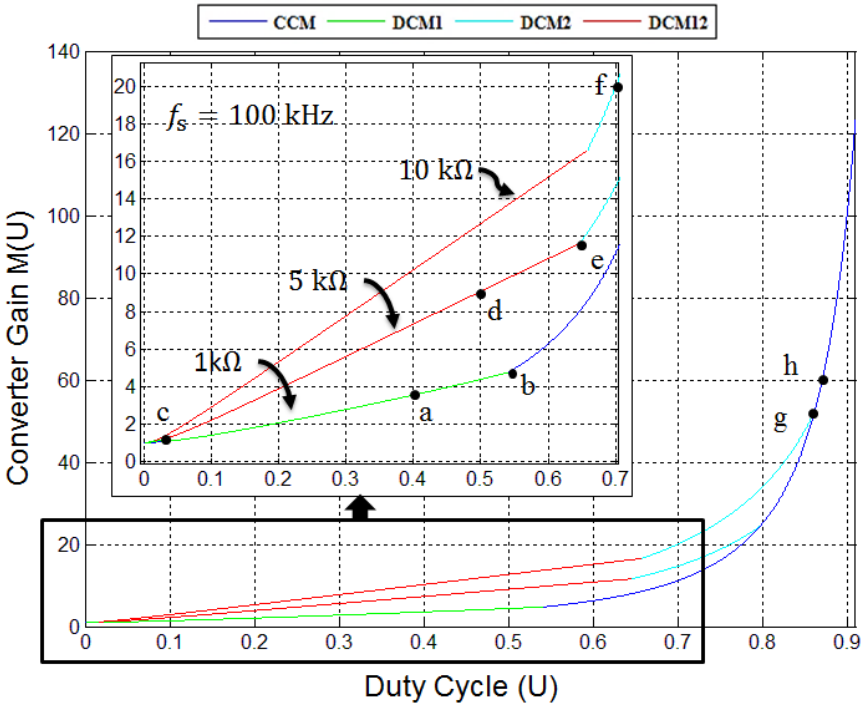

Fig. 3.9. Ideal converter gain vs. duty cycle (Parameters: $L_1 = 120\ \mu H, L_2 = 820\ \mu H, C_1 = C_2 = 10\ \mu F$)

In figure 3.9, three curves of the converter gain *M(U)* as a function of the duty cycle *U* are depicted. Each one corresponds to the converter operating with a constant output load resistance ($1k\Omega, 5k\Omega$ and $10k\Omega$). In these curves a distribution of the conduction modes can be observed.

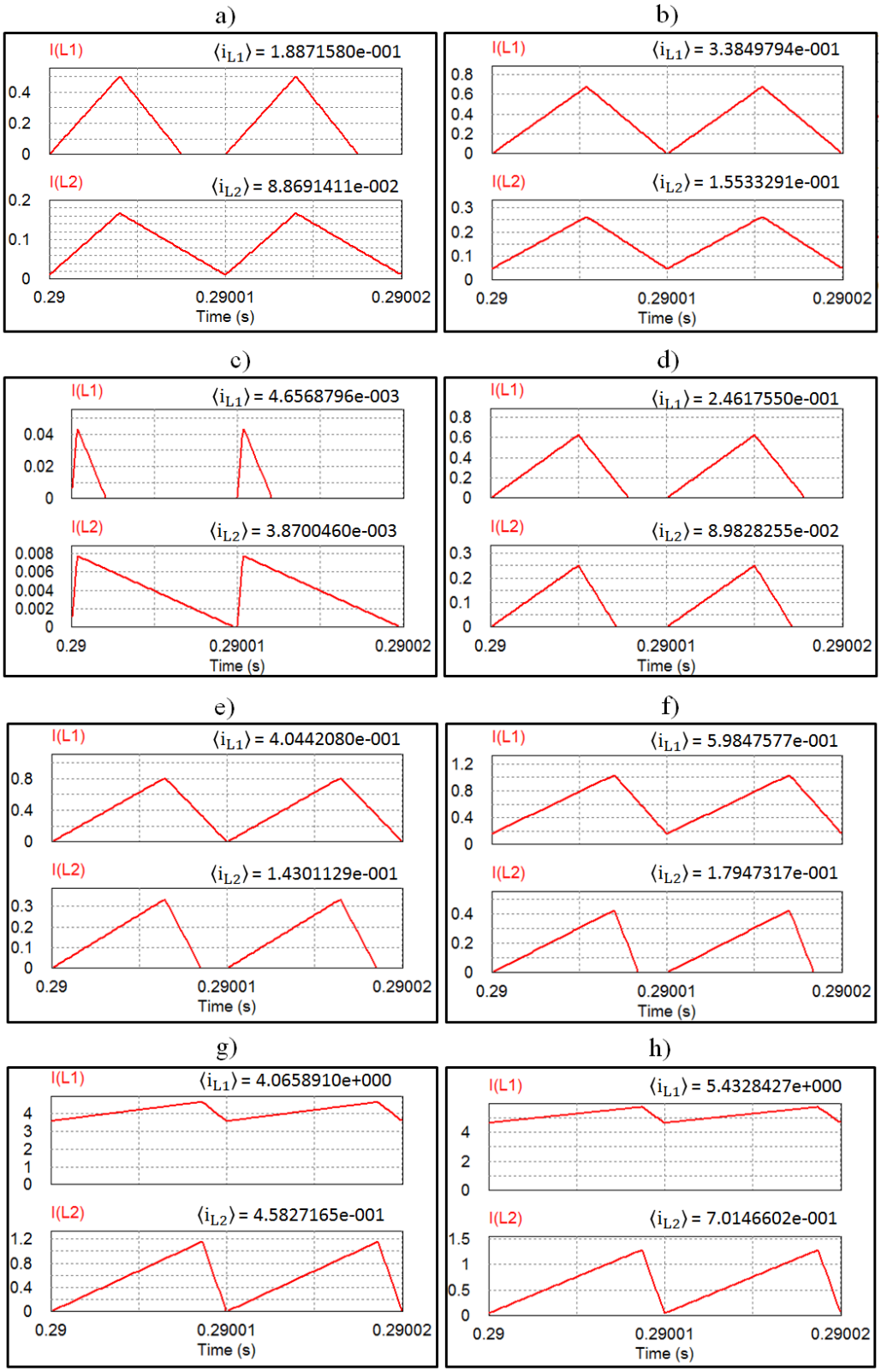

Fig. 3.10. Waveforms of the inductor currents for each marked point of figure 3.9.

In order to analyze these results, different points (**a**, **b**, **c**, **d**, **e**, **f**, **g** and **h**) have been marked on the gain characteristics to indicate a conduction mode or a limit between two of them. Further, each conduction mode has been highlighted by using the color code shown in the head of the figure. The point **a** ($U = 0.4$ and $M(U) = 3.546$) corresponds to DCL1 mode and the point **b** ($U = 0.5411, M(U) = 4.748$) corresponds to the boundary between DCL1 mode and CCM, both when the converter works with a load of 1 kΩ. The point **c** ($U = 0.0353, M(U) = 1.245$) corresponds to the boundary between DCL2 and DCL21 modes, the point **d** ($U = 0.5, M(U) = 9.057$) corresponds to DCL21 mode and the point **e** ($U = 0.6464,\ M(U) = 11.61$) corresponds to the boundary between DCL21 and DCL2 modes. In these last three points the converter works with a load of 5 kΩ. The point **f** ($U = 0.7, M(U) = 19.96$) corresponds to DCL2 mode, the point **g** ($U = 0.8621, M(U) = 52.58$) corresponds to the boundary between DCL2 mode and CCM, and the point **h** ($U = 0.8709, M(U) = 60$) corresponds to CCM. For the last three points the converter works with a load of 10 kΩ. The validity of the computed gains has been verified by means of simulation results using PSIM. The waveforms of the inductor currents have been captured in each point in order to verify the corresponding conduction modes and boundaries. The results are shown in figure 3.10.

3.3 SLIDING-MODE CONTROL

The use of the sliding-mode control in DC-DC power converters consist in imposing a desired behavior through a sliding surface by switching between the different structures of the converter. As was studied above, a DC-DC converter such as the quadratic boost converter can have two, three, four or five different structures and switches between them to operate in a desired conduction mode. For example, when the converter operates in CCM, it switches between two structures: the on-state and the off-state. In order to reach the sliding surface and remain there, the converter must change its controlled switch from the on-state to the off-state or vice versa depending on the evolution of the variables involved in the sliding surface. In general, two conditions have to be fulfilled: the reachability of the sliding surface and the permanence or invariance therein after it is reached.

To ensure the reachability of the sliding surface it is necessary that the trajectory generated directly lead the converter dynamics to the sliding surface. On the other hand, to ensure the invariance when the sliding motion is attained, it is necessary that switching between the different structures maintains the system in the sliding surface. Ideally, this switching takes place at an infinite switching frequency. However, in a real converter, a higher but not infinite frequency is only possible due to the limits of its semiconductor components, which is undesirable in terms of efficiency. Therefore, to impose a finite switching frequency, a hysteretic modulator can be used constraining the sliding surface within a hysteresis band guarantying a uniform switching. Figure 3.11 gives a graphic representation for two of the converter variables (V_{C2} and i_{L1}).

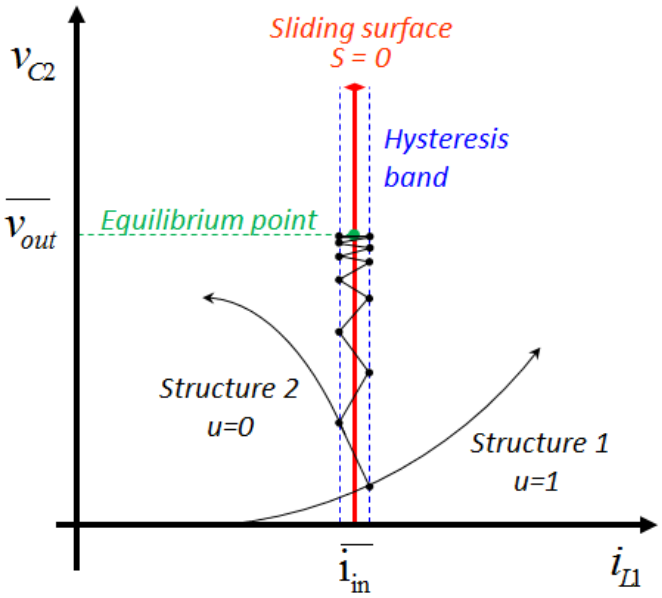

Fig. 3.11. Graphical representation of the reachability and invariance properties of the sliding mode control

It is easily to identify the evolution of the system towards the desired equilibrium point with coordinates ($\overline{\imath_{in}}, \overline{v_{out}}$). In the illustrated case, the converter operates in CCM having two possible structures, structure 1 and structure 2. From the origin, the structure 1 allows reaching the sliding surface $S(x) = i_{L1} - \overline{\imath_{in}}$ and switching between structure 1 and structure 2 allows the converter dynamics remaining in it. Further, a hysteresis band has been added showing the way to have a sliding surface as the average value of the variable i_{L1}. It is worth to note that the system switches between the two structures within the limits of the hysteresis band whereby the invariance is ensured. However, it

is also possible to observe in figure 3.11 that the system reaches the sliding surface long time before reaching the equilibrium point and later it attains the equilibrium point through the sliding surface. This remainder dynamic is known as the ideal sliding dynamic. The control signal *u* takes the values 0 or 1 in order to change the structure of the system.

To analyze the converter dynamics operating under a sliding motion, a well-known method can be applied to represent the nonlinear control variable *u* as the fictitious variable u_{eq} in such a way that the discontinuous nature of the control signal disappears but its influence in the dynamic of the converter model is preserved. This method is known in the literature as the *equivalent control method* introduced by V. Utkin in [108]. This method has been applied in many related works and will be the analysis tool in this work.

3.3.1 Hysteresis modulation- based SM controller

For a desired sliding surface $S(x)$, the ideal expected behavior in sliding motion is based on $S(x) = 0$. In a variable structure system with two possible configurations such as a DC-DC converter operating in CCM, a control law based on sliding mode can be given by:

$$u = \begin{cases} 1, & when\ S(x) < 0 \\ 0, & when\ S(x) > 0 \end{cases} \tag{3.74}$$

where it is mandatory that the control action $u = 1$ ensures the increment of $S(x)$ when its value is negative and the control action $u = 0$ ensures the decrement of $S(x)$ when its value is positive. As expected, the possible switching frequency of the systems will be undesirably higher. Then, a proper solution consists in using a hysteresis modulator to modify the control law (3.74) in the following way:

$$u = \begin{cases} 1, & when\ S(x) < -\delta \\ 0, & when\ S(x) > \delta \end{cases}$$

which allows enforcing the converter to operate with a finite switching frequency. The value of δ must be sufficiently high to avoid spurious switching produced by interference of noise and sufficiently low to ensure the validity of the approximation. Then, with the use of the hysteresis comparator, the expected sliding motion $S(x) = 0$ will correspond to the average value computed for a switching period. Then, the sliding mode control theory allows analyzing the average behavior of the converter variables when a hysteresis based modulator is used [74], or, in other words, a sliding mode control law can be easily implemented by means of a hysteresis modulator.

3.3.2 Indirect stabilization via input inductor current

As was explained above, a sliding surface can be obtained from the linear combination of the converter variables and/or some reference values. Then, the simpler sliding surface is obtained using only one converter variable and a reference variable which can be constant. Hence, when the output voltage is controlled by using a surface which includes this same output voltage, the converter is said to be stabilized in a direct way. However, in some converters, such as boost converters, this kind of sliding surfaces leads to an unstable equilibrium point. Therefore, a surface including other variables must be used in order to obtain a stable behavior in the output voltage. In these cases, the proposed surface leads to an indirect control of the output variable [105]-[107].

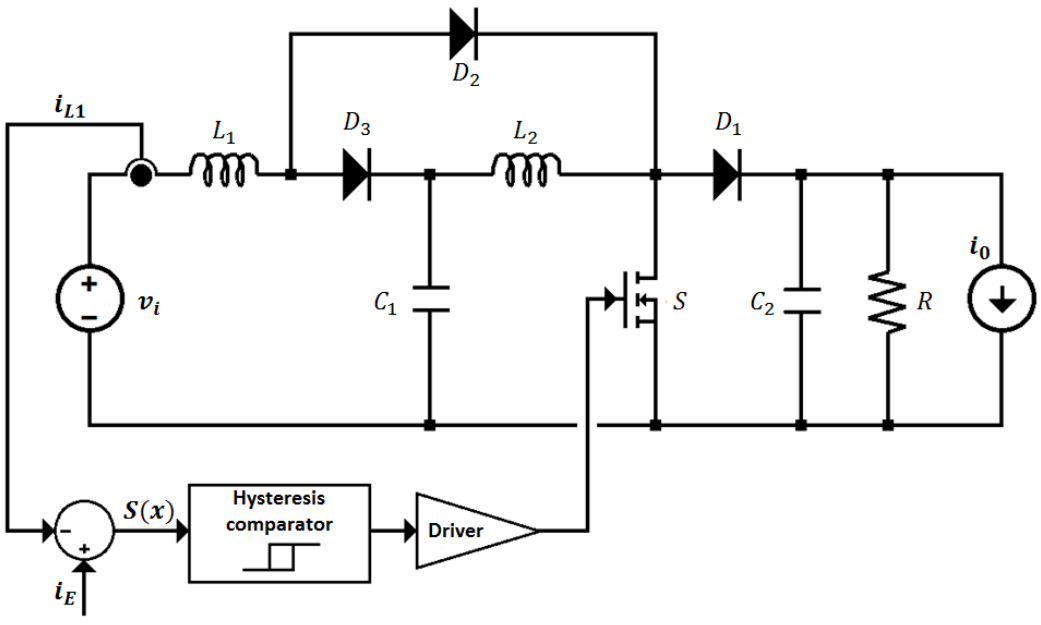

Fig. 3.12. Block diagram of the indirect stabilization of the quadratic boost converter

A simple indirect control law is obtained by only using the input inductor current which allows immediately attaining the sliding surfaces for a converter affected by disturbances and ensures stability of the equilibrium point. Figure 3.12 illustrates the proposed control applied to the quadratic boost converter.

The sliding surface is

$$S(x) = i_{L1} - i_E \tag{3.75}$$

where i_E is a current reference. The value of i_E can be a constant value or a slow signal given by an outer loop in order to achieve a second control objective such as impedance matching [103] or output voltage regulation [50]. In this case, we have that in sliding mode $S(x) = 0$ and then $i_{L1} = i_E(t)$. The switching function u corresponds to the expression (3.74).

3.3.2.1 Equivalent control analysis

By considering CCM operation, the model of the quadratic boost converter in (3.1) becomes

$$\begin{aligned}
\frac{di_{L1}}{dt} &= \frac{v_{in}}{L_1} - \frac{v_{C1}}{L_1}(1-u) \\
\frac{di_{L2}}{dt} &= \frac{v_{C1}}{L_2} - \frac{v_{C2}}{L_2}(1-u) \\
\frac{dv_{C1}}{dt} &= -\frac{i_{L2}}{C_1} + \frac{i_{L1}}{C_1}(1-u) \\
\frac{dv_{C2}}{dt} &= \frac{i_{L2}}{C_2}(1-u) - \frac{v_{C2}}{RC_2} - \frac{i_0}{C_2}
\end{aligned} \tag{3.76}$$

A current source i_0 is introduced in order to model disturbances in the output load.

A. Equivalent control

Applying the invariance conditions ($S(x) = 0$ *and* $\dot{S}(x) = 0$) in (3.75) and (3.76) leads to the equivalent control

$$u_{eq} = 1 - \frac{1}{v_{C1}}\left(v_i - L_1 \frac{dI_E}{dt}\right) \tag{3.77}$$

Evaluating the existence condition $S(x) \cdot \dot{S}(x) < 0$ using the control law (3.73) leads to the local reachability condition

$$0 < v_i - L_1 \frac{dI_E}{dt} < v_{C1} \tag{3.78}$$

B. Ideal sliding dynamics

By replacing the control variable *u* by the equivalent control u_{eq} in (3.76), the reduced order equation system (3.79) is obtained, which represents the resulting ideal sliding dynamics of the converter.

$$\begin{aligned}
\frac{di_{L2}}{dt} &= \frac{v_{C1}}{L_2} - \frac{v_{C2}}{L_2}\frac{1}{v_{C1}}\left(v_i - L_1 \frac{dI_E}{dt}\right) \\
\frac{dv_{C1}}{dt} &= -\frac{i_{L2}}{C_1} + \frac{i_{L1}}{C_1}\frac{1}{v_{C1}}\left(v_i - L_1 \frac{dI_E}{dt}\right) \\
\frac{dv_{C2}}{dt} &= -\frac{v_{C2}}{RC_2} + \frac{i_{L2}}{C_2}\frac{1}{v_{C1}}\left(v_i - L_1 \frac{dI_E}{dt}\right) - \frac{i_0}{C_2}
\end{aligned} \tag{3.79}$$

C. Equilibrium point

By solving the equilibrium point of (3.79), considering that $i_E(t)$ has the constant value I_E, $v_i(t)$ has the constant value V_i and then the converter has a purely resistive load at the equilibrium point ($\overline{i_0} = 0$), we have

$$\begin{aligned}
&\overline{i_{L1}} = I_E; && \overline{i_{L2}} = I_E{}^{\frac{3}{4}}(V_i/R)^{\frac{1}{4}}; \\
&\overline{v_{C1}} = (I_E R)^{\frac{1}{4}} v_i{}^{\frac{3}{4}}; && \overline{v_{C2}} = (I_E V_i R)^{\frac{1}{2}}
\end{aligned} \tag{3.80}$$

D. Linearized model

By linearizing (3.79) around the equilibrium point (3.80), the equation system (3.81) is obtained where the superscript (~) stands for the increments of the variables in (3.79) around the corresponding equilibrium values.

$$\frac{d\widetilde{i_{L2}}}{dt} = \frac{2}{L_2}\widetilde{v_{C1}} - \frac{1}{mL_2}\widetilde{v_{C2}} + \frac{mL_1}{L_2}\frac{d\widetilde{i_E}}{dt} - \frac{m}{L_2}\widetilde{v_i}$$
$$\frac{d\widetilde{v_{C1}}}{dt} = \frac{-1}{C_1}\widetilde{i_{L2}} - \frac{m^2}{RC_1}\widetilde{v_{C1}} + \frac{1}{mC_1}\widetilde{i_E} - \frac{m^3L_1}{RC_1}\frac{d\widetilde{i_E}}{dt} + \frac{m^3}{RC_1}\widetilde{v_i} \quad (3.81)$$
$$\frac{d\widetilde{v_{C2}}}{dt} = \frac{1}{mC_2}\widetilde{i_{L2}} - \frac{m}{RC_2}\widetilde{v_{C1}} - \frac{1}{RC_2}\widetilde{v_{C2}} - \frac{m^2L_1}{RC_2}\frac{d\widetilde{i_E}}{dt} + \frac{m^2}{RC_2}\widetilde{v_i} - \frac{1}{C_2}\widetilde{i_0}$$

Where $m=\overline{v_{C2}}/\overline{v_{C1}} = \overline{v_{C1}}/V_i$. By applying the Laplace transform to (3.81), the following polynomial identity is obtained

$$A(s)V_{C2}(s) = B(s)I_E(s) + C(s)V_i(s) + D(s)I_0(s) \quad (3.82)$$

This function can be represented by means of the block diagram in figure 3.13.

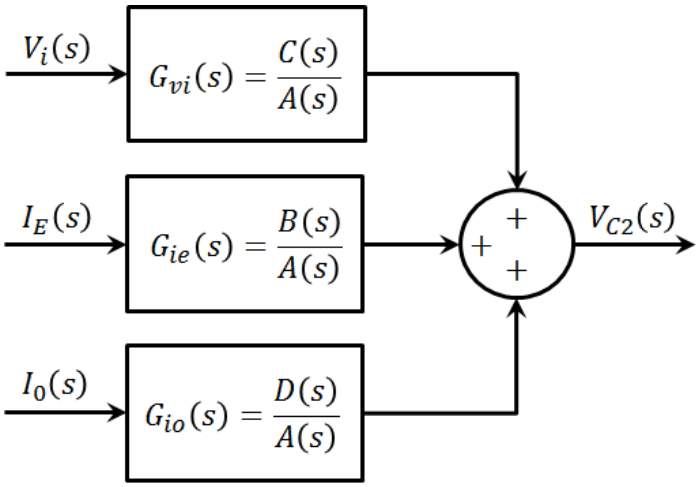

Fig. 3.13. Block diagram of the linearized model

$V_{C2}(s)$ is the linearized system output, $I_E(s)$ is the reference input, and $I_0(s)$ and $V_i(s)$ represent an output load disturbance and an input voltage perturbation respectively. The terms $A(s), B(s), C(s)$ and $D(s)$ are defined as (3.83), (3.84), (3.85) and (3.86) respectively.

$$A(s) = mC_1C_2s^3 + \frac{m}{R}(m^2C_2 + C_1)s^2 + \left[\frac{2mC_2}{L_2} + \frac{m^3}{R^2} + \frac{C_1}{mL_2}\right]s + \frac{4m}{RL_2} \quad (3.83)$$

$$B(s) = -\frac{m^3 L_1 C_1}{R}s^3 + \frac{mL_1 C_1}{L_2}s^2 - \left(\frac{2m^3 L_1}{RL_2} + \frac{m}{R}\right)s + \frac{2}{mL_2} \tag{3.84}$$

$$C(s) = \frac{m^3 C_1}{R}s^2 - \frac{mC_1}{L_2}s + \frac{2m^3}{RL_2} \tag{3.85}$$

$$D(s) = -mC_1 s^2 - \frac{m^3}{R}s - \frac{2m}{L_2} \tag{3.86}$$

Thus, by nullifying the dynamics of both disturbances, it is possible to obtain the transfer function from the incremental input inductor current to the incremental output voltage $G_{ie}(s) = V_{C2}(s)/G(s) = B(s)/A(s)$:

$$G_{ie}(s) = \frac{-\frac{m^3 L_1 C_1}{R}s^3 + \frac{mL_1 C_1}{L_2}s^2 - \frac{m}{R}\left(\frac{2L_1}{L_2}m^2 + 1\right)s + \frac{2}{mL_2}}{mC_1 C_2 s^3 + \frac{m}{R}(m^2 C_2 + C_1)s^2 + \left(\frac{m^3}{R^2} + \frac{2mC_2}{L_2} + \frac{C_1}{mL_2}\right)s + \frac{4m}{RL_2}} \tag{3.87}$$

Likewise, by nullifying the dynamics of the input current and one of the disturbances, it is possible to obtain the transfer function from either the input voltage variation or the output load perturbation to the incremental output voltage, given by (3.88) and (3.89) respectively. The resulted transfer functions are $G_{vi}(s) = V_{C2}(s)/V_i(s) = C(s)/A(s)$ and $G_{io}(s) = V_{C2}(s)/I_o(s) = D(s)/A(s)$ which are explicitly given by:

$$G_{vi}(s) = \frac{\frac{m^3 C_1}{R}s^2 - \frac{mC_1}{L_2}s + \frac{2m^3}{RL_2}}{mC_1 C_2 s^3 + \frac{m}{R}(m^2 C_2 + C_1)s^2 + \left(\frac{m^3}{R^2} + \frac{2mC_2}{L_2} + \frac{C_1}{mL_2}\right)s + \frac{4m}{RL_2}} \tag{3.88}$$

$$G_{io}(s) = \frac{-mC_1 s^2 - \frac{m^3}{R}s - \frac{2m}{L_2}}{mC_1 C_2 s^3 + \frac{m}{R}(m^2 C_2 + C_1)s^2 + \left(\frac{m^3}{R^2} + \frac{2mC_2}{L_2} + \frac{C_1}{mL_2}\right)s + \frac{4m}{RL_2}} \tag{3.89}$$

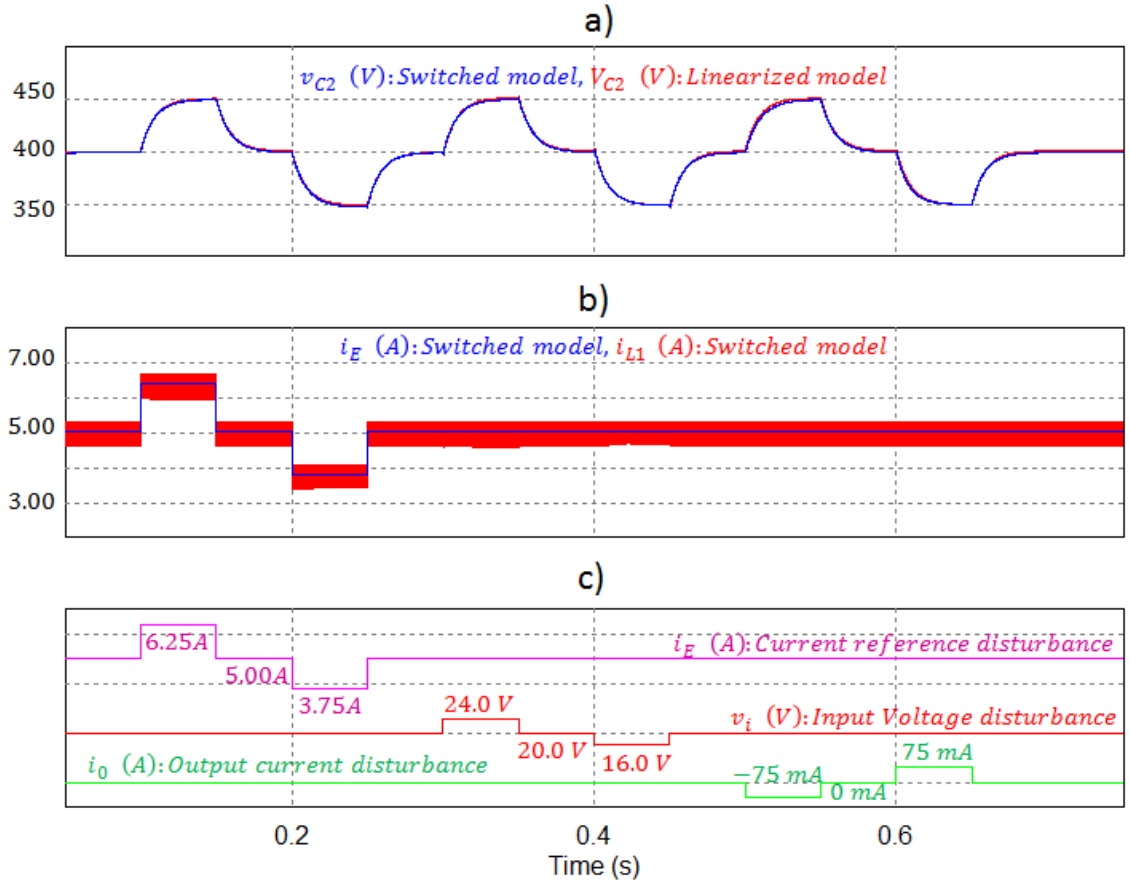

Fig. 3.14. Time response of the switching model compared with the linearized model when the converter operates with an input current controller (Parameters: L1=120 µH, L2=4.7 mH, C1=C2=11 µF, R=1600 Ω): a) output voltage $V_{C2}(s)$, b) input current compared with the input current reference, c) input waveforms $I_E(s)$, $V_i(s)$ and $I_0(s)$.

Figure 3.14 shows the transient response produced in the output voltage when a sequence of positive or a negative excitation is applied firstly in the current reference $I_E(s)$, subsequently in the input voltage $V_i(s)$ and finally in the output current $I_o(s)$.

The magnitudes of the applied excitation to obtain the waveforms in figure 3.14 have been computed ensuring the steady-state of the output voltage in 350, 400 and 450 V. As can be observed, the linearized model represents with a good precision the dynamical behavior of the converter in this set of magnitudes for the considered disturbances.

3.3.2.2 Stability analysis using a Lyapunov candidate function

When $I_E(t)$ is constant, the ideal sliding dynamics in (3.79) can be rewritten as:

$$\begin{aligned} L_2\frac{di_{L2}}{dt} &= v_{C1} - \frac{\overline{v_{C1}}^2 v_{C2}}{\overline{v_{C2}}\, v_{C1}} \\ C_1\frac{dv_{C1}}{dt} &= -i_{L2} + \frac{\overline{i_{L2}}\,\overline{v_{C1}}}{v_{C1}} \\ RC_2\frac{dv_{C2}}{dt} &= -v_{C2} + \frac{\overline{v_{C1}}\,\overline{v_{C2}}\, i_{L2}}{\overline{i_{L2}}\, v_{C1}} \end{aligned} \tag{3.90}$$

After some simple manipulations, (3.90) can be expressed as follows:

$$\begin{aligned} L_2\frac{di_{L2}}{dt} &= \left(1 + \frac{\overline{v_{C1}}}{v_{C1}}\right)(v_{C1} - \overline{v_{C1}}) - \frac{\overline{v_{C1}}^2}{\overline{v_{C2}}\, v_{C1}}(v_{C2} - \overline{v_{C2}}) \\ C_1\frac{dv_{C1}}{dt} &= -(i_{L2} - \overline{i_{L2}}) - \frac{\overline{i_{L2}}}{v_{C1}}\,(v_{C1} - \overline{v_{C1}}) \\ RC_2\frac{dv_{C2}}{dt} &= -(v_{C2} - \overline{v_{C2}}) + \frac{\overline{v_{C1}}\,\overline{v_{C2}}}{\overline{i_{L2}}\, v_{C1}}(i_{L2} - \overline{i_{L2}}) - \frac{\overline{v_{C2}}}{v_{C1}}(v_{C1} - \overline{v_{C1}}) \end{aligned}$$

Consider now the Lyapunov candidate function defined by:

$$\begin{aligned} \boldsymbol{V}(i_{L2}, v_{C1}, v_{C2}) &= \frac{1}{2}\left[L_2\frac{\overline{v_{C2}}}{\overline{v_{C1}}}(i_{L2} - \overline{i_{L2}})^2 + C_1\left(\frac{\overline{v_{C2}}}{\overline{v_{C1}}} + \frac{\overline{v_{C2}}}{v_{C1}}\right)(v_{C1} - \overline{v_{C1}})^2\right. \\ &\quad \left. + \frac{\overline{i_{L2}}}{\overline{v_{C2}}}RC_2(v_{C2} - \overline{v_{C2}})^2\right] \end{aligned} \tag{3.91}$$

Note that $V(i_{L2}, v_{C1}, v_{C2}) > 0, V(\overline{i_{L2}}, \overline{v_{C1}}, \overline{v_{C2}}) = 0$, and that this function is well defined because $v_{C1} > 0$ (see condition in (3.78)). The time derivative of $\boldsymbol{V}$ is given by:

$$\dot{\boldsymbol{V}}(i_{L2}, v_{C1}, v_{C2})$$

$$= \frac{\overline{v_{C2}}}{\overline{v_{C1}}}(i_{L2} - \overline{i_{L2}})L_2\frac{di_{L2}}{dt} + \left[\left(\frac{\overline{v_{C2}}}{\overline{v_{C1}}} + \frac{\overline{v_{C2}}}{v_{C1}}\right)(v_{C1} - \overline{v_{C1}}) - \frac{1}{2}\frac{\overline{v_{C2}}}{{v_{C1}}^2}(v_{C1} - \overline{v_{C1}})^2\right]C_1\frac{dv_{C1}}{dt} + \frac{\overline{i_{L2}}}{\overline{v_{C2}}}(v_{C2} - \overline{v_{C2}})RC_2\frac{dv_{C2}}{dt} \quad (3.92)$$

Developing each term of the previous expression leads to:

$$\dot{\boldsymbol{V}}(i_{L2}, v_{C1}, v_{C2})$$

$$= \frac{1}{2}\frac{\overline{v_{C2}}\, i_{L2}}{{v_{C1}}^2}(v_{C1} - \overline{v_{C1}})^2 - \frac{1}{2}\frac{\overline{i_{L2}}\,\overline{v_{C1}}\,\overline{v_{C2}}}{{v_{C1}}^3}(v_{C1} - \overline{v_{C1}})^2 - \frac{\overline{i_{L2}}}{v_{C1}}\left(\frac{\overline{v_{C2}}}{\overline{v_{C1}}} + \frac{\overline{v_{C2}}}{v_{C1}}\right)(v_{C1} - \overline{v_{C1}})^2 - \frac{\overline{i_{L2}}}{\overline{v_{C2}}}(v_{C2} - \overline{v_{C2}})^2 - \frac{\overline{i_{L2}}}{v_{C1}}(v_{C1} - \overline{v_{C1}})(v_{C2} - \overline{v_{C2}})$$

But, $\overline{i_{L2}} > 0, \overline{v_{C1}} > 0, \overline{v_{C2}} > 0$ because of the nature of the power circuit, then, $-\frac{\overline{\mathrm{i_{L2}}}\,\overline{\mathrm{v_{C1}}}\,\overline{\mathrm{v_{C2}}}}{{\mathrm{v_{C1}}}^3}(\mathrm{v_{C1}} - \overline{\mathrm{v_{C1}}})^2 < 0$. Therefore,

$$\dot{\boldsymbol{V}}(i_{L2}, v_{C1}, v_{C2})$$

$$\leq \frac{1}{2}\frac{\overline{v_{C2}}\, i_{L2}}{{v_{C1}}^2}(v_{C1} - \overline{v_{C1}})^2 - \frac{\overline{i_{L2}}}{v_{C1}}\left(\frac{\overline{v_{C2}}}{\overline{v_{C1}}} + \frac{\overline{v_{C2}}}{v_{C1}}\right)(v_{C1} - \overline{v_{C1}})^2 - \frac{\overline{i_{L2}}}{\overline{v_{C2}}}(v_{C2} - \overline{v_{C2}})^2 - \frac{\overline{i_{L2}}}{v_{C1}}(v_{C1} - \overline{v_{C1}})(v_{C2} - \overline{v_{C2}}) \quad (3.93)$$

If $\frac{1}{2}\mathrm{i_{L2}} < \overline{\mathrm{i_{L2}}}$, which is the same that:

$$\mathbf{i_{L2}} < \mathbf{2}\overline{\mathbf{i_{L2}}} \quad (3.94)$$

then:

$$\dot{\boldsymbol{V}}(i_{L2}, v_{C1}, v_{C2})$$

$$\leq -\frac{\overline{i_{L2}}\,\overline{v_{C2}}}{v_{C1}\overline{v_{C1}}}(v_{C1} - \overline{v_{C1}})^2 - \frac{\overline{i_{L2}}}{\overline{v_{C2}}}(v_{C2} - \overline{v_{C2}})^2 - \frac{\overline{i_{L2}}}{v_{C1}}(v_{C1} - \overline{v_{C1}})(v_{C2} - \overline{v_{C2}}) \quad (3.95)$$

Expressing (3.95) in matrix form, namely, $\dot{V} = x'Qx$, results in

$$\dot{\boldsymbol{V}}(i_{L2}, v_{C1}, v_{C2}) \leq$$

$$-\underbrace{\left[(i_{L2} - \overline{i_{L2}}) \quad (v_{C1} - \overline{v_{C1}}) \quad (v_{C2} - \overline{v_{C2}})\right]}_{x'} \underbrace{\begin{bmatrix} 0 & 0 & 0 \\ 0 & \frac{\overline{i_{L2}}\,\overline{v_{C2}}}{v_{C1}\overline{v_{C1}}} & \frac{\overline{i_{L2}}}{2v_{C1}} \\ 0 & \frac{\overline{i_{L2}}}{2v_{C1}} & \frac{\overline{i_{L2}}}{\overline{v_{C2}}} \end{bmatrix}}_{Q} \underbrace{\begin{bmatrix} i_{L2} - \overline{i_{L2}} \\ v_{C1} - \overline{v_{C1}} \\ v_{C2} - \overline{v_{C2}} \end{bmatrix}}_{x} \tag{3.96}$$

If $\left(\frac{\overline{i_{L2}}\,\overline{v_{C2}}}{v_{C1}\overline{v_{C1}}}\right)\frac{\overline{i_{L2}}}{\overline{v_{C2}}} - \frac{\overline{i_{L2}}^2}{4{v_{C1}}^2} = \frac{\overline{i_{L2}}^2}{v_{C1}}\left(\frac{1}{\overline{v_{C1}}} - \frac{1}{4v_{C1}}\right)$ is positive, then $Q \geq 0$. This is true if $4v_{C1} > \overline{v_{C1}}$, which is the same that:

$$\boldsymbol{v_{C1} > \frac{1}{4}\overline{v_{C1}}} \tag{3.97}$$

In conclusion, if the conditions $i_{L2} < 2\overline{i_{L2}}$ and $v_{C1} > \frac{1}{4}\overline{v_{C1}}$ are satisfied, then $\dot{V}(i_{L2}, v_{C1}, v_{C2}) \leq 0$. Moreover, $\dot{V}(i_{L2}, v_{C1}, v_{C2}) = 0$ for $v_{C1} = \overline{v_{C1}}$ and $v_{C2} = \overline{v_{C2}}$, which, considering the above conditions, implies $i_{L2} = \overline{i_{L2}}$, i_{L1} being equal to I_E. Then, $\dot{V}(i_{L2}, v_{C1}, v_{C2}) = 0$, only for the equilibrium point. Therefore, the system is asymptotically stable by the LaSalle's invariance principle [110].

3.3.3 Converter operating as a Loss-Free Resistor

The DC transformer, the DC gyrator and the Loss Free Resistor (LFR) are the three canonical elements to model a DC processing system. These elements can be classified into the two-port circuits denominated as POPI (Power Output = Power Input) which has been introduced by Singer in [92]. As shown in figure 3.15, the DC-DC stage must be a type of POPI circuit which extract the maximum power to process, and make it available to supply the DC-AC stage which has been represented as a constant current load. So, the converter used in the DC-DC stage must show a resistive behavior at the input port whereas it shows a power source behavior at the output port. To obtain such a behavior, a DC-DC power converter such as the quadratic boost one can be enforced to be a LFR if a proportional relation exists between the input voltage and the input current. Then, the control of the input port can be designed using either the input resistance or the input conductance as a control variable. A sliding surface which involves these two variables and a proportional constant (*R* or *G*), can be proposed to obtain a SM-LFR property.

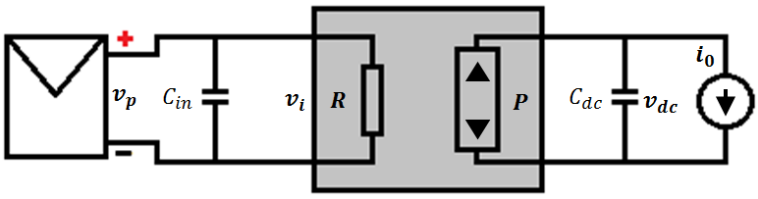

Fig. 3.15. Representation of a Loss-Free-Resistor (LFR) as a two-port conversion system.

The control strategy required to have the SM-LFR behavior can be expressed in terms of the sliding surface (3.75) written in the following form:

$$S(x) = i_{L1} - v_i(t)G(t) \tag{3.98}$$

where $G(t)$ is the conductance which is given by an outer loop controlled by a MPPT algorithm which ensures the tracking of the maximum power point. In sliding-mode $S(x) = 0$, which implies $i_{L1} = v_i(t)G(t)$. Figure 3.16 shows the diagram of the corresponding control system.

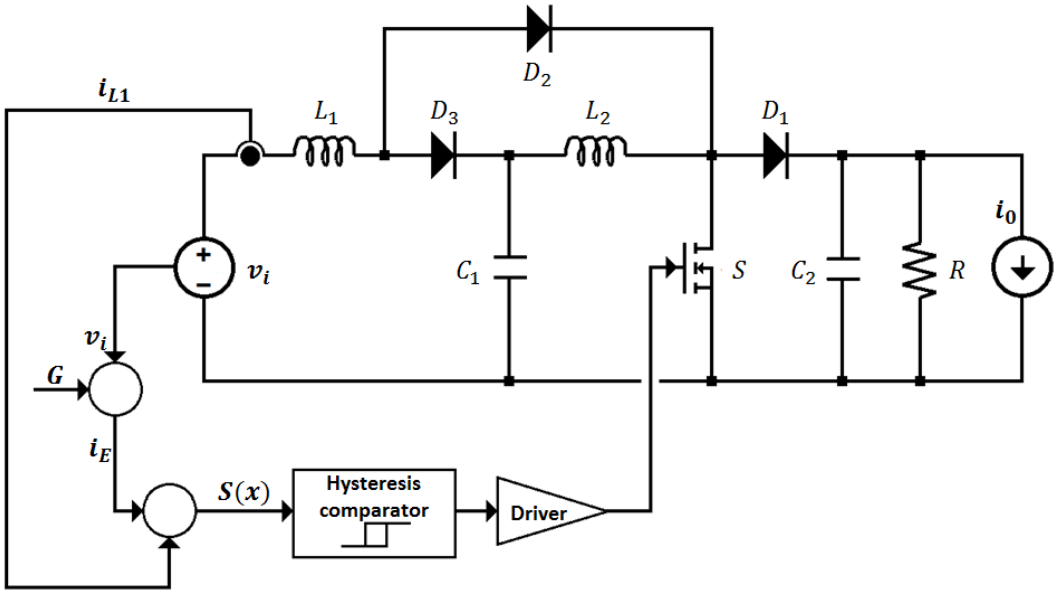

Fig. 3.16. Block diagram of the quadratic boost converter operating as a SM-LFR

Applying the invariance conditions ($S(x) = 0$ *and* $\dot{S}(x) = 0$) in (3.76) and (3.98) leads to the equivalent control

$$1 - u_{eq} = \frac{v_i}{v_{C1}} - \frac{L_1}{v_{C1}}\left(v_i\frac{dG}{dt} + G\frac{dv_i}{dt}\right) \tag{3.99}$$

Evaluating the existence condition $S(x) \cdot \dot{S}(x) < 0$ using the control law (3.79) leads to the local reachability condition (3.100).

$$0 < v_i - L_1 \left(v_i \frac{dG}{dt} + G \frac{dv_i}{dt} \right) < v_{C1} \tag{3.100}$$

By introducing both $S(x) = 0$ and the expression of the equivalent control in (3.76), the equation system (3.101) is obtained, which represents the resulting ideal sliding dynamics of the converter.

$$\begin{aligned}
\frac{di_{L2}}{dt} &= \frac{v_{C1}}{L_2} - \frac{v_{C2}}{L_2}\left[\frac{v_i}{v_{C1}} - \frac{L_1}{v_{C1}}\left(v_i \frac{dG}{dt} + G \frac{dv_i}{dt}\right)\right] \\
\frac{dv_{C1}}{dt} &= -\frac{i_{L2}}{C_1} + \frac{i_{L1}}{C_1}\left[\frac{v_i}{v_{C1}} - \frac{L_1}{v_{C1}}\left(v_i \frac{dG}{dt} + G \frac{dv_i}{dt}\right)\right] \\
\frac{dv_{C2}}{dt} &= -\frac{v_{C2}}{RC_2} + \frac{i_{L2}}{C_2}\left[\frac{v_i}{v_{C1}} - \frac{L_1}{v_{C1}}\left(v_i \frac{dG}{dt} + G \frac{dv_i}{dt}\right)\right] - \frac{i_0}{C_2}
\end{aligned} \tag{3.101}$$

On the one hand, by solving the equilibrium point of (3.101), considering $G(t)$ as the constant value G and a purely resistive load ($i_0 = 0$), we have

$$\begin{aligned}
\overline{i_{L1}} &= V_i G; & \overline{i_{L2}} &= V_i (G^3/R)^{\frac{1}{4}}; \\
\overline{v_{C1}} &= V_i (RG)^{\frac{1}{4}}; & \overline{v_{C2}} &= V_i (RG)^{\frac{1}{2}}
\end{aligned} \tag{3.102}$$

On the other hand, by solving the equilibrium point for a constant current load (i.e $i_0 = I_0$ and $R = \infty$), we have

$$\begin{aligned}
\overline{i_{L1}} &= V_i G; & \overline{i_{L2}} &= (V_i G I_0)^{\frac{1}{2}}; \\
\overline{v_{C1}} &= V_i^{\frac{3}{2}} (G/I_0)^{\frac{1}{2}}; & \overline{v_{C2}} &= \left(V_i{}^2 G\right)/I_0
\end{aligned} \tag{3.103}$$

It is worth to note that the equilibrium values of $\overline{i_{L1}}$ and $\overline{v_{C2}}$ are the same in both cases and also the condition $RG = (\overline{v_{C2}}/V_i)^2 = m^4$, where $m = \overline{v_{C1}}/V_i = \overline{v_{C2}}/\overline{v_{C1}}$.

3.3.3.1 Analysis with resistive load

By linearizing (3.101) around the equilibrium point (3.102), the equation system (3.104) is obtained where the superscript (~) stands for the increments of the variables in (3.101) around the corresponding equilibrium values.

$$\begin{aligned}
\frac{d\widetilde{i_{L2}}}{dt} &= \frac{2}{L_2}\widetilde{v_{C1}} - \frac{1}{mL_2}\widetilde{v_{C2}} - \frac{m}{L_2}\widetilde{v_i} + \frac{mGL_1}{L_2}\frac{d\widetilde{v_i}}{dt} + \frac{mL_1V_i}{L_2}\frac{d\tilde{G}}{dt} \\
\frac{d\widetilde{v_{C1}}}{dt} &= \frac{-1}{C_1}\widetilde{i_{L2}} - \frac{G}{m^2C_1}\widetilde{v_{C1}} + \frac{2G}{mC_1}\widetilde{v_i} + \frac{V_i}{mC_1}\tilde{G} - \frac{V_iGL_1}{mC_1}\frac{d\tilde{G}}{dt} - \frac{G^2L_1}{mC_1}\frac{d\widetilde{v_i}}{dt} \\
\frac{d\widetilde{v_{C2}}}{dt} &= \frac{1}{mC_2}\widetilde{i_{L2}} - \frac{m}{RC_2}\widetilde{v_{C1}} - \frac{1}{mC_2}\widetilde{v_{C2}} + \frac{m^2}{RC_2}\widetilde{v_i} - \frac{V_iL_1m^2}{RC_2}\frac{d\tilde{G}}{dt} - \frac{GL1m^2}{RC_2}\frac{d\widetilde{v_i}}{dt}
\end{aligned} \tag{3.104}$$

By applying the Laplace transform to (3.104), the following multiple input single output transfer function is obtained

$$V_{C2}(s) = G_g(s)G(s) + G_{vi}(s)V_i(s) + G_{io}(s)I_0(s) \tag{3.105}$$

This function can be represented by means of the block diagram in figure 3.17.

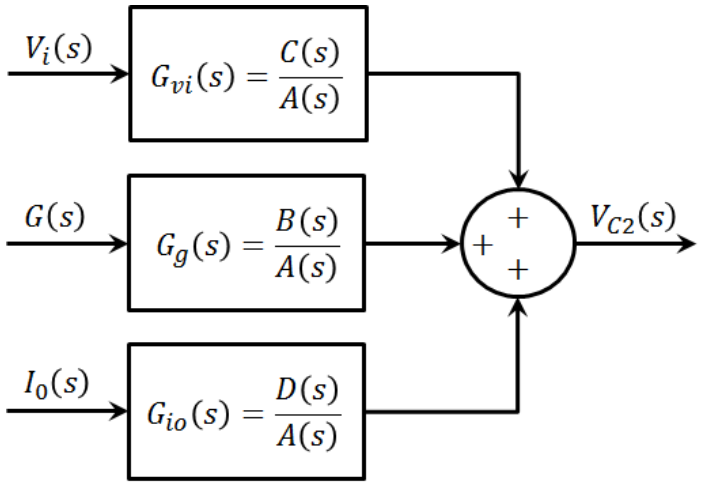

Fig. 3.17. Block diagram of the linearized model when the converter operates as a SM-LFR

The terms $A(s), B(s), C(s)$ and $D(s)$ are defined as (3.106), (3.107), (3.108) and (3.109) respectively.

$$A(s) = mC_1C_2s^3 + \frac{m}{R}(m^2C_2 + C_1)s^2 + \left(\frac{m^3}{R^2} + \frac{2mC_2}{L_2} + \frac{C_1}{mL_2}\right)s + \frac{4m}{RL_2} \tag{3.106}$$

$$B(s) = -\frac{m^3L_1C_1V_i}{R}s^3 + \frac{L_1C_1V_im}{L_2}s^2 - \frac{V_im}{R}\left(1 + \frac{3m^2L_1}{L_2}\right)s + \frac{2V_i}{mL_2} \tag{3.107}$$

$$C(s) = -\frac{m^3GL1C_1}{R}s^3 + C_1\left(\frac{m^3}{R} + \frac{mGL_1}{L_2}\right)s^2 + \left[\frac{2G^2L_1}{mL_2} + \frac{mC_1}{L_2} + \frac{2mG}{R}\right]s + \frac{4G}{L_2m} \tag{3.108}$$

$$D(s) = -mC_1s^2 - \frac{m^3}{R}s - \frac{2m}{L_2} \tag{3.109}$$

It is possible to obtain the transfer function from the incremental input inductor current to the incremental output voltage $G_g(s) = V_{C2}(s)/G(s) = B(s)/A(s)$

$$G_g(s) = \frac{-\frac{m^3L_1C_1V_i}{R}s^3 + \frac{L_1C_1V_im}{L_2}s^2 - \frac{V_im}{R}\left(1 + \frac{3m^2L_1}{L_2}\right)s + \frac{2V_i}{mL_2}}{mC_1C_2s^3 + \frac{m}{R}(m^2C_2 + C_1)s^2 + \left(\frac{m^3}{R^2} + \frac{2mC_2}{L_2} + \frac{C_1}{mL_2}\right)s + \frac{4m}{RL_2}} \tag{3.110}$$

and the transfer function from either the input voltage variation or the output current perturbation to the incremental output voltage. The resulted transfer functions are $G_{vi}(s) = V_{C2}(s)/V_i(s) = C(s)/A(s)$ and $G_{io}(s) = V_{C2}(s)/I_o(s) = D(s)/A(s)$ which are explicitly given by

$$G_{vi}(s) = \frac{-\frac{m^3L_1C_1V_i}{R}s^3 + \frac{L_1C_1V_im}{L_2}s^2 - \frac{V_im}{R}\left(1 + \frac{3m^2L_1}{L_2}\right)s + \frac{2V_i}{mL_2}}{mC_1C_2s^3 + \frac{m}{R}(m^2C_2 + C_1)s^2 + \left(\frac{m^3}{R^2} + \frac{2mC_2}{L2} + \frac{C_1}{mL_2}\right)s + \frac{4m}{RL_2}} \tag{3.111}$$

$$G_{io}(s) = \frac{-mC1s^2 - \frac{m^3}{R}s - \frac{2m}{L2}}{mC_1C_2s^3 + \frac{m}{R}(m^2C_2 + C_1)s^2 + \left(\frac{m^3}{R^2} + \frac{2mC_2}{L2} + \frac{C_1}{mL_2}\right)s + \frac{4m}{RL_2}} \tag{3.112}$$

Figure 3.18 shows a simulation test in PSIM validating the model by comparing the linearized model with the switching model when different input excitations are applied in the input variable $G(s)$ or the disturbance variables $V_i(s)$ and $I_o(s)$.

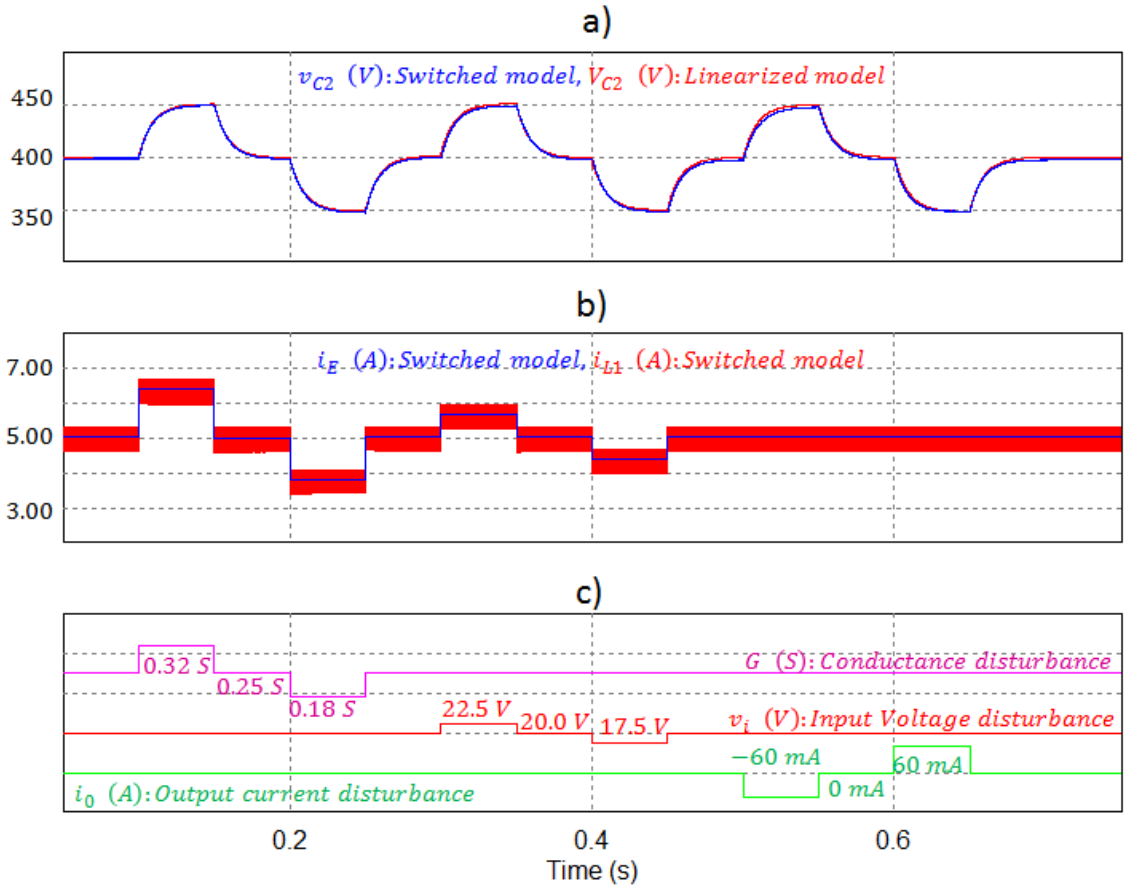

Fig. 3.18. Time response of the switching model compared with the linearized model when the converter operates with an input current controller (Parameters: L1=120 µH, L2=4.7 mH, C1=C2=11 µF, R=1600 Ω): a) output voltage $V_{C2}(s)$, b) input current compared with the input current reference, c) input waveforms$G(s)$, $V_i(s)$ and $I_0(s)$.

3.3.3.2 Analysis with constant current load

By linearizing (3.101) around the equilibrium point (3.103), the equation system (3.113) is obtained where the superscript (~) stands for the increments of the variables in (3.101) around the corresponding equilibrium values.

$$\begin{aligned}
\frac{d\widetilde{i_{L2}}}{dt} &= \frac{2}{L_2}\widetilde{v_{C1}} - \frac{1}{mL_2}\widetilde{v_{C2}} - \frac{m}{L_2}\tilde{v}_i + \frac{mGL_1}{L_2}\frac{d\tilde{v}_i}{dt} + \frac{mL_1V_i}{L_2}\frac{d\tilde{G}}{dt} \\
\frac{d\widetilde{v_{C1}}}{dt} &= \frac{-1}{C_1}\widetilde{i_{L2}} - \frac{G}{m^2C_1}\widetilde{v_{C1}} + \frac{2G}{mC_1}\tilde{v}_i + \frac{V_i}{mC_1}\tilde{G} - \frac{V_iGL_1}{mC_1}\frac{d\tilde{G}}{dt} - \frac{G^2L_1}{mC_1}\frac{d\tilde{v}_i}{dt} \\
\frac{d\widetilde{v_{C2}}}{dt} &= \frac{1}{mC_2}\widetilde{i_{L2}} - \frac{I_0}{C_2mV_i}\widetilde{v_{C1}} + \frac{I_0}{C_2V_i}\tilde{v}_i - \frac{I_0GL_1}{V_iC_2}\frac{d\tilde{v}_i}{dt} - \frac{I_0L_1}{C_2}\frac{d\tilde{G}}{dt} - \frac{1}{C_2}\tilde{\imath}_0
\end{aligned} \tag{3.113}$$

As in the case of resistive load, it is possible to obtain the transfer function from the incremental conductance to the incremental output voltage $G_g(s) = V_{C2}(s)/G(s) = B(s)/A(s)$:

$$G_g(s) = \frac{-I_0 m L_1 C_1 s^3 + \frac{V_i m L_1 C_1}{L_2} s^2 - \frac{I_0}{m}\left(1 + \frac{m^2 L_1}{L_2}\right) s + \frac{2V_i}{mL_2}}{mC_1C_2 s^3 + \frac{GC_2}{m} s^2 + \frac{1}{mL_2}(2m^2C_2 + C_1)s + \frac{2G}{m^3 L_2}} \tag{3.114}$$

and the transfer function from either the input voltage variation or the output current perturbation to the incremental output voltage. The resulted transfer functions are:

$$G_{vi}(s) = \frac{-\frac{I_0 m G L_1 C_1}{V_i} s^3 + mC_1\left[\frac{I_0}{V_i} + \frac{GL_1}{L_2}\right] s^2 - \left[\frac{I_0 m L_1 G}{V_i L_2} + \frac{mC_1}{L_2} + \frac{I_0 G}{V_i m}\right] s + \frac{I_0 m}{V_i L_2}}{mC_1C_2 s^3 + \frac{GC_2}{m} s^2 + \frac{1}{mL_2}(2m^2C_2 + C_1)s + \frac{2G}{m^3 L_2}} \tag{3.115}$$

$$G_{io}(s) = \frac{-mC_1 s^2 - \frac{G}{m} s - \frac{2m}{L_2}}{mC_1C_2 s^3 + \frac{GC_2}{m} s^2 + \frac{1}{mL_2}(2m^2C_2 + C_1)s + \frac{2G}{m^3 L_2}} \tag{3.116}$$

From the Routh Hurwitz test, this system is stable satisfying the condition:

$$\boldsymbol{m > \sqrt{\frac{C_1}{2C_2}}} \tag{3.117}$$

. As it is shown in figure 3.19, a simulation test in PSIM validating the model by comparing the linearized model with the switching model when different input excitations are applied in either the input variable $G(s)$ or the disturbance variable $V_i(s)$ or the load $I_o(s)$. To regulate the output voltage it is possible to introduce an external control loop. As shown in figure 3.20, it is possible to consider that the current load connected to the converter is defined as a function of the output voltage. In this approach the energy of the output capacitor is maintained constant. The output power of the converter is defined by the output voltage and the output current which are internal variables of the control system. This approach requires a controller operating over the load (DC-AC stage) defining the instantaneous current demanded to the DC-DC stage so that the output voltage can be stabilized and regulated.

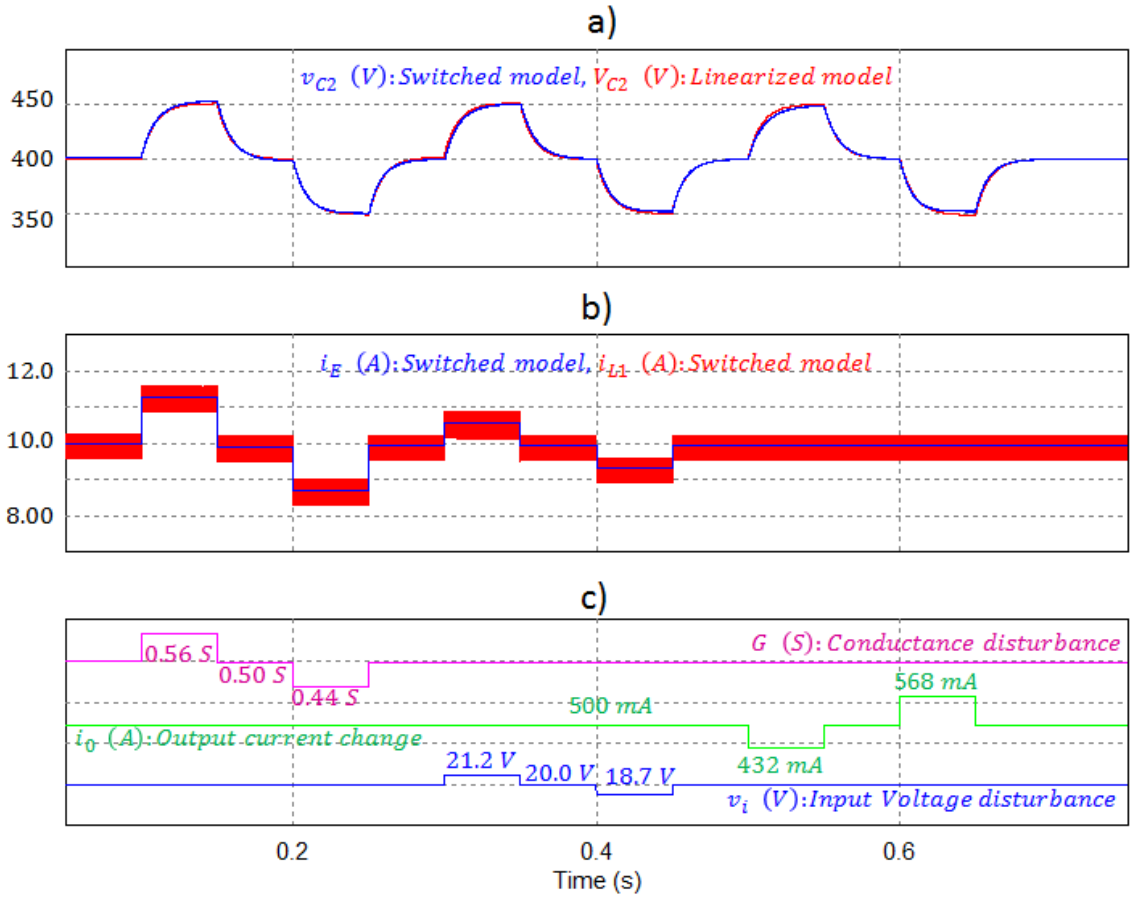

Fig. 3.19. Time response of the switching model compared with the linearized model when the converter operates with an input current controller (Parameters: L1=120 µH, L2=4.7 mH, C1=C2=11 µF): a) output voltage $V_{C2}(s)$, b) input current compared with the input current reference, c) input waveforms$G(s)$, $V_i(s)$ and $I_0(s)$.

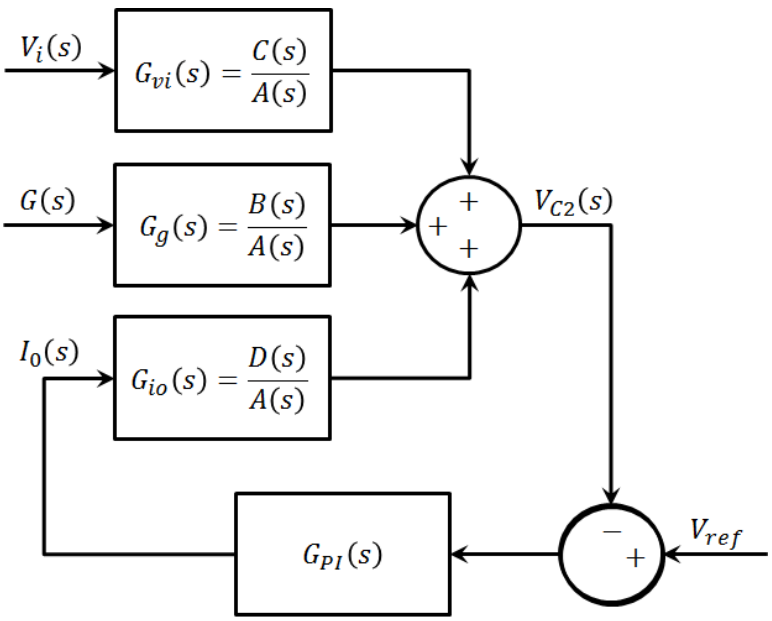

Fig. 3.20. Block diagram of the controlled system stabilizing the SM-LFR operation when converter copes with a constant current source load.

In order to illustrate the above described control, figure 3.19 shows simulation results obtained by using a controlled current source as a converter load and output voltage regulation by means of a PI compensator. The PI controller operates over the output voltage error with a reference value of 400 V. Values of 0.01 and 1 are used for the proportional and integral gains respectively considering the form $PI(s) = k_p + \frac{k_i}{s}$.

As it can be shown in figure 3.20, the regulation of the output voltage around 400 V is accomplished. Further, positive and negative disturbances are applied on the input voltage at 0.1 and 0.15 s in order to obtain a transient deviation of 5% from the steady-state value. Moreover, positive and negative disturbances are applied on the conductance at 0.2 and 0.25 s respectively to have a similar transient deviation of 5%. A simple controller system allows efficiently controlling the quadratic boost converter. It is worth to note, that this illustrative approach considers a constant load, which is indeed the case of a power converter connected to a grid. Hence, this control problem will be explained in more details in the chapters devoted to the DC-AC conversion stage.

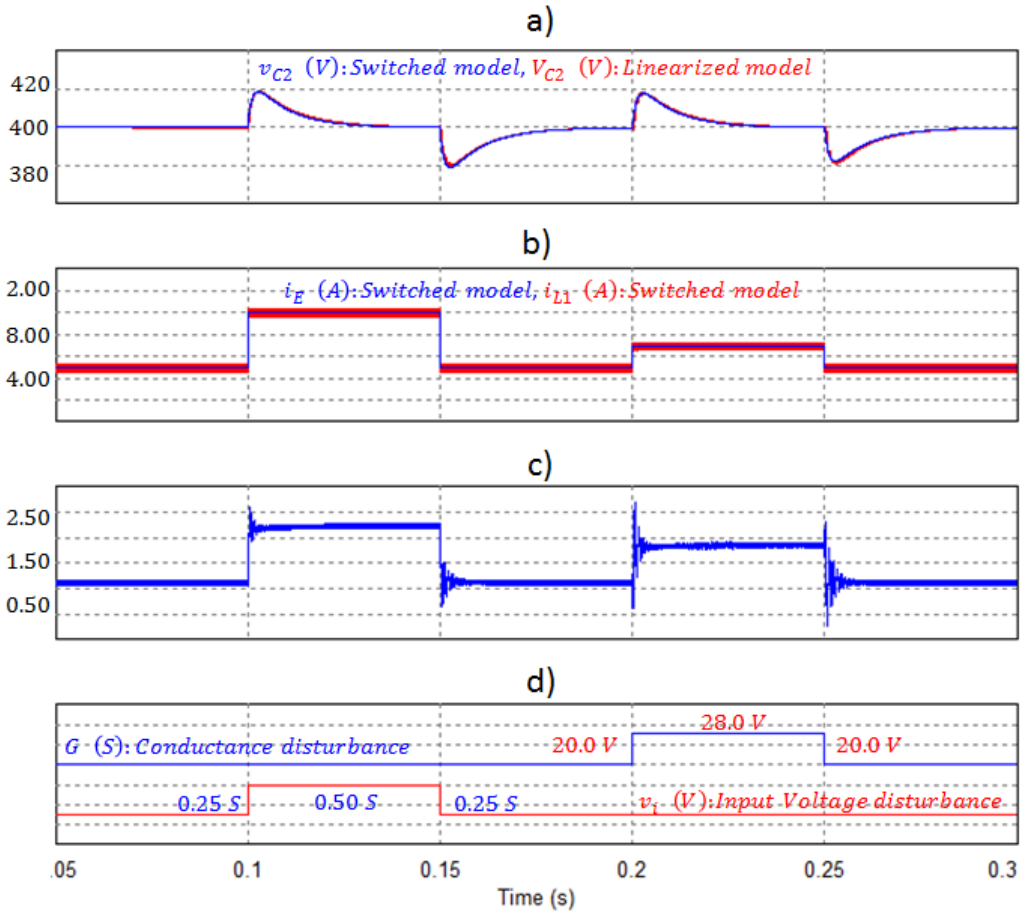

Fig. 3.20. Comparison of the switching model with the linearized model when the converter operates as a SM-LFR with output voltage regulation via output current (Parameters: L1=120 µH, L2=4.7 mH, C1=C2=11 µF, Kp=0.01 and Ki=1): a) output voltage $v_{C2}(t)$; b) input current $i_{L1}(t)$ and current reference $i_E(t)$; c) current on inductor L2 $i_{L2}(t)$; and d) input disturbance waveforms $G(s)$ and $V_i(s)$.

3.4 EFFICIENCY ASPECTS

A complete study of the efficiency of a quadratic boost converter operating in conditions similar to the one required in our application has been reported in [59]. In that work the quadratic boost converter is controlled using a two-loop controller to regulate the output voltage at 400 VDC. An inner loop corresponds to the sliding mode indirect stabilization described in subsection 3.3.2. To evaluate the efficiency, it is considered that the converter must operate in a range of input voltage and output power. This section compiles the main elements of that work and proposes other experimental results with a different set of parameter in order to complete and enhance the understanding about the effects of a sliding mode strategy on the converter efficiency.

As analyzed in the above sections, the use of a hysteretic comparator to enforce a sliding surface leads to a non-constant frequency operation depending on the input voltage (V_i) and the output load (P_o). However, it is worth nothing that the frequency is constant for each point (V_i, P_o) in the overall operational range of the converter. Therefore, the frequency variations affect the efficiency because the switching losses of the semiconductor devices are proportional to the switching frequency. In addition, this fact constitutes a significant difference with respect to a PWM -based control which deserves a special attention.

3.4.1 Conduction losses

In order to analyze the effect of the conduction losses on the converter gain and the efficiency of the converter, the ideal circuit configurations depicted in figure 3.2 can be complemented by introducing the parasitic resistive components in inductors, capacitors and controlled switches. Further, a complete model of diodes can be included using a series resistor and a DC source which allows representing the effect of the current in the forward voltage. The circuit diagrams corresponding to the improved model of the converter operating in CCM are shown if figure 3.21.

This model is adapted for evaluating theoretically the converter efficiency or the converter dynamics. However, introducing the parasitic elements in differential equations can increase considerably the required computation. Hence, the complete model has been only used in the steady-state analysis of the converter to evaluate the efficiency within its operational range.

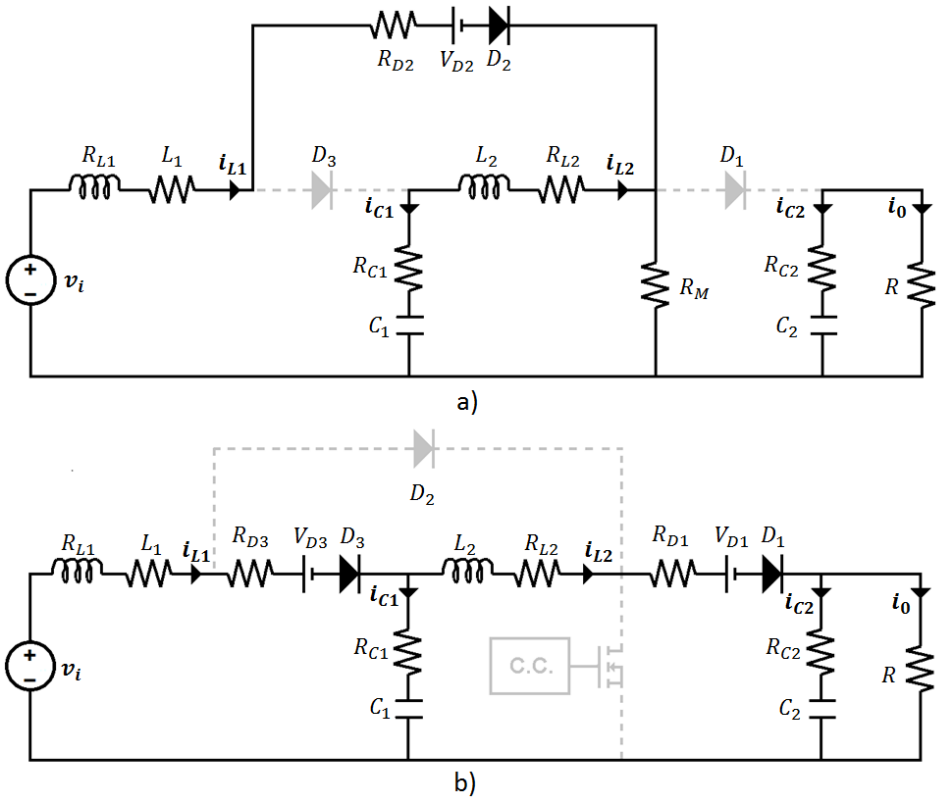

Fig. 3.21. Circuit diagram of the ON-state of the non-ideal quadratic boost converter

Note that each element in the circuit has been replaced by a more complete model. The inductors are represented using an ideal inductance and the equivalent series resistance R_{Lx}, the capacitors are represented by the ideal capacitance and the equivalent series resistance R_{Cx}, the diodes have been represented using a series resistance R_{Dx} and a voltage source V_{Dx}, and the controlled switch is represented using the on-resistance R_M. Considering only a resistive load, the model (3.76) becomes

$$
\begin{aligned}
L_1\frac{di_{L1}}{dt} &= v_i - v_{C1}(1-u) - i_{L1}[R_{L1} + (R_{D2}+R_M)u + (R_{D3}+R_{C1})(1-u)] \\
&\quad - i_{L2}[R_M u + R_{C1}(1-u)] - V_{D2}u - V_{D3}(1-u) \\
L_2\frac{di_{L2}}{dt} &= v_{C1} - v_{C2}K_o(1-u) - i_{L1}[R_M u - R_{C1}(1-u)] \\
&\quad - i_{L2}[R_{L2} + R_{C1} + R_M u + (R_{D1} + R_{C2}K_{out})(1-u)] \\
&\quad - v_{D1}(1-u) \\
C_1\frac{dv_{C1}}{dt} &= -i_{L2} + i_{L1}(1-u) \\
C_2\frac{dv_{C2}}{dt} &= i_{L2}(1-u) - \frac{v_{C2}}{R}
\end{aligned}
\tag{3.118}
$$

where $K_o = R/(R + R_{C2})$. Evaluating (3.118) at an equilibrium point (derivatives equal to zero and $u = U$), it is possible to derive the following linear system

$$\begin{bmatrix} R_{L1} + R_a U + R_b U' & R_M U - R_{C1} U' & U' & 0 \\ R_M U - R_{C1} U' & R_{L2} + R_{C1} + R_M U + R_e U' & -1 & K_o U' \\ U' & -1 & 0 & 0 \\ 0 & RU' & 0 & -1 \end{bmatrix} \begin{bmatrix} I_{L1} \\ I_{L2} \\ V_{C1} \\ V_{C2} \end{bmatrix} = \begin{bmatrix} V_i - V_{D2} U - V_{D3} U' \\ -V_{D1} U' \\ 0 \\ 0 \end{bmatrix}$$

where $U' = 1 - U$, $R_a = R_M + R_{D2}$, $R_b = R_{D3} + R_{C1}$, and $R_e = R_{D1} + K_o R_{C2}$. Hence, solving this linear system leads to the mean value of the converter variables. Further, the effect of the voltage drops in resistive elements can be observed evaluating the converter gain. Figure 3.22 shows a comparison of output voltage curves obtained with the ideal model, two different values of resistive load and two different values of output voltage. As it can be observed, the converter must operate in a range of duty cycle from 0.72 to 0.83 approximately to obtain an output voltage of 400 V for input voltages between 15 V and 30 V, and output loads between 16 W and 100 W. However, it is worth mentioning that the switching losses have not been already considered and hence some deviations can be observed.

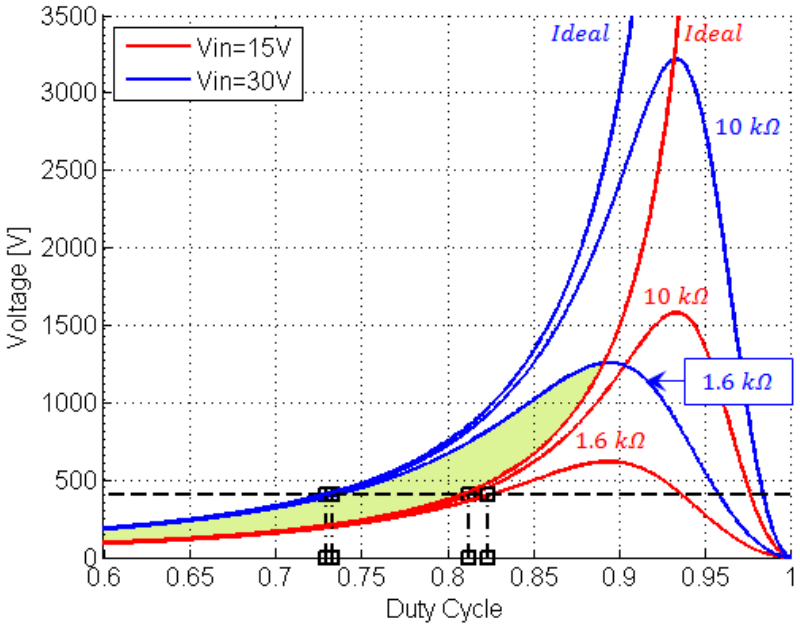

Fig. 3.22. Output voltage vs. duty cycle for different input voltages and output loads

On the other hand, note that this analysis covers the effect of the voltage drops on the mean values of the variables but it does not include the mean values of the converter variables. Moreover, it is possible to compute the DC conduction losses in the converter using the formulas given in table 3.2 (I_S represents the current of the controlled switch (MOSFET in the case of the table) and I_D represents the diode currents).

Table 3.2. Expressions to compute the power conduction losses

Element	Expressions
Inductors	$P_L = P_{core} + P_{Copper} = P_{core} + {I_{L_{RMS}}}^2 \cdot R_L$
Capacitors	$P_C = {I_{C_{RMS}}}^2 \cdot R_C$
MOSFET	$P_S = {I_{S_{RMS}}}^2 \cdot R_{DSon}$
Diodes	$P_D = {I_{D_{RMS}}}^2 \cdot R_D + \overline{I_D} \cdot V_D$

The RMS value of the currents is slightly different of the average value in normal load conditions but is considerably different in lower load conditions because the amplitude of the current ripple begins to be comparable with the average. An accurate estimation of the conduction power losses must compute both components (AC and DC) for the case of triangular or trapezoidal waveforms.

3.4.2 Switching losses

Quantifying the switching losses is a really complex problem even for the more basic converters. For a power converter operating with hard switching at a switching frequency f_s, some approximations use the analysis of the switching transitions (rise and fall) by computing the energy required to change from one state to another. Figure 3.23 shows these transitions and the involved variables considering diodes with no reverse recovery (SiC diodes).

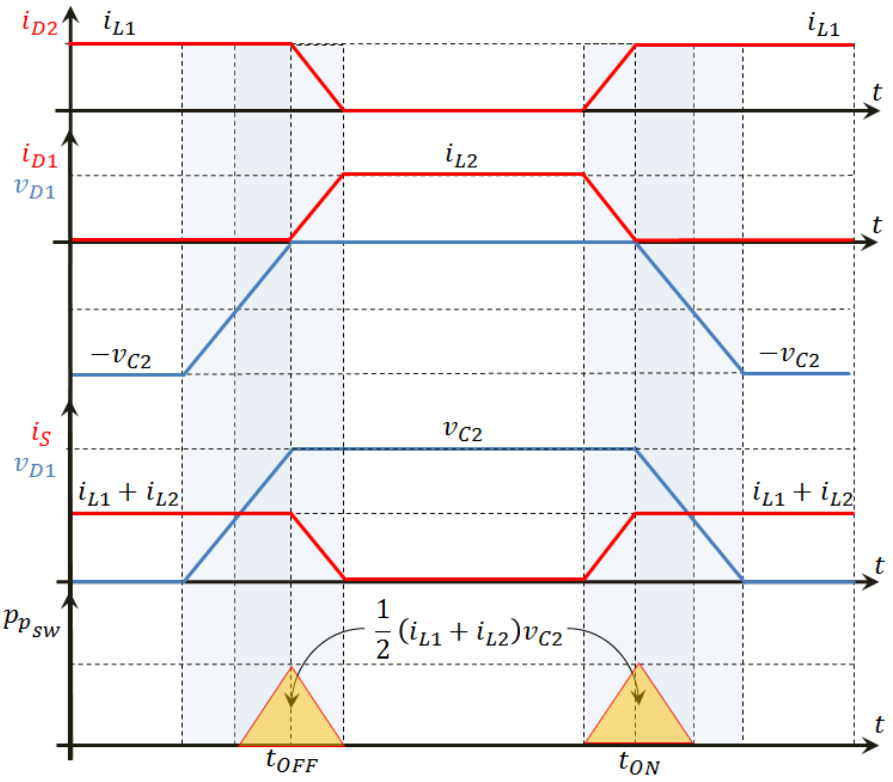

Fig. 3.23. Circuit diagram of the on-state of the non-ideal quadratic boost converter

We obtain the expressions to compute the switching losses listed in table 3.3 from the graphics in figure 3.23 by adding the corresponding effect of the current ripples in each transition (t_r , t_f and C_{gate} from the datasheet of the controlled switch).

Table 3.3. Expressions to compute the power switching losses

Element	Expression
ON transition	$P_{ON} = \frac{1}{2}\left(\overline{I_{L1}} + \overline{I_{L2}} - \delta - \frac{1}{2}\Delta I_{L2}\right) t_r \cdot V_{C2} \cdot f_s$
OFF transition	$P_{OFF} = \frac{1}{2}\left(\overline{I_{L1}} + \overline{I_{L2}} + \delta + \frac{1}{2}\Delta I_{L2}\right) t_f \cdot V_{C2} \cdot f_s$
Gate charge	$P_{GATE} = \frac{1}{2} V_{gate}{}^2 \cdot C_{gate} \cdot f_s$

3.4.3 Estimation of the converter efficiency

In order to estimate the efficiency of the converter, a MATLAB algorithm has been performed following the diagram in figure 3.24.

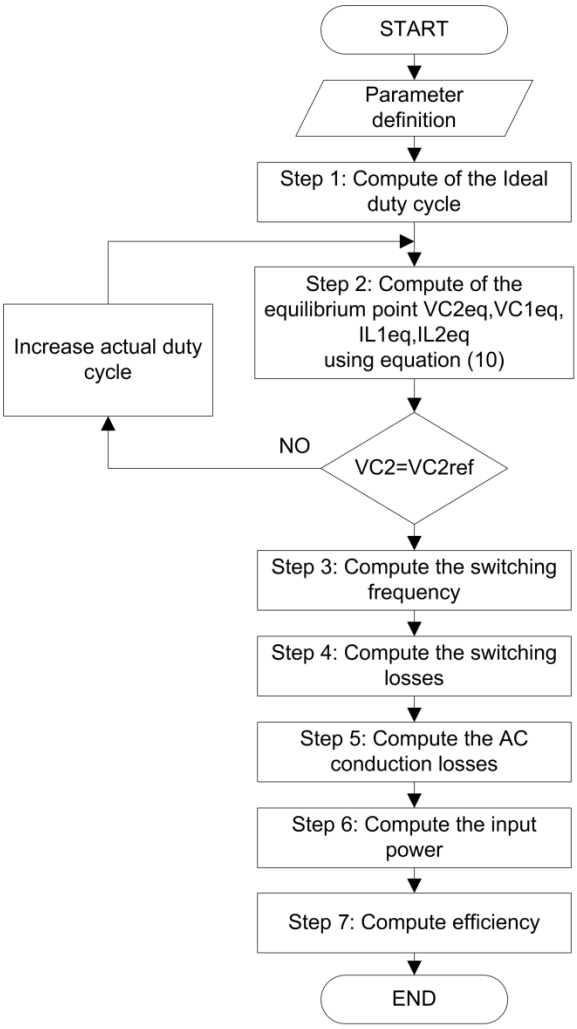

Fig. 3.24. Algorithm to estimate the efficiency of the quadratic boost converter.

The algorithm uses the model in (3.116) and the expressions to compute both conduction and switching losses (Tables 3.2 and 3.3). In step1, the ideal duty cycle is computed using only the input and output voltage (desired value). After that, using the loops with step 2, the algorithm computes the required duty cycle to obtain the desired output voltage with the voltage drops. At this point we have the average values of the converter variables. In steps 3 and 5 the conduction losses are evaluated. In step 4, the switching losses are computed involving the switching frequency which is calculated for each operational point using (3.118) [59].

$$f_s = \frac{1}{T_s} = \frac{V_i U}{2L_1\Delta} = \frac{V_i}{2L_1\Delta}\left(1 - \sqrt{\frac{V_i}{V_{C2}}}\right) \tag{3.118}$$

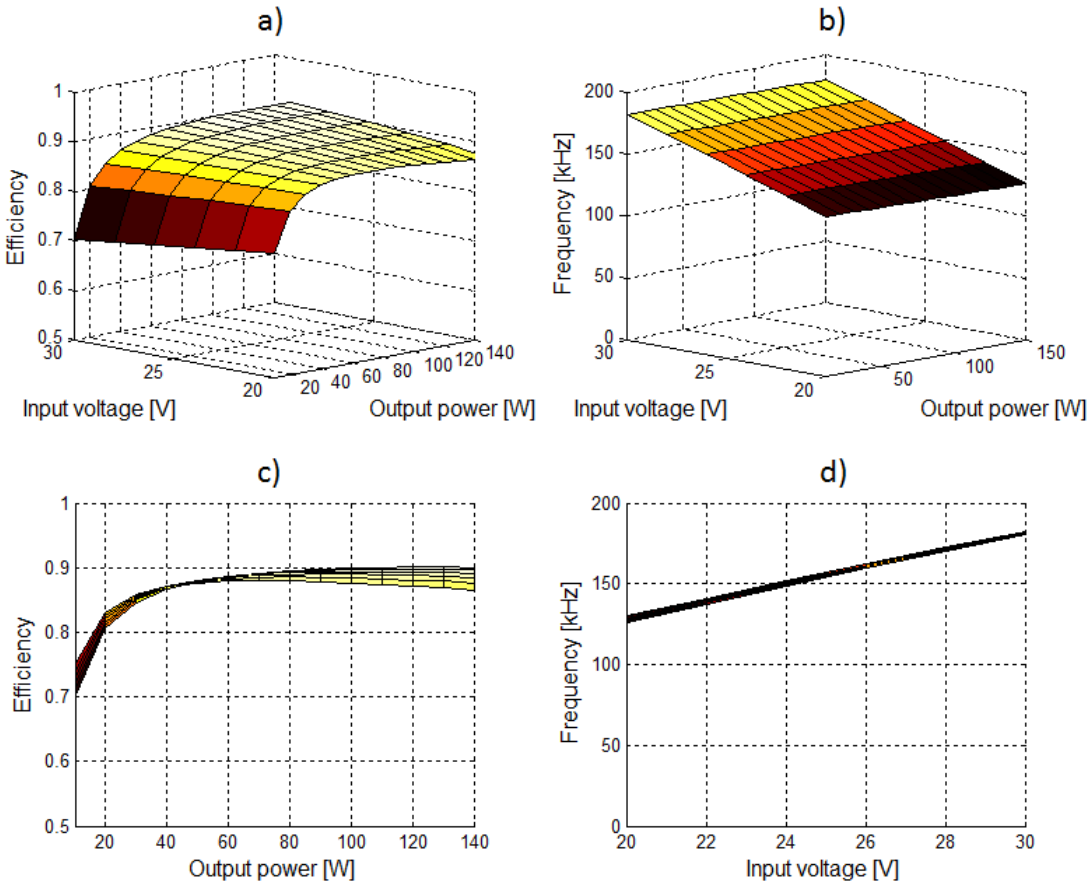

Fig. 3.25. Results of the efficiency prediction algorithm: a) Efficiency surface; b) Switching frequency surface; c) Efficiency as a function of the output load; d) Frequency as a function of the input voltage.

With the output power and the input power which is computed in step 6, it is possible to calculate the converter efficiency. This procedure is repeated for a complete set of operational conditions and the resulting data is represented graphically in figure 3.25 for the set of parameters listed in tables 3.4.

3.5 EXPERIMENTAL RESULTS

Several theoretical expressions have been derived to explain the static and dynamic characteristics of the quadratic boost converter as a competitive solution to cover the requirements of the DC-DC stage in a dual stage microinverter. Each of the different topics has been illustrated and verified through simulation results using specialized computational tools such as PSIM and MATLAB. The interest of this section is to highlight some topics directly related with the final application examining the behaviors induced by the use of sliding mode control.

3.5.1 Experimental set-up and converter prototype

A 100 W prototype of the quadratic boost converter has been implemented to work with an output voltage of 400 V. The input voltage is constrained between 20 and 30 V. The parameters of the converter are listed in table 3.4. The values of the passive elements have been selected to have low ripples on the inductance currents and the capacitor voltages [40], also considering the estimated limits of the frequency in all operational conditions. The conditions to ensure the continuous conduction mode in both inductors have been exceeded in order to provide an acceptable range to support transitory variation in variables. As will be observed in the results of the experimental validation, the design of the converter perfectly covers the stability conditions.

Table 3.4. Details of the power semiconductor used in the converter prototype

Element	Parameter	Symbol	Value
Inductor L1	Inductance	L_1	120 µH
	Equivalent Series Resistance (ESR)	R_{L1}	28 mΩ
Inductor L2	Inductance	L_2	4.7 mH
	Equivalent Series Resistance (ESR)	R_{L1}	1.14 Ω
Capacitors C1 and C2 (C4ATHBW4900A3LJ)	Capacitance	$C_{1,2}$	10 µF
	Equivalent Series Resistance (ESR)	$R_{C1,C2}$	1.9 mΩ
MOSFET (APT94N60L2C3)	Drain – Source ON-resistance	R_M	35 mΩ
	Rise time	t_r	27 ns
	Fall time	t_f	8 ns
	Gate voltage	V_{gate}	12 V
	Input capacitance	C_{gate}	13.6 nF
Diodes (C3D06060A)	Static forward voltage	R_{Dx}	0.75 V
	Series resistance	V_{Dx}	110 mΩ

The control circuit has been implemented using simple analog electronic circuits. The current reference is generated using an analog multiplier and simple conditioning circuits for the signal *G* and the input voltage v_p. The hysteresis comparator is implemented using two comparators and a flip-flop circuit obtaining the limits of the

hysteresis band from op-amp- based circuits. The driver of the power MOSFET is implemented using a totem-pole configuration. The schematic diagram of the circuit is depicted in figure 3.26.

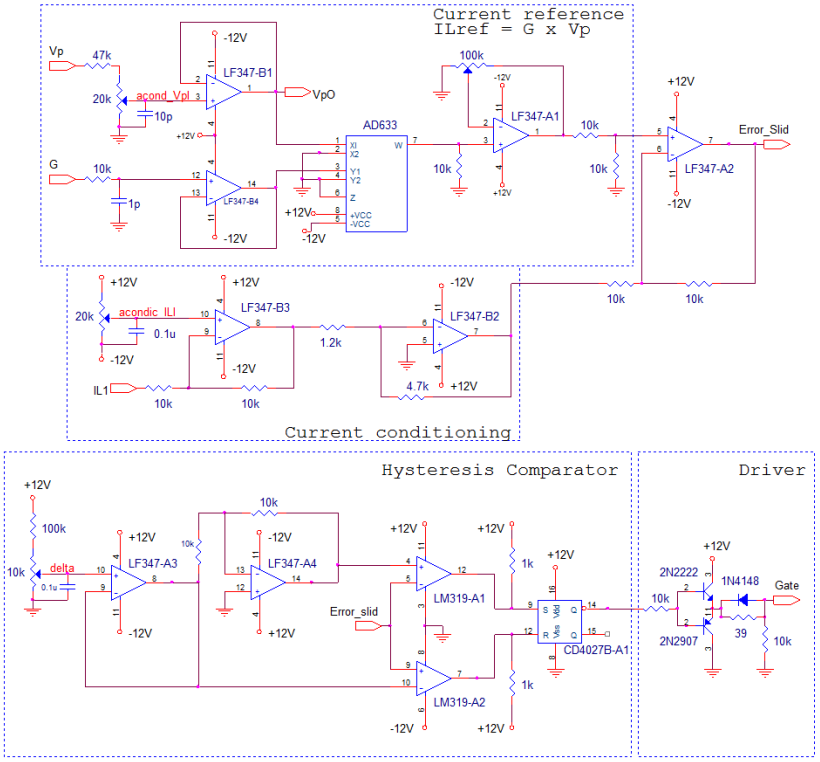

Fig. 3.26. Schematic circuit of the control board of the DC-DC converter

The set-up for measurements shown in figure 3.27 is composed of the oscilloscope MSO3014 from Tektronix, the current probes TCP202 and TCPA300 from Tektronix, power supplies Rohde & Schwartz NGSM 60/5 and Multimeteix XA3033, and multimeter HP34401A from Hewlett Packard.

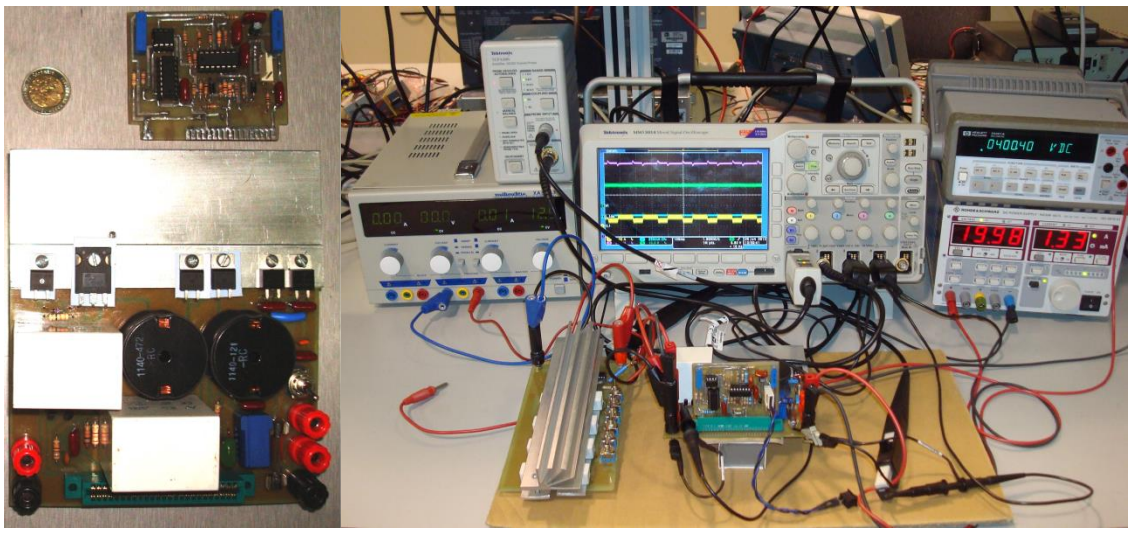
Fig. 3.27. Experimental set-up and converter prototype

3.5.2 Dynamical behavior tests

3.5.2.1 Changes in the input reference (conductance G)

Two different step changes are applied in order to observe the transient behavior of the converter working with conductance variations. In both cases the converter has a resistance of 4.58 kΩ as output load and is fed by a constant DC source of 20 V.

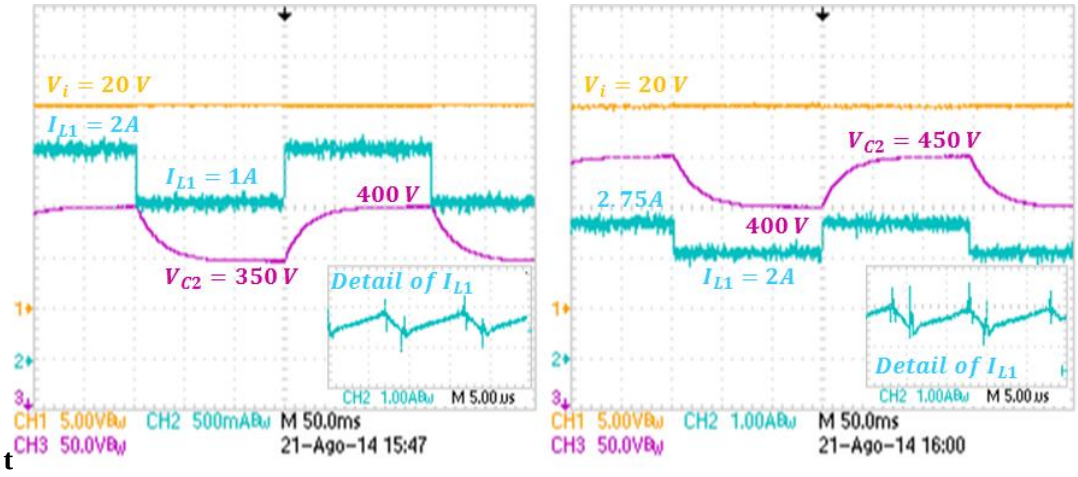

t Fig. 3.28. Oscilloscope waveforms of the output voltage and the input current when step type changes are introduced in the current reference: a) 400 V – 450 V – 400 V, b) 350 V – 400 V – 350 V.

The conductance signal is a square wave that allows 50 V changes in the output voltage. In the first test, which is shown in figure 3.28a, the output voltage changes from 350 to 400 V and vice versa. In the second case shown in figure 3.28b, the output voltage changes from 400 to 450 V and vice- versa. A first order response is observed with a time constant of approximately 150 ms.

3.5.2.2 Changes in the output current

Two different step changes are applied in order to observe the transient behavior of the converter working with output current variations. In both cases the converter is fed by a constant DC source of 20 V. A square wave signal is used to switch a resistive load connected to the output voltage thought a power MOSFET in such a way that the output resistance changes between 3.14 and 4.58 kΩ. In the first test shown in figure 3.29a, the conductance is adjusted to have the maximum output voltage aligned at 400 VDC. In the second case shown in figure 3.29b, the conductance is adjusted to have the minimum output voltage aligned at 400 VDC. A first order response is also observed in both cases with a time constant of approximately 110 ms.

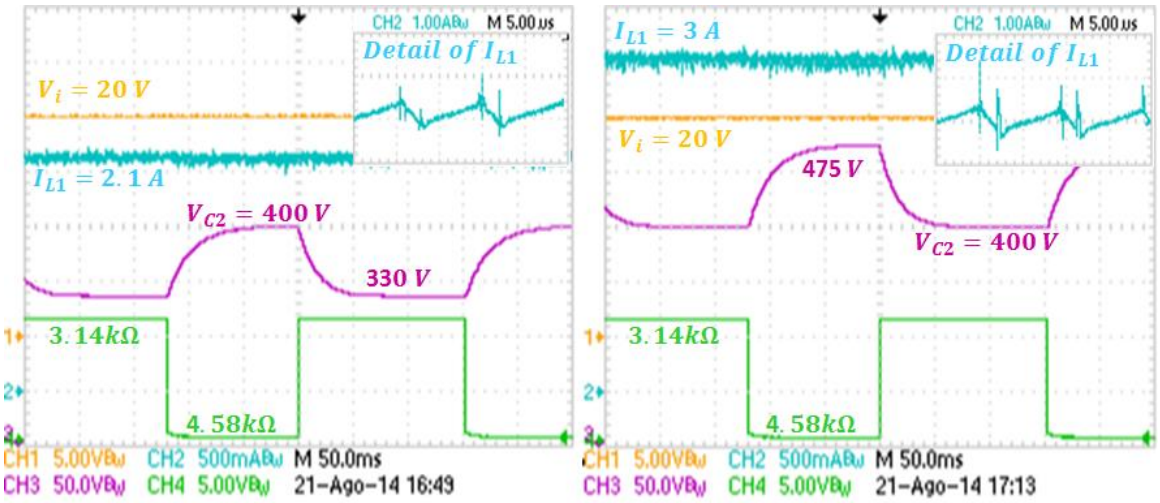

Fig. 3.29. Oscilloscope waveforms of the output voltage when step type changes are introduced in the output load: a) 400 V – 340 V – 400 V, b) 400 V – 470 V – 400 V.

3.5.2.3 Changes in the input voltage

Two different step changes are applied in order to observe the transient behavior of the converter working with input voltage variations. In both cases, the converter has a resistance of 4.58 kΩ as output load and a constant current reference of 2 A. Two DC sources are switched by means of a power relay and a fast recovery power diode employing a square wave signal that allows 5 V changes in the input voltage. In the first test shown in figure 3.30a, the input voltage changes from 15 to 20 V and vice-versa. In the second case shown in figure 3.30b, the input voltage changes from 20 to 25 V and vice- versa. A first order response is observed with a time constant of approximately 150 ms.

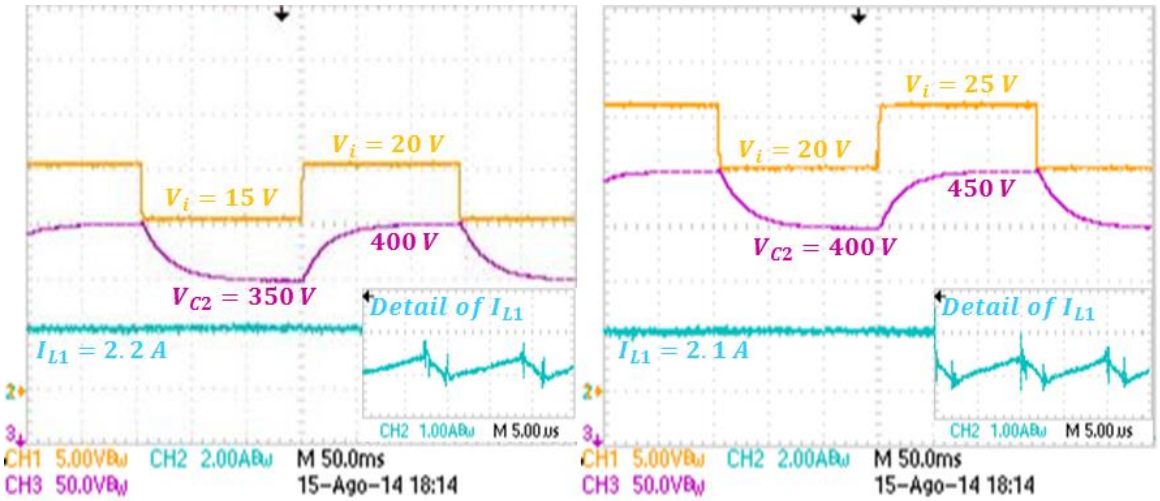

Fig. 3.30. Oscilloscope waveforms of the output voltage when step type changes are introduced in the input voltage: a) 400 V – 340 V – 400 V, b) 400 V – 470 V – 400 V.

3.5.3 Efficiency measurements

To test the efficiency of the converter, a control loop has been introduced in order to maintain regulated the output voltage as shown figure 3.31.

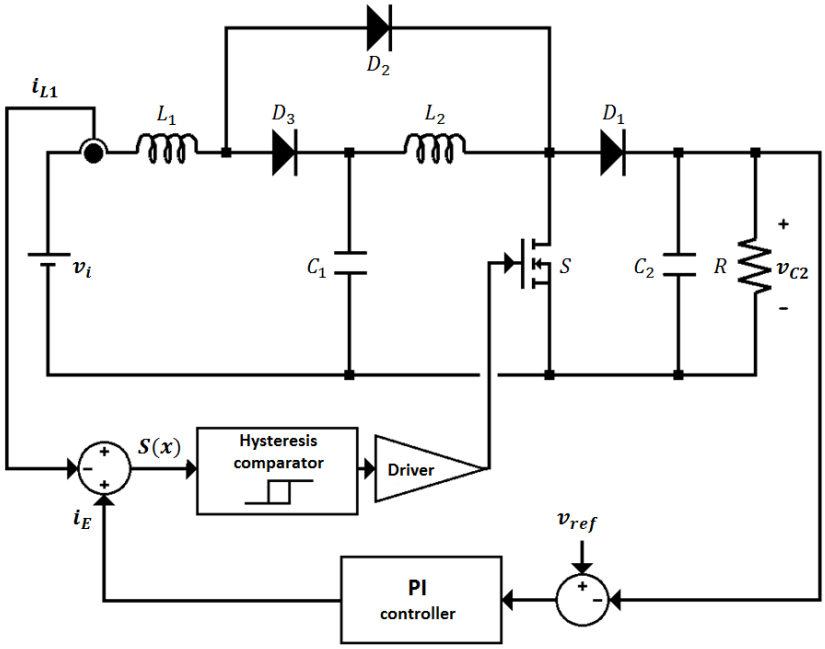

Fig. 3.31. Block diagram of the converter control used in the efficiency measurements

The outer control loop operates over the output voltage control error modifying the value of the current reference of the indirect sliding-mode control law. Values of 0.01 and 3 have been used for K_p and K_i respectively. The test evaluates the efficiency of the converter in an operational point with constant input voltage and constant output load. A complete operational range of input voltage and output load is covered with ranges from 20 to 30 V and from 20 to 100 W respectively.

As observed in figure 3.32, an efficiency surface is obtained. As expected from the simulated results with the prediction algorithm, a wide region of the operational range have similar efficiencies. A maximum efficiency of 93.1% is obtained at high loads (100 W) and high input voltages (30 V). The average efficiency is about 89 % which is more or less the efficiency at mid power levels. A minimum efficiency of 82% is identified at lower powers (20 W) and lower voltages (20 W). By using a lower input voltage such as 15 V, lower efficiencies around 75% are obtained.

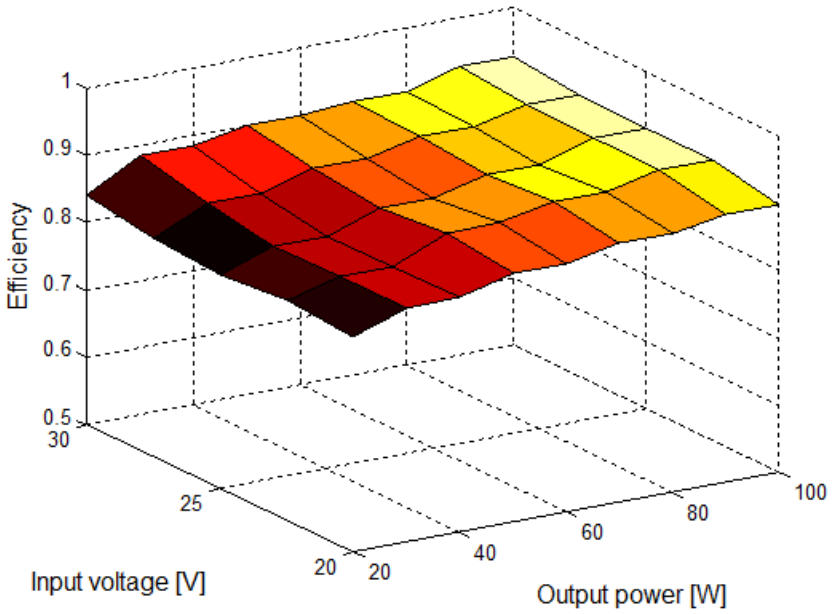

Fig. 3.32. Efficiency surface as a function of the input voltage and the output power (Parameters: $L_1 = 120\ \mu H, L_2 = 4.7\ mH, C_1 = C_2 = 10\ \mu F, R = 10\ k\Omega, V_o = 400\ V$)

3.6 CONCLUSIONS

A deep study of the conventional quadratic boost converter has been provided in this chapter. A comprehensive description of the converter as a variable structure system with all possible discontinuous conduction modes and the transitions between them has been developed. A theoretical analysis allows the derivation of the converter gains in each case.

Being central in this work, the case of the control of the quadratic boost converter operating in continuous conduction mode using a sliding mode indirect stabilization strategy has been particularly investigated. After linearizing the reduced model obtained by the equivalent control method, the main transfer functions of interest have been obtained and the resulting model has been validated. The associated stability analysis has been also developed in the context of the Lyapunov stability theory. The sliding mode indirect stabilization strategy has been particularly adopted for enforcing the converter to operate as a Loss Free Resistor, this playing a central role in the microinverter application here reported.

The chapter ends by an analysis of the converter efficiency controlled by sliding modes validating the approach. Through the chapter, the theoretical developments have been validated by simulations with PSIM and MATLAB, and by experimental implementations.

3.7 REFERENCES

Isolated topologies in module oriented converter applications

[1] LM5046, SM72295. Application Note 2116. SolarMagic ICs in Micro-Inverter Applications, Literature Number: SNVA471A, National Semiconductor, 2011.

[2] Application Note AN 1338. Grid-Connected Solar Microinverter Reference Design Using a dsPIC Digital Signal Controller, Literature Number: DS01338D, Microchip Technology Inc., 2011.

[3] Y. Xue, L. Chang, S.B. Kjaer, J. Bordonau, and T. Shimizu, "Topologies of Single-Phase Inverters for Small Distributed Power Generators: An Overview," IEEE Trans. Power Electron., vol. 19, no. 5, pp. 1305- 1314, Sep. 2014.

[4] M. Das and V. Agarwal, "PV Fed high efficiency, high voltage gain DC-DC converter for micro-inverter applications," IEEE 39th Photovoltaic Specialists Conference (PVSC), pp. 2862-2866, 16-21 June 2013.

[5] W-Y. Choi, and J-S.J. Lai, "High-Efficiency Grid-Connected Photovoltaic Module Integrated Converter System with High-Speed Communication Interfaces for Small-Scale Distribution Power Generation," Solar Energy, vol. 84, no. 4, pp. 639-649, 2010.

[6] Q. Li, and P. Wolfs, "A Review of the Single Phase Photovoltaic Module Integrated Converter Topologies with Three Different DC-Link Configurations," IEEE Trans. Power Electron., vol. 23, no. 3, pp. 1320-1333, May. 2008.

[7] J.-M. Kwon, B.-H. Kwon, and K.-H. Nam, "High-Efficiency Module-Integrated Photovoltaic Power Conditioning System," IET Power. Electron., vol. 2, no. 4, pp. 410-420, Mar. 2008.

[8] W. Li, J. Liu, J. Wu, X. He, "Design and Analysis of Isolated ZVT Boost Converters for High-Efficiency and High-Step-Up Applications," IEEE Trans. Power Electron., vol. 22, no. 6, pp. 2363-2374, Nov. 2007.

[9] T. Shimizu, K. Wada, and N. Nakamura, "Flyback-Type Single-Phase Utility Interactive Inverter with Power Pulsation Decoupling on the DC Input for an AC Photovoltaic Module System," IEEE Trans. Power Electron., vol. 21, no. 5, pp. 1264-1272, Sep. 2006.

[10] B.M.T. Ho, and H.S-H. Chung, "An Integrated Inverter with Maximum Power Point Tracking for Grid-Connected PV Systems," IEEE Trans. Power Electron., vol. 20, no. 4, pp. 953-962, Jul. 2005.

[11] S.B. Kjaer, J.K. Pedersen, and F. Blaabjerg, "A Review of Single-Phase Grid-Connected Inverters for Photovoltaic Modules," IEEE Trans. Ind. Applications, vol. 41, no. 5, pp. 1292-1306, Sep. 2005.

[12] T.J. Liang, and K.C. Tseng, "Analysis of Integrated boost-flyback step-up converter," IEE Proc. Electric. Power Applications, vol. 152, no. 2, pp. 217-225, Mar. 2005.

Transformer-less DC-DC converters

[13] L. Palma, M. Harfman Todorovic, P. Enjeti, "A High Gain Transformer-Less DC-DC Converter for Fuel-Cell Applications," in proc. of the 36th IEEE Power Electron. Specialists Conf. (PESC), pp. 2514-2520, 16-16 Jun. 2005.

Other applications

[14] X. Zhang, H. Ren, S. Pyo, J. Lee, J. Kim and J. Chae, "A High Efficiency DC-DC Boost Converter for a Miniaturized Microbial Fuel Cell," IEEE Trans. Power Electron., vol. PP, no. 99, pp. 1-1, 2014.

[15] M. Das and V. Agarwal, "A novel, high efficiency, high gain, front end DC-DC converter for low input voltage solar photovoltaic applications," 38th Annual Conf. on IEEE Ind. Electron. Society (IECON), pp. 5744-5749, 25-28 Oct. 2012.

[16] W-Y. Choi, J-S. Yoo and J-Y. Choi, "High efficiency dc-dc converter with high step-up gain for low PV voltage sources," IEEE 8th Int. Conf. on Power Electron. and ECCE Asia (ICPE & ECCE), pp. 1161-1163, Jun. 3 2011.

[17] R-J. Wai and C-Y. Lin, "High-efficiency, high-step-up DC-DC convertor for fuel-cell generation system," IEE Proc. Electric. Power Applications, vol. 152, no. 5, pp. 1371-1378, 9 Sept. 2005.

Review of transformer-less DC-DC topologies

[18] D. Meneses, F. Blaabjerg, O. García, J.A. Cobos, "Review and Comparison of Step-Up Transformerless Topologies for Photovoltaic AC-Module Application," IEEE Trans. Power Electron., vol. 28, no. 6, pp. 2649-2663, Jun. 2013.

[19] W. Li, X. Lv, Y. Deng, J. Liu, X. He, "A Review of Non-Isolated High Step-Up DC/DC Converters in Renewable Energy Applications," in proc. of the 24th Annual IEEE Applied Power Electron. Conf. and Exposition (APEC), pp. 364-369, 15-19 Feb. 2009.

[20] L-S. Yang, T-J. Liang, J-F. Chen, "Transformerless DC–DC Converters with High Step-Up Voltage Gain," IEEE Trans. Ind. Electron., vol. 56, no. 8, pp. 3144-3152, Aug. 2009.

Coupled-inductors

[21] L-S. Yang, T-J. Liang, H-C. Lee, J-F. Chen, "Novel High Step-Up DC–DC Converter With Coupled-Inductor and Voltage-Doubler Circuits," IEEE Trans. Ind. Electron., vol. 58, no. 9, pp. 4196-4206, Sept. 2011.

[22] S. Dwari, L. Parsa, "An Efficient High-Step-Up Interleaved DC–DC Converter with a Common Active Clamp," IEEE Trans. Power Electron., vol. 26, no. 1, pp. 66-78, Jan. 2011.

[23] Y-P. Hsieh, J-F. Chen, T-J. Liang, L-S. Yang, "A Novel High Step-Up DC–DC Converter for a Microgrid System," IEEE Trans. Power Electron., vol. 26, no.4, pp. 1127-1136, Apr. 2011.

[24] K-B. Park, G-W. Moon, M-J. Youn, "Nonisolated High Step-up Boost Converter Integrated With SEPIC Converter," IEEE Trans. Power Electron., vol. 25, no. 9, pp. 2266-2275, Sept. 2010.

[25] S-K. Changchien, T.-J.Liang, J-F. Chen, L-S. Yang, "Novel High Step-Up DC–DC Converter for Fuel Cell Energy Conversion System," IEEE Trans. Ind. Electron., vol. 57, no. 6, pp. 2007-2017, Jun. 2010.
[26] R-J. Wai, C-Y. Lin, R-Y. Duan , and Y-R . Chang, "High efficiency DC-DC converter with high voltage gain and reduced switch stress" IEEE Trans. Ind. Electron., vol. 54. no. 1, pp. 354-364, Feb. 2007.
[27] R-J Wai, R.Y. Duan, "High-efficiency DC/DC converter with high voltage gain," IEE Proc. Electric. Power Applications, vol. 152, no. 4, pp. 793-802, Jul. 2005.
[28] R-J. Wai, R-Y Duan, "High step-up converter with coupled-inductor," IEEE Trans. Power Electron., vol. 20, no. 5, pp. 1025-1035, Sept. 2005.
[29] K.C. Tseng, and T.J. Liang, "Novel high-efficiency step-up converter," IEE Proc. Electric. Power Applications, vol. 151, no.2, pp.182-190, Mar. 2004.

Switched capacitors

[30] O. Abutbul, A.Gherlitz, Y.Berkovich, and A. Ioinovici, "Step-up switching-mode converter with high voltage gain using a switched –capacitor circuit "IEEE Trans. Circuits and Syst.-Part I, vol. 50, no. 8, pp. 1098-1102, 2003.
[31] B. Axelrod, Y. Berkovich, A. Ioinovici, "Transformerless DC-DC converters with a very high DC line-to-load voltage ratio," in proc. of the Int. Symp. On Circuits and Systems, (ISCAS), vol. 3, pp. 435- 438, 25-28 May 2003.

Multiplied Cells

[32] F.H. Dupont, C. Rech, R. Gules and J.R. Pinheiro, "Reduced-order model and control approach for the boost converter with a voltage multiplier cell," IEEE Trans. Power Electron., vol. 28, no. 7, pp. 3395-3404, Jul. 2013.
[33] S. Lee, P. Kim and S. Choi, "High step-up soft-switched converters using voltage multiplier cells," IEEE Trans. Power Electron., vol. 28, no. 7, pp. 3379-3387, Jul. 2013.

Adding resonant circuits

[34] H. Athab, A. Yazdani, B. Wu, "A transformer-Less DC-DC converter with large voltage transformation ratio for medium-voltage DC grid applications," in proc. of the IEEE Power and Energy Society General Meeting (PES), pp. 1-5, 21-25 July 2013.

Other circuits

[35] J.C. Rosas-Caro, F. Mancilla-David, J.C. Mayo-Maldonado, J.M. Gonzalez-Lopez, H.L. Torres-Espinosa, J.E. Valdez-Resendiz, "A Transformer-less High-Gain Boost Converter With Input Current Ripple Cancelation at a Selectable Duty Cycle," IEEE Trans. Ind. Electron., vol. 60, no. 10, pp. 4492-4499, Oct. 2013.
[36] E.H. Ismail, M.A. Al-Saffar, A.J. Sabzali, A.A. Fardoun, "A Family of Single-Switch PWM Converters With High Step-Up Conversion Ratio," IEEE Trans. Circuits and Systems I: Regular Papers, vol. 55, no. 4, pp. 1159-1171, May 2008.
[37] Q. Zhao, F.C. Lee, "High-efficiency, high step-up DC-DC converters," IEEE Trans. Power Electron., vol. 18, no. 1, pp. 65-73, Jan. 2003.

Floating output

[38] S. Choi, V.G. Agelidis, J. Yang, D. Coutellier, P. Marabeas, "Analysis, design and experimental results of a floating-output interleaved-input boost-derived DC-DC high-gain transformer-less converter," IET Power Electron., vol. 4, no. 1, pp.168-180, Jan. 2011.
[39] D. Coutellier, V.G. Agelidis, S. Choi, "Experimental verification of floating-output interleaved-input DC-DC high-gain transformer-less converter topologies," in proc. of the Power Electronics Specialists Conference (PESC), pp. 562-568, 15-19 June 2008.

Description of boost converter and comparison with other common topologies

[40] R.W. Erickson, and D. Maksimovic, Fundamentals of power electronics, 2th. Edition. Massachussetts: Kluwer Academic Publishers, 2000.
[41] G.R. Walker and P.C. Sernia, "Cascaded DC-DC converter connection of photovoltaic modules", IEEE Trans. Power Electron., 2004, vol. 19, no. 4, pp. 1130- 1139.

Cascaded connection of converters

[42] H. Matsuo and K. Harada, "The cascade connection of switching regulators", IEEE Trans. Indust. Applic. vol .3, no 2, pp. 192-198, Mar. 1976.
[43] D. Maksimovic, S. Cuk, "Switching converters with wide DC conversion range," IEEE Trans. Power Electron., vol. 6, no. 1, pp.151-157, Jan. 1991.
[44] R. Haroun, A. El Aroudi, A. Cid-Pastor, L. Martinez-Salamero, "Sliding Mode Control of output-parallel-connected two-stage boost converters for PV systems," in proc. of the 11th Int. Multi-Conf. on Systems, Signals & Devices (SSD), pp. 1-6, 11-14 Feb. 2014.
[45] R. Haroun, A. Cid-Pastor, A. El Aroudi and L. Martinez-Salamero, "Synthesis of Canonical Elements for Power Processing in DC Distribution Systems Using Cascaded Converters and Sliding-Mode Control," IEEE Trans. Power Electron., vol. 29, no. 3, pp. 1366-1381, Mar. 2014.
[46] M. Delshad, S. Mohammadi, S. Moosavi, "A new cascaded high step-up DC-DC converter," in proc. of the 9th Int. Conf. on Electrical Engineering, Electron., Computer, Telecom. and Information Technology (ECTI-CON), pp. 1-4, 16-18 May 2012.
[47] S-M. Chen; T-J. Liang; L-S. Yang, J-F. Chen, "A Cascaded High Step-Up DC–DC Converter With Single Switch for Microsource Applications," IEEE Trans. Power Electron., vol. 26, no. 4, pp. 1146-1153, Apr. 2011.
[48] M. Aamir and M.Y. Shinwari, "Design, implementation and experimental analysis of two-stage boost converter for grid connected photovoltaic system," in Proc. IEEE Int. Conf. on Computer Science and Information Technology (ICCSIT), pp. 194-199, Jul. 2010.

Cascade connection with single-switch

[49] M.G. Ortiz-Lopez, J. Leyva-Ramos, E.E. Carbajal-Gutierrez, and J.A. Morales-Saladaña, "Modeling and analysis of switch –mode cascade converters with a single active switch", IET Power Electron., 2008, vol. 1, no. 4, pp. 478-487.

Control of the quadratic boost

[50] O. Lopez-Santos, L. Martinez-Salamero, G. Garcia, H. Valderrama-Blavi, T. Sierra-Polanco, "Robust Sliding-Mode Control Design for a Voltage Regulated Quadratic Boost Converter," IEEE Trans. Power Electron., DOI: 10.1109/TPEL.2014.2325066, vol. 30, no. 4, pp. 1-15.

[51] J. Leyva-Ramos, M.G. Ortiz-Lopez, L.H. Diaz-Saldierna and J.A. Morales-Sandaña, "Switching regulator using a quadratic boost converter for wide DC conversion ratios", IET Power Electronics, 2009, vol. 2, no. 5, pp. 605-613.

[52] J.A. Morales-Saldaña, R. Loera-Palomo, E. Palacios-Hernández, J.L. González-Martínez, "Modelling and control of a DC-DC quadratic boost converter with R2P2," IET Power Electronics, vol. 7, no. 1, pp. 11-22, Jan. 2014.

[53] P. Yang, J. Xu, G. Zhou, F. Zhang, "Analysis of sensorless peak current mode controlled quadratic boost converter," in proc. of the IEEE Int. Symposium on Ind. Electron. (ISIE), pp. 200-204, 28-31 May 2012.

[54] J.A. Morales-Saldana, R. Galarza-Quirino, J. Leyva-Ramos, E. Carbajal-Gutierrez, M.G. Ortiz-Lopez, "Multiloop controller design for a quadratic boost converter," IET Electric Power Appl., vol. 1, no. 3, pp. 362-367, May 2007.

[55] J. Leyva-Ramos, M.G. Ortiz-Lopez, L.H. Diaz-Saldierna, "The effect of ESR of the capacitors on modeling of a quadratic boost converter," in proc. of the 11th Workshop on Control and Modeling for Power Electron. (COMPEL), pp. 1-5, 17-20 Aug. 2008.

[56] M. Hernandez-Gomez, R. Ortega, F. Lamnabhi-Lagarrigue, O. Bethoux, G. Escobar, "Robust adaptive PI stabilization of a quadratic converter: Experimental results," in proc. of the IEEE Int. Symposium on Ind. Electron. (ISIE), pp. 2999-3004, 4-7 July 2010.

[57] J.A. Morales-Saldaña, R. Galarza-Quirino, J. Leyva-Ramos, E.E. Carbajal-Gutierrez and M.G. Ortiz-Lopez, "Multiloop controller design for a quadratic boost converter," IET Elect. Power Appl., vol. 1, no. 3, pp. 362-367, May. 2007.

[58] J.A. Morales-Saldaña, R. Loera-Palomo, E. Palacios-Hernández and J.L. González-Martínez, "Modelling and control of a DC-DC quadratic boost converter with R2P2," IET Power Electron., vol. 7, no. 1, pp. 11-,22, Jan. 2014.

Analysis of efficiency of the quadratic boost

[59] O. Lopez-Santos, L. Martinez-Salamero, G. Garcia, H. Valderrama-Blavi and D.O. Mercuri, "Efficiency analysis of a sliding-mode controlled quadratic boost converter," IET Power Electron., vol. 6, no. 2, pp. 364-373, Feb. 2013.

Improving the efficiency of the quadratic boost

[60] L.H. Barreto, E.A. Coelho, V.J. Farias, J.C. de Oliveira, L.C. de Freitas, J.B. Vieira, "A quasi-resonant quadratic boost converter using a single resonant network," IEEE Trans. Ind. Electron., vol. 52, no. 2, pp. 552-557, Apr. 2005.

[61] L. Sousa Vilefort, W. Gomes Silva, D. Alves de Andrade, F. Vincenzi Romualdo da Silva, L.C. de Freitas, E.A. Coelho, J.B. Vieira, "Quadratic boost converter using a soft single switch," in proc. of the Brazilian Power Electron. Conf. (COBEP), pp. 44-49, 27-31 Oct. 2013.

[62] P. Yang, J. Xu, G. Zhou, S. Zhang, "A new quadratic boost converter with high voltage step-up ratio and reduced voltage stress," in proc. of the 7th Int. Power Electron. and Motion Control Conf. (IPEMC), vol. 2, pp. 1164-1168, 2-5 Jun. 2012.

[63] Y-M. Ye, K.W.E. Cheng, "Quadratic boost converter with low buffer capacitor stress," IET Power Electron., vol. 7, no. 5, pp. 1162-1170, May 2014.

[64] M.A. Al-Saffar, E.H. Ismail, A.J. Sabzali, "High efficiency quadratic boost converter," in proc. of the 27th Annual IEEE Applied Power Electronics Conference and Exposition (APEC), pp. 1245-1252, 5-9 Feb. 2012.

Adding circuits to the quadratic boost converter

[65] F.L. Tofoli, A.E. Demian, C.A. Gallo, F.R. Vincenzi, E.A. Coelho, L.C. de Freitas, V.J. Farias, J.B. Vieira, "Proposal of a switched mode power supply employing a quadratic boost converter and a new topology of soft-switched two-switch forward converter," in proc. of the 19th Annual IEEE Applied Power Electronics Conference and Exposition, vol. 3, pp. 1384-1388, 2004.

[66] Y-S. Lee; Z-H. Chou; S-S. Huang; S-Y. Huang, "Quadratic boost converter with switched capacitor and coupled inductor for PV system applications," in proc. of the 10th Int. Conf. on Power Electron. and Drive Systems (PEDS), pp. 38-43, 22-25 Apr. 2013.

[67] L.H. Barreto, E.A. Coelho, V.J. Farias, L.C. de Freitas, J.B. Vieira, "A quasi-resonant quadratic boost converter using a single resonant network," in proc. of the 34th Annual IEEE Power Electron. Specialist Conf. (PESC), vol. 2, pp. 595-599, 15-19 Jun. 2003.

[68] F.L. Tofoli, C.A. Gallo, E.A. Coelho, L.C. de Freitas, V.J. Farias, J.B. Vieira, "A switched-mode power supply employing a quadratic boost converter and a soft-switched two-switch forward converter," in proc. of the IEEE 35th Annual Power Electron. Specialists Conf. (PESC), vol. 4, pp. 2611-2614, 2004.

[69] P. Agarwal, R.K. Singh, "A modular magnetically coupled quadratic boost converter for microsource applications," in proc. of the 7th IET Int. Conf. on Power Electron., Machines and Drives (PEMD), pp. 1-5, 8-10 April 2014.

[70] S. Zhang, J. Xu, P. Yang, "A single-switch high gain quadratic boost converter based on voltage-lift-technique," in proc. of the Conference on Power & Energy (IPEC), pp. 71-75, 12-14 Dec. 2012.

Quadratic boost converter topologies

[71] R. Kadri, J-P. Gaubert, G. Champenois, M. Mostefai. "Performance Analysis of Transformless Single Switch Quadratic Boost Converter for Grid Connected Photovoltaic Systems," in proc. of the XIX International Conference on Electrical Machines (ICEM). pp. 1-7. 2010.

[72] D. Lascu, M. Lascu, I. Lie, M. Tanase. "A new Quadratic Boost Converter with PFC Applications," in proc. of the 10th WSEAS International Conference on Circuits. pp. 223-228. 2006.

[73] O. Lopez-Santos, L. Martinez-Salamero, G. Garcia, H. Valderrama-Blavi, T. Sierra-Polanco, "Comparison of quadratic boost topologies operating under sliding-mode control," in proc. of the Brazilian Power Electronics Conference (COBEP), pp. 66-71, 27-31 Oct. 2013.

Sliding-mode control

[74] J.A. Barrado, A. El Aroudi, H. Valderrama-Blavi, J. Calvente and L. Martínez-Salamero, "Analysis of a Self-Oscillating Bidirectional DC-DC Converter in Battery Energy Storage Applications", IEEE Trans. Power Delivery, vol. 27, no. 3, pp. 1292-1300, 2012.

[75] A. Kavitha and G. Uma, "Comparative study between peak current mode and hysteretic current mode control of a single-ended primary inductance converter," IET Power Electron., vol. 5, no. 7, pp. 1226-1235, Aug. 2012.

[76] E. Mamarelis, G. Petrone and G. Spagnuolo, "Design of a Sliding-Mode-Controlled SEPIC for PV MPPT Applications," IEEE Trans. Industrial Electronics, vol. 61, no. 7, pp. 3387-3398, Jul. 2014.

[77] Z. Chen, "PI and Sliding Mode Control of a Cuk Converter," IEEE Trans. Power Electron., vol. 27, no. 8, pp. 3695-3703, Aug. 2012.

[78] P.K. Singh, Y.V. Hote, M.M. Garg, "Comments on "PI and sliding mode control of a Cûk converter"," IEEE Trans. Power Electron., vol. 29, no. 3, pp. 1551-1552, Mar. 2014.

[79] H. Sira-Ramirez and M. Rios-Bolivar, "Sliding mode control of DC-to-DC power converters via extended linearization," IEEE Trans. Circuits and Systems I: Fundamental Theory and Appl., vol. 41, no. 10, pp. 652-661, Oct 1994.

[80] H. Sira-Ramirez, "Sliding motions in bilinear switched networks," IEEE Trans. Circuits and Systems, vol. 34, no. 8, pp. 919-933, Aug. 1987.

[81] P. Mattavelli, L. Rossetto and G. Spiazzi, "Small-signal analysis of DC-DC converters with sliding mode control," IEEE Trans. Power Electron., vol. 12, no. 1, pp. 96-102, Jan. 1997.

[82] S.-C. Tan; Y.M. Lai and C.K. Tse, "General Design Issues of Sliding-Mode Controllers in DC–DC Converters," IEEE Trans. Ind. Electron., vol. 55, no. 3, pp. 1160-1174, Mar. 2008.

[83] Y. He and F.L. Luo, "Sliding-mode control for dc-dc converters with constant switching frequency," IEE Proc. Control Theory and Appl. vol. 153, no. 1, pp. 37-45, 16 Jan. 2006.

[84] S-C. Tan, Y.M. Lai and C.K. Tse, "A unified approach to the design of PWM-based sliding-mode voltage controllers for basic DC-DC converters in continuous conduction mode," IEEE Trans. Circuits and Systems I: Regular Papers, vol. 53, no. 8, pp. 1816-1827, Aug. 2006.

[85] S-C. Tan; Y.M. Lai, C.K. Tse and M.K.H. Cheung, "Adaptive feedforward and feedback control schemes for sliding mode controlled power converters," IEEE Trans. Power Electron., vol. 21, no. 1, pp. 182-192, Jan. 2006.

[86] L. Martinez-Salamero, G. Garcia, M. Orellana, C. Lahore and B. Estibals, "Start-up control and voltage regulation in a boost converter under sliding-mode operation," IEEE Trans. Ind. Electron., vol. 60, no. 10, pp. 4637-4649, Oct. 2013.

[87] L. Martínez-Salamero, G. García, M. Orellana, C. Lahore, B. Estibals, C. Alonso, C.E. Carrejo, "Analysis and design of a sliding-mode strategy for start-up control and voltage regulation in a buck converter," IET Power Electron., vol. 6, no. 1, pp. 52-59, Jan. 2013.

[88] E. Vidal-Idiarte, L. Martinez-Salamero, F. Guinjoan, J. Calvente and S. Gomariz, "Sliding and fuzzy control of a boost converter using an 8-bit microcontroller," IEE Proc. Electric Power Applications, vol. 151, no. 1, pp. 5-11, 9 Jan. 2004.

[89] E. Mamarelis, G. Petrone and G. Spagnuolo, "A Hybrid Digital-Analog Sliding Mode Controller for Photovoltaic Applications," IEEE Trans. Ind. Informatics, vol. 9, no. 2, pp. 1094-1103, May. 2013.

[90] M. Lopez, L.G. de Vicuna, M. Castilla, P. Gaya and O. Lopez, "Current distribution control design for paralleled DC/DC converters using sliding-mode control," IEEE Trans. Ind. Electron., vol. 51, no. 2, pp. 419-428, Apr. 2004

[91] R. Giral, L. Martinez-Salamero, R. Leyva and J. Maixe, "Sliding-mode control of interleaved boost converters," IEEE Trans. Circuits and Systems I: Fund. Theory and Appl., vol. 47, no. 9, pp. 1330-1339, Sep 2000.

Loss-Free-Resistor

[92] S. Singer, R.W. Erickson, "Canonical modeling of power processing circuits based on the POPI concept," IEEE Trans. Power Electron., vol. 7, no. 1, pp. 37-43, Jan. 1992.

[93] S. Singer, "Realization of loss-free resistive elements," IEEE Trans. Circuits and Systems, vol. 37, no. 1, pp. 54-60, Jan. 1990.

[94] S. Singer, "The application of `loss-free resistors' in power processing circuits," in proc. of the 20th Annual IEEE Power Electronics Specialists Conference, pp. 843-846 vol. 2, 26-29 Jun. 1989.

[95] S. Singer, S. Ozeri and D. Shmilovitz, "A pure realization of loss-free resistor," IEEE Trans. Circuits and Systems I: Regular Papers, vol. 51, no. 8, pp. 1639-1647, Aug. 2004.

[96] A. Cid-Pastor, L. Martinez-Salamero, N. Parody and AE. Aroudi, "Analysis and design of a loss-free resistor based on a boost converter in PWM operation," in proc. of the IEEE International Symposium on Circuits and Systems (ISCAS), pp. 2742-2745, May 30 2010.
[97] A. Cid-Pastor, L. Martinez-Salamero, A. El Aroudi, R. Giral, J. Calvente, R. Leyva, "Synthesis of loss-free-resistors based on sliding-mode control and its applications in power processing," Control Engineering Practice, vol. 21 no. 5 pp. 689-699. May. 2013.
[98] A. Marcos-Pastor, E. Vidal-Idiarte, A. Cid-Pastor and L. Martinez-Salamero, "Digital Loss-Free Resistor for power factor correction applications," in proc. of the 39th Annual Conf. of the IEEE Ind. Electron. Society (IECON) pp. 3468-3473, 10-13 Nov. 2013.
[99] A. Marcos-Pastor, E. Vidal-Idiarte, A. Cid-Pastor and L. Martinez-Salamero, "Synthesis of a sliding loss-free resistor based on a semi-bridgeless boost rectifier for power factor correction applications," in proc. of the 39th Annual Conference of the IEEE Industrial Electronics Society, pp. 1343-1348, 10-13 Nov. 2013.
[100] D.G. Lamar, M. Arias, M.M. Hernando and J. Sebastian, "Using the loss-free resistor concept to design a simple ac-dc HB-LED driver for retrofit lamp applications," in proc. of the 29th Annual IEEE Applied Power Electron. Conf. and Exposition (APEC), pp. 117-124, 16-20 March 2014.
[101] M. Bodetto, A. El Aroudi, A. Cid-Pastor, J. Calvente and L. Martínez-Salamero, "Sliding Mode Control of a Ćuk converter with variable hysteresis width for HBLEDs applications," in proc. of the 11th Int. Multi-Conf. on Systems, Signals & Devices (SSD), pp. 1-6, 11-14 Feb. 2014.
[102] M. Bodetto, A. Cid-Pastor, L. Martinez-Salamero and A. El-Aroudi, "Design of an LFR based on a SEPIC converter under sliding mode control for HBLEDs applications," in proc. of the IEEE Int. Symposium on Circuits and Systems (ISCAS), pp. 2901-2904, 15-18 May 2011
[103] R. Haroun, A. El Aroudi, A. Cid-Pastor, G. Garcia, C. Olalla and L. Martinez-Salamero, "Impedance Matching in Photovoltaic Systems Using Cascaded Boost Converters and Sliding-Mode Control," IEEE Trans. Power Electron, vol. PP, no. 99, pp. 1-1, 2014.
[104] R. Haroun, A. El Aroudi, A. Cid-Pastor, L. Martinez-Salamero, "Sliding Mode Control of output-parallel-connected two-stage boost converters for PV systems," in proc. of the 11th Int. Multi-Conf. on Systems, Signals & Devices (SSD), pp. 1-6, 11-14 Feb. 2014.

Indirect stabilization

[105] O. Lopez-Santos, L. Martinez-Salamero, G. Garcia, H. Valderrama-Blavi, "Sliding-mode indirect control of the quadratic boost converter operating in continuous conduction mode or discontinuous conduction mode," in proc. of the IEEE 4th Colombian Workshop on Circuits and Systems (CWCAS), pp. 1-6, 1-2 Nov. 2012.
[106] H. Sira-Ramirez, "On the Generalized PI Sliding Mode Control of DC-to-DC Power Converters: A Tutorial," Int. Journal of Control, vol. 76, no. 9-10, pp. 1018-1033, 2003.

Books

[107] H. Sira-Ramirez and R. Silva-Ortigoza, Control Design Techniques in Power Electronic Devices, 1th. Edition. Germany: Springer, 2006.
[108] V.I. Utkin, J. Guldner and J. Shi, Sliding mode control in electromechanical systems, CRC Press, 2th. Edition, Taylor and Francis Group, 2009.
[109] F. Golnaraghi and B.C. Kuo, Automatic Control Systems, 9th Edition USA: John Wiley and Sons, 2010.

Stability

[110] J.P. LaSalle, "The stability of Dynamical Systems," In proc. of the Regional Conference Series in Applied Mathematics, vol. 25, 1976.

Chapter 4

DC-AC stage:
Full-Bridge Power Source Inverter

4.1 INTRODUCTION

As introduced in chapter 1, many converter topologies can be used to accomplish the grid-connection objective [1]-[6]. The selection of an appropriate topology is determinant for efficiency, dynamic performance, reliability and power density. Nowadays, the use of a low frequency transformer to give isolation and to boost the voltage at the AC side is less and less considered because of the size and cost of the transformer [7]. This fact has put in evidence the advantages of topologies with high frequency transformers based on the fly-back converter [8]-[13], or the push-pull converter [14]-[15]. However, at low power levels, it is not necessary to have an isolation, which motivates the use of transformer-less topologies [16]-[21] without ignoring the advantages to use an isolation transformer. Among these, the multilevel inverters and the cascade connection of inverters have been recently proposed in single-phase applications improving power quality aspects [22]-[28]. Also, it is worth to note that many of the existing topologies use one or more full-bridge inverters or a slight variation, this justifying our interest for this kind of structure.

On the other hand, it is possible to classify the grid-connected inverters in topologies involving DC-Link, pseudo DC-Link or no DC-Link as it is described and studied in [29]. These topologies can be distinguished not only from the configuration of the converter but also from the control strategy. Since the control applied to the DC-DC stage of the microinverter enforces a power source with an unregulated DC voltage to feed the DC-AC stage, the full bridge inverter is controlled by a sliding mode control strategy which in addition regulates the voltage of the DC link.

The full bridge converter connected to the grid can be used as either a power conditioner or a grid-tied inverter. Having in mind that in both cases the grid voltage is not a controlled variable but it is constant, then, the energy flow is fixed by the current delivered by the converter. The connection between the converter and the grid is done using a passive array such as L, CL, LC, LCL networks and hence the control objective consists on enforcing a desired value for the current of this coupling element [30]. In power conditioning, the inverter contributes totally or partially to both distortion and reactive power and has to prevent that the corresponding components circulate through the electrical networks. The control must generate a corresponding current reference to compensate the harmonics, the reactive power and the power losses. In this application, the DC side is only connected to a capacitive storage element (not to a load or a source) whose voltage is regulated to ensure power balance in the converter [31]-[33]. On the other hand, the grid-tied inverter converts a certain amount of power available at the DC side injecting it in the grid [34]-[36]. As a grid-connected inverter, the full-bridge shows a buck behaviour and hence it must be ensured that the voltage of the DC link be always higher that the peak value of the grid voltage.

The control of a grid-connected inverter requires the generation of a proper current reference and a way to robustly track it. To generate this reference it is necessary to measure the frequency and phase of the grid voltage which can be extracted either directly using the grid voltage signal or indirectly using a synchronization system. Among these two possibilities, the more relevant difference is that in the direct way approach, the harmonic content of the voltage is transferred to the current increasing the levels of its Total Harmonic Distortion (THD). In the indirect case, a Phase Looked Loop (PLL) is used in order to generate a synchronized sinusoidal signal with normalized amplitude and a very low harmonic content [37]-[39]. The amplitude of the current can be given by a control loop ensuring the power balance of the overall system [40]-[42]. Using a dual stage topology, the control of the inverter can regulate the voltage of the DC link by modifying the power injected to the grid through the modification of the output current.

In order to obtain the tracking of the current reference, many control methods have been applied. The simplest one consists in using an analog comparator operating at constant frequency [43]. Other method which implies a lower complexity is the hysteresis control which can be applied using either a constant hysteresis band or an adaptive hysteresis band or other variants [44]-[47]. Like in other reference tracking

applications, the predictive control is also an interesting option when digital implementation is possible [48]-[49]. Beside of the study of these kinds of control, the sliding mode control has been also used in grid-connected applications due to its well-known robustness, stability and simple implementation [50]-[53]. Sliding mode control strategies for grid-tied inverters has been also implemented using digital devices retaining its main advantages [54].

This chapter introduces the full bridge inverter working as a Power Source Inverter (PSI) using sliding-mode to ensure a flawless tracking of the sinusoidal current reference. A first order sliding surface is employed to control the output current of the inverter which is studied using the equivalent control method [55]. The resulting sliding motion is used to derive a linear model between the DC link voltage and the amplitude of the output current. This model is used to design a two loop controller with a current controller as the inner loop and a voltage regulator in the outer one. The voltage regulator defines the instantaneous amplitude of the output current while the sinusoidal waveform synchronized with the grid is given by a PLL. The relation between the Total Harmonic Distortion (THD) and the Power Factor (PF) with the voltage of the DC link is modelled and analyzed through the harmonic balance method. A linear controller is proposed to have a simple but effective reduction of the oscillations in the output of the outer control loop reducing the harmonics. A feed-forward strategy is also proposed to predict the ripple and compensate it. The theoretical analysis is verified along the chapter by means of simulation, which is complemented with experimental results.

4.2 CONVERTER MODEL

The connection of a full bridge converter to the grid through a series inductor is a well-known topology which can be used as a rectifier, inverter or shunt active power filter, among other applications. To control these structures it is commonly employed a current tracking loop combined with other algorithms to meet the control objectives. As shown in figure 4.1, the full bridge converter operating as an inverter works with an energy source always available at the DC side. Depending on the nature of this source, the inverters have been classified as Voltage Source Inverters (VSI) or Current Source Inverters (CSI) [56]. However, considering that the microinverter structure is a double-stage topology and also that the first stage behaves as a power source, the inverter will be treated as a Power Source Inverter (PSI). This characteristic follows from the

operation of the first stage as a SM-LFR ensuring the availability of a certain amount of power and having the H-bridge as load.

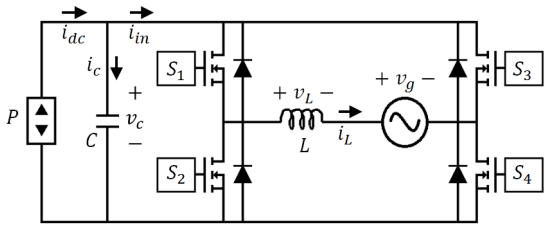

Fig. 4.1. H-bridge grid-connected PSI.

4.2.1 Bipolar commutation

Using bipolar or two-level commutation, the switches of each leg operate complementarily, in such a way that, the high-side switch is off when the low-side switch is on and the high-side switch is on when the low-side switch is off. Further, each leg operates complementarily with respect to the other one. Due to this, the inverter allows tracking a current reference with relative simplicity. Further, it is worth to mention that some studies reveal that in photovoltaic systems the ground current is less important when the inverter uses bipolar commutation [57]. However, the switching losses increase because both legs commute at high-frequency and the input current has a higher harmonic content. In order to obtain the converter model, the diagrams of the two possible structures of the circuit and its corresponding equations are shown in table 4.1.

Table 4.1. Converter circuit structures using bipolar commutation.

	Circuit configuration and power flow	**Expressions**
a)	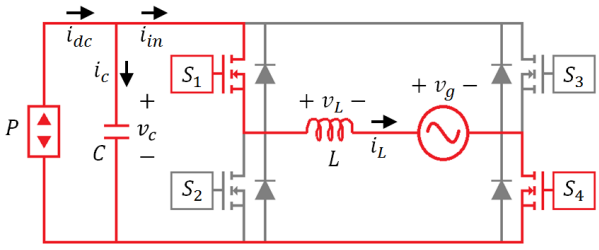	$\boldsymbol{S_1, S_4}$ **are ON** $\boldsymbol{S_2, S_3}$ **are OFF** $v_L = v_C - v_g$ $i_C = i_{dc} - i_{in}$ $i_{in} = i_L$
b)	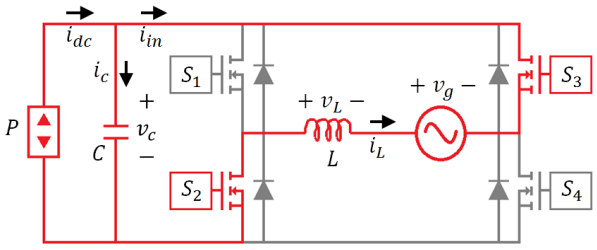	$\boldsymbol{S_1, S_4}$ **are OFF** $\boldsymbol{S_2, S_3}$ **are ON** $v_L = -v_C - v_g$ $i_C = i_{dc} - i_{in}$ $i_{in} = -i_L$

By defining the control variable u such that $u = 1$ when S_1 and S_4 are on, and $u = -1$ when S_2 and S_3 are on, the following equations are obtained:

$$L\frac{di_L}{dt} = -v_g + v_C u \tag{4.1}$$

$$C\frac{dv_C}{dt} = i_{dc} - i_L u = \frac{P}{v_c} - i_L u \tag{4.2}$$

4.2.2 Unipolar commutation

The unipolar operation is obtained forcing a leg to switch at high frequency while the other one switches at grid frequency. Also, it is possible to switch the high side switches of both legs at high frequency while the low side switches commute at grid frequency. Using this method, the switching losses are reduced because only two switches operate at high frequency and also because the switching frequency is lower than in the bipolar case for a fixed hysteresis band. Four circuit structures are possible, two for each half-cycle. Diagrams of the two possible structures of the circuit operating in the positive half-cycle and its corresponding equations are shown in table 4.2.

Table 4.2. Converter circuit structures for the positive half cycle using unipolar commutation.

	Circuit configuration and power flow	Expressions
a)	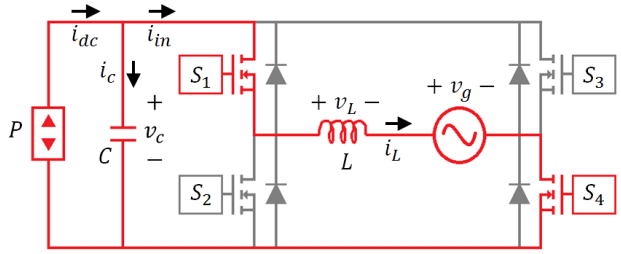	**S_1, S_4 are ON** **S_2, S_3 are OFF** $v_L = v_C - v_g$ $i_C = i_{dc} - i_{in}$ $i_{in} = i_L$
b)	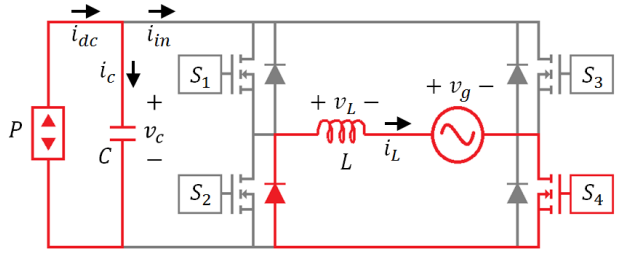	**S_2, S_4 are ON** **S_1, S_3 are OFF** $v_L = -v_g$ $i_C = i_{dc}$

By defining the control variable w such that $w = 1$ when S_1 and S_4 are on, and $w = -1$ when S_2 and S_3 are on, the following equations are obtained for the positive half-cycle of the grid voltage:

$$L\frac{di_L}{dt} = -v_g + v_C w \tag{4.3}$$

$$C\frac{dv_C}{dt} = i_{dc} - i_L w = \frac{P}{v_c} - i_L w \tag{4.4}$$

Operation in the negative half-cycle is similar but the inductor current flows in the opposite direction. Diagrams of the two possible structures of the circuit operating in the positive half-cycle and its corresponding equations are shown in table 4.3. The following equations are obtained for the negative half-cycle of the grid voltage:

$$L\frac{di_L}{dt} = -v_g - v_C(1-w) \tag{4.5}$$

$$C\frac{dv_C}{dt} = i_{dc} - i_L w = \frac{P}{v_c} + i_L(1-w) \tag{4.6}$$

Table 4.3. Converter circuit structures for the negative half cycle using unipolar commutation.

	Circuit configuration and power flow	**Expressions**
a)	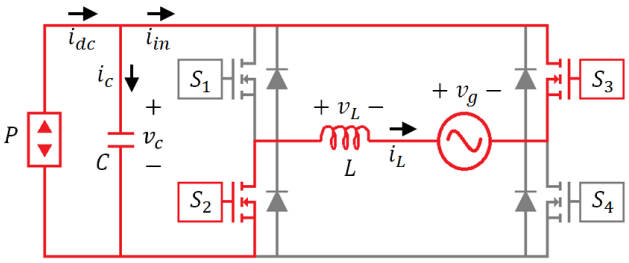	**S_1, S_4 are OFF** **S_2, S_3 are ON** $v_L = -v_C - v_g$ $i_C = i_{dc} - i_{in}$ $i_{in} = -i_L$
b)	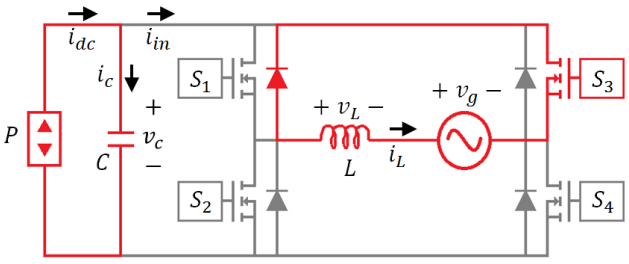	**S_2, S_4 are OFF** **S_1, S_3 are ON** $v_L = -v_g$ $i_C = i_{dc}$

Then, it is possible to write equations (4.3), (4.4), (4.5) and (4.6) in a more compact form given below:

$$L\frac{di_L}{dt} = -v_g + v_C w - \frac{v_C}{2}\left(1 - \text{sign}(v_g)\right) \tag{4.7}$$

$$C\frac{dv_C}{dt} = \frac{P}{v_c} - i_L w + \frac{i_L}{2}\left(1 - \text{sign}(v_g)\right) \tag{4.8}$$

4.3 FUNDAMENTALS OF GRID-CONNECTED GENERATION

Since the lower harmonic distortion of the grid voltage is normally below the 3%, the grid is ideally considered as a pure sine-wave AC voltage source of the form:

$$v_g = V_{max} \sin \omega t \tag{4.9}$$

where $\omega = 2\pi f$, and f is the fundamental frequency. A power generator can inject real power to the grid at unitary power factor when its current is defined as:

$$i_g = I_{max} \sin(\omega t + \varphi) \tag{4.10}$$

being I_{max} a constant value which determines the amount of power injected into the grid and the displacement angle φ is almost zero . Then, the real power is given by:

$$P = P_g = \frac{I_{max} V_{max}}{2} = I_g \cdot V_g \tag{4.11}$$

, where I_g and V_g are the RMS values of the grid voltage and current respectively. However, depending on the control performance, the current injected may be more or less distorted or may be more or less out of phase with respect to the main voltage. In these cases, the above definition of the grid current can be generalized as:

$$i_g = I_1 \sin(\omega t + \varphi) + \sum_{k=2}^{n} I_n \sin(n\omega t + \varphi_n) \tag{4.12}$$

The current THD-R (relative to the RMS value) is computed as follows:

$$THD - R = \frac{I_h}{I_g} = \sqrt{1 - \left(\frac{I_1}{I_g}\right)^2} \tag{4.13}$$

, where I_h is the RMS value of the harmonic content in the current I_g and the power factor (PF) is defined by:

$$PF = \frac{P}{S} = \frac{V_g \cdot I_1 \cos(\varphi)}{V_g \cdot I_g} \tag{4.14}$$

Therefore, the DC-AC converter must convert the power available in the DC link in order to inject it into the grid. This has to be done ensuring a high power quality level in the grid connection, or in other words a unitary PF along with a lower current THD. These two problems are the challenge for the control of a grid-connected inverter.

Due to the adopted control strategy, the amplitude of the current injected to the grid is not constant introducing some differences with respect to the expected ideal behavior. Therefore the current of the inverter will be forced to follow a current reference given by $i_{g_{ref}} = i_{max} \sin \omega t$.

4.4 SLIDING MODE CURRENT CONTROL

Both types of commutation for the full-bridge inverter allow obtaining the tracking of a current reference to inject power into the grid. The use of the sliding mode to control this kind of system consists in defining a sliding surface using a sinusoidal current reference for the output current of the inverter. A fundamental condition ensuring that this strategy is efficient is that the dynamic behavior of the current reference is significantly slower than the current dynamics of the inductive array that couples the inverter to the grid. This fact imposes a switching frequency for the converter much higher than the frequency of the grid. Under these conditions, the output current of the inverter is constrained in a neighborhood of the current reference, obtaining the expected power injection. To prevent the problems associated with a very high switching frequency, a hysteresis band is introduced limiting the current variation around the current reference in the way illustrated in figure 4.2.

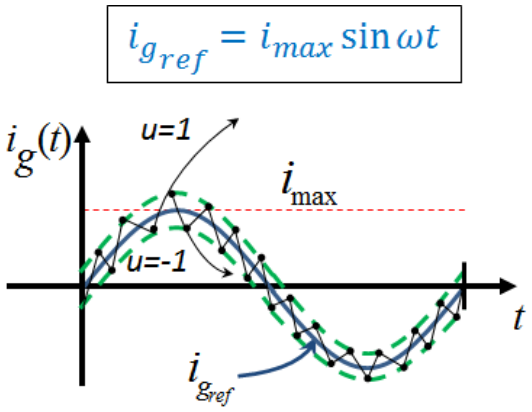

Fig. 4.2. H-bridge grid-connected PSI.

Our full bridge inverter is coupled to the grid through a single inductor and decoupled to the DC link through a simple capacitor, so that it can be described by a second order PSI. Applying the equivalent control method to analyze the sliding motion [58], a reduced model of the converter dynamics is obtained. This model describes the dynamics of the system for a current reference imposed by the sliding surface. However, if some harmonics are introduced in the reference by the control, they will also appear in the current of the inverter and therefore it will be necessary to consider the amplitude of the reference as a time-varying signal i_{max}.

4.4.1 Bipolar commutation

Defining the first order sliding surface:

$$S(x) = i_{g_{ref}} - i_L = i_{max} \sin \omega t - i_L \tag{4.15}$$

the current loop enforces that $i_L = i_{g_{ref}}$, and hence $i_g = i_{max} \sin \omega t$. The sliding motion is achieved using the control law:

$$u = \begin{cases} 1 & when\ S(x) > 0 \\ -1 & when\ S(x) < 0 \end{cases} \tag{4.16}$$

Applying the invariance conditions $\left(S(x) = 0, \dot{S}(x)\big|_{u=u_{eq}} = 0\right)$ leads to:

$$\frac{dS(x)}{dt} = \frac{i_{g_{ref}}}{dt} - \frac{di_L}{dt} = \frac{di_{max}}{dt} \sin \omega t + \omega i_{max} \cos \omega t + \frac{v_g}{L} - \frac{v_C u}{L} = 0 \tag{4.17}$$

The equivalent control is deduced as:

$$u_{eq} = \frac{1}{v_C}\left(L \frac{di_{max}}{dt} \sin \omega t + \omega L i_{max} \cos \omega t + V_{max} \sin \omega t\right) \tag{4.18}$$

which is constrained in the interval $-1 < u_{eq} < 1$. Replacing the equivalent control (4.18) in (4.2), the following resulting sliding dynamics is obtained.

$$C\frac{dv_C}{dt} = \frac{P}{v_C} - \frac{i_{max}\sin\omega t}{v_C}\left(L\frac{di_{max}}{dt}\sin\omega t + \omega L i_{max}\cos\omega t + V_{max}\sin\omega t\right) \quad (4.19)$$

When i_{max} is constant and equal to I_{max}, the reachability of the sliding surface can be obtained analyzing the condition $S(x)\,\dot{S}(x) < 0$, which leads to:

$$v_C(t) > \sqrt{L^2\omega^2 {I_{max}}^2 + {V_{max}}^2}\sin\left(\omega t + \operatorname{atan}\left[\frac{\omega L I_{max}}{V_{max}}\right]\right) \quad (4.20)$$

4.4.2 Unipolar commutation

Defining the previous first order sliding surface $S(x) = i_{g_{ref}} - i_L$, the equality $i_L = i_{g_{ref}}$ is enforced. The sliding motion is achieved using the same control law (4.16). Now, the invariance conditions $\left(S(x) = 0, \dot{S}(x)\big|_{u=u_{eq}} = 0\right)$, lead to $\frac{dS(x)}{dt} = \frac{di_{g_{ref}}}{dt} - \frac{di_L}{dt}$, from which:

$$\frac{dS(x)}{dt} = \frac{di_{max}}{dt}\sin\omega t + \omega i_{max}\cos\omega t + \frac{v_g}{L} - \frac{v_C}{L}u + \frac{v_C}{2L}\left(1 - \operatorname{sign}(v_g)\right) \quad (4.21)$$

The equivalent control can be deduced and is given by:

$$u_{eq} = \frac{1}{v_C}\left(L\frac{di_{max}}{dt}\sin\omega t + \omega L i_{max}\cos\omega t + V_{max}\sin\omega t + \frac{v_C}{2}\left(1 - \operatorname{sign}(v_g)\right)\right) \quad (4.22)$$

This equivalent control is then constrained to be in the interval $-1 < u_{eq} < 1$. Replacing the equivalent control (4.22) into (4.8), the following resulting sliding dynamics is obtained

$$C\frac{dv_C}{dt} = \frac{P}{v_C} - \frac{i_{max}\sin\omega t}{v_C}\left(L\frac{di_{max}}{dt}\sin\omega t + \omega L i_{max}\cos\omega t + V_{max}\sin\omega t\right) \quad (4.23)$$

When i_{max} is constant and equal to I_{max}, the reachability conditions of the sliding surface are deduced from $S(x)\,\dot{S}(x) < 0$ and leads to the condition

$$v_C(t) > \sqrt{L^2\omega^2 {I_{max}}^2 + {V_{max}}^2}\,\sin\left(\omega t + \operatorname{atan}\left[\frac{\omega L I_{max}}{V_{max}}\right]\right) \text{ and}$$
$$2k\pi - \operatorname{atan}\left|\frac{I_{max}L\omega}{V_{max}}\right| < \omega t < (2k+1)\pi - \operatorname{atan}\left|\frac{I_{max}L\omega}{V_{max}}\right| \quad (4.24)$$

The bipolar operation of the inverter and the corresponding model will be retained in the following in order to simplify the experimental validation of the control design. Figure 4.3 shows the use of a current control loop in the inverter, obtaining the reference calculated from the value of the available power in the DC bus. The sine waveform synchronized with the grid is obtained from a PLL. However, the stability of the voltage in the DC bus is not guaranteed and hence it is necessary to complete the control strategy using an outer loop.

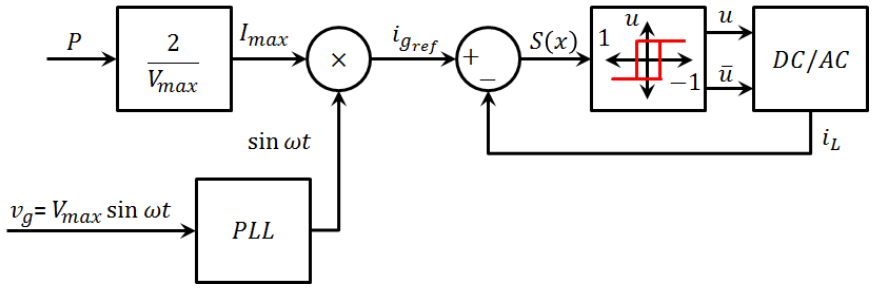

Fig. 4.3. Block diagram representing the current loop control of the inverter.

4.5 CONTROL OF THE DC-LINK

An interesting way to stabilize and regulate the DC voltage consists in considering the current control as the inner loop of a cascade type controller whose voltage outer controller modifies the current amplitude of the reference of the inner loop (see figure 4.4). In fact, the outer loop ensures that the average value of the voltage in the DC link is permanently regulated. Thus, the power balance on the overall microinverter is guaranteed because the voltage in the storage energy element of the middle-point (DC-link) is kept around a constant value.

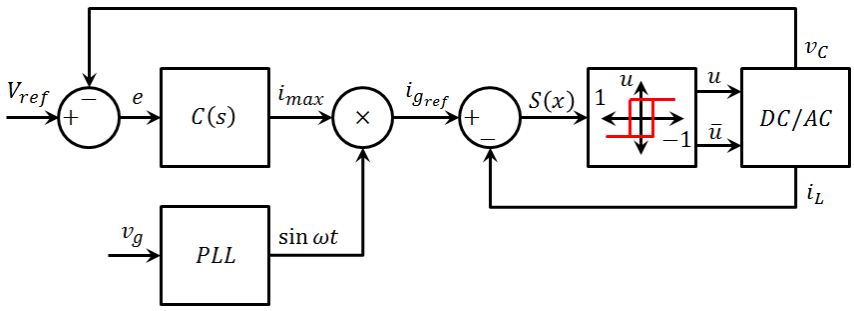

Fig. 4.4. Block diagram of the two-loop controller for the grid-connected inverter.

Now, a dynamic model having the voltage of the DC link as function of the amplitude of the output current is necessary for designing appropriately the outer loop controller $C(s)$.

4.5.1 Model of the DC-Link voltage

Note that both types of commutation (unipolar, bipolar) lead to the same resulting sliding dynamics. Recalling that $\sin\omega t\cos\omega t = \sin 2\omega t\,/2$ and $\sin^2\omega t = (1-\cos 2\omega t)/2$, expression (4.19) can be equivalently written as:

$$Cv_C\frac{dv_C}{dt} = P - \frac{Li_{max}}{2}\frac{di_{max}}{dt} + \frac{Li_{max}}{2}\frac{di_{max}}{dt}\cos 2\omega t - \frac{L\omega {i_{max}}^2}{2}\sin 2\omega t - \frac{V_{max}i_{max}}{2} + \frac{V_{max}i_{max}}{2}\cos 2\omega t \tag{4.25}$$

Now, if $i_{max}(t)$ is not a constant but a slow variable over an interval of time of length $T = \pi/\omega$, we can suppose that $i_{max}(t)$, $\frac{di_{max}}{dt}(t)$ and P do not vary significantly. Then, integrating (4.25) from t to $t+T$ leads to:

$$\frac{1}{T}\int_t^{t+T} Cv_C\frac{dv_C}{du}du = P - \frac{V_{max}i_{max}}{2} - \frac{Li_{max}}{2}\frac{di_{max}}{dt}$$

It is obtained that:

$$\frac{1}{2}C\left[\frac{{v_c}^2(t+T) - {v_c}^2(t)}{T}\right] = P - \frac{V_{max}i_{max}}{2} - \frac{Li_{max}}{2}\frac{di_{max}}{dt} \tag{4.26}$$

which leads to the equilibrium point where $v_c(t+T) \cong v_c(t)$:

$$\bar{P} = \frac{V_{max}I_{max}}{2} \tag{4.27}$$

Since $T = \frac{\pi}{\omega}$ is small, the following approximation can be considered:

$$\frac{1}{2}C\left(\frac{{v_c}^2(t+T)-{v_c}^2(t)}{T}\right)\cong C\frac{dv_C}{dt}$$

and the model is given by:

$$C\frac{dv_C}{dt}\cong P-\frac{V_{max}I_{max}}{2}-\frac{Li_{max}}{2}\frac{di_{max}}{dt} \tag{4.28}$$

where the last term on the right side is nonlinear. Denoting by $\hat{*}$ the linearized variables, the linearized model around $I_{max}, V_{max}, V_C, \bar{P}$ is obtained:

$$C\frac{d\hat{v}_C}{dt}=\frac{1}{V_C}\hat{P}-\frac{V_{max}}{2V_C}\hat{\imath}_{max}-\frac{LI_{max}}{2V_C}\frac{d\hat{\imath}_{max}}{dt} \tag{4.29}$$

Taking the Laplace transform of the previous expression for zero initial conditions, we have:

$$V_C(s)=-\frac{LI_{max}s+V_{max}}{2CV_{ref}s}I_{max}(s)+\frac{1}{CV_{ref}s}P(s) \tag{4.30}$$

As it can be noted in (4.30), the voltage of the DC link is affected by the amplitude of the output current and also by the input power. Because the amplitude of the current will be considered as the manipulated variable, the power will be considered as a disturbance. By applying a simple feedback strategy, the block diagram depicted in figure 4.5 represents the closed loop system.

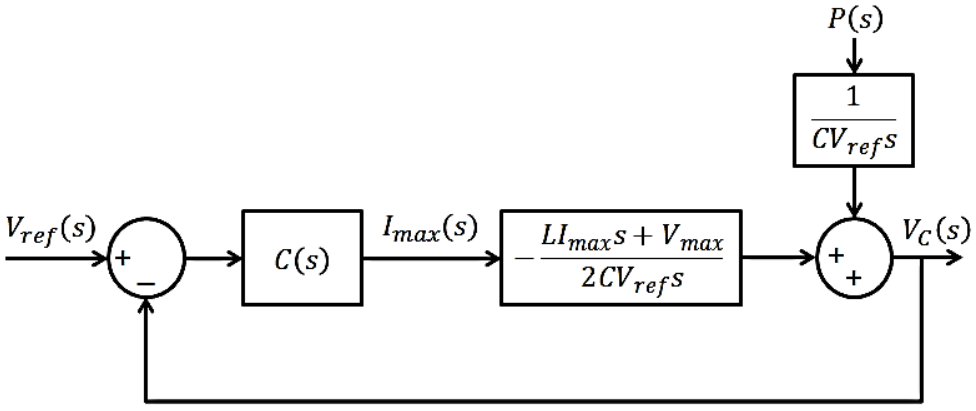

Fig. 4.5. Block diagram of the closed-loop control system.

Note that the transfer function from $I_{max}(s)$ to $V_C(s)$ exhibits a negative sign, and it is, in fact, a simple integrator with a stable zero. Note also that integration characterizes the transfer function from power to voltage variation. If we consider that the power varies by steps, the loop will be affected by disturbances of order 2 (ramps). The controller design has to be done taking into account all these specificities.

4.5.2 Synthesis of a linear controller

From the above discussion, since the system naturally possesses one integration, the controller must add another one. Moreover, the controller must attenuate the effect of the DC voltage ripple in the loop signals. For this reason, a first order filter is introduced in the controller; its bandwidth will be tuned for filtering the ripple whose frequency is 2ω. Considering the previous analysis the selected controller will be fixed as:

$$C(s) = -\frac{K_c(T_c s + 1)}{s(T_f s + 1)}, \qquad K_C, T_C, T_f > 0 \tag{4.31}$$

, where T_f is fixed to filter the ripple of the error signal and the sign minus compensates the sign of the converter transfer function. In addition, an analysis of the zero of the converter transfer function shows that, for the frequencies involved, it can be neglected, this leading to a simplified transfer function $G(s)$ given by:

$$G(s) = \frac{V_C(s)}{I_{max}(s)} = -\frac{V_{max}}{2CV_{ref}s} = -\frac{K_{max}}{s} \tag{4.32}$$

For example, the value of L considered in section 4.9 (experimental results) is 10 mH, $V_{max} = 220\sqrt{2}\ V$ and $I_{max} \leq 0.65\ A$ $(P \leq 200\ W)$, leading to a zero in $s = \frac{310.2}{0.65*10} \times 10^3\ Rad/s$. From the above analysis, the controlled open loop transfer function is:

$$L(s) = C(s)G(s) = \frac{K_{max}K_c(T_c s + 1)}{s^2(T_f s + 1)} \tag{4.33}$$

, where T_f being fixed, the free parameters are K_c and T_c. They will be determined in order to have a phase margin of 45°. The first step consists in identifying the

frequencies corresponding to a phase of -135° for the controlled open loop transfer function. We have:

$$\text{Arg}[L(j\omega)] = -180° - \text{atan}(T_f\omega) + \text{atan}(T_c\omega) = -135° \tag{4.34}$$

or equivalently, $\text{atan}(T_c\omega) - \text{atan}(T_f\omega) = 45°$. Using the identity $\text{atan}(x) - \text{atan}(y) = \text{atan}\left(\frac{x+y}{1-xy}\right)$, then, the previous equation is expressed as:

$$\text{atan}(T_c\omega) - \text{atan}(T_f\omega) = \text{atan}\left(\frac{\omega(T_c - T_f)}{1 + T_cT_f\omega^2}\right) = 45° \tag{4.35}$$

Then, $\frac{\omega(T_c-T_f)}{1+T_cT_f\omega^2} = 1$, which implies that $T_cT_f\omega^2 - \omega(T_c - T_f) + 1 = 0$. Since the discriminant $\Delta = {T_f}^2 - 6T_cT_f + {T_c}^2 > 0$, there exist two real roots given by:

$$\omega_{1,2} = \frac{1}{2T_fT_c}\left(-T_f + T_c \pm \sqrt{{T_f}^2 - 6T_cT_f + {T_c}^2}\right) \tag{4.36}$$

Writing $T_c = aT_f$ with $a > 0$, the discriminant Δ will be positive if:

$$a > 3 + 2\sqrt{2} > 1 \tag{4.37}$$

And the roots can be expressed in terms of T_f and a as:

$$\omega_{1,2} = \frac{1}{2aT_f}\left((a-1) \pm \sqrt{a^2 - 6a + 1}\right) \tag{4.38}$$

It is easy to verify that the two roots are positive for the values of a satisfying (4.37). For the two frequencies $\omega_{1,2}$, the phase of the controlled open loop transfer function is equal to -135°. If the gain for $\omega_{1,2}$is equal to 1, then the phase margin will be equal to 45°. This is true if the gain of the controller K_c is selected as:

$$K_{c_{1,2}} = \frac{{\omega_{1,2}}^2}{K_{max}} \sqrt{\frac{1 + {T_f}^2 {\omega_{1,2}}^2}{1 + a^2 {T_f}^2 {\omega_{1,2}}^2}} \tag{4.39}$$

Figure 4.6 shows the Bode plots for the two cases. As predicted by the theory, the gains $K_{c_{1,2}}$ allow fixing the phase margin at 45°. Note that a satisfying (4.37) is a freedom degree which can be used to adjust the bandwidth of the closed loop transfer function (i.e. settling time) while the phase margin has an influence on overshoots.

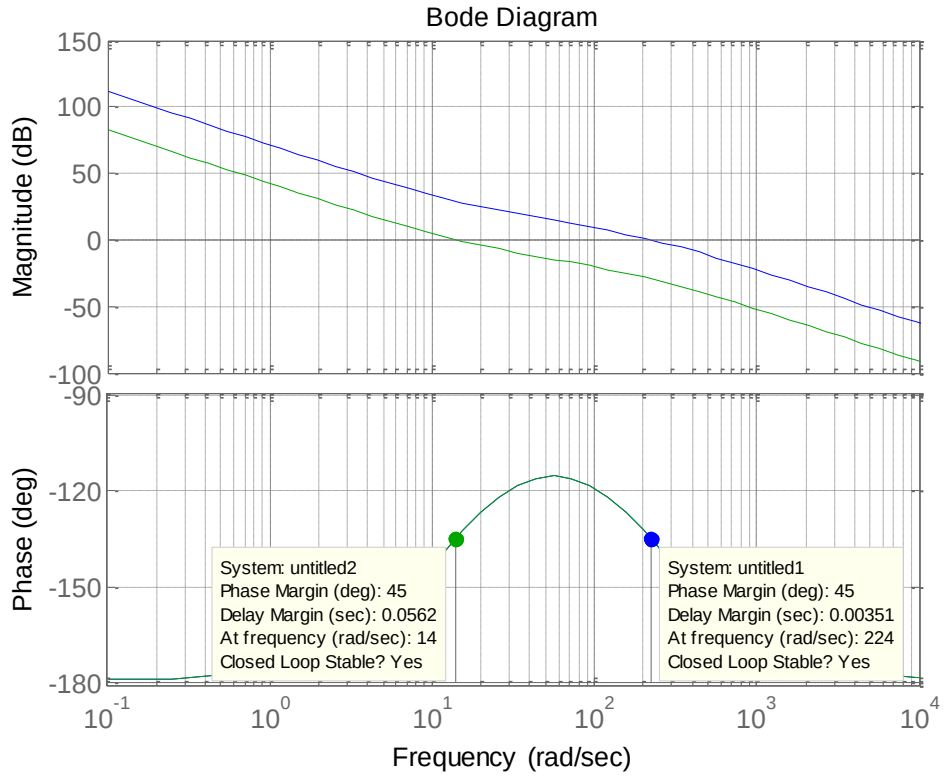

Fig. 4.6. Bode plot showing the two possible frequencies to achieve a phase margin of 45° using the proposed controller

Finally, the design method can be summarized by the following step by step procedure:

- Select $T_f = 1/2\pi f_f$ to reject the ripple in the measurement of the DC voltage. Values of f_f around 50Hz show a good trade-off between ripple-rejection and time response performance.
- Select the value of a satisfying the condition (4.37). The value of a affects considerably the time response only in a range near to the constraint (4.37).
- Compute the value of T_c, ω_1 and consequently the controller gain $K_C = K_1$.

To design the controller using the aforementioned method, the set of parameters for the power converter and the power sources are listed in Table 4.4, which will be used afterwards to illustrate the theory by simulations and experimental results.

Table 4.4. Parameters of the converter and power sources

Parameter	Symbol	Value
Inductance	L	$10\ mH$
DC bus Capacitor	C	$22\ \mu F$
DC bus Voltage	V_C	$400\ V$
Grid RMS Voltage	V_g	$220\ V$
Grid Frequency	f_g	$50\ Hz$
Power Range	P	$20 - 100\ W$

For the set of parameters in table 4.4, the controller parameters are listed in table 4.5 for different values of a. The values of a are generated by a MATLAB algorithm which considers $a_k = 1 + 0.05a_{k-1}$ for values of k between 1 and 6, having $a_0 = 5.828$ satisfying (4.37).

Table 4.5. Controller parameters for $T_f = 0.004$

Parameter	$a = 5.828$	$a = 6.119$	$a = 6.731$	$a = 7.741$	$a = 9.289$	$a = 11.614$
$\omega_1(Rad/s)$	103.55	77.68	61.22	47.40	35.95	26.67
$\omega_2(Rad/s)$	103.55	131.46	151.63	170.30	187.13	201.80
$T_c(s)$	0.0233	0.0245	0.0269	0.0310	0.0372	0.0464
$K_{c_1}(\Omega^{-1}/s)$	0.5711	0.3781	0.2573	0.1656	0.1006	0.0578
$K_{c_2}(\Omega^{-1}/s)$	0.5711	0.7450	0.8224	0.8405	0.8005	0.7138

Figure 4.7 shows the transient responses of the closed-loop system using the results in Table 4.5. The responses have been generated considering a step change in the voltage reference of 20 V. It is worth pointing out that only a slight difference can be noted in the overshoot and settling time. Also, increasing the value of a does not lead to significant changes in the form of transient response.

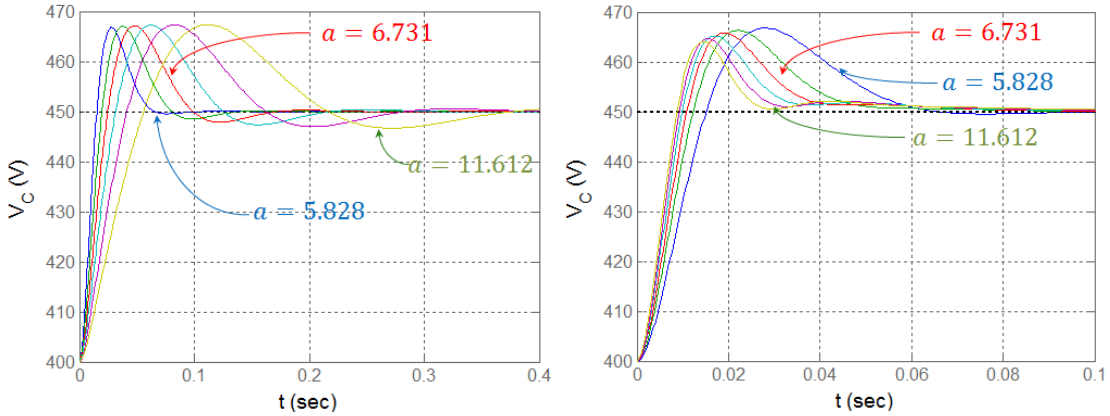

Fig. 4.7. Responses of the closed-loop system to a step change in the reference of 50V, having controllers for the values of a in table 4.5: a) $K_c = K_{c_1}$; and, b) $K_c = K_{c_2}$

However, as shown in figure 4.8, by increasing the value of a it is possible to reduce the maximum deviation of the output voltage when the converter copes with a change in the input power. In consequence, for $T_f = 0.004$, the value of $a = 11.632$ with $K_c = K_{c_2}$ allows obtaining the best response, i.e., a voltage deviation below 3.8% rejected within 0.1 s, which corresponds to five cycles at the grid-frequency approximately.

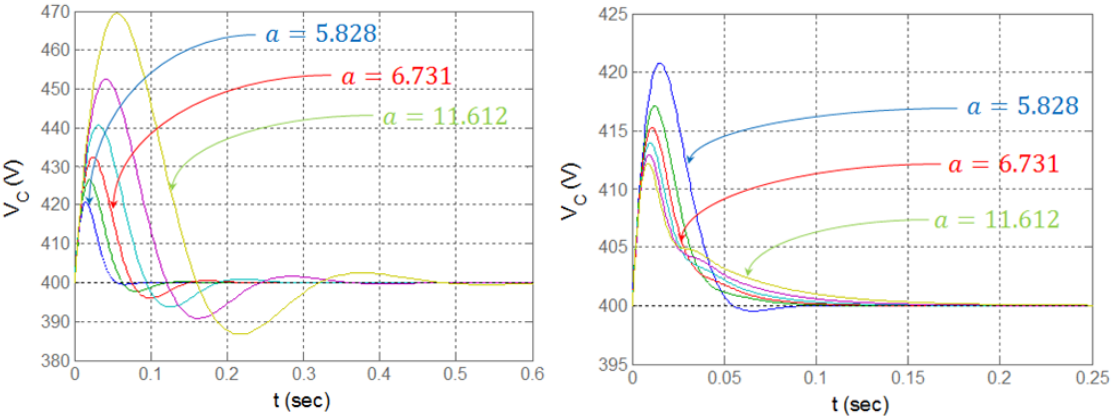

Fig. 4.8. Disturbance rejection of the closed-loop system using the values of a in table 4.5: a) responses for $K_c = K_{c_1}$; and, b) responses for $K_c = K_{c_2}$

4.5.3 Simulation results

In order to verify the theoretical approach, several simulations have been implemented in MATLAB for the converter model and PSIM for the converter circuit. In the PSIM

model, the power source is implemented using a voltage controlled source whose value is defined by the output current for a constant value of power.

The ripple in the voltage of the DC bus is due to the AC nature of the output power but also to the harmonic content of the grid voltage. However, the rejection of the component oscillating at double frequency of the grid by a low pass filter ensures that the other components must be mainly attenuated. Hence, the value of the parameter T_f in the controller transfer function must be selected to reject the double frequency component without enforcing a slow transient response. Considering a grid frequency of 50 Hz, then the low pass filter must reject a 100 Hz (628 Rad/s) component. If a value of 5 ms is selected for T_f, then, an attenuation of more or less -10 dB is ensured at the double grid frequency. So, from the analysis in the above section, a value of $a = 12$ is selected, with a value of 0.06 s for T_c. A value of 0.4477 for K_c is then computed for a frequency $\omega_2 = 162.86$ Rad/s. The resulted controller is

$$C(s) = -\frac{0.4477(0.06s + 1)}{s(0.005s + 1)} \tag{4.40}$$

Figure 4.9 shows the transient response of the system when a step is applied to the reference value. When the equilibrium point of 400 V for the DC bus voltage is attained, the reference value changes to 450 V at 0.6 s. The reference value returns to 400 V abruptly after one second. It is possible to observe that the controlled system has the desired regulation with zero error and shows a good performance in the time response.

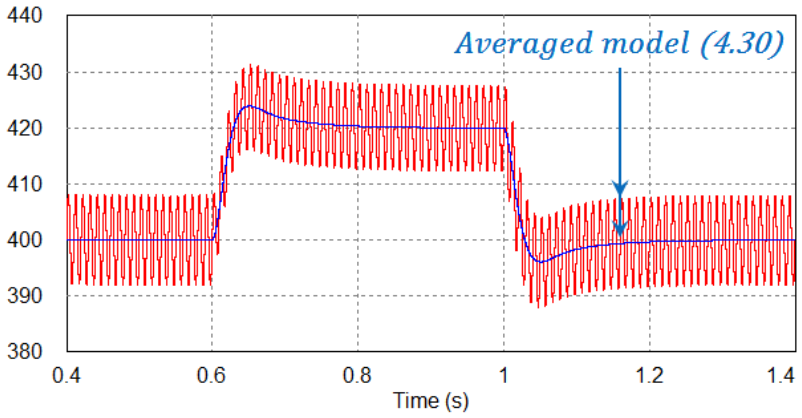

Fig. 4.9. Simulation results to set-point changes of the DC-bus voltage reference value

Figure 4.10 shows the transient responses of the system when a sudden additive disturbance is applied to the input power. After reaching the equilibrium point of 400 V for an input power of 50 W, the input power changes to 100 W at 0.2 s. The power returns to 50 W after 0.5 seconds. It is possible to observe that the controlled system rejects the disturbance showing a maximum voltage deviation of 15% controlled within 0.2 s.

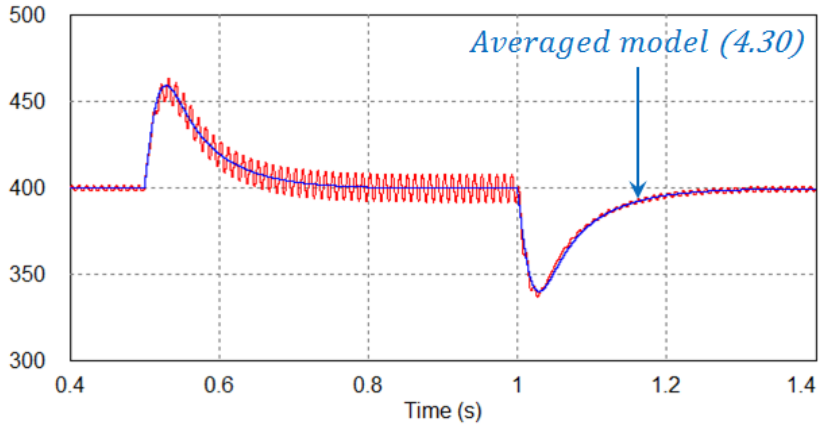

Fig. 4.10. Simulation results of disturbance rejection for sudden changes in the input power

It is worth to note that both figures 4.9 and 4.10 show a good correspondence between the behaviors of the average model in comparison with the switched one. At the same time, the controller must reject the influence of the ripple of the DC bus voltage ensuring a quality level of the injected power. Figure 4.11 shows the waveform of the inductor current for the two limits of power in the operational range: 20 W and 100W. THD values lower than 5% are obtained for both cases.

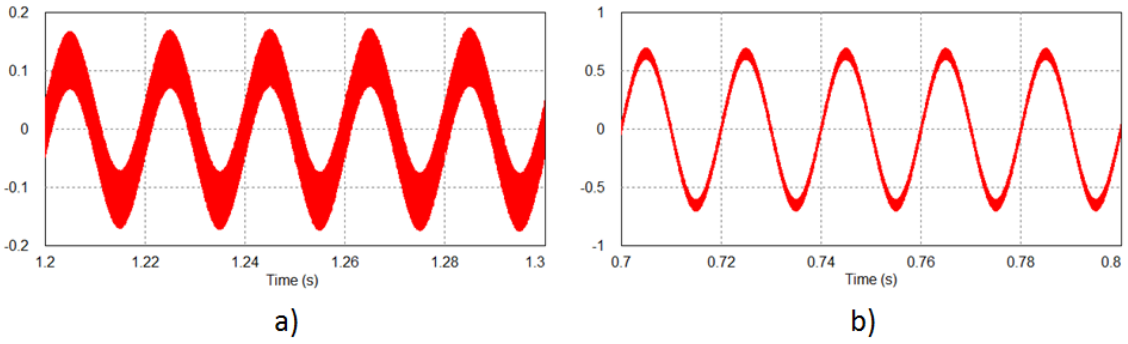

Fig. 4.11. Current waveforms for two operational points of the grid connected inverter: a) 20 W; b) 100 W.

4.6 POWER QUALITY ANALYSIS

4.6.1 Modeling of the voltage ripple of the DC-Link

In order to have a more accurate representation of the system variables and quantify the parametric dependence between them, it is possible to study the harmonic balance of the power between the DC side and the grid side. The AC side is defined by the expressions:

$$v_g(t) = V_{max}\, sin\, \omega t \tag{4.41}$$

$$i_g(t) = i_{max}(t)\, sin\, \omega t \tag{4.42}$$

Whereas the voltage of the DC side can be defined as:

$$v_C(t) = V_{dc} + V_2\, sin(2\omega t + \gamma) \tag{4.43}$$

Note that only an oscillatory component at the double frequency of the grid has been introduced and also note that this component has a phase displacement γ with respect to the grid voltage, which is considered as the phase reference. This assumption allows working with a moderate mathematical complexity in the analysis. As a consequence of the voltage regulation loop, the oscillatory component of the DC voltage appears in the current amplitude $i_{max}(t)$ with an average value of I_{max} and a harmonic of amplitude I_2 and phase ϕ which will depend on the frequency response of the loop compensator. Then, $i_{max}(t)$ is expressed as:

$$i_{max}(t) = I_{max} + I_2\, sin(2\omega t + \phi) \tag{4.44}$$

The sliding surface is defined by $S(x) = i_g - i_L$. At the surface, the invariance condition is fulfilled if $S(x) = 0$ *and* $\dot{S}(x) = 0$. The derivative of the current reference is given by:

$$\frac{di_{max}}{dt} = \frac{dI_{max}}{dt} + 2I_2\omega\cos(2\omega t + \phi) + I_2\frac{d\phi}{dt}\cos(2\omega t + \phi) + \frac{dI_2}{dt}sin(2\omega t + \phi) \tag{4.45}$$

Then, we have:

$$\frac{dS}{dt} = \frac{di_g}{dt} - \frac{di_L}{dt} = \frac{di_{max}}{dt} sin\,\omega t + \omega i_{max} \cos \omega t + \frac{v_g}{L} - u\frac{v_C}{L} \tag{4.46}$$

Since $\left.\frac{dS}{dt}\right|_{u=u_{eq}} = 0$, it can be derived:

$$u_{eq} = \frac{1}{v_C}\left(L\frac{di_{max}}{dt} sin\,\omega t + L\omega i_{max}\, cos\,\omega t + V_{max}\, sin\,\omega t\right) \tag{4.47}$$

Replacing in the equation describing the motion of v_C, we obtain:

$$C\frac{dv_C}{dt} = \frac{P}{v_C} - \frac{1}{v_C} i_{max}\, sin\,\omega t \left(L\frac{di_{max}}{dt} sin\,\omega t + L\omega i_{max}\, cos\,\omega t + V_{max}\, sin\,\omega t\right) \tag{4.48}$$

Then:

$$\begin{aligned} Cv_C\frac{dv_C}{dt} = P - Li_{max}\frac{di_{max}}{dt} sin^2\,\omega t - L\omega {i_{max}}^2\, sin\,\omega t\, cos\,\omega t \\ - V_{max} i_{max}\, sin^2\,\omega t \end{aligned} \tag{4.49}$$

$$\begin{aligned} Cv_C\frac{dv_C}{dt} = P - \frac{Li_{max}}{2}\frac{di_{max}}{dt}(1 - cos\,2\omega t) - \frac{L\omega {i_{max}}^2}{2} sin 2\omega t \\ - \frac{V_{max} i_{max}}{2}(1 - cos\,2\omega t) \end{aligned} \tag{4.50}$$

And:

$$\begin{aligned} Cv_C\frac{dv_C}{dt} = P - \frac{V_{max} i_{max}}{2} - \frac{Li_{max}}{2}\frac{di_{max}}{dt} - \frac{L\omega {i_{max}}^2}{2}\sin 2\omega t \\ + \frac{Li_{max}}{2}\frac{di_{max}}{dt}\cos 2\omega t + \frac{V_{max} i_{max}}{2}\cos 2\omega t \end{aligned} \tag{4.51}$$

Considering (4.42) and (4.44), (4.51) becomes after some tedious calculations:

$$
\begin{aligned}
Cv_C\frac{dv_C}{dt} = P &- \frac{V_{max}I_{max}}{2} + \frac{V_{max}I_2}{4}\sin\phi - \frac{V_{max}I_2}{2}sin(2\omega t+\phi) \\
&+ \frac{LI_2{}^2\omega}{8}\sin(2\omega t+2\phi) - LI_{max}I_2\omega\cos(2\omega t+\phi) \\
&- \frac{L\omega I_{max}{}^2}{2}sin\,2\omega t - \frac{LI_2{}^2\omega}{4}sin\,2\omega t + \frac{V_{max}I_{max}}{2}\cos 2\omega t \\
&+ \frac{V_{max}I_2}{4}\sin(4\omega t+\phi) + LI_{max}I_2\omega\cos(4\omega t+\phi) \\
&- \frac{LI_2{}^2\omega}{2}\sin(4\omega t+2\phi) + \frac{LI_2{}^2\omega}{4}\sin(6\omega t+2\phi) \\
&+ \frac{L\omega I_2{}^2}{8}\sin(6\omega t+2\phi) - \frac{LI_2}{4}\frac{dI_2}{dt} + \frac{LI_2}{4}\frac{dI_{max}}{dt}\sin\phi \\
&+ \frac{LI_{max}}{4}\frac{dI_2}{dt}\sin\phi + \frac{LI_{max}I_2}{4}\frac{d\phi}{dt}\cos\phi - \frac{LI_{max}}{2}\frac{dI_{max}}{dt} \\
&+ \frac{LI_{max}}{2}\frac{dI_{max}}{dt}cos\,2\omega t - \frac{LI_{max}I_2}{2}\frac{d\phi}{dt}\cos(2\omega t+\phi) \\
&- \frac{LI_{max}}{2}\frac{dI_2}{dt}sin(2\omega t+\phi) - \frac{LI_2}{2}\frac{dI_{max}}{dt}sin(2\omega t+\phi) \\
&+ \frac{LI_2{}^2}{8}\frac{d\phi}{dt}\sin(2\omega t+2\phi) + \frac{LI_2}{4}\frac{dI_2}{dt}\cos 2\omega t \\
&- \frac{LI_2}{8}\frac{dI_2}{dt}\cos(2\omega t+2\phi) - \frac{LI_2{}^2}{4}\frac{d\phi}{dt}\sin(4\omega t+2\phi) \\
&+ \frac{LI_2}{4}\frac{dI_2}{dt}\cos(4\omega t+2\phi) + \frac{LI_{max}I_2}{4}\frac{d\phi}{dt}\cos(4\omega t+\phi) \\
&+ \frac{LI_{max}}{4}\frac{dI_2}{dt}\sin(4\omega t+\phi) + \frac{LI_2}{4}\frac{dI_{max}}{dt}\sin(4\omega t+\phi) \\
&+ \frac{LI_2{}^2}{8}\frac{d\phi}{dt}\sin(6\omega t+2\phi) - \frac{LI_2}{8}\frac{dI_2}{dt}\cos(6\omega t+2\phi)
\end{aligned}
\tag{4.52}
$$

At the equilibrium point (derivatives equal to zero), we have:

$$
\begin{aligned}
P = \frac{V_{max}I_{max}}{2} &- \frac{V_{max}I_2}{4}\sin\phi + \frac{V_{max}I_2}{2}sin(2\omega t+\phi) - \frac{LI_2{}^2\omega}{8}\sin(2\omega t+2\phi) \\
&+ LI_{max}I_2\omega\cos(2\omega t+\phi) + \frac{L\omega I_{max}{}^2}{2}sin\,2\omega t + \frac{LI_2{}^2\omega}{4}sin\,2\omega t \\
&- \frac{V_{max}I_{max}}{2}\cos 2\omega t - \frac{V_{max}I_2}{4}\sin(4\omega t+\phi) \\
&- LI_{max}I_2\omega\cos(4\omega t+\phi) + \frac{LI_2{}^2\omega}{2}\sin(4\omega t+2\phi) \\
&- \frac{LI_2{}^2\omega}{4}\sin(6\omega t+2\phi) - \frac{L\omega I_2{}^2}{8}\sin(6\omega t+2\phi)
\end{aligned}
\tag{4.53}
$$

By averaging the expression for a period of π, the average power is obtained as:

$$P = \frac{V_{max} I_{max}}{2} - \frac{V_{max} I_2}{4} \sin\phi \tag{4.54}$$

Then, since $\mathrm{P} = \overline{\mathrm{P}}$, then:

$$\bar{P} = \frac{V_{max}}{2}\left(I_{max} - \frac{I_2}{2}\sin\phi\right) \tag{4.55}$$

On the other hand, from (4.42) and (4.44) after some simple manipulations, we have:

$$i_g(t) = [I_{max} + I_2\, sin(2\omega t + \phi)]\, sin(\omega t) \tag{4.56}$$

$$i_g(t) = \left(\frac{1}{2}\sqrt{4{I_{max}}^2 - 4I_{max}I_2 \sin\phi + {I_2}^2}\right) sin(\omega t + \varphi) - \frac{I_2}{2} cos(3\omega t + \phi) \tag{4.57}$$

where:

$$\varphi = \mathrm{atan}\left(\frac{I_2 \cos\phi}{2I_{max} - I_2 \sin\phi}\right) \tag{4.58}$$

The power on the AC side is computed as $p_g(t) = v_g(t) i_g(t)$:

$$p_g(t) = V_{max}\left[\left(\sqrt{{I_{max}}^2 - I_{max}I_2 \sin\phi + \frac{{I_2}^2}{4}}\right) sin(\omega t + \varphi) - \frac{I_2}{2} cos(3\omega t + \phi)\right] sin\,\omega t \tag{4.59}$$

$$p_g(t) = \frac{V_{max}}{2}\left(\sqrt{{I_{max}}^2 - I_{max}I_2 \sin\phi + \frac{{I_2}^2}{4}}\right)(\cos\varphi - \cos(2\omega t + \alpha)) - \frac{V_{max}I_2}{2}[\sin(4\omega t + \phi) - \sin(2\omega t + \phi)] \tag{4.60}$$

The mean value of the power is obtained as:

$$\left|\overline{p_g}\right| = \frac{V_{max}}{2}\left(\sqrt{{I_{max}}^2 - I_{max}I_2\sin\phi + \frac{{I_2}^2}{4}}\right)\cos\left[\operatorname{atan}\left(\frac{I_2\cos\phi}{2I_{max} - I_2\sin\phi}\right)\right] \tag{4.61}$$

Since $\cos\left[\operatorname{atan}\left(\frac{I_2\cos\phi}{2I_{max}-I_2\sin\phi}\right)\right] = \frac{1}{\sqrt{1+x^2}}$, we obtain:

$$\overline{p_g} = \frac{V_{max}}{2}\left(I_{max} - \frac{I_2}{2}sin\,\phi\right) \tag{4.62}$$

, which confirms (4.55) for the mean power on the DC side. From (4.43), we have:

$$\frac{dv_C}{dt} = \frac{dV_{dc}}{dt} + 2\omega V_2\cos(2\omega t+\gamma) + V_2\cos(2\omega t+\gamma)\frac{d\gamma}{dt} + \frac{dV_2}{dt}\sin(2\omega t+\gamma) \tag{4.63}$$

and then:

$$\begin{aligned} Cv_C\frac{dv_C}{dt} = C\Big[&V_{dc}\frac{dV_{dc}}{dt} + V_2\frac{dV_{dc}}{dt}\sin(2\omega t+\gamma) + 2V_{dc}V_2\omega\,cos(2\omega t+\gamma) \\ &+ V_{dc}V_2\frac{d\gamma}{dt}\cos(2\omega t+\gamma) + V_{dc}\frac{dV_2}{dt}sin(2\omega t+\gamma) \\ &+ {V_2}^2\omega\,sin(4\omega t+2\gamma) + 2{V_2}^2\frac{d\gamma}{dt}\sin(4\omega t+2\gamma) + \frac{V_2}{2}\frac{dV_2}{dt} \\ &- V_2\frac{dV_2}{dt}\cos(4\omega t+2\gamma)\Big] \end{aligned} \tag{4.64}$$

By equalizing (4.52) and (4.64), evaluated at the equilibrium point (derivatives equal to zero) and keeping only the double frequency components, we have:

$$\begin{aligned} &2CV_{dc}V_2\omega\,cos(2\omega t+\gamma) \\ &\quad= -\frac{V_{max}I_2}{2}sin(2\omega t+\phi) + \frac{L{I_2}^2\omega}{8}\sin(2\omega t+2\phi) \\ &\quad- LI_{max}I_2\omega\cos(2\omega t+\phi) - \frac{L\omega{I_{max}}^2}{2}sin\,2\omega t - \frac{L{I_2}^2\omega}{4}sin\,2\omega t \\ &\quad+ \frac{V_{max}I_{max}}{2}\cos 2\omega t \end{aligned} \tag{4.65}$$

, from which, after some tedious calculations, we have:

$$V_2 = \frac{\sqrt{\left[\omega L\left(4{I_{max}}^2 + {I_2}^2(2-\cos 2\phi)\right) + 4V_{max}I_2\cos\phi - 8LI_{max}I_2\omega\sin\phi\right]^2 + \left(\omega L{I_2}^2\sin 2\phi + 4V_{max}I_{max} - 4\omega LI_{max}I_2\cos\phi - 8V_{max}I_2\sin\phi\right)^2}}{16CV_{dc}\omega} \quad (4.66)$$

and:

$$\gamma = \operatorname{atan}\left(\frac{\omega L\left(4{I_{max}}^2 + {I_2}^2(2-\cos 2\phi)\right) + 4V_{max}I_2\cos\phi - 8LI_{max}I_2\omega\sin\phi}{\omega L{I_2}^2\sin 2\phi + 4V_{max}I_{max} - 4\omega LI_{max}I_2 - 8V_{max}I_2\sin\phi}\right) \quad (4.67)$$

Considering the ideal case with $I_2 = 0$, and $\phi = 0$, then, we have:

$$V_2 = \frac{I_{max}}{4CV_{dc}\omega}\sqrt{\omega^2L^2{I_{max}}^2 + {V_{max}}^2} \quad (4.68)$$

and that:

$$\gamma = \operatorname{atan}\left(\frac{\omega LI_{max}}{V_{max}}\right) \quad (4.69)$$

Therefore, the parameters which define the DC link voltage ripple have been determined. Figure 4.12 shows simulation results of the ripple voltage obtained in PSIM for different sets of parameters validating the above theoretical predictions.

In both cases of figure 4.12 a regulated DC bus voltage of 800 V and an input power of 1 kW have been used. The levels of voltage and power have been selected in order to better illustrate the studied behaviors in the voltage ripple. A grid source of 220 V / 50 Hz is used. Differences between the amplitude and phase displacement of the voltage ripple are observed for two set of values of the passive parameters (L and C). The differences between the simulated values and the theoretically computed values of the amplitude and phase displacement of the voltage ripple are lower than 0.5%. It is worth to note that the phase displacement appears for higher values of inductance; however, for an equal value of power the effect is negligible when the inductance has a value ten

times lower. Then, the desired maximum amplitude of the voltage ripple can be imposed by means of the passive elements. The inductor constrains the derivative of the output current and hence is designed for a maximum current value and a hysteresis size, so that, the parameter which defines the voltage ripple is the DC bus capacitor.

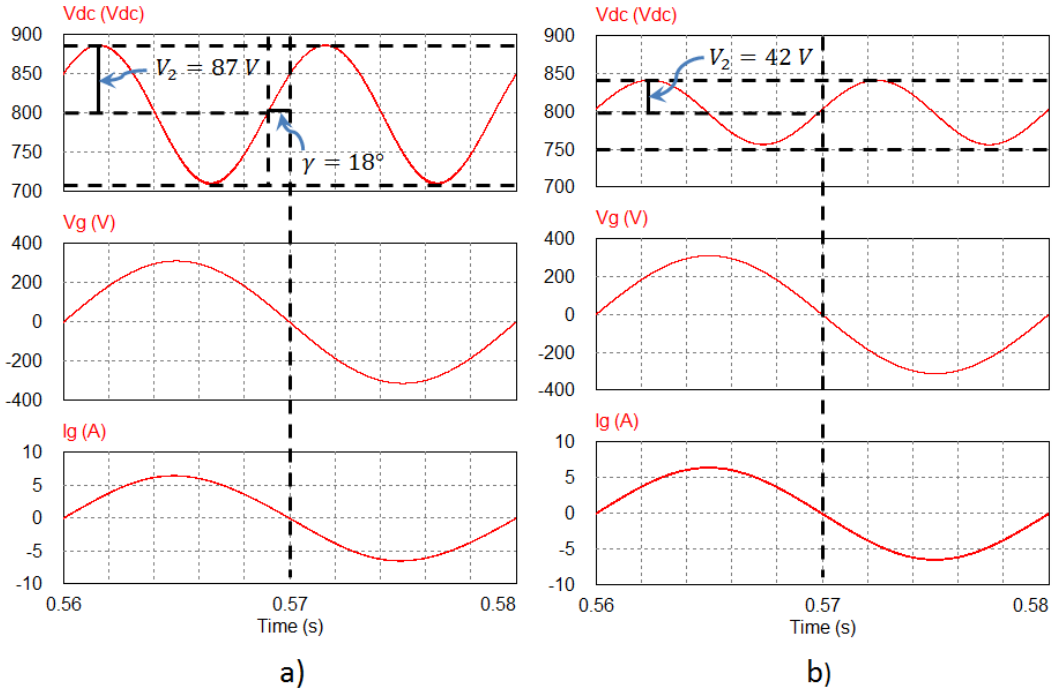

Fig. 4.12. Validation of the predicted parameters of the ripple in the voltage of the DC bus a) case 1 (L = 100 mH, C = 27 µF); b) case 2 (L = 10mH, C = 47 µF).

4.6.2 Total Harmonic Distortion of the output current

The presence of the component I_2 is a consequence of the ripple in the voltage of the DC bus and its propagation through the outer control loop. To quantify this aspect, the frequency response of the controller must be analyzed. We have:

$$C(s) = \frac{I_{max}(s)}{E(s)} = \frac{I_{max}(s)}{V_{ref}(s) - V_c(s)} = -\frac{K_c(T_c s + 1)}{s(T_f s + 1)} \tag{4.70}$$

The gain and phase of the controller as a function of the frequency are:

$$K_{v_c i_m} = |C(\omega)| = \frac{K_c}{\omega}\sqrt{\frac{1 + {T_c}^2\omega^2}{1 + {T_f}^2\omega^2}} \tag{4.71}$$

$$\beta(\omega) = -270° + \text{atan}\left(\frac{1 + T_C T_f \omega^2}{\omega\left(T_f - T_C\right)}\right) \tag{4.72}$$

Then, with $\omega = 2\pi f$ and $f = 2f_{grid}$, the amplitude and phase of the component I_2 is given by:

$$I_2 = \frac{K_c V_2}{4\pi f_{grid}}\sqrt{\frac{1 + 16\pi^2 {T_c}^2 {f_{grid}}^2}{1 + 16\pi^2 {T_f}^2 {f_{grid}}^2}} \tag{4.73}$$

and:

$$\phi = \gamma - \text{atan}\left(\frac{1 + 16\pi^2 T_C T_f {f_{grid}}^2}{4\pi f_{grid}\left(T_f - T_C\right)}\right) \tag{4.74}$$

The validation of the above expression is graphically presented in figure 4.13. A reference of 400 V is used to the voltage regulation loop. The inverter is connected to a 220 V/ 50 Hz grid injecting a power of 100 W. The transfer function of the voltage controller is defined as follows:

$$C(s) = -\frac{0.1(0.06s + 1)}{s(0.005s + 1)} \tag{4.75}$$

The 100 Hz component of the voltage ripple is attenuated for the controller with a gain of -54.7 dB. Further, a phase lead of 74° is observed between the AC components of the voltage and the current reference.

Considering that the PLL gives a perfect sinusoidal waveform with normalized amplitude, the harmonic content of the current can be only introduced through the amplitude signal i_{max}. The current i_g in expression (4.57) can be rewritten as:

$$i_g = \underbrace{\frac{1}{2}\sqrt{4{I_{max}}^2 - 4I_{max}I_2\sin\phi + {I_2}^2}}_{I_{g1}} sin(\omega t + \varphi) - \underbrace{\frac{I_2}{2}}_{I_{g3}}\cos(3\omega t + \phi) \tag{4.76}$$

where $i_{g1} = I_{g1}\,sin(\omega t + \varphi)$ and $i_{g3} = I_{g3}\cos(3\omega t + \phi)$. Then, we have:

$$i_g = i_{g1} + i_{g3} = I_{g1}\,sin(\omega t + \varphi) - I_{g3}\cos(3\omega t + \phi) \tag{4.77}$$

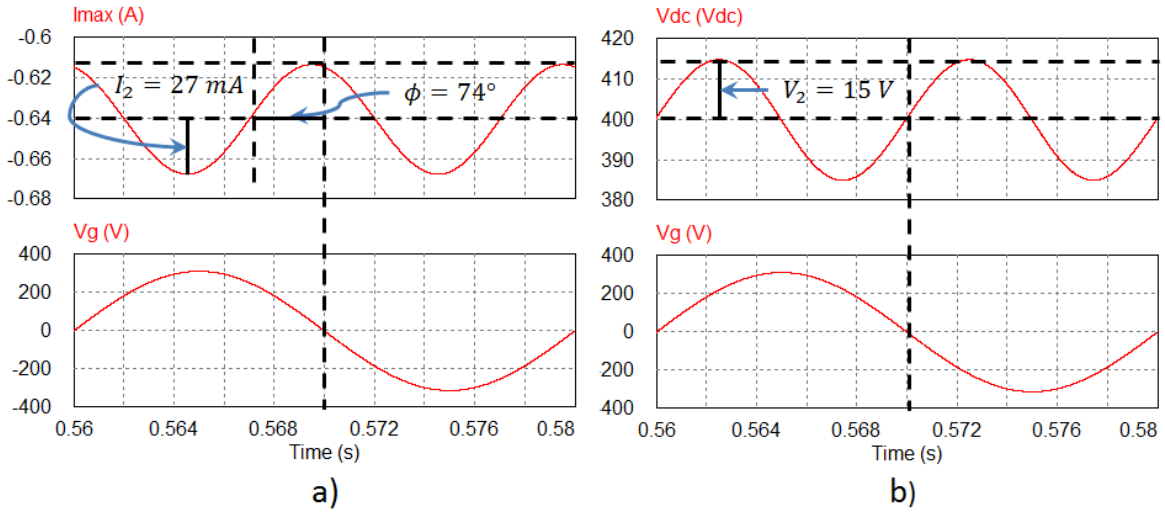

Fig. 4.13. Validation of the predicted parameters of the current amplitude i_{max} (L = 10mH, C = 47 µF).

However, the ripple content of the current has a non-negligible effect in the THD and hence must be also considered. Although the frequency varies in the ripple waveform, because of its triangular shape, the RMS value of the ripple can be approximated as $i_{rip} = \Delta/\sqrt{3}$. Then, it is possible to obtain the RMS values of the current components and then to compute the total harmonic distortion given by:

$$THD - F \cong \frac{\sqrt{RMS(i_{g3})^2 + {i_{rip}}^2}}{RMS(i_{g1})} = \sqrt{\frac{3{I_2}^2 + 8\Delta^2}{6(4{I_{max}}^2 - 4I_{max}I_2\sin\phi + {I_2}^2)}} \tag{4.78}$$

As it can be shown in figure 4.14, different THD values can be obtained for a same value of amplitude in the voltage ripple. The figure 4.14a shows the effect of the voltage ripple when a value of 0.00005 seconds is settled in the filter time constant of the controller (T_f). This value corresponds to a poor filtering at 100 Hz. Figure 4.14b shows the result using a value of 0.005 for T_f , which is the selected value in the design procedure. The action of the filter is too relevant because the harmonic distortion is reduced from a 7.98% to a 4.45%.

It is worth to note that the effect of the ripple component of the current is considerable. Considering an ideal sliding motion in the current ($\Delta = 0$), the THD reduces to 7.01% and 2.17% for the cases in figure 4.13 respectively.

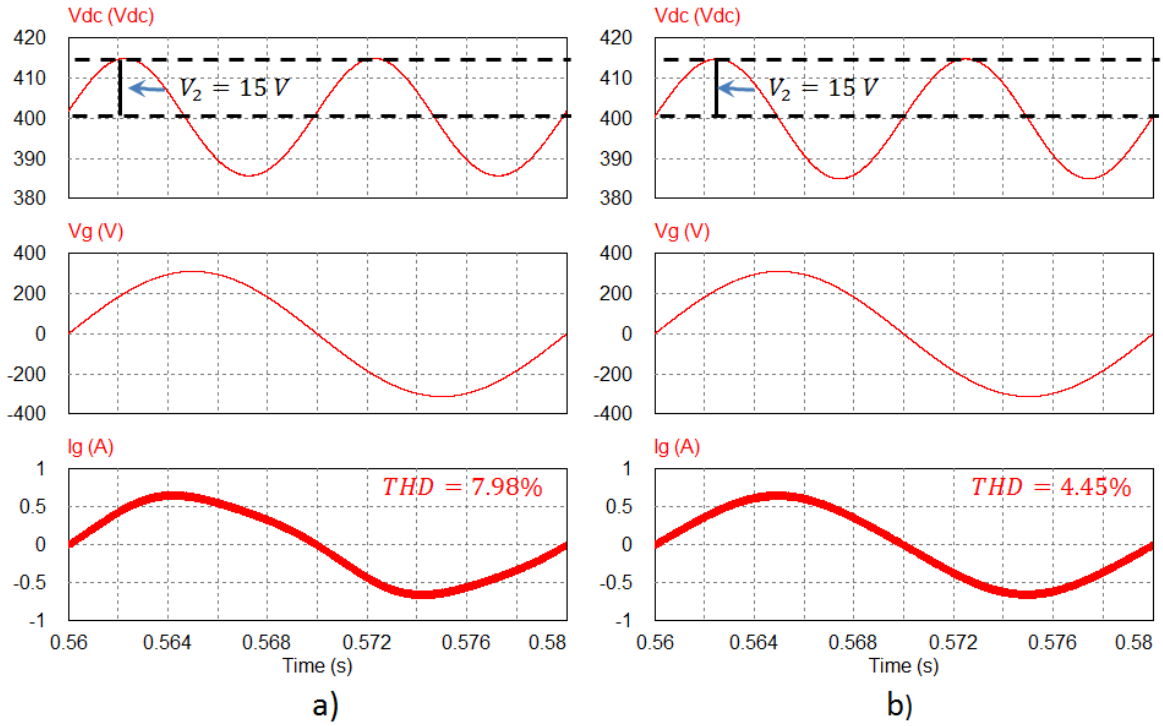

Fig. 4.14. Influence of the voltage ripple in the current harmonic distortion (L = 10 mH, C = 27 µF): a) case 1 ($T_f = 0.00005$); b) case 2 ($T_f = 0.005$).

4.6.3 Power factor and displacement power factor

The power factor is a key aspect of the grid connected systems. Because of the presence of some harmonic content, it is possible to differentiate the effect of the current phase displacement using the Displacement Power Factor (DPF) or to have combined the effect of the current displacement and the harmonic content in the Power Factor (PF). From (4.58), we have:

$$\varphi = \operatorname{atan}\left(\frac{\frac{I_2}{2}\cos\phi}{I_{max} - \frac{I_2}{2}\sin\phi}\right)$$

Hence, the displacement power factor is obtained as:

$$DPF = \cos\varphi = \cos\left[\operatorname{atan}\left(\frac{\frac{I_2}{2}\cos\phi}{I_{max} - \frac{I_2}{2}\sin\phi}\right)\right] = \frac{2I_{max} - I_2\sin\phi}{\sqrt{4{I_{max}}^2 - 4I_{max}I_2\sin\phi + {I_2}^2}} \tag{4.79}$$

On the other hand, from (4.77), we have that $i_g = I_{g1}\,sin(\omega t + \varphi) - I_{g3}\cos(3\omega t + \phi)$, where the RMS value of the grid current i_g can be obtained from the RMS values of its frequency components as:

$$RMS(i_g) = \sqrt{\frac{{I_{g1}}^2}{2} + \frac{{I_{g3}}^2}{2} + \frac{\Delta^2}{3}} = \sqrt{\frac{6{I_{max}}^2 - 6I_{max}I_2\sin\phi + 3{I_2}^2 + 4\Delta^2}{12}} \tag{4.80}$$

From (4.57), we have:

$$RMS(i_{g1}) = \sqrt{\frac{4{I_{max}}^2 - 4I_{max}I_2\sin\phi + {I_2}^2}{8}} \tag{4.81}$$

Then, the power factor can be obtained from:

$$PF = \frac{P_g}{S_g} = \frac{RMS(v_g)RMS(i_{g1})\cos\varphi}{RMS(v_g)RMS(i_g)} = \frac{RMS(i_{g1})}{RMS(i_g)}\cos\varphi = \frac{RMS(i_{g1})}{RMS(i_g)}DPF$$

Therefore:

$$PF = \left[\sqrt{\frac{12{I_{max}}^2 - 12I_{max}I_2\sin\phi + 3{I_2}^2}{12{I_{max}}^2 - 12I_{max}I_2\sin\phi + 6{I_2}^2 + 8\Delta^2}}\right]DPF \tag{4.82}$$

Note that a reduced current component I_2 directly increases the power factor; also, observe the effect of the angle ϕ in the power factor. As an illustrative example, the DPF and the PF have been computed for the same parameters used in the simulated results in subsection 4.5.2. For the first case (THD=7.98%) which corresponds to the

worst THD, the values of DPF and PF are 0.997 and 0.994 respectively. For the second case (THD=4.45%) which corresponds to the best THD, the values of DPF and PF are 1.000 and 0.999 respectively.

4.6.4 Effect of a DC component in the current reference

The existence of a DC component in the current reference is a spurious phenomenon which can affect the general behavior of the grid-connected inverter either because the output current will exhibit a DC component or because this component can generate other effects [58]. The following analysis allows quantifying this effect.

If the current reference is given by:

$$i_g(t) = i_{max}(t)[a + sin(\omega t)]$$

, where a is the DC component, then, we will have:

$$i_g(t) = [I_{max} + I_2\, sin(2\omega t + \phi)][a + sin(\omega t)] \tag{4.83}$$

Or equivalently:

$$\begin{aligned} i_g(t) = I_{max}a + I_{max}\, sin\,(\omega t) + I_2 a\, sin(2\omega t + \phi) + \frac{I_2}{2} cos(\omega t + \phi) \\ - \frac{I_2}{2} cos(3\omega t + \phi) \end{aligned} \tag{4.84}$$

The instantaneous power at the grid side is computed as follows:

$$\begin{aligned} p_g(t) = v_g i_g = V_{max}\, sin\,\omega t \Big[I_{max}a + I_{max}\, sin\,(\omega t) + I_2 a\, sin(2\omega t + \phi) \\ + \frac{I_2}{2} cos(\omega t + \phi) - \frac{I_2}{2} cos(3\omega t + \phi) \Big] \end{aligned}$$

$$p_g(t) = \underbrace{\frac{V_{max}}{2}(I_{max} - I_2 \sin\phi)}_{DC\ component} + \underbrace{\left(aV_{max}\sqrt{4{I_{max}}^2 - 4I_{max}I_2 \sin\phi + {I_2}^2}\right) sin(\omega t + \varphi)}_{Grid\ frequency\ component} - \frac{V_{max}I_{max}}{2}\cos 2\omega t + \frac{V_{max}I_2}{2} cos(2\omega t + \phi) - aV_{max}I_2\, cos(3\omega t + \phi) - \frac{V_{max}I_2}{4}\sin(4\omega t + \phi) \quad (4.85)$$

Note that the mean value of the power is not modified by the effect of the DC component a. However, note that a power component at grid frequency appears. Since each of the alternative components in the output power represents an alternative component at the same frequency in the DC-Link voltage, then, a grid frequency component appears in the ripple of the DC-Link. This is the main effect of the DC component. However, this component will appears also in the voltage regulation loop and hence it can have also an effect in the harmonic content of the current reference amplitude.

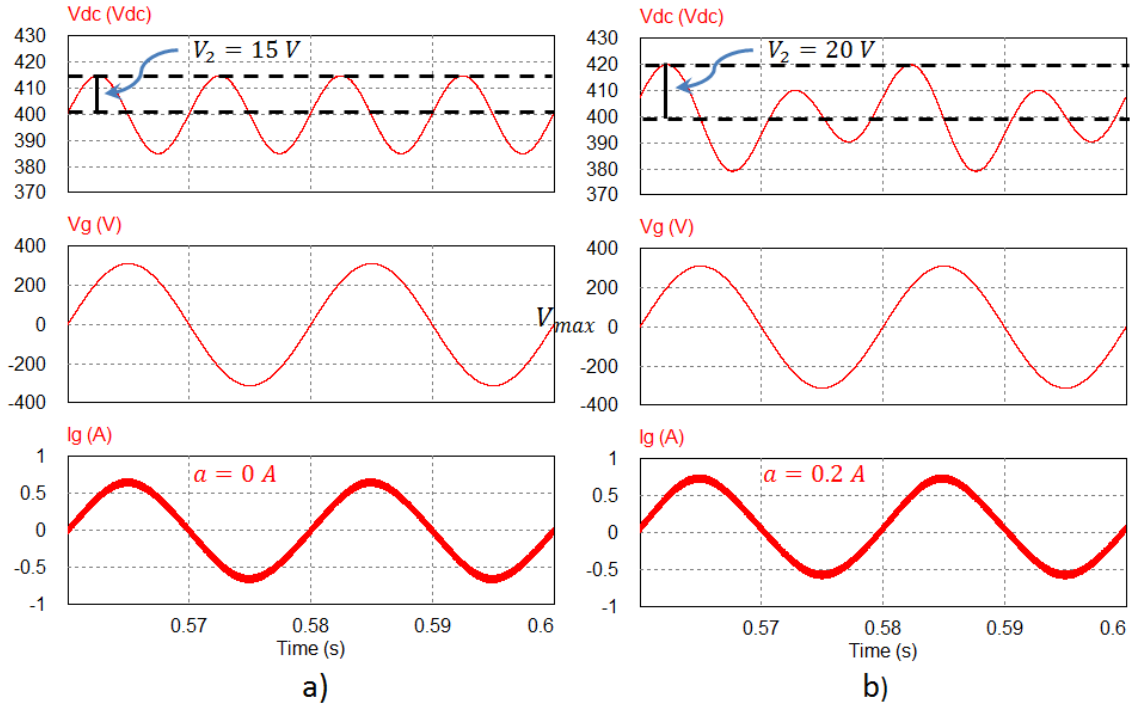

Fig. 4.15. Simulated voltage ripple on the DC bus: a) without DC component; b) with DC component.

Figure 4.15 shows some simulated results when a DC component of 0.2A is introduced in the current reference. As it can be observed a component at the grid frequency appears in the voltage of the DC bus also increasing the effective amplitude of the ripple.

4.7 RIPPLE COMPENSATION USING A FEED-FORWARD LOOP

Despite the presence of a low pass filter in the control loop, a small double frequency component is always perturbing current i_{max}. Hence, a complementary compensation can be added in order to obtain a more important reduction of the spurious component without increasing the order of the control system. This section introduces a feed-forward approach which predicts the amplitude of the voltage ripple and reproduces it using the PLL system to generate a sinusoidal component with a frequency two times higher than the frequency of the grid. Thus, the main component of the ripple can be effectively attenuated before entering into the control loop, so that the filter can remove the remaining component more easily. The amplitude of the voltage ripple is predicted from (4.68) reproduced below:

$$V_2 = \frac{\sqrt{\left(\omega L {I_{max}}^2\right)^2 + (V_{max} I_{max})^2}}{4 C V_{dc} \omega}$$

Figure 4.16 shows the ripple compensation scheme. The PLL is one of the more important components of the system because it is used to generate both the sinusoidal grid frequency and the double grid frequency components.

For the mathematical operations required to compute the amplitude of the ripple, a digital implementation is preferred for practical reasons, taking into account that a complete digital implementation of the overall control scheme is possible. In this case, the current reference i_{ref} is generated and given to an analog hysteresis comparator to obtain the desired tracking with a good frequency response. Thus, the proposed system requires the measurement of the DC bus voltage, the current in the coupling inductor and the voltage of the grid. Depending on the technique used in the PLL, this measure can be either detect the zero crossing or obtain an instantaneous measurement of the grid voltage signal. In a first approach, we propose the use of a zero crossing detection

circuit which exploits a discrete square wave synchronized with the grid frequency. This type of PLL offers the possibility to have another square wave output with a frequency multiple of the grid frequency. This signal can be used to define a sampling frequency with the same number of samples per period.

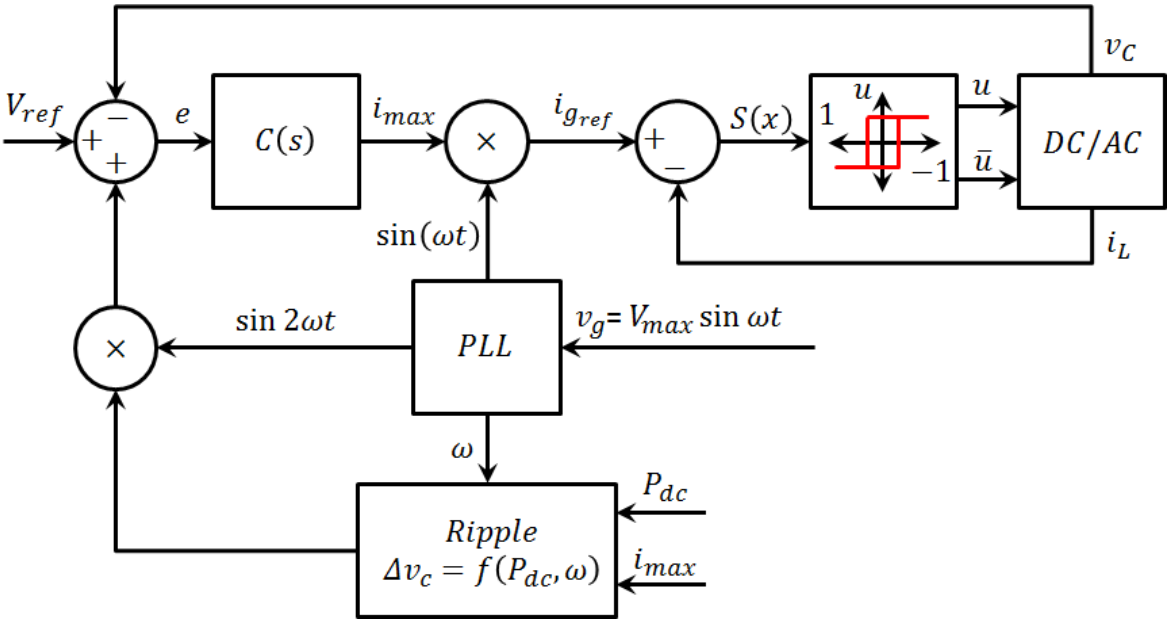

Fig. 4.16. Block diagram of the two-loop controller for the grid-connected inverter including the feed-forward ripple compensation based on the double-frequency PLL.

Figure 4.17 illustrates the proposed sine-wave generation using a low sampling frequency to obtain a better graphical representation. It is possible to identify both sampled sine-waves using the same switching frequency: the high frequency signal (HF) generated by means of the discrete PLL and the zero crossing signal. Although this solution is not efficient with distorted voltage signals, it is important to note that the microinverter will work connected to a system which must satisfy the international standards which impose a THD less than 5% in the grid voltage. The sampling frequency used in the simulations is 2 kHz and it can be increased until 40 or 50 kHz.

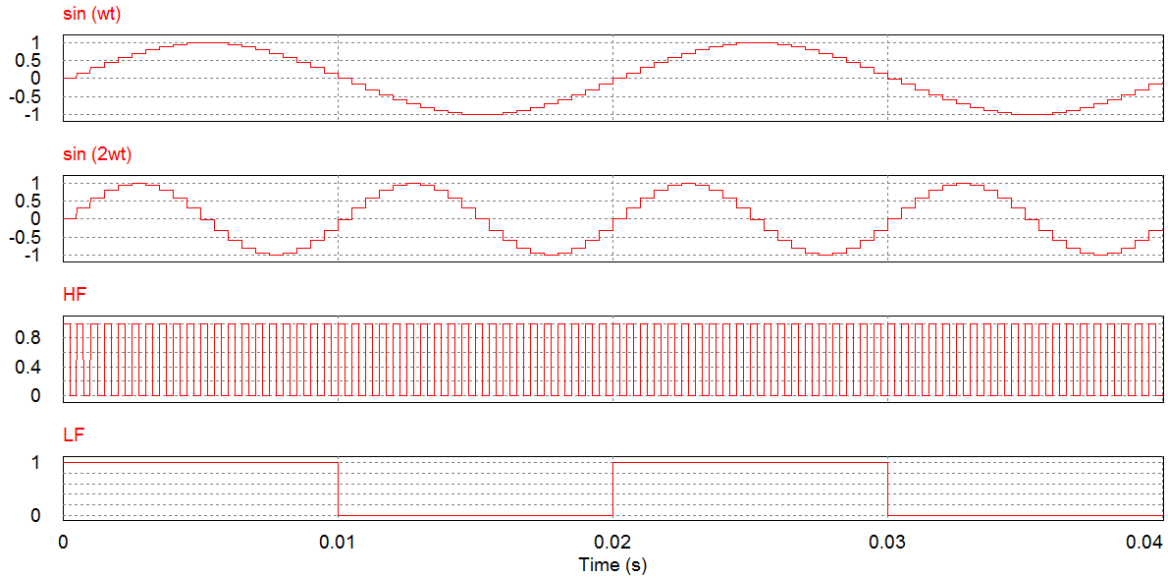

Fig. 4.17. Signals involved in the proposed PLL system.

With this system, the mathematical computations required for the sine-wave generation are reduced since the signal waveform can be digitally stored in an electronic memory. In that case, it is possible during the released computational time to execute the required calculations to predict the ripple amplitude. The proposed control has been implemented in the PSIM simulations obtaining the results shown in Figure 4.18. As it can be noted, a reduction of 0.6% is obtained with the ripple compensation.

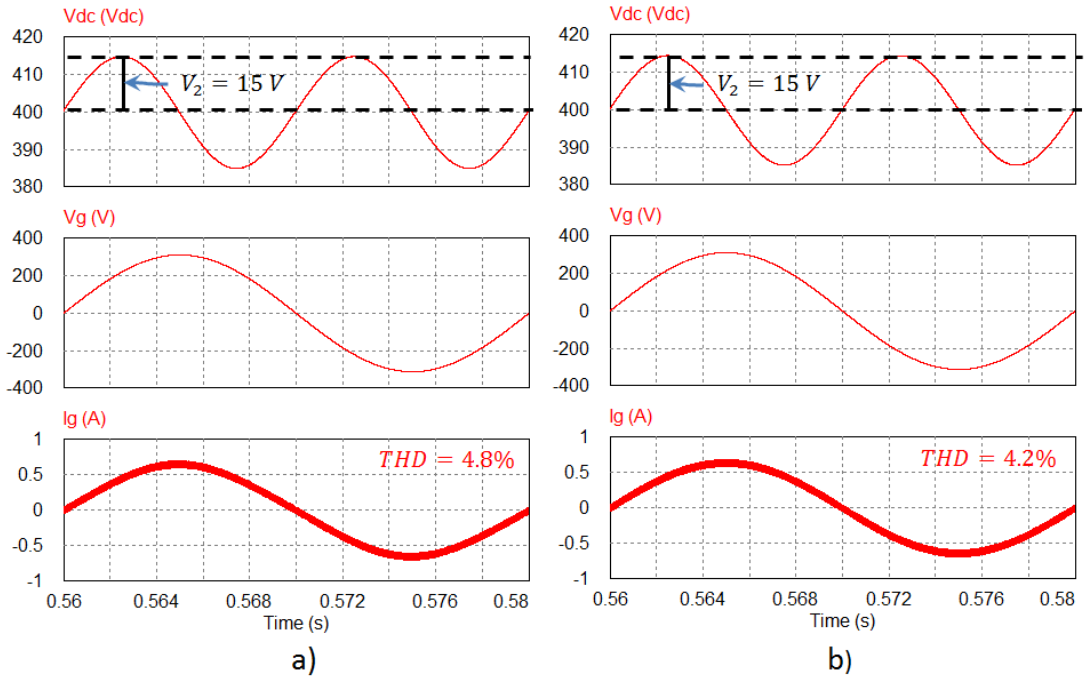

Fig. 4.18. Influence of the voltage ripple in the current harmonic distortion (L = 10 mH, C = 27 µF): a) case 1 (L = 100 mH, C = 27 µF); b) case 2 (L = 10mH, C = 47 µF).

4.8 INPUT CURRENT OF THE INVERTER

In the microinverter structure, the inverter shown in Figure 4.19 is fed by a DC-DC converter connected to A PV module. The converter has an output capacitor which is also the coupling element of the inverter. Hence, the interaction between both converters can be studied determining the behavior of the input current i_{in}.

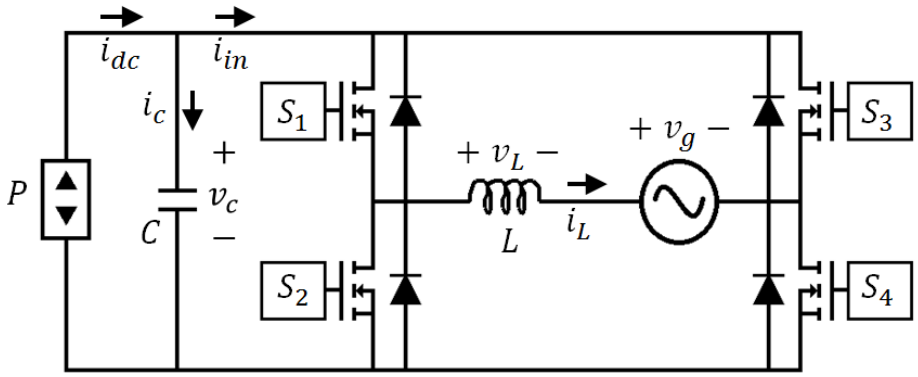

Fig. 4.19. Currents in the H-bridge grid-connected PSI.

Considering a constant value of the power source *P*, it is possible to write:

$$i_{dc}(t) = \frac{P}{v_C(t)} = \frac{P}{V_{dc} + V_2\, sin(2\omega t + \gamma)} \tag{4.87}$$

In order to simplify the study, we apply the change of coordinates $v_C' = V_2\, sin(2\omega t')$ and then:

$$i_{dc}'(t) = \frac{P}{V_{dc} + V_2\, sin\, 2\omega t'} \tag{4.88}$$

Considering only the DC and a double frequency component of the input current $i_{dc}'(t)$, we have:

$$i_{dc}'(t) = I_{p_{dc}} + i_{p_2} = I_{p_{dc}} + I_{p_2}\, sin(2\omega t' + \beta) \tag{4.89}$$

The magnitude $I_{p_{dc}}$ can be deduced as follows:

$$I_{p_{dc}} = \frac{P}{2\pi}\int_{-\pi}^{\pi}\frac{d\omega t'}{V_{dc} + V_2\, sin\, 2\omega t'}$$

$$I_{p_{dc}} = \frac{P}{2V_{dc}\pi}\int_{-\pi}^{\pi}\frac{d\omega t'}{1 + \frac{V_2}{V_{dc}}\, sin\, 2\omega t'} \tag{4.90}$$

Applying the change of variable $t = \tan\frac{\omega t}{2}$, the integral can be evaluated and leads to:

$$I_{p_{dc}} = \frac{P}{\sqrt{{V_{dc}}^2 - {V_2}^2}} \tag{4.91}$$

The value of I_{p_2} can be deduced from the Fourier series expansion, having that $I_{p_2} = \sqrt{{a_1}^2 + {b_1}^2}$, where a_1 and b_1 are the corresponding Fourier coefficients of the fundamental frequency, that is:

$$i'_{dc}(t) = I_{p_{dc}} + i_{p_2} = I_{p_{dc}} + a_1 \cos 2\omega t' + b_1 \sin 2\omega t' \tag{4.92}$$

with

$$a_1 = \frac{2}{T}\int_{-\frac{\pi}{2}}^{\frac{\pi}{2}}\frac{P\cos 2\omega t'\, d\omega t'}{V_{dc} + V_2\, sin\, 2\omega t'} = \frac{P}{\pi}\int_{-\pi}^{\pi}\frac{\cos 2\omega t'\, d\omega t'}{V_{dc} + V_2\, sin\, 2\omega t'} \tag{4.93}$$

After the substitutions$x = 2\omega t'$ and $y = V_{dc} + V_2 \sin x$, we have:

$$a_1 = \frac{P}{2\pi V_2}\ln(V_{dc} + V_2\, sin\, 2\omega t')\Big|_{-\frac{\pi}{2}}^{\frac{\pi}{2}} \tag{4.94}$$

From which it is obtained that $a_1 = 0$. On the other hand:

$$b_1 = \frac{2}{T}\int_{-\frac{\pi}{2}}^{\frac{\pi}{2}}\frac{P\sin 2\omega t'\, d\omega t'}{V_{dc} + V_2\, sin\, 2\omega t'} = \frac{P}{\pi}\int_{-\frac{\pi}{2}}^{\frac{\pi}{2}}\frac{\sin 2\omega t'\, d\omega t'}{V_{dc} + V_2\, sin\, 2\omega t'} \tag{4.95}$$

By applying the substitution $x = 2\omega t'$, we have:

$$b_1 = \frac{P}{2\pi V_2}\left[\int_{\alpha}^{\beta} dx - V_{dc}\int_{\alpha}^{\beta}\frac{du}{V_{dc} + V_2\, sin\, u}\right] \tag{4.96}$$

where $\alpha = -\pi$ and $\beta = \pi$. Note that the second integral is the same in (4.90), from which it is obtained that:

$$b_1 = \frac{P}{2\pi V_2}\left[2\omega t' - \frac{1}{\sqrt{1-\left(\frac{V_2}{V_{dc}}\right)^2}}\left[\text{atan}\left(\frac{\tan\frac{2\omega t'}{2} + \frac{V_2}{V_{dc}}}{\sqrt{1-\left(\frac{V_2}{V_{dc}}\right)^2}}\right)\right]\right]_{-\frac{\pi}{2}}^{\frac{\pi}{2}} \tag{4.97}$$

$$= \frac{2P}{V_2}\left(\frac{-V_{dc} + \sqrt{{V_{dc}}^2 - {V_2}^2}}{\sqrt{{V_{dc}}^2 - {V_2}^2}}\right)$$

Another expression of i'_{dc} is given by:

$$i'_{dc}(t) = I_{p_{dc}} + i_{p_2} = \frac{P}{\sqrt{{V_{dc}}^2 - {V_2}^2}} + \frac{2P}{V_2}\left(\frac{-V_{dc} + \sqrt{{V_{dc}}^2 - {V_2}^2}}{\sqrt{{V_{dc}}^2 - {V_2}^2}}\right) sin(2\omega t') \tag{4.98}$$

The current of the capacitor is defined as:

$$i'_c(t') = C\frac{dv_c}{dt} = C\frac{d}{dt}(V_{dc} + V_2\, sin\, 2\omega t') \tag{4.99}$$

$$i'_c(t') = 2\omega C V_2 \cos 2\omega t' \tag{4.100}$$

Then, the current $i'_{in}(t)$ is:

$$i'_{in}(t') = i'_{dc}(t') - i'_c(t')$$

and:

$$i'_{in}(t) = \frac{P}{\sqrt{{V_{dc}}^2 - {V_2}^2}} + \frac{2P}{V_2}\left(\frac{-V_{dc} + \sqrt{{V_{dc}}^2 - {V_2}^2}}{\sqrt{{V_{dc}}^2 - {V_2}^2}}\right)\sin 2\omega t' - 2\omega C V_2 \cos 2\omega t' \tag{4.101}$$

These mathematical expressions have been verified using PSIM simulations. The current waveforms in figure 4.20 are obtained for a power of 100 W, a DC voltage of 400 V and a coupling capacitor of 27 µF. The average component and the amplitude of the fundamental components are represented.

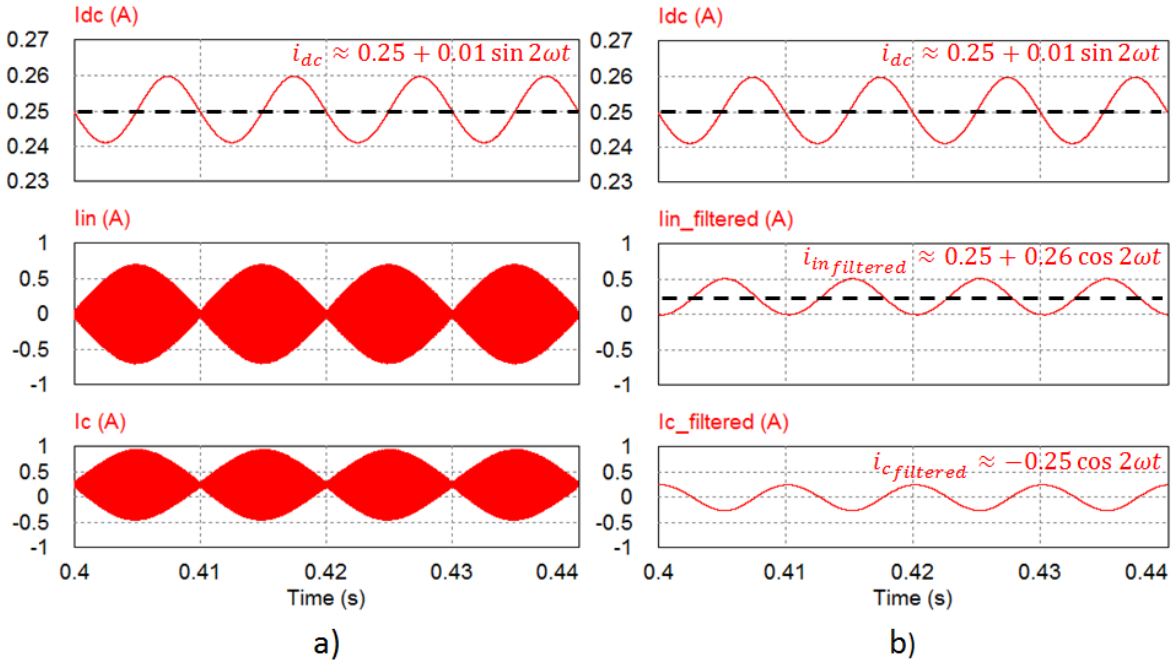

Fig. 4.20. a) Current waveforms of the inverter; b) average and fundamental current components.

Now, on the one hand, it is possible to represent the Power Source Inverter as a controlled current load which can involve the PI controller regulating the voltage of the DC bus and also the dynamic model of the DC-DC converter. On the other hand, it is possible to estimate the THD of the input current which is a key performance indicator when the converter can be considered as an independent device fed by a DC source.

4.9 EFFICIENCY ASPECTS

4.9.1 Analysis of the switching frequency

The sliding-mode based controller can be easily implemented using a hysteresis comparator. Using this, the control law (4.16) becomes

$$u = \begin{cases} 1 & when\ S(x) > \delta \\ -1 & when\ S(x) < -\delta \end{cases} \tag{4.102}$$

Then, the inductor current is constrained between two envelopes defined by the expressions

$$i_{g_+} = I_{max} \sin \omega t + \delta \tag{4.103}$$

$$i_{g\_} = I_{max} \sin \omega t - \delta \tag{4.104}$$

Figure 4.21 shows the current inductor waveforms delimited by the envelopes (4.103) and (4.104) for two commutation methods of the inverter.

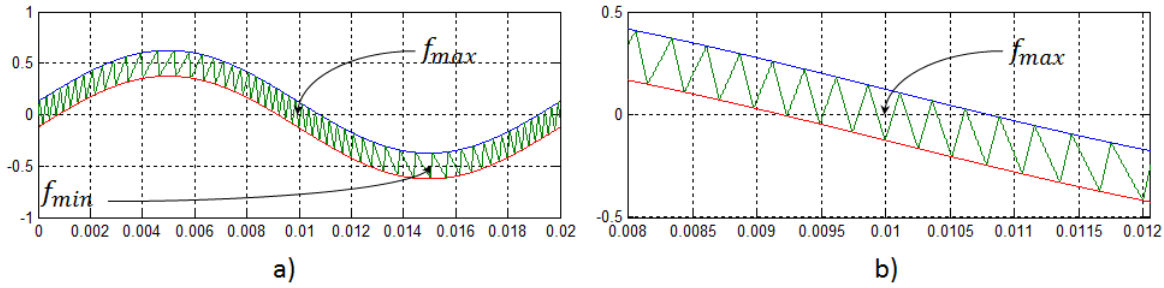

Fig. 4.21. Simulated inductor current waveform: a) frequency variation in a period; b) detail of the zero crossing.

Considering that the switching frequency is much higher than the grid frequency and that the hysteresis band is small when compared with the current amplitude, it is possible to analyze the motion of the current waveform considering a linear evolution during both intervals of the variable *u (u=1, u=-1).* Hence, the switching period and switching frequency in the bipolar commutation mode can be determined as follows:

$$T_s = \Delta t|_{u=1} + \Delta t|_{u=-1} = \frac{2\delta L}{V_C - V_g} + \frac{2\delta L}{V_C + V_g} = \frac{4\delta L V_C}{{V_C}^2 - {V_g}^2}$$

$$f_s = \frac{{V_C}^2 - {V_g}^2}{4\delta L V_C} \tag{4.106}$$

The switching frequency is constrained within the interval $f_{s_{min}} > f_s > f_{s_{max}}$. The maximum frequency corresponds to the zero crossing of V_g and is given by:

$$f_{s_{max}} = \frac{V_C}{4\delta L} \tag{4.107}$$

while the minimum one corresponds to the maximum value of V_g, having the expression:

$$f_{s_{min}} = \frac{{V_C}^2 - {V_{max}}^2}{4\delta L V_C} \tag{4.108}$$

Using the same analysis for unipolar commutation, it is obtained that:

$$T_s = \Delta t|_{u=1} + \Delta t|_{u=-1} = \frac{2\delta L}{V_C - V_g} + \frac{2\delta L}{V_g} = \frac{2\delta L V_C}{V_g(V_C - V_g)}$$

$$f_s = \frac{V_g(V_C - V_g)}{2\delta L V_C} \tag{4.109}$$

Only the maximum frequency can be determined by equalizing df_s/dV_g to zero, having the maximum frequency when the voltage V_g is equal to $V_C/2$, and:

$$f_{s_{max}} = \frac{V_C}{8\delta L} \tag{4.110}$$

4.9.2 Efficiency analysis

In order to assess the efficiency of the sliding-mode current controlled inverter, both conduction and switching losses are considered. The conduction losses are produced in the ON resistance of the switches and also in the copper resistance of the inductor. To compute these losses, it is considered that the inductor current which is the same current flowing from inverter to the grid, continuously passes through two switches and the series resistance of the inductor. Then, considering that an amplitude value of the current ripple below 30% does not introduce a considerable deviation of the conduction power losses [59], we have

$$P_{P_{con}} = \frac{{I_{max}}^2}{\sqrt{2}}(2R_M + R_L) \tag{4.111}$$

where R_M is the on-resistance of the MOSFETs and R_L is the equivalent series resistor of the inductor. The coupled capacitor is not considered in this analysis because it is included in chapter 2 as a part of the DC-DC converter.

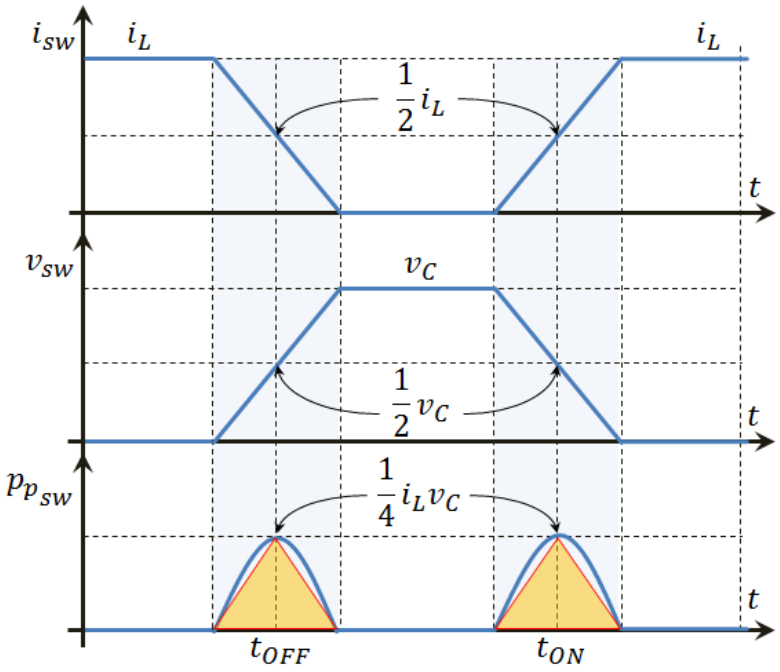

Fig. 4.22. Graphical analysis of the turn-off and turn-on commutations in the power MOSFETs.

To obtain an estimation of the switching losses, the analysis of the current and voltage transitions in both turn-on and turn-off commutations is proposed. Figure 4.22 shows the approximation of these transitions without considering the ripple values in the current or the effect of the body diodes of the MOSFET. This assumption allows concentrating the complexity of the analysis problem in the frequency variation introduced by the hysteresis- based implementation of the sliding mode control. Now, the switching losses in each power switch can be estimated as:

$$E_{P_{ON}} = \frac{1}{8} I_L V_C t_{on} \tag{4.112}$$

$$E_{P_{OFF}} = \frac{1}{8} I_L V_C t_{off} \tag{4.113}$$

However, the time varying nature of the current waveform leads to the expression:

$$\begin{aligned} P_{P_{sw}}(t) &= \frac{V_C f_s I_{max}\left(t_{on} + t_{off}\right)}{8} \sin \omega t \\ &= \frac{I_{max}\left(t_{on} + t_{off}\right)}{32\pi\delta L}\left[{V_C}^2 \sin \omega t - {V_{max}}^2 \sin^3 \omega t\right] \end{aligned} \tag{4.114}$$

where f_s has been taken of (4.108). Then, the power switching losses can be computed as the average of the function $P_{P_{sw}}(t)$ during a half period of the grid ($T = \pi$):

$$\overline{P_{P_{sw}}} = \frac{1}{T}\int_0^T P_{P_{sw}}(t)\,dt = \frac{I_{max}V_C\left[t_{on}+t_{off}\right]}{32\pi\delta L V_C}\int_0^{\pi}\left[{V_C}^2\sin\omega t - {V_{max}}^2\sin^3\omega t\right]d\omega t \tag{4.115}$$

After solving some simple calculations, the power switching losses are computed as follows:

$$\overline{P_{P_{sw}}} = \frac{I_{max}\left[t_{on}+t_{off}\right]}{16\delta L\pi}\left({V_C}^2 - \frac{2}{3}{V_{max}}^2\right) \tag{4.116}$$

Figure 4.23 shows the grid voltage and current waveforms as references to analyze the frequency and switching power losses waveforms. The average values of the frequency and the power switching losses are identified to be subsequently introduced in the expressions of the losses.

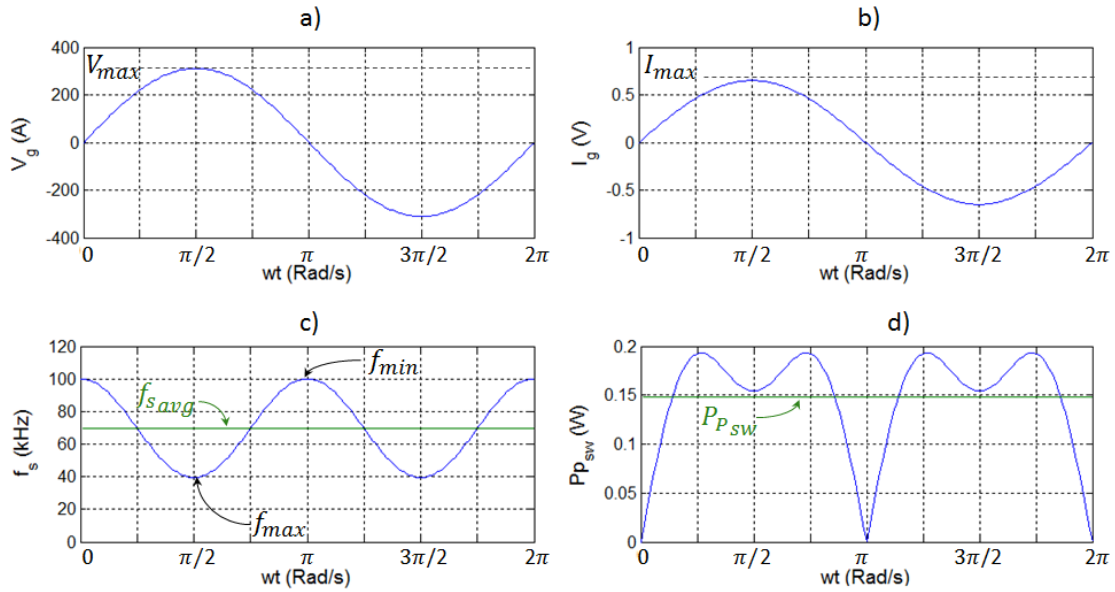

Fig. 4.23. Waveforms to analyze the power switching losses: a) grid voltage, b) average grid current, c) instantaneous switching frequency, and d) instantaneous and average power switching losses.

4.9.3 Simulated results

From the above analysis it is possible to estimate the efficiency of the inverter by means of a computational tool. In this case a MATLAB- based algorithm has been created in order to have an approximation of the converter efficiency for different operational points of the inverter. Then, the efficiency is computed for a set of values of grid voltage and output power considering the voltage in the DC bus regulated at a constant value. Figure 4.24 shows the simulated results for bus voltage of 400 VDC using the parameters listed in table 4.6. Intervals t_{off} and t_{on} have been approximated by t_f and t_r respectively.

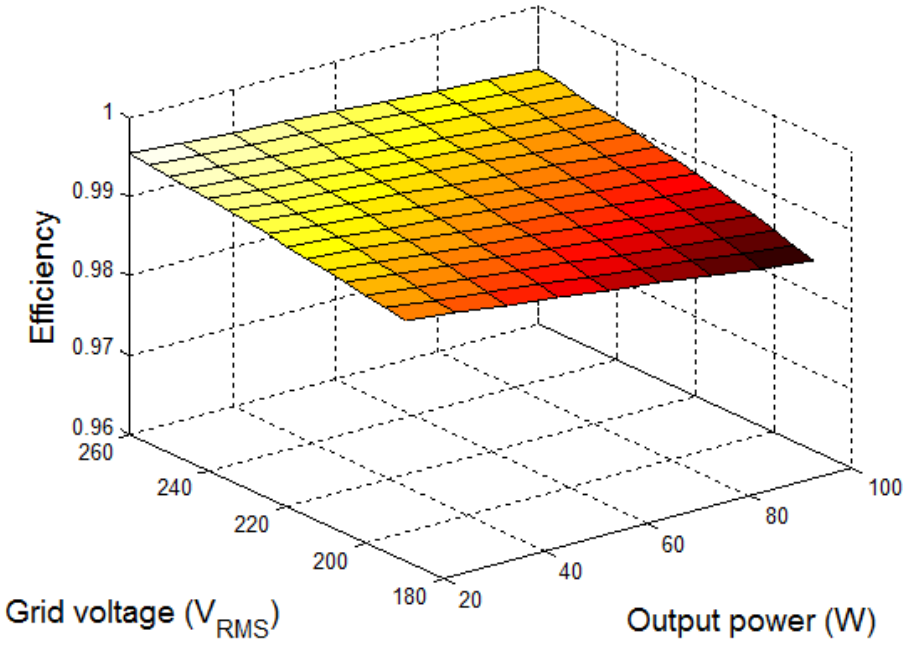

Fig. 4.24. Inverter efficiency as a function of the grid voltage and output power considering a regulated DC-bus.

As it can be shown in the figure, better efficiency levels are obtained with high values of grid voltage and low powers while low efficiencies appear for low grid voltages and high output powers. The difference between the maximum and minimum values of the simulated efficiency is limited.

4.10 EXPERIMENTAL RESULTS

Several theoretical analyses have been made to explain the static and dynamic behavior of the full bridge PSI covering the requirements of the DC-AC stage of a dual stage microinverter. Parameters of the signal waveforms and power quality factors are derived and verified through numerical simulations. This section shows experimental results of the system behavior under sliding mode control.

4.10.1 Prototype and experimental set-up

A 100 W prototype of the full bridge grid connected inverter has been implemented to work with an input voltage of 400 VDC and a grid voltage of 220 V and 50 Hz. The parameters of the converter are listed in table 4.6.

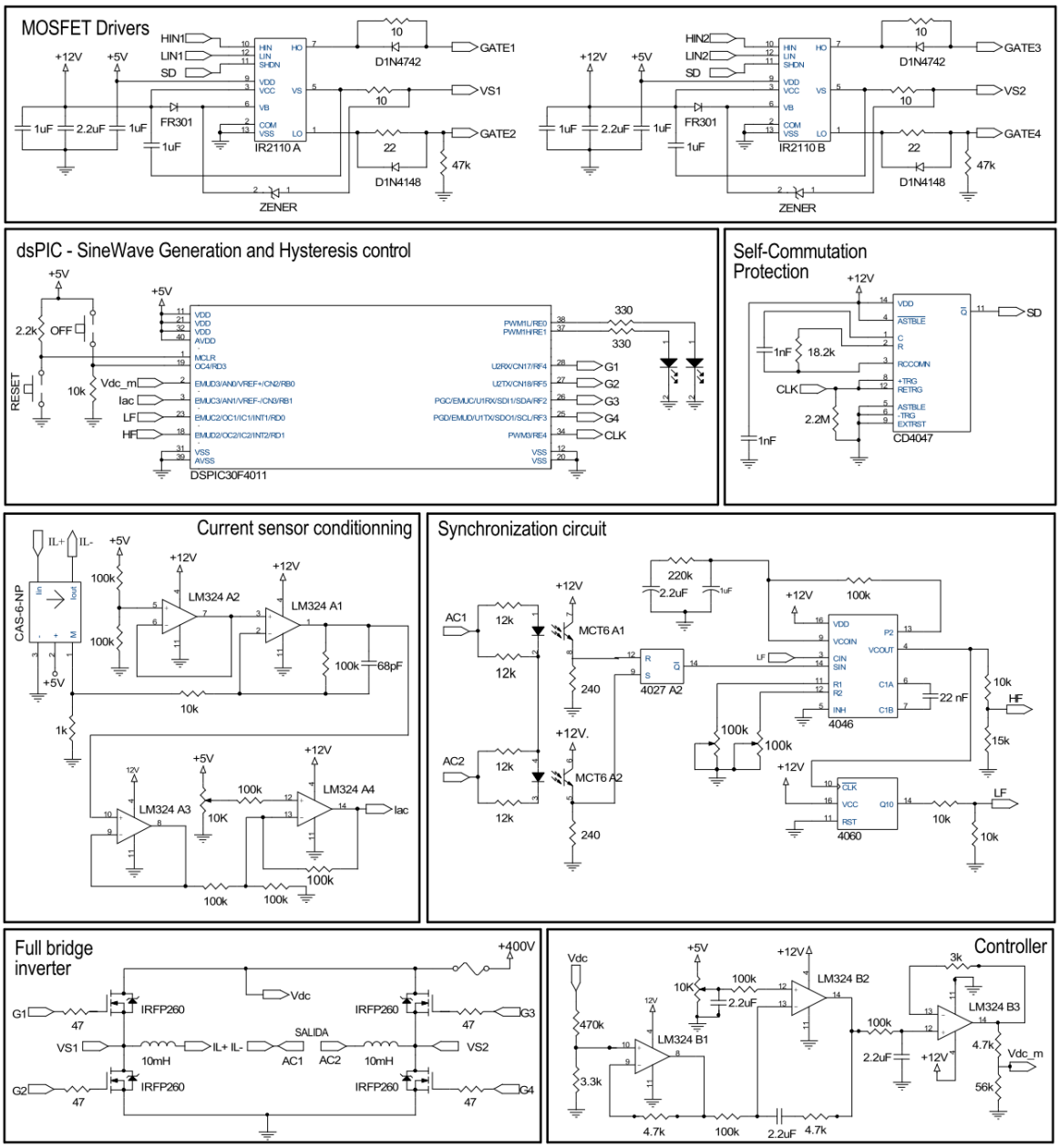

Fig. 4.25. Schematic circuit diagram of the power source inverter

The set-up for measurements shown in figure 4.26 consists of the oscilloscope MSO3014 from Tektronix, the current probes TCP202 and TCPA300 from Tektronix, high voltage differential probe P5210 from Tektronix, power supplies Rohde & Schwartz NGSM 32/10 and Multimeteix XA3033, multimeter HP34401A from Hewlett Packard.

Table 4.6. Passive elements and semiconductor used in the converter prototype

Element	Parameter	Symbol	Value
Inductor L	Inductance	L	10 mH
	Equivalent Series Resistance (ESR)	R_L	28 mΩ
Capacitor C (C4ATHBW4900A3LJ)	Capacitance	C	27 µF
	Equivalent Series Resistance (ESR)	R_C	1.9 mΩ
MOSFETs (APT94N60L2C3)	Drain – Source ON-resistance	R_M	35 mΩ
	Rise time	t_r	27 ns
	Fall time	t_f	8 ns

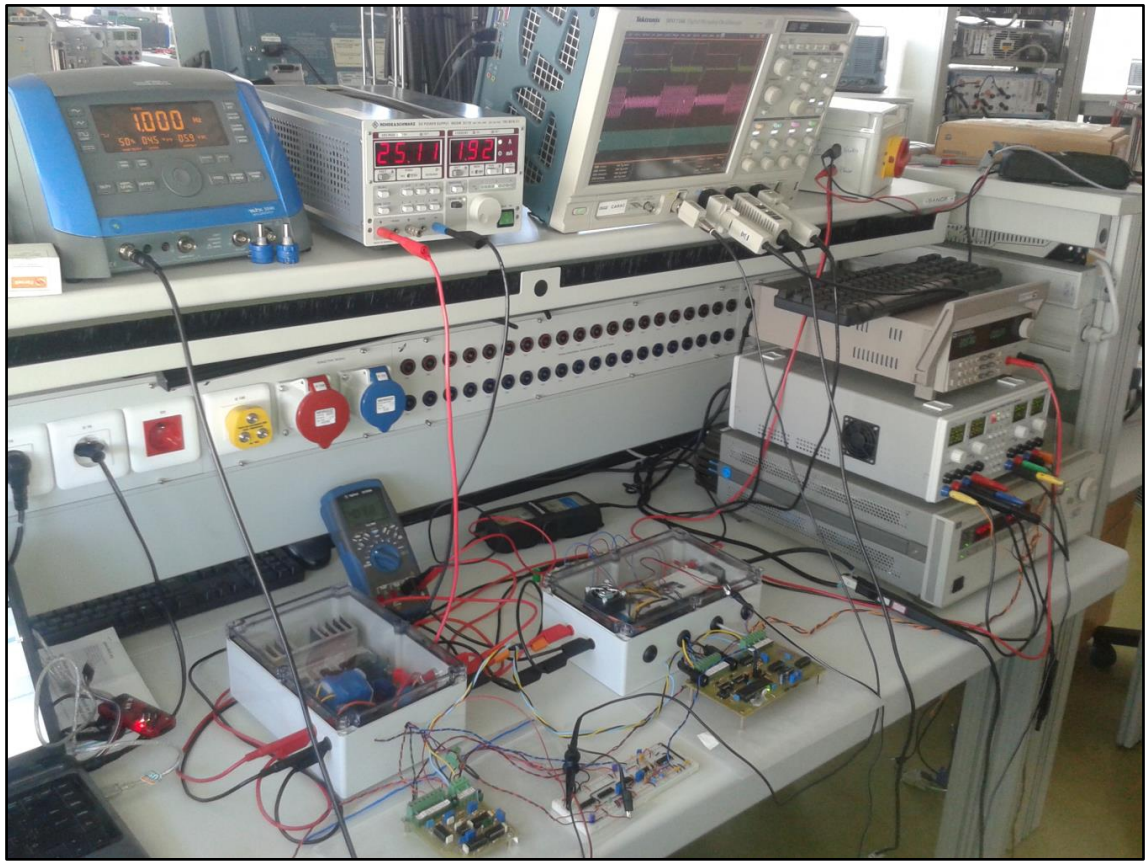

Fig. 4.26. Experimental set-up and inverter prototype.

The control circuit is implemented using a microcontroller dsPIC30F4011 and some classical discrete electronic circuits. The current reference is stored in the microcontroller using a pre-sampled table with 1024 samples per period. The microcontroller uses an external signal given by an external PLL to make the corresponding counter. The current controller is digitally implemented by means of the

microcontroller whereas the voltage controller is implemented with analog electronics. Two integrated circuit IR2120 has been used as MOSFET drivers. Figure 4.25 shows the schematic diagram of the inverter.

4.10.2 Current signal generation and current controller

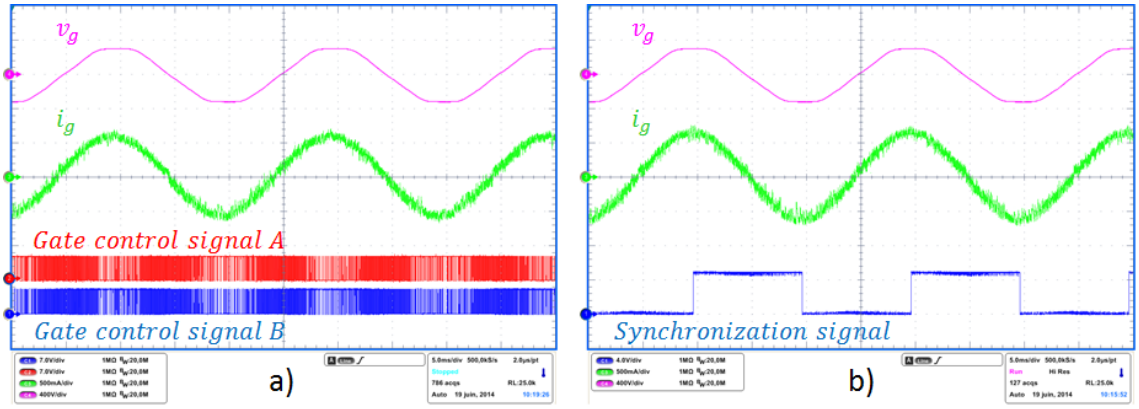

Fig. 4.27. Oscilloscope captures: a) grid voltage, output current and control signals (gate signals); b) grid voltage, output current and synchronization signal (90° of phase displacement).

The current reference signal is generated using a pre-sampled sine-waveform stored in the memory of the microcontroller, which has 1024 samples per grid period. An external PLL uses a simple zero crossing detection circuit to generate a square-wave signal at the grid frequency. A discrete PLL based on the integrated circuits CD4046 and CD4060 synchronizes with this signal generating a high frequency signal (HF: four times the sampling frequency) and a low frequency signal (LF: grid frequency). The low frequency signal has a phase-lag of 90° inherent to the PPL operation. The algorithm of the microcontroller uses the low frequency signal to start the reference compensating the phase-lag. The high frequency signal increases the pointer of the table once every four cycles drawing the sine-wave reference synchronized with the grid. The current controller is also implemented in the microcontroller constraining the switching frequency at the frequency of the HF signal. The figure 4.27 shows the grid voltage compared with the sinusoidal current, together with the gate signals of the H-bridge (4.27a) or the low frequency signal LF (4.27b). As it can be observed, the flattening of the grid voltage has no influence in the grid current, which illustrates the advantages of using a PLL to generate the current reference.

4.10.3 Voltage regulation of the DC-Link

In order to assess the dynamic response of the regulated DC bus, a power perturbation has been inserted using the DC-DC converter as a SM-LFR. The conductance value of the control is changed introducing a symmetrical square-wave signal (duty cycle equal 0.5) with an off-set level as shown in figure 4.28. In figure 4.28a it is illustrated the case of a change from 50 W to 80 W and from 80 W to 50 W using a frequency of 1 Hz. In figure 4.28b, the change of the power involves the 100 W and 20 W power levels.

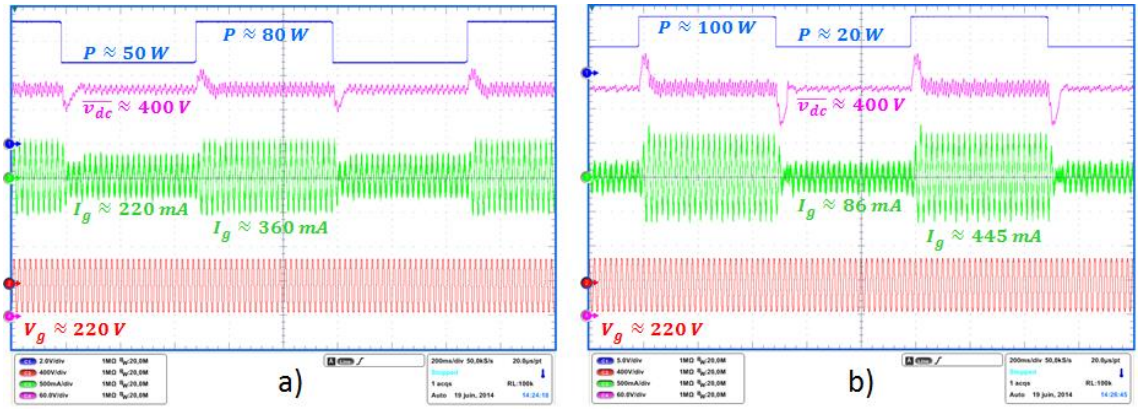

Fig. 4.28. Experimental results showing the transient response of the DC voltage loop: a) power changes from 50 W to 80 W and vice versa; b) power changes from 20 W to 100 W and vice versa.

4.10.4 Effect of the low pass filter on the current distortion

The effect of the filtering time- constant T_f of the controller in the harmonic distortion of the output current can be observed in the oscilloscope captures of figure 4.29. As it is shown for the same amplitude of the ripple in the DC bus, the current waveform is cleaner when the parameter T_f is close to the optimum value (fig. 4.29b). Also, it is possible to observe that the amplitude of the current reference i_{max} has more important harmonic contents when the current signal has higher THD (fig. 4.29a). This result confirms the expected reduction in the effect of the voltage ripple in the current THD. Future experimental work can introduce the proposed feed-forward compensation.

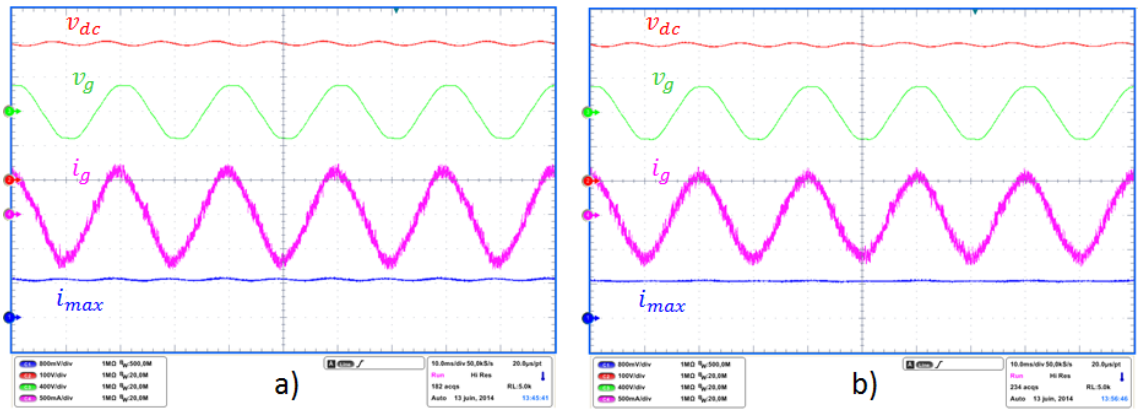

Fig. 4.29. Experimental results showing the filter effect a) $T_f = 0.0005$; b) $T_f = 0.005$.

4.11 CONCLUSIONS

In this chapter, the concept of Power Source Inverter (PSI) has been introduced in order to theoretically obtain all the parameters which describe the dynamic performance and the power quality of a grid-connected inverter operating with a first order sliding mode control law tracking a pure sine current reference. From the ideal sliding dynamic model a proportional-integral controller with an additional pole has been designed to regulate the voltage of the DC bus attenuating at the same time the oscillatory component at double grid frequency. This design has been verified in simulations and experimental results.

Although the full-bridge inverter is a well-known topology and its behavior has been deeply studied for inverters working with PWM and hysteresis comparators, this chapter has proposed an analysis of the operation of the converter in an ideal sliding motion connected to the grid, this involving many aspects which have not been discussed previously in the literature. Among the most important ones, these aspects are the power factor, the displacement power factor, the total harmonic distortion, the effect of a DC component in the current and in general, the harmonic balance of the converter. Simulations results have illustrated the theory and have been complemented at the end of the chapter by means of experimental results, which has shown the potentialities of the proposed PSI under sliding mode control.

4.12 REFERENCES

General aspects

[1] F. Schimpf, L. E. Norum, "Grid connected Converters for Photovoltaic, State of the Art, Ideas for Improvement of Transformerless Inverters," in Nordic Workshop on Power and Ind. Electron., Jun. 2008.

[2] M. A. Eltawil, Z. Zhao, "Grid-Connected Photovoltaic Power Systems: Technical and Potential Problems—A review," Renewable and Sustainable Energy Reviews, Vol. 14, pp 112-129, Jan. 2010.

[3] S. B. Kjaer, J. K. Pedersen and F. Blaabjerg, "Power Inverter Topologies for Photovoltaic Modules – A Review," in Conf. Record of the 37th Annual Meeting Industry Application Conf. (IAS), Oct. 2002, vol.2, pp. 782-788.

[4] S. B-Kjaer, J. K. Pedersen, and F. Blaabjerg, "A Review of Single-Phase Grid-Connected Inverters for Photovoltaic Modules," *IEEE Trans. on Industry Appl.*, vol. 41, no. 5, pp. 1292-1306, Sep/Oct 2005.

[5] M. Calais, J. Myrzik, T. Spoone and V. G. Agelidis, "Inverters for Single-phase Grid Connected Photovoltaic Systems - An Overview," *IEEE Trans. Ind. Appl.*,vol.41, no.5, pp.1292,1306, Sept.-Oct. 2005.

[6] T. Shimizu, O. Hashimoto and G. Kimura, "A Novel High-Performance Utility-Interactive Photovoltaic Inverter System," *IEEE Trans. Power Electron.*, vol. 18, no. 2, pp. 704-711, Mar.2003.

Transformer low frequency

[7] Guo Xiaoqiang, Zhao Qinglin and Wu Weiyang, "A Single-Phase Grid-Connected Inverter System with Zero Steady-State Error," in 5th IEEE Int. Power Electronics and Motion Control Conf. (IPEMC), Aug. 2006. vol.1, pp.1-5.

Fly-back

[8] AC. Nanakos, E.C. Tatakis, N.P. Papanikolaou, "A Weighted-Efficiency-Oriented Design Methodology of Flyback Inverter for AC Photovoltaic Modules," IEEE Trans. Power Electron., vol. 27, no. 7, pp. 3221-3233, Jul. 2012.

[9] Y. Kim, J. Jang, S. Shin, C. Won, "Weighted-Efficiency Enhancement Control for a Photovoltaic AC Module Interleaved Flyback Inverter Using a Synchronous Rectifier," IEEE Trans. Power Electron., vol. 29, no. 12, pp. 6481-6493, Dec. 2014.

[10] Y-H. Kim, Y.-H. Ji, J-G. Kim, Y-C. Jung, C-Y. Won, "A New Control Strategy for Improving Weighted Efficiency in Photovoltaic AC Module-Type Interleaved Flyback Inverters," IEEE Trans Power Electron., vol. 28, no. 6, pp. 2688-2699, Jun. 2013

[11] M. Gao, M. Chen, C. Zhang, Z. Qian, "Analysis and Implementation of an Improved Flyback Inverter for Photovoltaic AC Module Applications," IEEE Trans. Power Electron., vol. 29, no. 7, pp. 3428-3444, Jul. 2014.

[12] Y. Li, R. Oruganti, "A Low Cost Flyback CCM Inverter for AC Module Application," IEEE Trans. Power Electron., vol. 27, no. 3, pp. 1295-1303, Mar. 2012.

[13] F.F. Edwin, X. Weidong, V. Khadkikar, "Dynamic Modeling and Control of Interleaved Flyback Module-Integrated Converter for PV Power Applications," IEEE Trans. Ind. Electron., vol. 61, no. 3, pp. 1377-1388, Mar. 2014.

Push-pull

[14] Y-H. Kim, S-C. Shin, J-H. Lee, Y-C. Jung, C-Y. Won, "Soft-Switching Current-Fed Push–Pull Converter for 250-W AC Module Applications," IEEE Trans. Power Electron., vol. 29, no. 2, pp. 863-872, Feb. 2014.

[15] D. Cruz Martins and R. Demonti, "Interconnection of a Photovoltaic Panels Array to a Single-phase Utility Line from a Static Conversion System," in IEEE 31st Annual Power Electronics Specialists Conf. (PESC), 2000, vol.3, pp. 1207-1211.

Transformer-less

[16] M. Kusakawa, H. Nagayoshi, K. Kamisako and K. Kurokawa, "Further Improvement of a Transformerless, Voltage-Boosting Inverter for AC Modules," Solar Energy Materials and Solar Cells, vol. 67, Mar. 2001, Pages 379-387.

[17] P. Xu, X. Zhang, C.-w. Zhang, Ren-Xian, Cao and L. Chang, "Study of Z-Source Inverter for Grid-Connected PV Systems," in 37th IEEE Power Electronics Specialists Conf. (PESC), Jun. 2006, pp. 1-5.

[18] T. Kerekes, R. Teodorescu and U. Borup, "Transformerless Photovoltaic Inverters Connected to the Grid," in 22nd Annu. IEEE Applied Power Electronics Conf. (APEC), Mar. 2007, pp.1733-1737.

[19] S. Vasconcelos Araújo, P. Zacharias and R. Mallwitz, "Highly Efficient Single-Phase Transformerless Inverters for Grid-Connected Photovoltaic Systems," *IEEE Trans. Ind. Electron.*, vol. 57, no. 9, pp. 3118-3128, Sept. 2010.

[20] H. Xiao, S. Xie, Y. Chen, and R. Huang, "An Optimized Transformerless Photovoltaic Grid-Connected Inverter," *IEEE Trans. Ind. Electron.*, vol. 58, no. 5, pp. 1887-1895, May 2011.

[21] W. Yu, J-S. Lai, H. Qian, C. Hutchens, "High-Efficiency MOSFET Inverter with H6-Type Configuration for Photovoltaic Nonisolated AC-Module Applications," IEEE Trans. Power Electron., vol. 26, no. 4, pp. 1253-1260, Apr. 2011.

Multilevel Grid-Connected

[22] O. Lopez, Remus Teodorescu and J. Doval-Gandoy, "Multilevel transformerless topologies for single-phase grid-connected converters," in 32nd IEEE Annual Conf. on Industrial Electronics (IECON), Nov. 2006, pp.5191-5196.

[23] M. Calais, V. G. Agelidis,L. J. Borle and M. S. Dymond, "A Transformerless Five Level Cascaded Inverter Based Single Phase Photovoltaic System," in IEEE 31st Annual Power Electronics Specialists Conf. (PESC), vol. 3, 2000, pp.1173-1178.

[24] M. Calais and V. G. Agelidis, "Multilevel Converters for Single-Phase Grid-Connected Photovoltaic Systems – An Overview," in Proc. IEEE Int. Symp. on Industrial Electronics (ISIE), Jul. 1998, vol.1, pp.224-229.
[25] E. Beser, B. Arifoglu, S. Camur and E. K. Beser, "A grid-connected photovoltaic power conversion system with single-phase multilevel inverter," Solar Energy, vol. 84, pp. 2056-2067, Dec. 2010.

Cascaded

[26] M. Calais, V. G. Agelidis, M. S. Dymond, "A cascaded inverter for transformerless single-phase grid-connected photovoltaic systems," Renewable Energy, vol. 22, pp 255-262, Jan/Mar 2001.
[27] E. Villanueva, P. Correa, J. Rodríguez and M. Pacas, "Control of a Single-Phase Cascaded H-Bridge Multilevel Inverter for Grid-Connected Photovoltaic Systems," *IEEE Trans. Ind. Electron.,* vol. 56, no. 11, pp. 4399-4406, Nov. 2009.
[28] Y. Zhou; L. Liu, H. Li, "A High-Performance Photovoltaic Module-Integrated Converter (MIC) Based on Cascaded Quasi-Z-Source Inverters (qZSI) Using eGaN FETs," IEEE Trans. Power Electron., vol. 28, no. 6, pp. 2727-2738, Jun. 2013.

DC-Link Configuration

[29] Q. Li, and P. Wolfs, "A Review of the Single Phase Photovoltaic Module Integrated Converter Topologies with Three Different DC Link Configurations," *IEEE Trans. Power Electron.,* vol. 23, no. 3, pp. 1320-1333, May 2008.

Coupling element

[30] Y. Chen and F. Liu, "Research on Design and Control of a Grid Connected Photovoltaic Inverter," in 6th IEEE Int. Power Electronics and Motion Control Conf. (IPEMC), May 2009, pp. 2165-2169.

Power Conditioners

[31] M. Sedighy, S.B. Dewan, F.P.Dawson, "A Robust Digital Current Control Method for Active Power Filters," IEEE Trans. Ind. Applications, vol. 36, no. 4, pp. 1158-1164, Jul. 2000.
[32] M. Rukonuzzaman, M. Nakaona, "Single-Phase Shunt Active Power Filter with Harmonic Detection," IEE Proceedings, vol. 149, no.5, pp. 343-350, Sep. 2002.
[33] S. Rahmani, K. Al-Haddad, H.Y. Kanaan, "Two PWM Techniques for Single-Phase Shunt Active Power Filters Employing a Direct Current Control Strategy," IET Power Electron., vol. 1, no. 3, pp. 376-385, Jul 2008.

Grid-Connected Inverters

[34] E. Koutroulis, F. Blaabjerg, "Design optimization of grid-connected PV inverters," in proc. of the Annual IEEE Applied Power Electronics Conference and Exposition (APEC), pp. 691-698, Mar. 2011.
[35] B. Yang, W. Li, Y. Zhao, and X. He, "Design and Analysis of a Grid-Connected Photovoltaic Power System," *IEEE Trans. Power Electron.,* vol. 25, no. 4, pp. 992-1000, Apr. 2010.
[36] F.-S. Kang, C.-U Kim, S.-J. Park and H.-W. Park, "Interface Circuit for Photovoltaic System Based on Buck-Boost Current-Source PWM Inverter," in IEEE 28th Annual Conf. of the Industrial Electronics Society (IECON), Nov. 2002, vol. 4, pp.3257-3261.

PLL Control

[37] R.M. Santos-Filho, P.F. Seixas, P.C. Cortizo, L.A.B. Torres, A.F. Souza, "Comparison of Three Single-Phase PLL Algorithms for UPS Applications," IEEE Trans. Ind. Electron., vol. 55, no. 8, pp. 2923-2932, Aug. 2008.
[38] J.-W. Choi, Y.-K. Kim, H.-G. Kim, "Digital PLL control for single-phase photovoltaic system," IEE Proceedings, vol. 153, no. 1, pp. 40-46, Jan. 2006.
[39] S. Golestan, M. Monfared, F.D. Freijedo, J.M. Guerrero, "Dynamics Assessment of Advanced Single-Phase PLL Structures," IEEE Trans. Ind. Electron., vol. 60, no. 6, pp. 2167-2177, Jun. 2013.

DC-Link Control

[40] L. Zhang, K. Sun, Y. Xing, L. Feng, H. Ge, "A Modular Grid-Connected Photovoltaic Generation System Based on DC bus," IEEE Trans. Power Electron., vol. 26, no. 2, pp. 523-531, Feb. 2011.
[41] C. Meza, J.J. Negroni, D. Biel, F. Guinjoan, "Energy-Balance Modeling and Discrete Control for Single-Phase Grid-Connected PV Central Inverters," IEEE Trans. Ind. Electron., vol. 55, no. 7, pp. 2734-2743, Jul. 2008.
[42] M. Karimi-Ghartemani, S.A. Khajehoddin, P. Jain, A. Bakhshai, "A Systematic Approach to DC-Bus Control Design in Single-Phase Grid-Connected Renewable Converters," IEEE Trans. Power Electron., vol. 28, no. 7, pp. 3158-3166, Jul. 2013.

Current mode control

[43] C. Rodriguez, G.AJ. Amaratunga, "Dynamic maximum power injection control of AC photovoltaic modules using current-mode control," IEE Proceedings Electric Power Applications, vol. 153, no. 1, pp. 83-87, Jan. 2006.

Hysteresis current control

[44] Krismadinata, N. A. Rahim and J. Selvaraj, "Implementation of Hysteresis Current Control for Single-Phase Grid Connected Inverter," in 7th Int. Conf. on Power Electronics and Drive Systems (PEDS), Nov. 2007, pp.1097-1101.
[45] X. Dai and Q. Chao, "The Research of Photovoltaic Grid-Connected Inverter Based on Adaptive Current Hysteresis Band Control Scheme," in Int. Conf. on Sustainable Power Generation and Supply (SUPERGEN), Apr. 2009, pp. 1-8.
[46] C. N.-m Ho, V. S. P. Cheung and H. S.-. Chung, "Constant-Frequency Hysteresis Current Control of Grid-Connected VSI Without Bandwidth Control," *IEEE Trans. Power Electron*., vol. 24, no. 11, pp. 2484-2495, Nov. 2009.

[47] J. Gao, "Research on Photovoltaic Grid-Connected Inverter Based on Fuzzy Hysteresis Current Controller," in Asia-Pacific Power and Energy Engineering Conf. (APPEEC), Mar. 2011, pp.1-4.

Repetitive control

[48] S. Jiang, D. Cao, Y. Li, and F Z. Peng, "Grid-Connected Boost-Half-Bridge Photovoltaic Microinverter System Using Repetitive Current Control and Maximum Power Point Tracking," *IEEE Trans. Power Electron*, vol. 27, no. 11, pp. 4711-4722, Nov. 2012.

[49] H. M. Kojabadi, B. Yu, I. A. Gadoura, L. Chang, and M. Ghribi, "A Novel DSP-Based Current-Controlled PWM Strategy for Single Phase Grid Connected Inverters," *IEEE Trans. Power Electron.*, vol. 21, no. 4, pp. 985-993, Jul. 2006.

Sliding mode Grid Connected

[50] H. Jiabing, Z.Q. Zhu, H. Nian, L. Shang, Y. He, "Sliding mode current control of grid-connected voltage source converter," in proc. of the IEEE Energy Conversion Congress and Exposition (ECCE), pp. 912-919, Sep. 2010.

[51] V. Fernao Pires, D.M. Sousa, J.F. Martins, "Controlling a grid-connected T-type three level inverter system using a sliding mode approach," in proc. of the IEEE International Symposium on Industrial Electronics, pp. 2002-2007, Jun. 2014.

[52] H. Qunhai, L. Kong, T. Wei, G. Zhang, L. Kong, "A new method for the photovoltaic grid-connected inverter control," in proc. of the Third Int. Conf. on Electric Utility Deregulation and Restructuring and Power Technologies, pp. 2626-2629, Apr. 2008.

[53] I.-S. Kim, "Sliding mode controller for the single-phase grid-connected photovoltaic system," Applied Energy, vol. 83, Oct. 2006, pp. 1101-1115.

Digital sliding mode

[54] J.J. Negroni, C. Meza, D. Biel, F. Guinjoan, "Control of a buck inverter for grid-connected PV systems: a digital and sliding mode control approach," in proc. of the IEEE International Symposium on Industrial Electronics, vol. 2, pp. 739-744, Jun. 2005.

VSI and CSI

[55] M. Rashid, Power Electronics Handbook, Academic Press, 2001.

2-Levels and 3-Levels

[56] D.M. Baker, V.G. Agelidis and C.V. Nayer, "A comparison of tri-level and bi-level current controlled grid-connected single-phase full-bridge inverters," in Proc. IEEE Int. Symp. Ind. Electron. (ISIE), vol. 2, Jul. 1997, pp.463-468.

Equivalent control

[57] V. Utkin, J. Guldner and J. Shi, Sliding mode control in electromechanical systems, CRC Press, 2th. Edition, Taylor and Francis Group, 2009.

Ground current and DC current

[58] V. Salas, E. Olías, M. Alonso, F. Chenlo and A. Barrado, "DC Current Injection Into The Network From PV Grid Inverters," in Conf. Record of the 2006 IEEE 4th World Conf. on Photovoltaic Energy Conversion, May 2006, vol.2, pp.2371-2374.

Losses

[59] R.W. Erickson, and D. Maksimovic, Fundamentals of power electronics, 2th. Edition. Massachussetts: Kluwer Academic Publishers, 2000.

Chapter 5

Microinverter:
A Complete Sliding-Mode Approach

5.1. INTRODUCTION

In the introduction of this dissertation, a state-of the art of the module-integrated converters [1]-[4], micro-inverters [5]-[10] or AC modules [11]-[12] has been presented and our proposal concerning an "entirely-sliding-mode-controlled transformer-less single-phase dual-stage grid-connected micro-inverter" introduced [13]. As it can be observed in figure 5.1a, the proposed microinverter is composed of a power and a control blocks. A DC-DC and DC-AC converters are connected in series through a bus of 400 VDC.

In terms of control, as presented in figure 5.1b, three building blocks constitute the microinverter: the MPPT algorithm, the DC-DC converter and the DC-AC converter decomposing the microinverter and following respectively the contents of chapters 2, 3 and 4 respectively. The PV module and the DC-DC converter interact through the voltage (v_p) which is the voltage of an input capacitor connected in parallel with the PV module absorbing the high frequency component of the input current of the converter and smoothing the rapid changes of the PV voltage. The MPPT algorithm uses the measurement of the input voltage (v_p) and the input current (i_p) to compute the input power (p_p) and to set the conductance reference (G). The value of the conductance is then used in the control of the DC-DC converter to compute the corresponding current reference with also the measurement of the voltage (v_p). The output of the DC-DC stage interacts with its load (DC-AC stage) through the output current (i_o). The control of the DC-AC stage regulates the DC bus voltage and fixes the

amplitude of the grid current reference $\left(i_{g_{ref}}\right)$ defining the power output. The DC-AC converter is connected with the grid through the AC output current $\left(i_g\right)$. The measurement of the grid voltage $\left(v_g\right)$ is only used to synchronize the current reference.

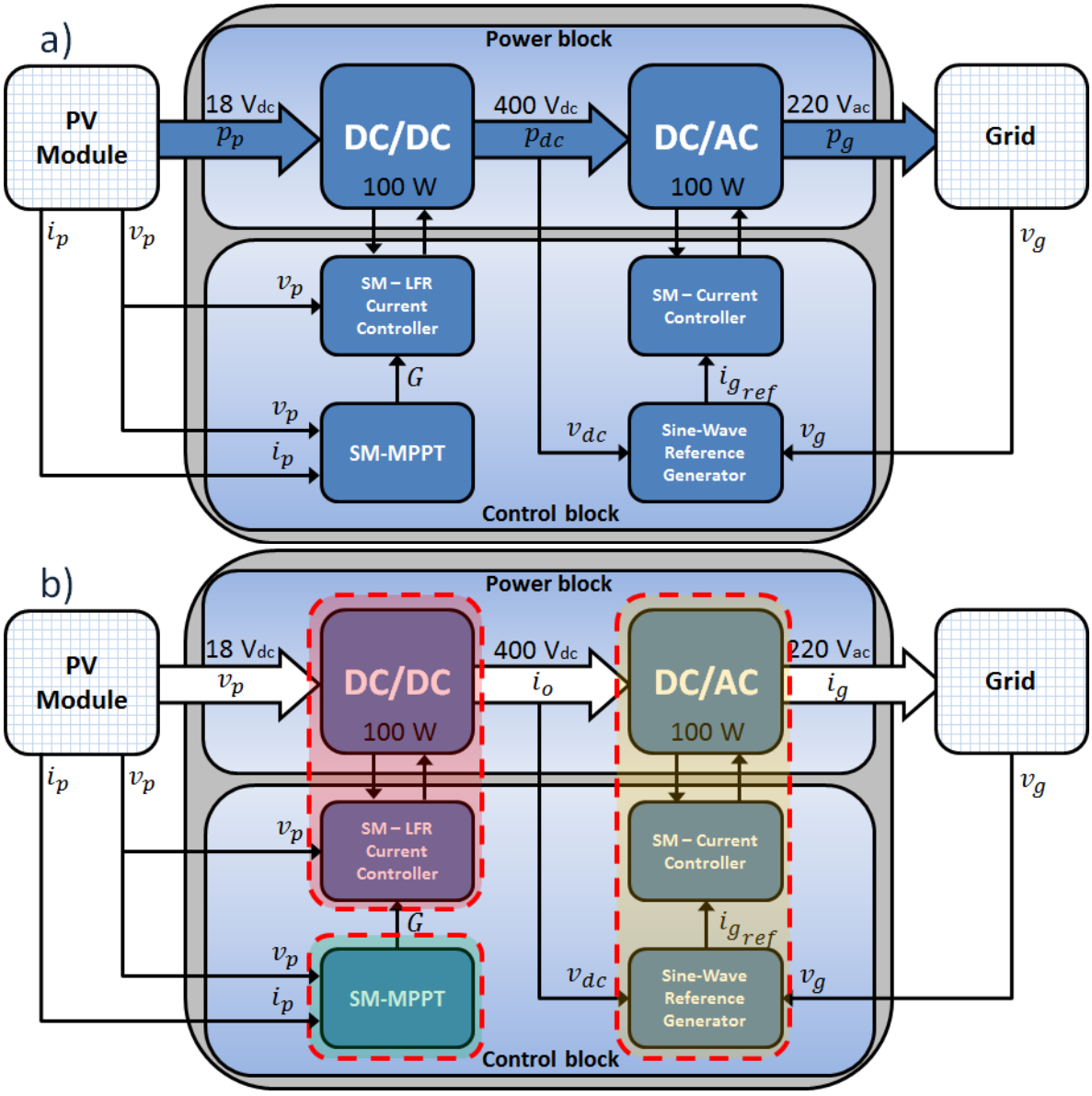

Fig. 5.1. General scheme of the sliding-mode controlled microinverter: a) Differentiation of the power stage and the control stages; b) differentiation of the studied pieces

This chapter uses the results derived in the three previous chapters in order to determine a global representation of the sliding-mode controlled microinverter system and study its stability. The model of the DC-DC converter developed in chapter 3 is

completed by introducing an input capacitor and a representation of the MPPT considering its internal stable dynamics and also convergence to the maximum power point. Furthermore, the regulation loop of the DC-AC output stage is combined with the model of the DC-DC stage in order to have a complete control scheme allowing a first approximation of a global model. The study is illustrated by simulations and experimental results developed in a 120 W prototype.

5.2. DERIVATION OF A GLOBAL MODEL

In chapter 3, the quadratic boost converter [14]-[15] has been studied to cover the requirements of the DC-DC stage of the microinverter. A linear model of the ideal sliding dynamics has been derived for the converter operating as a SM-LFR having a current source as load [16]. In that model, the system has three inputs and one output. The inputs are the incremental values of conductance (G), input voltage (v_p) and output current (i_o), and the output is the voltage of the output capacitor which is the same voltage of the DC bus (v_{dc}). To complete that model to give a more realistic approach of the DC-DC converter inserted in the microinverter structure, we propose the insertion of the input capacitor obtaining the input current (i_p) as the input variable given by the PV module retaining the conductance (G) as a variable given by the MPPT. Furthermore, the DC-AC converter is modeled as a load considering the DC component of its input current (i_o) as a function of the control loop used to regulate the voltage of the DC bus. Then, we have an averaged model of the internal microinverter dynamics with two input variables and an output variable.

5.2.1. DC-DC converter including the input capacitor

First of all, a coupling capacitor is inserted in the input port of the DC-DC converter changing the model of the quadratic boost converter studied in chapter 3. The obtained equations are:

$$
\begin{aligned}
\frac{dv_p}{dt} &= \frac{i_p}{C_p} - \frac{i_{L1}}{C_p} \\
\frac{di_{L1}}{dt} &= \frac{v_p}{L_1} - \frac{v_{C1}}{L_1}(1-u) \\
\frac{di_{L2}}{dt} &= \frac{v_{C1}}{L_2} - \frac{v_{C2}}{L_2}(1-u) \\
\frac{dv_{C1}}{dt} &= -\frac{i_{L2}}{C_1} + \frac{i_{L1}}{C_1}(1-u) \\
\frac{dv_{C2}}{dt} &= \frac{i_{L2}}{C_2}(1-u) - \frac{i_0}{C_2}
\end{aligned}
\tag{5.1}
$$

Recalling from chapter 3, the control strategy defining the SM-LFR behavior can be expressed as follows:

$$S(x) = i_{L1} - v_p(t)G(t) \tag{5.2}$$

Applying the invariance conditions ($S(x) = 0$ *and* $\dot{S}(x) = 0$) in (5.1) and (5.2) leads to the equivalent control:

$$1 - u_{eq} = \frac{v_p}{v_{C1}} - \frac{L_1}{v_{C1}}\left(v_p\frac{dG}{dt} + G\frac{dv_p}{dt}\right) \tag{5.3}$$

By introducing both $S(x) = 0$ and the expression of the equivalent control in (5.1), the equation system (5.4) will represent the resulting ideal sliding dynamics of the converter.

$$
\begin{aligned}
\frac{dv_p}{dt} &= \frac{i_p}{C_p} - \frac{v_p G}{C_p} \\
\frac{di_{L2}}{dt} &= \frac{v_{C1}}{L_2} - \frac{v_{C2}}{L_2}\left[\frac{v_p}{v_{C1}} - \frac{L_1}{v_{C1}}\left(v_p\frac{dG}{dt} + G\frac{dv_p}{dt}\right)\right] \\
\frac{dv_{C1}}{dt} &= -\frac{i_{L2}}{C_1} + \frac{i_{L1}}{C_1}\left[\frac{v_p}{v_{C1}} - \frac{L_1}{v_{C1}}\left(v_i\frac{dG}{dt} + G\frac{dv_p}{dt}\right)\right] \\
\frac{dv_{C2}}{dt} &= \frac{i_{L2}}{C_2}\left[\frac{v_p}{v_{C1}} - \frac{L_1}{v_{C1}}\left(v_p\frac{dG}{dt} + G\frac{dv_p}{dt}\right)\right] - \frac{i_0}{C_2}
\end{aligned}
\tag{5.4}
$$

The equilibrium point is then defined by:

$$\begin{aligned} &\overline{i_{L1}} = \overline{i_p} = V_p G; && \overline{i_{L2}} = \left(V_p G I_0\right)^{\frac{1}{2}}; \\ &\overline{v_{C1}} = {V_p}^{\frac{3}{2}}(G/I_0)^{\frac{1}{2}}; && \overline{v_{C2}} = \left({V_p}^2 G\right)/I_0 \end{aligned} \tag{5.5}$$

Linearizing (5.4) around the equilibrium point (5.5), the equation system (5.6) is obtained where the superscript (~) stands for the increments of the variables in (5.4) around the corresponding equilibrium values.

$$\begin{aligned} &\frac{d\widetilde{v_p}}{dt} = \frac{1}{C_p}\widetilde{i_p} - \frac{G}{C_p}\widetilde{v_p} + \frac{V_p}{C_p}\tilde{G} \\ &\frac{d\widetilde{i_{L2}}}{dt} = \frac{2}{L_2}\widetilde{v_{C1}} - \frac{1}{mL_2}\widetilde{v_{C2}} - \frac{m}{L_2}\widetilde{v_p} + \frac{mGL_1}{L_2}\frac{d\widetilde{v_p}}{dt} + \frac{mL_1V_p}{L_2}\frac{d\tilde{G}}{dt} \\ &\frac{d\widetilde{v_{C1}}}{dt} = \frac{-1}{C_1}\widetilde{i_{L2}} - \frac{G}{m^2C_1}\widetilde{v_{C1}} + \frac{2G}{mC_1}\widetilde{v_p} + \frac{V_p}{mC_1}\tilde{G} - \frac{V_pGL_1}{mC_1}\frac{d\tilde{G}}{dt} - \frac{G^2L_1}{mC_1}\frac{d\widetilde{v_p}}{dt} \\ &\frac{d\widetilde{v_{C2}}}{dt} = \frac{1}{mC_2}\widetilde{i_{L2}} - \frac{I_0}{mC_2V_p}\widetilde{v_{C1}} + \frac{I_0}{C_2V_p}\widetilde{v_p} - \frac{GL_1I_0}{C_2V_p}\frac{d\widetilde{v_p}}{dt} - \frac{L_1I_0}{C_2}\frac{d\tilde{G}}{dt} - \frac{1}{C_2}\widetilde{i_0} \end{aligned} \tag{5.6}$$

where $m = \overline{v_{C1}}/V_i = \overline{v_{C2}}/\overline{v_{C1}}$ and $G = m^2G/I_o$. Taking the Laplace transform of (5.6), the following multiple -input single- output transfer equation can be obtained:

$$A(s)V_{C2}(s) = B(s)G(s) + C(s)I_p(s) + D(s)I_0(s) \tag{5.7}$$

where:

$$\begin{aligned} A(s) = {} & mC_1C_2C_ps^4 + \left(\frac{GC_2C_p}{m} + mC_1C_2G\right)s^3 + \left[\frac{C_p}{L_2m}(2m^2C_2 + C_1) + \frac{G^2C_2}{m}\right] \\ & + \left[\frac{2GC_p}{L_2m^3} + \frac{G}{L_2m}(2m^2C_2 + C_1)\right]s + \frac{2G^2}{L_2m^3} \end{aligned} \tag{5.8}$$

$$\begin{aligned} B(s) = {} & -mI_oL_1C_1C_ps^4 + \frac{mC_1C_pV_pL_1}{L_2}s^3 - \left[\frac{I_oC_p}{m}\left(1 + m^2\frac{L_1}{L_2}\right) + mC_1I_o\right]s^2 \\ & + \left[\frac{2V_pC_p}{L_2m} - \frac{I_oGmL_1}{L_2} + \frac{mC_1V_p}{L_2}\right]s - \frac{2V_pG}{L_2m} \end{aligned} \tag{5.9}$$

$$\begin{aligned} C(s) = {} & -\frac{G^2C_1L_1}{m}s^3 + mC_1\left(\frac{G}{m^2} + \frac{GL_1}{L_2}\right)s^2 - \left(\frac{G^2}{m^2} + \frac{C_1m}{L_2} + \frac{2G^2L_1}{mL_2}\right)s \\ & + \frac{4G}{L_2m} \end{aligned} \tag{5.10}$$

$$D(s) = -mC_1C_ps^3 - \left(\frac{GC_p}{m} + C_1Gm\right)s^2 - \left(\frac{2mC_p}{L_2} + \frac{G^2}{m}\right)s - \frac{2mG}{L_2} \tag{5.11}$$

5.2.2. Modeling of the grid-connected DC-AC converter as a load

In chapter 4, a linear model has been derived for the ideal sliding dynamics of the inverter when it tracks a sinusoidal current reference. In that study, the converter has been treated as a Power Source Inverter (PSI) including the power decoupling capacitor and a voltage controller regulating the voltage of the DC bus. However, the coupling capacitor is also included in the study of the quadratic boost converter. Recalling that:

$$v_g = V_{max} \sin \omega t \tag{5.12}$$

$$i_g = I_{max} \sin(\omega t + \varphi) \tag{5.13}$$

being the displacement angle φ near to zero . Then, the real power is given by:

$$P_g \approx \frac{I_{max} V_{max}}{2} \tag{5.14}$$

Ideally the power at the DC bus is equal to the output power and then, we can write:

$$P_{dc} = P_g \approx \overline{v_{C2}} I_{dc} = V_{dc} I_o \approx \frac{I_{max} V_{max}}{2} \tag{5.15}$$

where V_{dc} is the reference of the regulated voltage of the DC bus and I_{dc} is the mean value of the output current of the DC-DC converter (which is the input current of the DC-AC converter). Then, the current I_o can be approximated by:

$$I_o \approx \frac{I_{max} V_{max}}{2 V_{dc}} \tag{5.16}$$

Then, the relation between incremental variations of the current I_o and the amplitude of the output current is given by:

$$\widetilde{\imath_o} \approx \frac{V_{max}}{2 V_{dc}} \widetilde{\imath_{max}} - \frac{I_{max} V_{max}}{2 {V_{dc}}^2} \widetilde{v_{dc}} \tag{5.17}$$

This last expression can be approximated as in (5.18) supposing that the amplitude of the oscillatory component of the voltage of the DC bus is considerably small in comparison with its average value. Further, the factor $\frac{V_{max}I_{max}}{2{V_{dc}}^2}$ is a few times smaller than one which further reduces the effect of that component.

$$\widetilde{\imath_o} \approx \frac{V_{max}}{2V_{dc}}\widetilde{\imath_{max}} \approx K_g\widetilde{\imath_{max}} \tag{5.18}$$

Taking the Laplace transform, it is obtained that:

$$I_o(s) = K_g I_{max}(s) \tag{5.19}$$

5.2.3. Derivation of a model for the chain DC-DC-AC

Considering the voltage regulation loop developed in Chapter 4, the current $I_{max}(s)$ is defined by a compensator with the form:

$$C_{dc}(s) = -\frac{K_c(T_c s + 1)}{s(T_f s + 1)} \tag{5.20}$$

Then, the block diagram depicted in figure 5.2 can be deduced.

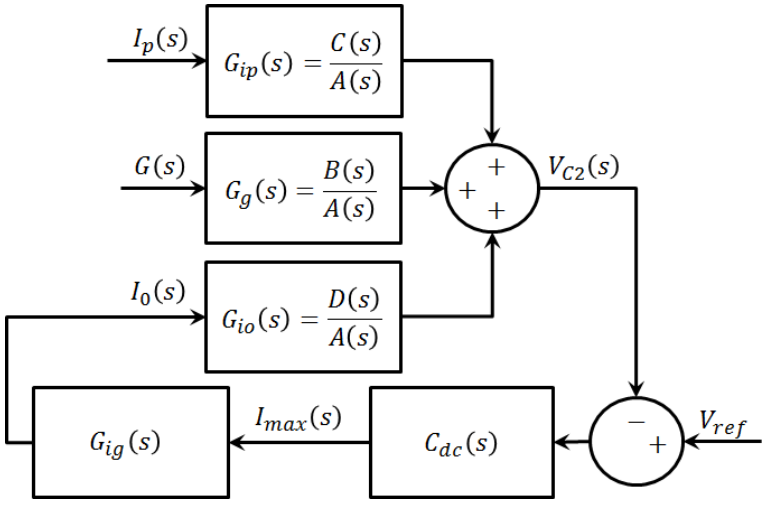

Fig. 5.2. Block diagram of the linear approach coupling the DC-DC stage and the DC-AC stage

The loop transfer function is given by:

$$L(s) = \frac{Num(s)}{Den(s)} = K_g G_{ig}(s)\left(\frac{D(s)}{A(s)}\right) = \frac{K_g K_c (T_c s + 1)}{s\left(T_f s + 1\right)}\left(\frac{D(s)}{A(s)}\right) \tag{5.21}$$

where:

$$\begin{aligned} Num(s) = {} & K_c K_g T_c C_1 C_p m s^4 + K_c K_g \left(C_1 C_p m + \frac{T_c G C_p}{m} + T_c C_1 m G\right) s^3 \\ & + K_c K_g \left(\frac{G C_p}{m} + C_1 G m + \frac{2 T_c m C_p}{L_2} + \frac{T_c G^2}{m}\right) s^2 \\ & + K_c K_g \left(\frac{2 m C_p}{L_2} + \frac{G^2}{m} + \frac{2 m G T_c}{L_2}\right) s + \frac{2 K_c K_g m G}{L_2} \end{aligned} \tag{5.22}$$

$$\begin{aligned} Den(s) = {} & m C_1 C_2 C_p T_f s^6 + \left(m C_1 C_2 C_p + \frac{G C_2 C_p T_f}{m} + m C_1 C_2 G T_f\right) s^5 \\ & + \left[\frac{G C_2 C_p}{m} + m C_1 C_2 G + \frac{C_p T_f}{L_2 m}(2 m^2 C_2 + C_1) + \frac{G^2 C_2 T_f}{m}\right] s^4 \\ & + \left[\left(\frac{C_p}{L_2 m} + \frac{G T_f}{L_2 m}\right)(2 m^2 C_2 + C_1) + \frac{G^2 C_2}{m} + \frac{2 G T_f}{L_2 m^3}\right] s^3 \\ & + \left[\frac{2G}{L_2 m^3}\left(C_p + G T_f\right) + \frac{G}{L_2 m}(2 m^2 C_2 + C_1) + \frac{2 G^2 T_f}{L_2 m^3}\right] s^2 + \frac{2 G^2}{L_2 m^3} s \end{aligned} \tag{5.23}$$

Then, the characteristic polynomial is $P(s) = Den(s) + Num(s)$:

$$\begin{aligned} P(s) = {} & m C_1 C_2 C_p T_f s^6 + \left(m C_1 C_2 C_p + \frac{G C_2 C_p T_f}{m} + m C_1 C_2 G T_f\right) s^5 \\ & + \left[\frac{G C_2 C_p}{m} + m C_1 C_2 G + \frac{C_p T_f}{L_2 m}(2 m^2 C_2 + C_1) + \frac{G^2 C_2 T_f}{m}\right. \\ & \left. + K_c K_g T_c C_1 C_p m\right] s^4 \\ & + \left[\left(\frac{C_p + G T_f}{L_2 m}\right)(2 m^2 C_2 + C_1) + \frac{G^2 C_2}{m} + \frac{2 G T_f}{L_2 m^3}\right. \\ & \left. + K_c K_g \left(C_1 C_p m + \frac{T_c G C_p}{m} + T_c C_1 m G\right)\right] s^3 \\ & + \left[\frac{2G}{L_2 m^3}\left(C_p + G T_f\right) + \frac{G}{L_2 m}(2 m^2 C_2 + C_1)\right. \\ & \left. + \frac{2 G^2 T_f}{L_2 m^3} K_c K_g \left(\frac{G C_p}{m} + C_1 G m + \frac{2 T_c M C_p}{L_2} + \frac{T_c G^2}{m}\right)\right] s^2 \\ & + \left[K_c K_g \left(\frac{2 m C_p}{L_2} + \frac{G^2}{m} + \frac{2 m G T_c}{L_2}\right) + \frac{2 G^2}{L_2 m^3}\right] s + \frac{2 K_c K_g m G}{L_2} \end{aligned} \tag{5.24}$$

As it can be noted in (5.24) the coefficients of the characteristic polynomial depends on the equilibrium values of the input and output voltages (m), the converter parameters, the instantaneous conductance given by the MPPT (G) and the voltage controller parameters. The stability of the system in the neighborhood of each equilibrium point can be evaluated. However, the operational range of the PV module variables is required and hence a brief analysis is presented before.

5.2.4. Characterization of the PV module

The operational ranges of the PV module have been obtained from the I-V and P-V characteristics shown in figure 5.3. The curves have been generated by means of the analytical model of the PV module using the Lambert-W function:

$$i_p = I_{pv} + I_0 - \frac{V_{ta}}{R_s} W\left(\frac{R_s I_0}{V_{ta}} \exp\left(\frac{v_p + R_s\left(I_{pv} + I_0\right)}{V_{ta}}\right)\right) \tag{5.25}$$

I_0 is the saturation current, R_s is the series resistance, I_{pv} is the photogenerated current and $V_{ta}$is the thermal voltage. I_{pv} and V_{ta} are given by:

$$I_{pv} = I_{sc}\left(\frac{S}{S_n} + C_t(T - T_n)\right) \tag{5.26}$$

$$V_{ta} = N_s AKT/q \tag{5.27}$$

N_s is the number of cells conforming the PV module, A is the diode quality factor, K is the Boltzmann constant ($1.3806504 \times 10^{-23}$ J/K) and q is the electron charge (-1.602×10^{-19} C). The values of the parameters are listed in table 5.1.

It is possible to note in figure 5.3 that the voltage of the PV module varies in a reduced interval (20.6 to 22.2 V) working with a wide range of powers (24.81 to 103.5 W). The conductance at the maximum power point of the PV module takes values between 0.06 and 0.21 S for currents between 1.203 and 4.602 A. Thus, a change in the power of the PV module results from a simultaneous change of conductance $G(s)$ and input current $I_p(s)$.

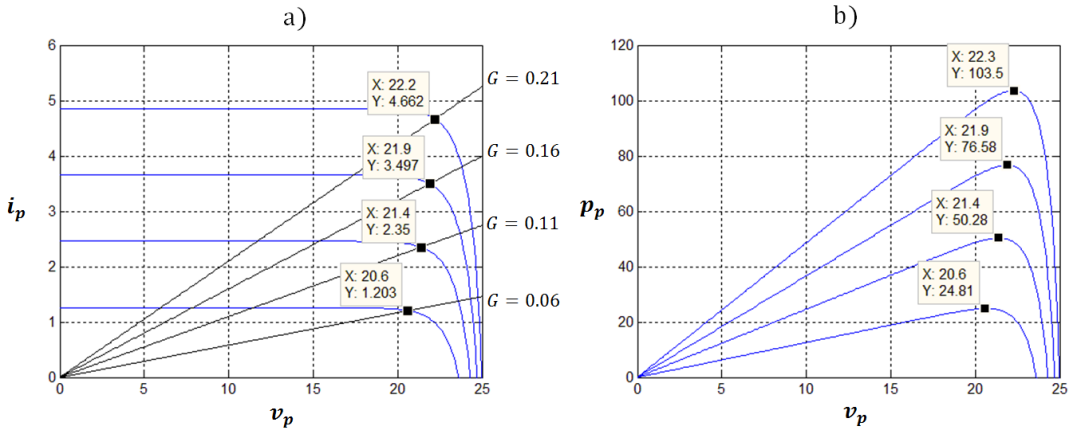

Fig. 5.3. Characteristics of the PV module: a) I-V; b) P-V.

Table 5.1. Parameters to define the I-V characteristic of the PV module

Parameter	Symbol	Value
Short Circuit Current	I_{sc}	6 A
Nominal Light Intensity	S_n	1000 W/m^2
Light Intensity	S	1000 W/m^2
Temperature Coefficient	C_t	0.0039 A/C
Nominal Temperature	T_n	25 °C
PV module temperature	T	25 °C
Saturation Current	I_0	6.87×10^{-11} A
Number of cells	N_s	36
Diode Quality Factor	A	1.2
Series resistance	R_s	0.0137 Ω

5.2.5. Stability of the linear model

In order to assess the stability of the closed loop system, the characteristic polynomial is numerically evaluated using values in table 5.2. The parameters of the PI controller are the same as in chapter 4 ($K_c = 0.7138, T_c = 0.06, T_f = 0.004$).

Table 5.2. Parameters of the DC-DC converter

Parameter	Symbol	Value
Input inductance	L_1	120 μH
Intermediate inductance	L_2	4.7 mH
Input capacitor	C_p	11 μF
Intermediate capacitor	C_1	11 μF
DC bus Capacitor	C_2	20 μF
DC bus Voltage	V_{dc}	400 V
Grid RMS Voltage	V_g	220 V $\pm$ 10%

The roots of the characteristic polynomial are evaluated for all the limit conditions (ranges of parameters M, G, and V_{max}) finding that the system is asymptotically stable. The resulted loci are shown in figure 5.4.

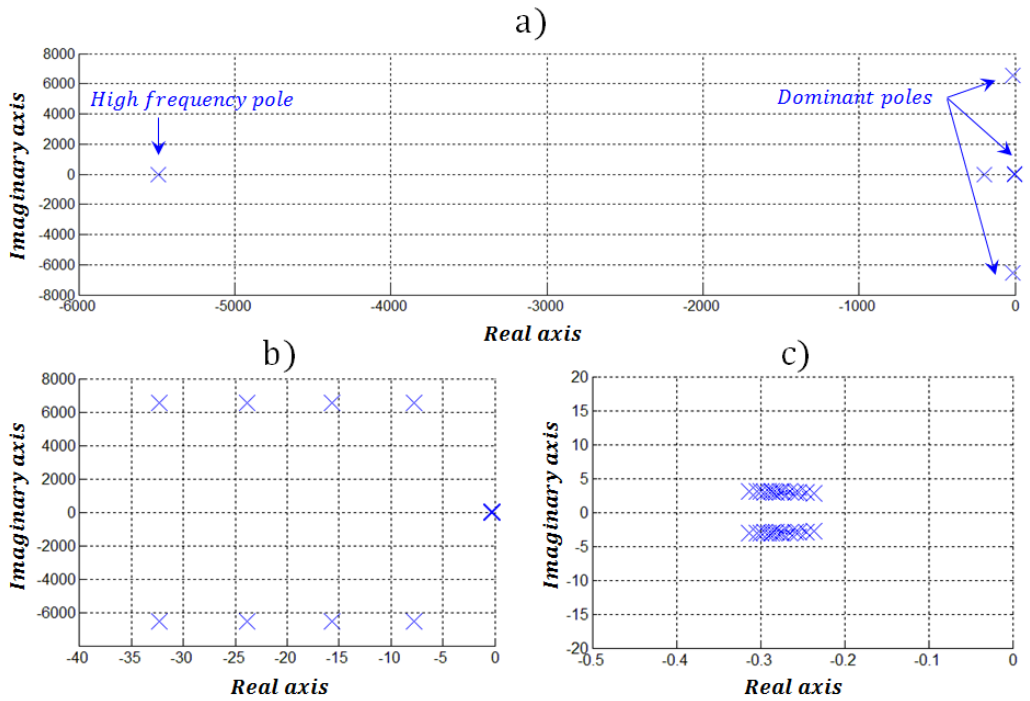

Fig. 5.4. Roots of the closed- loop system in the complex plane for different equilibrium points.

As it can be noted in figure 5.4a, the system has five roots. One root is completely real and two pairs are complex conjugate. The real root is far from the origin and hence their influence is negligible. Figure 5.4b shows that a pair of complex conjugate roots are much closer to the origin that the other one and hence the pair of roots depicted in figure 5.4c is dominant. Also, it is possible to observe that the system is always stable for the complete range of operational conditions and the given set of parameters.

5.2.6. Inclusion of the MPPT algorithm

Figure 5.2 shows a block diagram which represents the average model of the chain DC-DC-AC of the microinverter. However, that model does not include the MPPT dynamics or the PV module equation. Considering the analysis of chapter 2, the MPPT can be represented as a stable system which tracks the maximum power $p_m(t)$ and fix the values of $i_p(t)$ and $G(t)$ in the way depicted in figure 5.5 (variables in frequency domain).

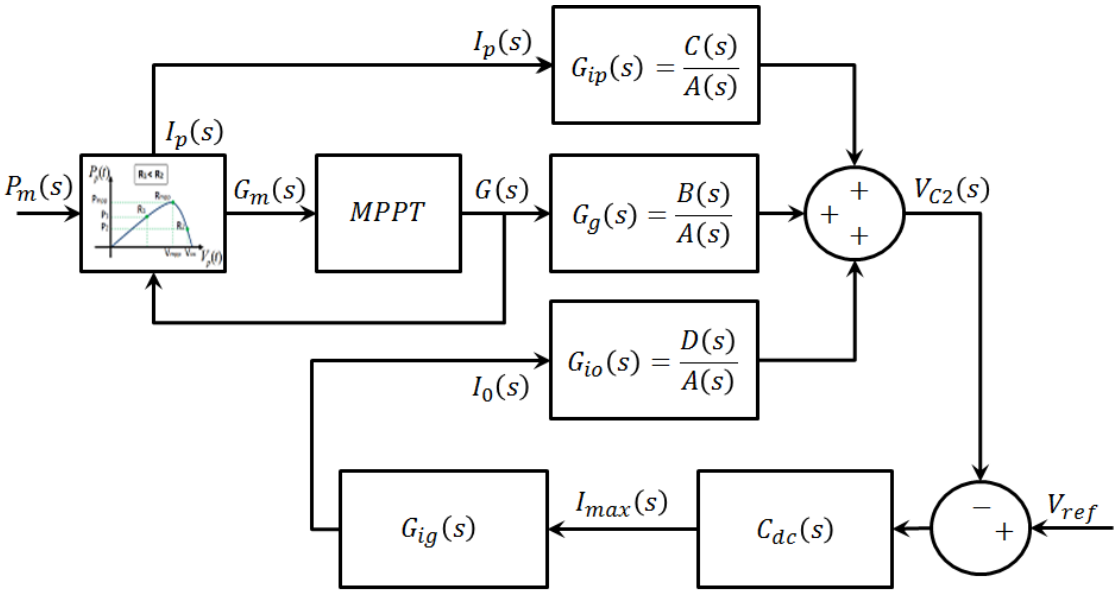

Fig. 5.5. Block diagram of the linear approach including the MPPT and the PV module

As it can be observed, the PV module is modeled as the incremental variation of the current controlled source $I_p(s)$ which is a function of the incremental variation in the conductance $G(s)$ and the maximum power $P_m(s)$. Then, from this approach, each maximum power point is represented by its associated conductance $G_m(s)$.

After some manipulations, it is possible to transform the block diagram of figure 5.5 into the one in figure 5.6. From the analysis of paragraph 5.2.3, the stability of the transfer function from $P_m(s)$ to $I_{max}(s)$ is ensured if polynomials $A(s)$ and $1 + K_g C_{dc}(s) G_{io}(s)$ are Hurwitz.

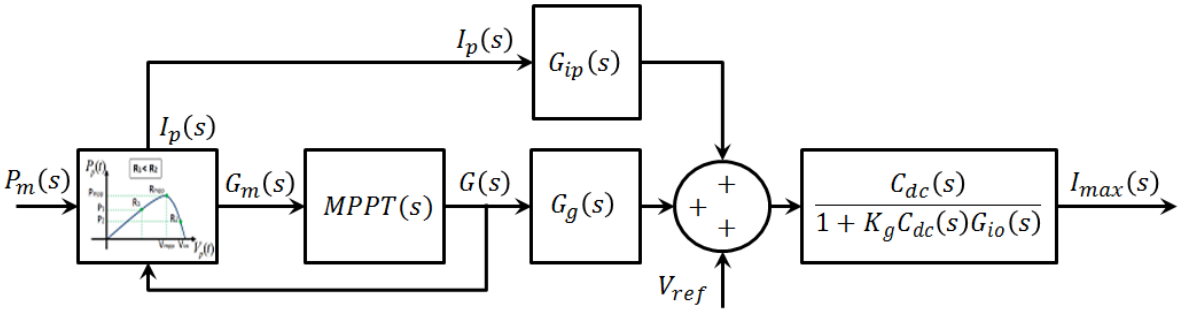

Fig. 5.6. Block diagram of the transfer from $P_m(s)$ to $I_{max}(s)$

This is the case for the values of parameters in table 5.1.

To be complete, it would be interesting to obtain a model for the MPPT block of figure 5.6. We will see in the following section that it can be approximated by a unitary gain linear model of order one or two, that is:

$$\frac{G(s)}{G_m(s)} = \frac{{\omega_n}^2}{s^2 + 2\xi\omega_n s + {\omega_n}^2} = MPPT(s) \tag{5.28}$$

5.3. SIMULATION RESULTS

In order to verify the theoretical predictions done in this work and summarized in this chapter, a simulation of the overall system has been performed in PSIM verifying the derived linear models, the stability and the performance of the control system.

5.3.1. Validation of the model of the chain DC-DC-AC

In order to test the validity of the derived linear model, the block diagram depicted in figure 5.2 has been simulated using the parameters listed in the table 5.2. The controller parameters are $K_c = 0.1791$, $T_c = 0.06$ and $T_f = 0.004$. The grid voltage is considered as constant with a RMS value of 220 V. The model is compared with a simulation of the DC-DC and DC-AC converters connected in cascade while the DC-DC converter is fed by a current source.

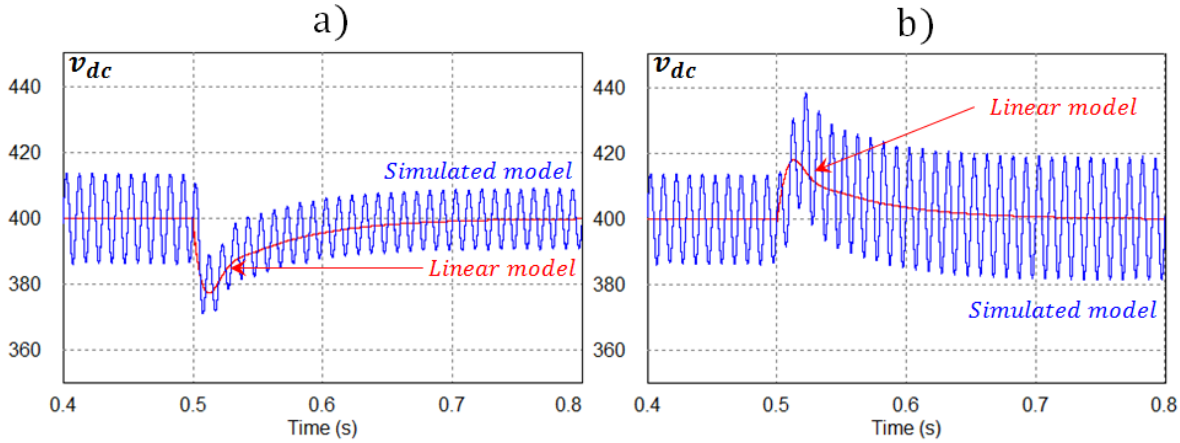

Fig. 5.7. Validation of the microinverter averaged model in comparison with the complete PSIM model

In a first test, the conductance value is initially fixed to 0.1 S and the input current source is fixed to 3 A. After reaching the equilibrium point, a change of 0.05 S (from 0.1 to 0.15 S) is applied to the conductance at 0.5 s in both models obtaining the

waveforms shown in figure 5.7a. In the second test, the conductance value is fixed in 0.1 S while the initial value of the current is set to 3 A. After reaching the equilibrium point, in 0.5 s, a change of 0.5 A (from 3 to 3.5 A) is applied to the current source in both models obtaining the waveforms shown in figure 5.7b. It is clear that the derived model represents to a great extent the average dynamics of the microinverter.

In order to complete the above described simulation, the MPPT block in figure 5.6 has been represented by the following second order numerical transfer function:

$$\frac{G(s)}{G_m(s)} = \frac{360 \times 10^3}{s^2 + 600s + 360 \times 10^3} \tag{5.29}$$

A change in the irradiance value of the model has been applied in order to evaluate the dynamic response of the system. Note that this test involves a dynamical motion in the main variables of the microinverter in the PV module side, the DC bus and the grid side. The figure 5.8 shows the parameters used in the Solar Module of PSIM beside the I-V and P-V characteristics working with irradiances of 600 and 200 W/m^2, which correspond to maximum power values of 120 and 40 W respectively.

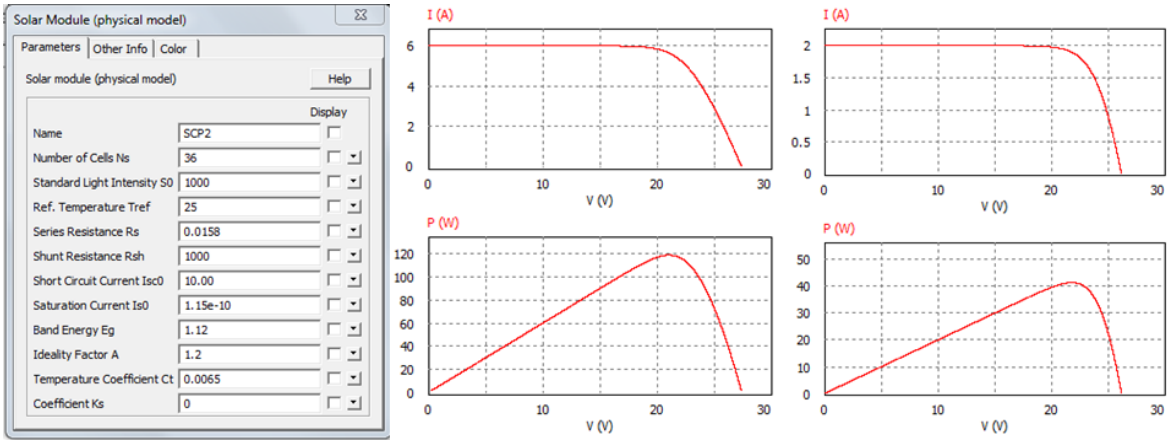

Fig. 5.8. Validation of the microinverter averaged model in comparison with the complete PSIM model

In this test, the initial conditions of the system are $G = 0.28$ S, $i_p = 5.76$ A, $v_p = 21.2$ V, $p_{p_{max}} = 120$ W, $E = 600$ W/m^2 and the final conditions are $G = 0.10$ S, $i_p = 1.98$ A, $v_p = 21.6$ V, $p_{p_{max}} = 40$ W, $E = 200$ W/m^2. To compare the simulated results using the complete circuit model in PSIM and the linearized model, the value of the

initial conductance is added to the incremental value given by the MPPT block obtaining the current conductance seen by the PV module. Then, in the block diagrams of figures 5.5 and 5.6, when the step change of irradiance is applied $G_m(s)$ is a step.

In figure 5.9 a negative step change of irradiance from 600 to 200 W/m^2 is introduced at 0.5 s. It is possible to observe the convergence of the extracted power to the value of available power which corresponds to the maximum power point. It is also observed that the dynamics of the bus of the DC voltage are coherent with the linearized model and the switching circuit model validating our approximation of $MPPT(s)$ as a unitary second order system (5.28).

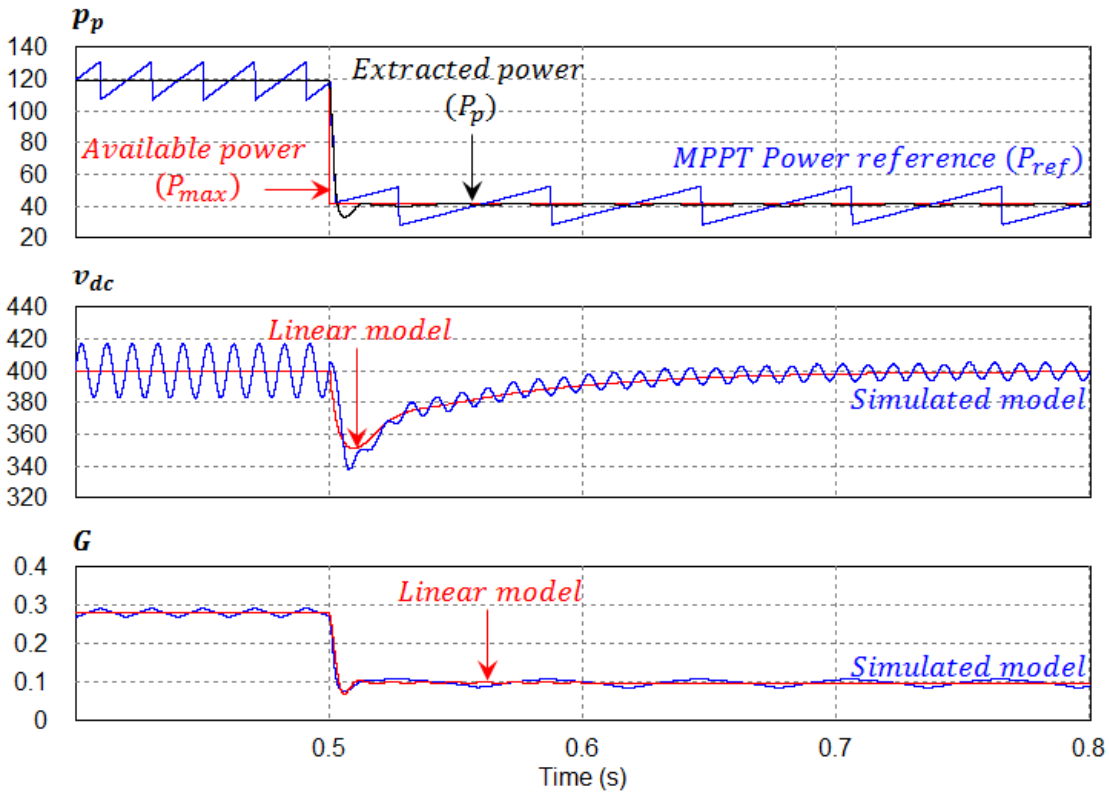

Fig. 5.9. Simulation including the MPPT as a stable second order system

In figure 5.10 a positive step change of irradiance from 200 to 400 W/m^2 is introduced at 0.5 s. As in the case of the negative stimulus, it is possible to observe the convergence of the extracted power to the maximum power point and the coherence between the linearized model and the switching circuit model.

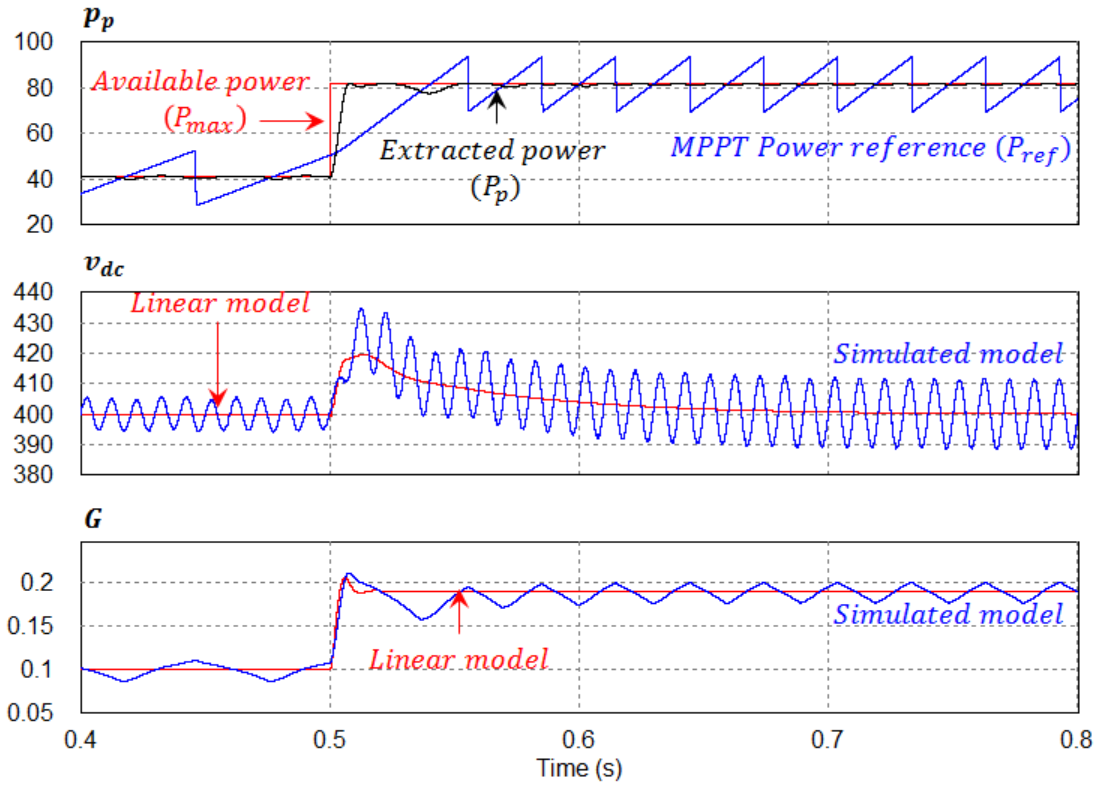

Fig. 5.10. Simulation including the MPPT as a stable second order system

5.3.2. Steady-state of the microinverter variables

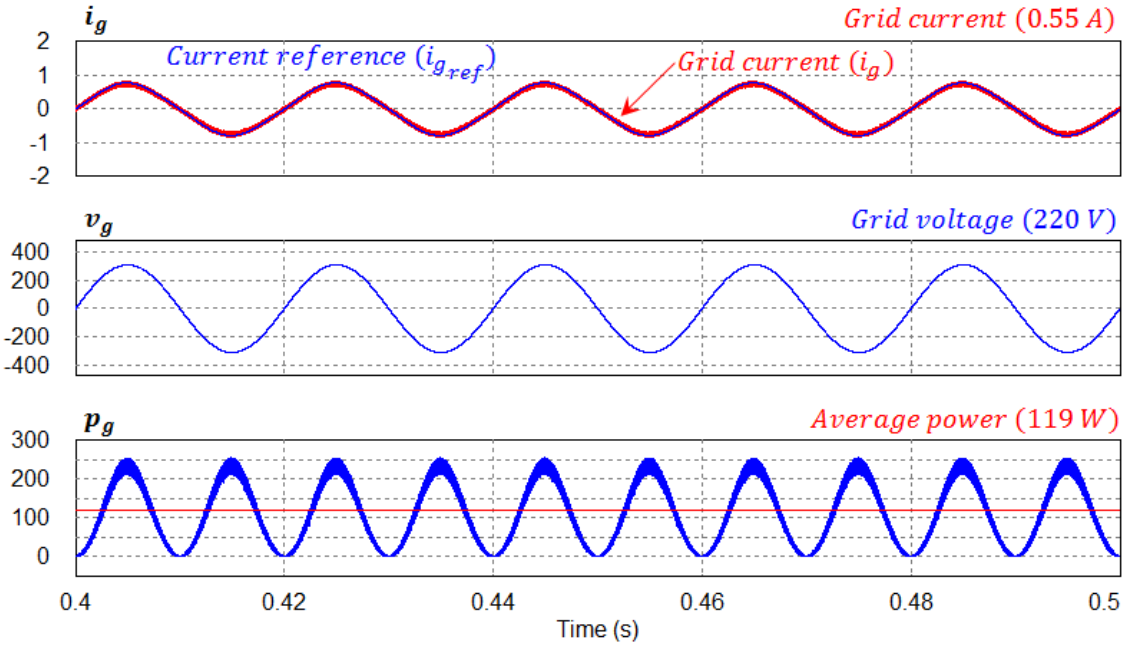

Fig. 5.11. Detail of the steady state of the current and voltage waveforms at the grid side.

Figure 5.11 shows the simulated steady-state waveforms of the microinverter at the grid side working with the irradiance value of 600 W/m^2. As it can be observed, the grid

voltage follows the given current reference showing the variation inside the hysteresis band, and exhibiting a null phase displacement and a reduced THD (measured as 7.6 % including the high frequency component) which implies a power factor near one (0.99). The average power is computed showing that the total amount of power available at the PV module side is injected into the grid. It is worth to note that these simulations have been performed without including parasitic resistive elements.

Figure 5.12 shows the simulated steady-state waveforms of the DC bus. The voltage of the bus is regulated to the desired value of 400 V showing an acceptable voltage ripple. The input current of the inverter is depicted and its average value is about 0.28 A, which allows injecting a power of about 120 W. These results confirm that the control of the DC-AC stage as in the way studied in chapter 4 is consistent and compatible with the other control parts of the microinverter.

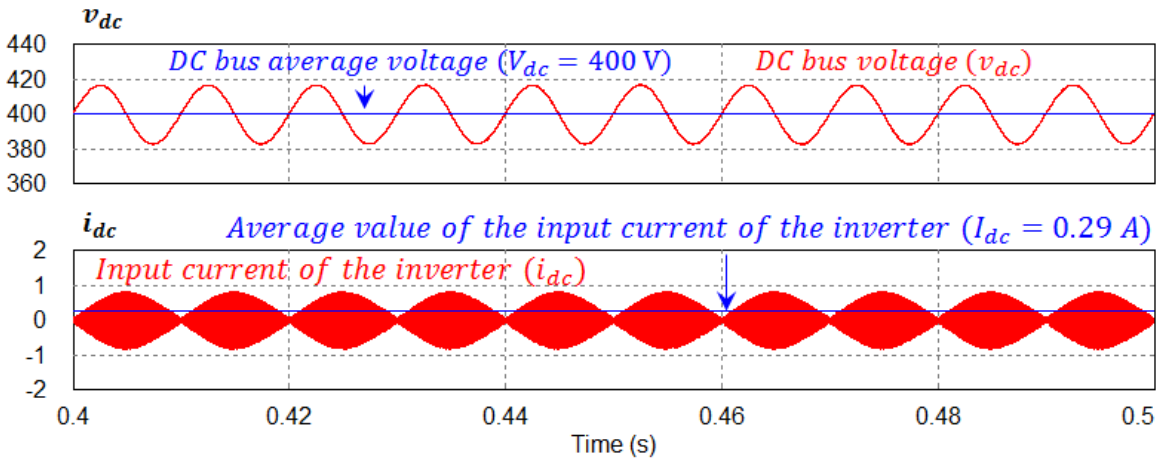

Fig. 5.12. Detail of the steady state of the current and voltage waveforms at the DC bus.

Figure 5.13 shows the simulated steady-state waveforms of the microinverter at the PV module side including also the more relevant MPPT signals. It is possible to observe that the extracted power is around the maximum available power and also that the power presents the characteristic double frequency with respect to the current and voltage waveforms. The power reference of the algorithm is depicted to show that its average value corresponds to the maximum available power and is predicted by the existing sliding motion. The conductance waveform is also depicted showing its coherence with the power reference signal and also confirming the average values used to validate the linear model. In general, the steady-state behavior of the signals is the expected one and validates the application of the MPPT algorithm and the DC-DC converter control laws when the overall microinverter is considered.

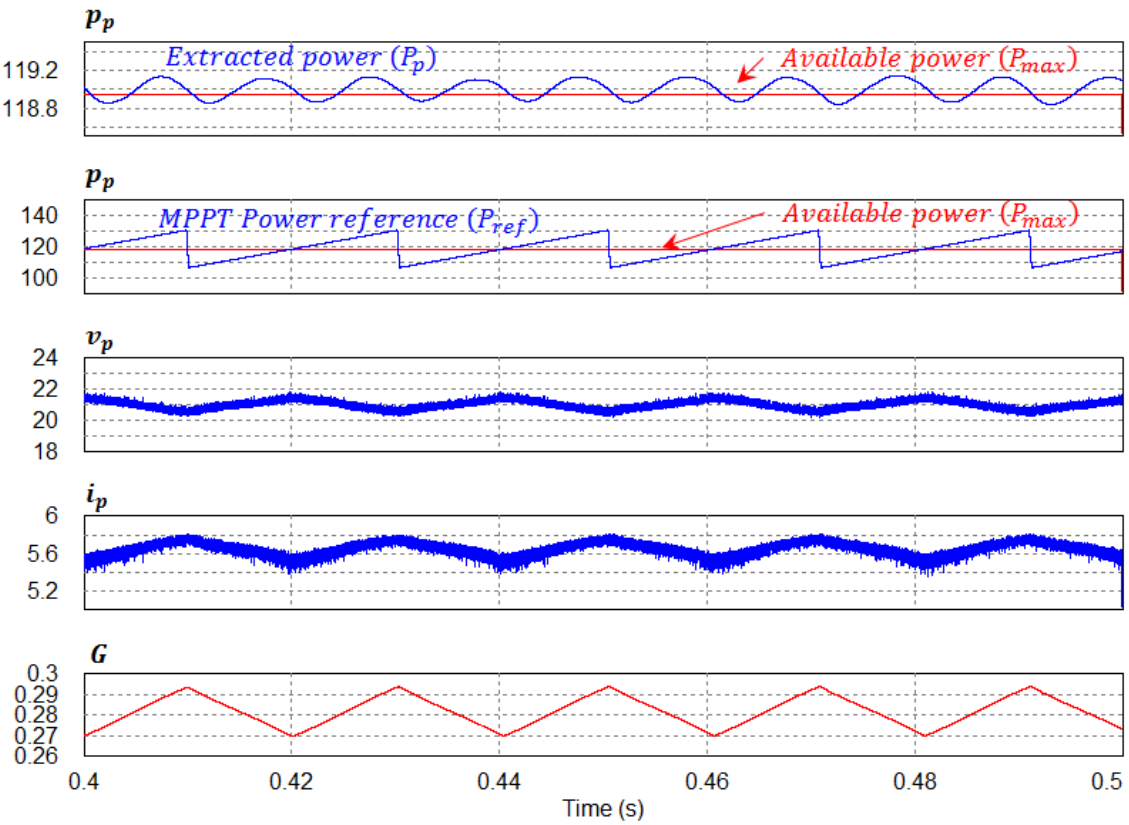

Fig. 5.13. Detail of the steady state of the current, voltage and power waveforms at the PV module side.

5.3.3. Dynamic response in front of changes in the P-V characteristic

A simulation is performed in order to assess the dynamic response of the microinverter system working with changes in irradiance of the Solar Module from 600 W/m^2 to 200 W/m^2 and vice versa holding each value during 0.5 s. Note that these changes are equivalent to positive and negative step disturbances of 80 W. The simulated results shown in figure 5.14 demonstrate that the system remains stable showing robustness at PV side, DC bus, grid side and MPPT algorithm.

5.3.4. Start-up of the microinverter system

The start-up of the microinverter has been simulated to show the transient behavior from the start (zero initial conditions) to an equilibrium point at a maximum power of 120 W. As it can be observed in figure 5.15, the steady- state is reached in around 100 ms. Note that the current of the PV module evolves quickly to the short circuit value and in consequence the power attains values in the neighborhood of the maximum power point ensuring a good performance.

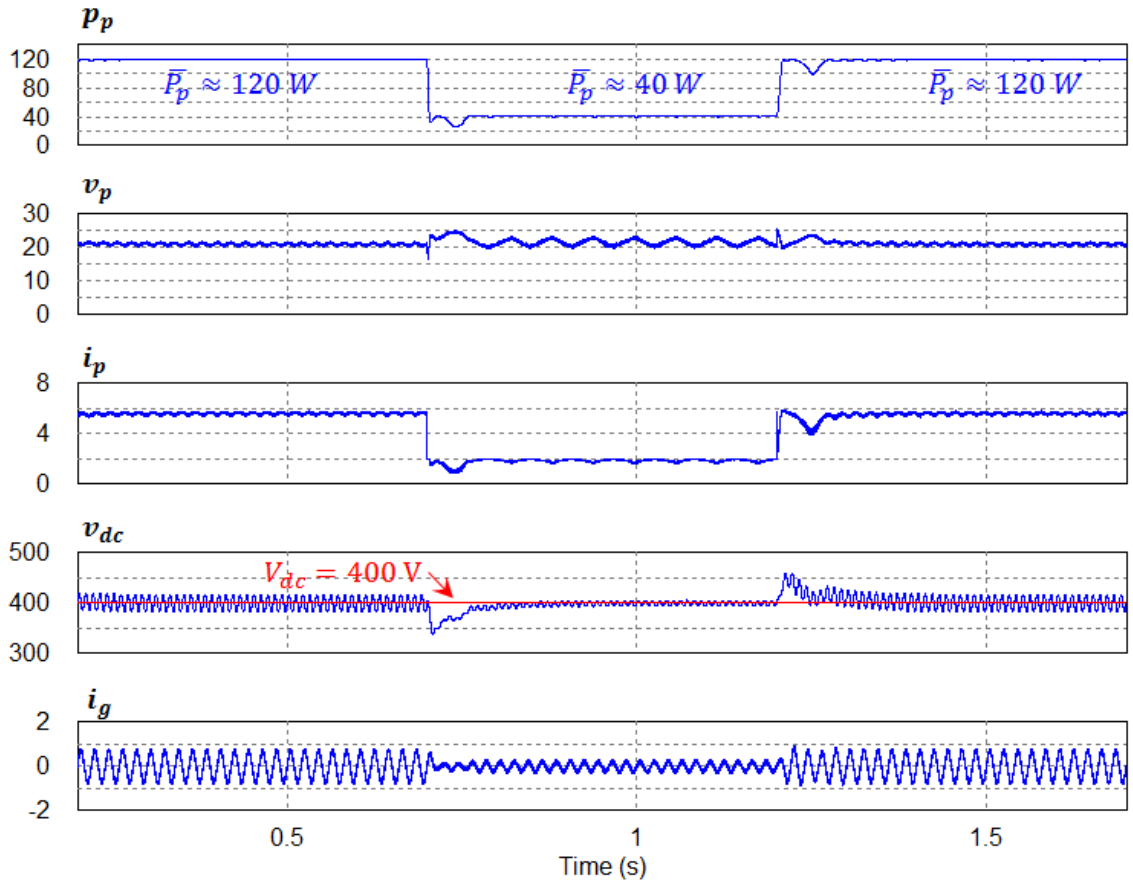

Fig. 5.14. Simulated results using sudden changes of 80 W in the maximum power P-V characteristic.

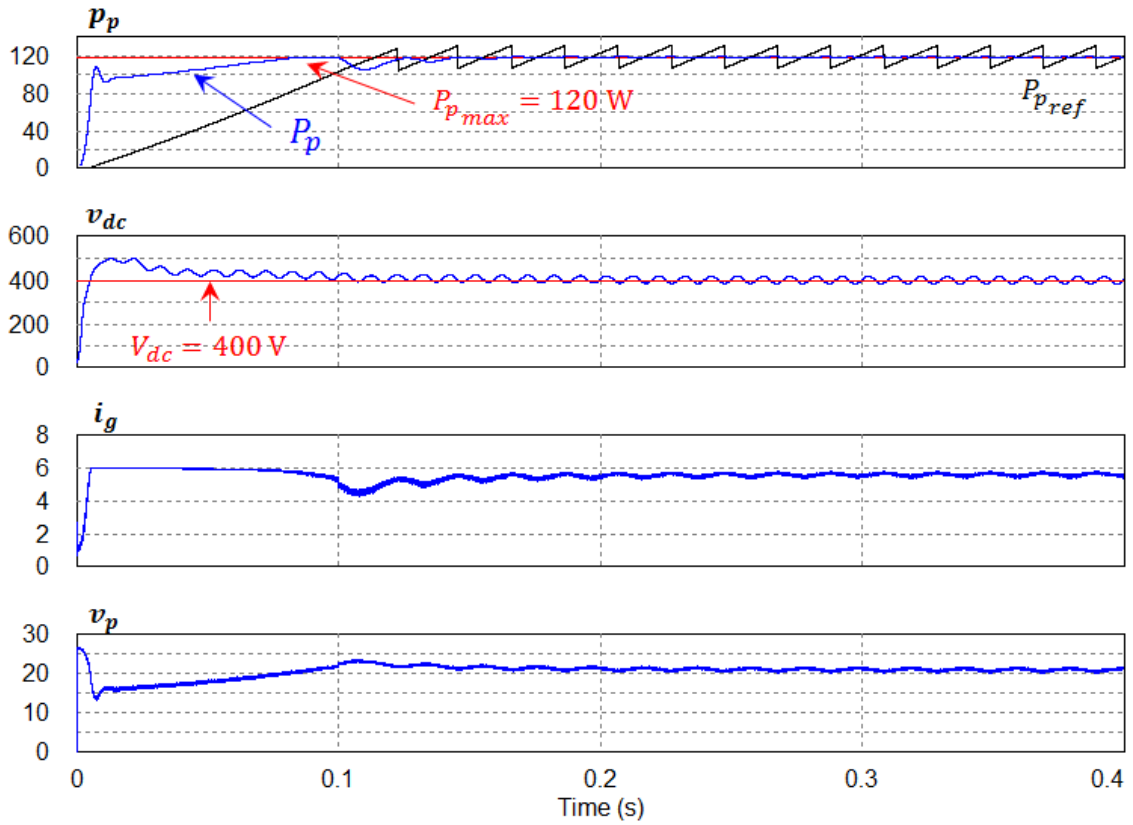

Fig. 5.15. Simulated time response of the voltage, current and power of the system during a start-up

It is worth to note that during the start-up, the voltage controller of the DC bus suffers a large deviation which is quickly controlled. The maximum observed variation in this case is around 100 V over the reference value of 400 V.

5.4. EXPERIMENTAL RESULTS

The entire microinverter system has been studied in a single experimental set-up in order to validate the theoretical predictions and simulation results.

5.4.1. Prototype and experimental set-up

The microinverter system is obtained by assembling the circuits developed in chapter 2, 3 and 4. The set-up for measurements, photovoltaic modules, microinverter prototype and control circuit are shown in figure 5.16. The experimental set-up is composed of a solar panel emulator E4360A from Agilent, an oscilloscope MSO3014 from Tektronix, current probes TCP202 and TCPA300 from Tektronix, high voltage differential probe P5210 from Tektronix, power supply Multimeteix XA3033, multimeter HP34401A from Hewlett Packard, electronic load IT8512B from ITEC, I-V Curve Tracer MP-160 from EKO and pyranometer SP LITE from KIPP & ZONEN.

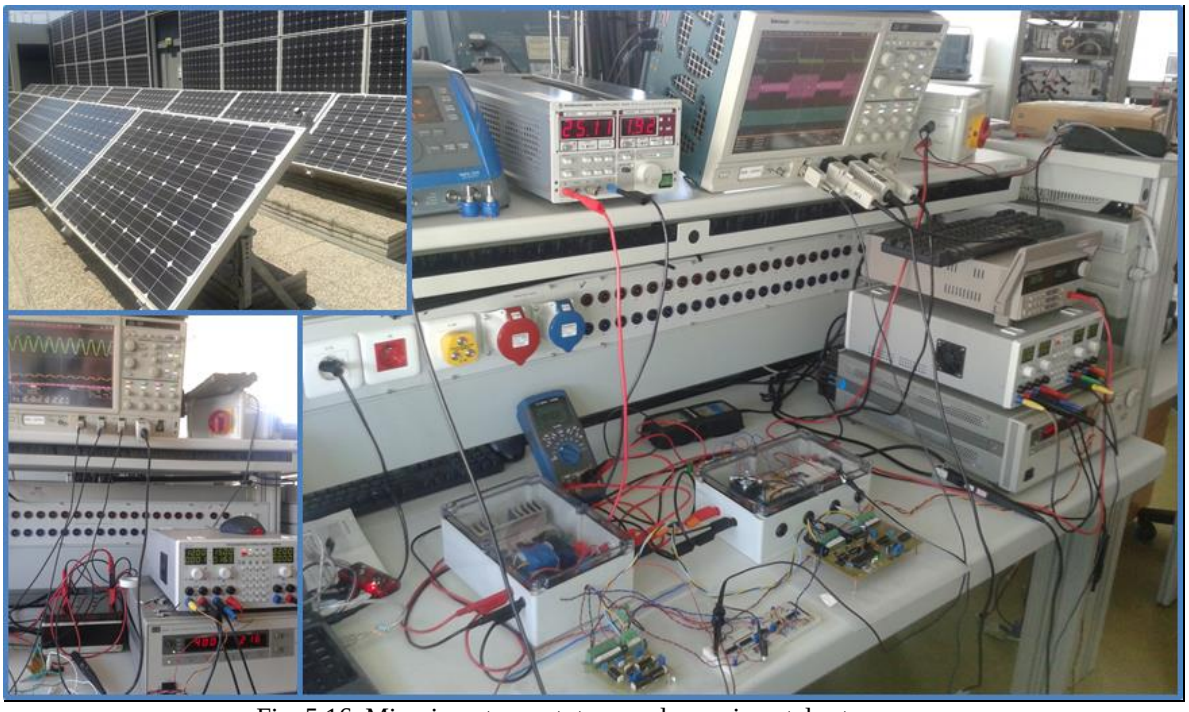

Fig. 5.16. Microinverter prototype and experimental set-up

Two solar panels BP 585 from BP SOLAR has been used in the experimental test. The characteristics and parameters are listed in figure 5.17.

	BP 585
Maximum power (P_{max})[2]	85W
Voltage at P_{max} (V_{mp})	18.0V
Current at P_{max} (I_{mp})	4.72A
Warranted minimum P_{max}	80.8W
Short-circuit current (I_{sc})	5.0A
Open-circuit voltage (V_{oc})	22.1V
Temperature coefficient of I_{sc}	(0.065±0.015)%/°C
Temperature coefficient of voltage	-(80±10)mV/°C
Temperature coefficient of power	-(0.5±0.05)%/°C
NOCT[3]	47±2°C
Maximum system voltage	600V (U.S. NEC rating) 1000V (TÜV Rheinland rating)
Maximum series fuse rating	20A (U, H versions) 15A (S, L versions)

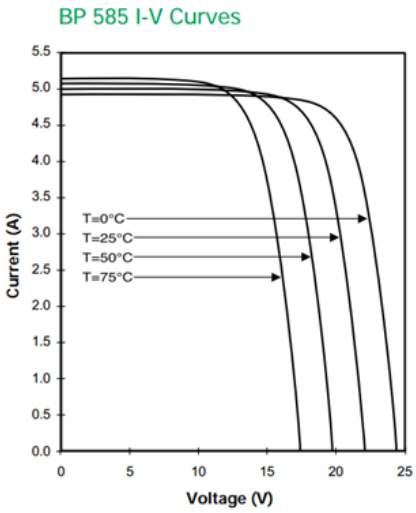

Fig. 5.17. Technical specification of the PV module BP585

5.4.2. Steady-state of the microinverter variables

In figures 5.18 and 5.19, the steady-state waveforms of the microinverter are shown when an approximate average power of 86 W is extracted from the PV module and injected into the grid of 220 V. The double frequency of the power waveform confirms that the system works at the maximum power point. The voltage of the DC bus is regulated at 400 VDC whereas a current with THD of 7.1% is injected into the grid. The displacement power factor is unitary whereas the power factor is 0.99.

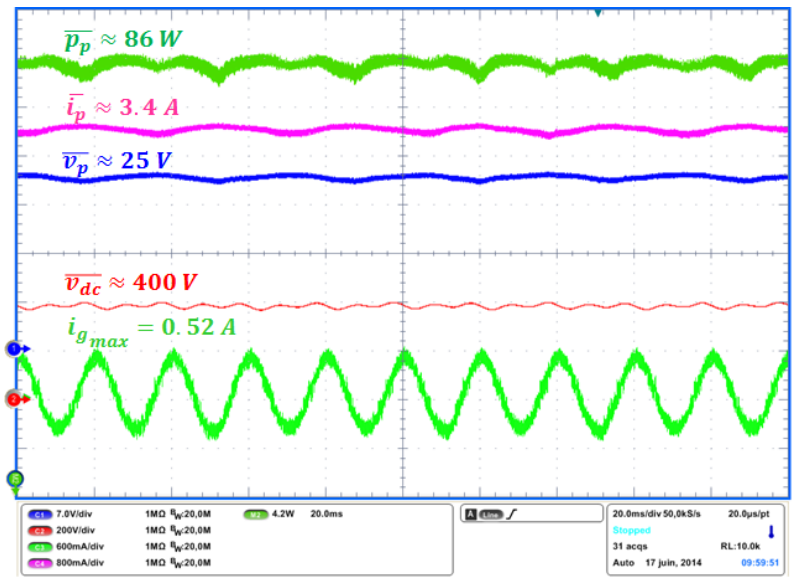

Fig. 5.18. Waveforms of the PV module voltage, current and power, DC bus voltage and grid current.

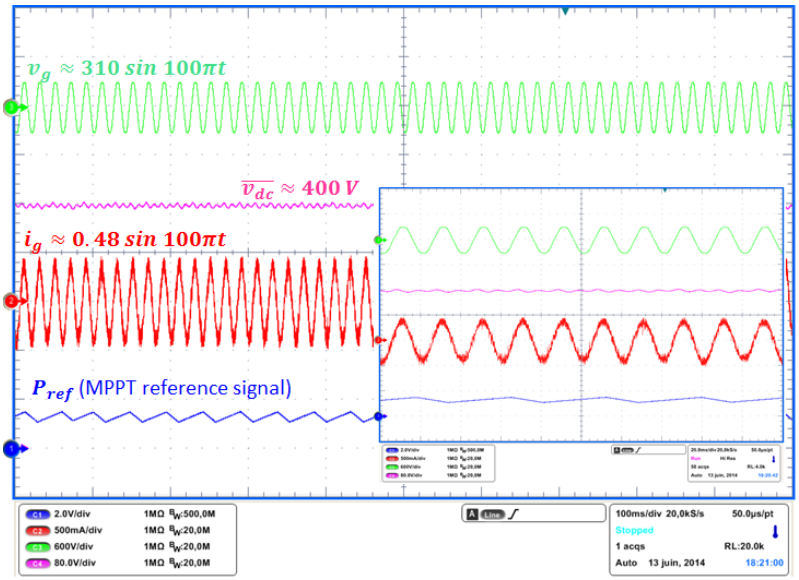

Fig. 5.19. Waveforms of the grid current, grid voltage, DC bus voltage and MPPT power reference.

5.4.3. Dynamic response in front of changes in the P-V characteristic

As it can be shown in figure 5.20, the dynamic response of the entire system has been assessed simulating a change of irradiance leading to a change of the I-V characteristic in the ideal panel emulator from a first point with a maximum power value about of 45 W to another one with a maximum power value of 110 W and vice versa. Each I-V characteristic is maintained during 1 s. It is observed that the objective of having a motion towards the new maximum power point keeping regulated the voltage of the DC bus is correctly managed in both changes.

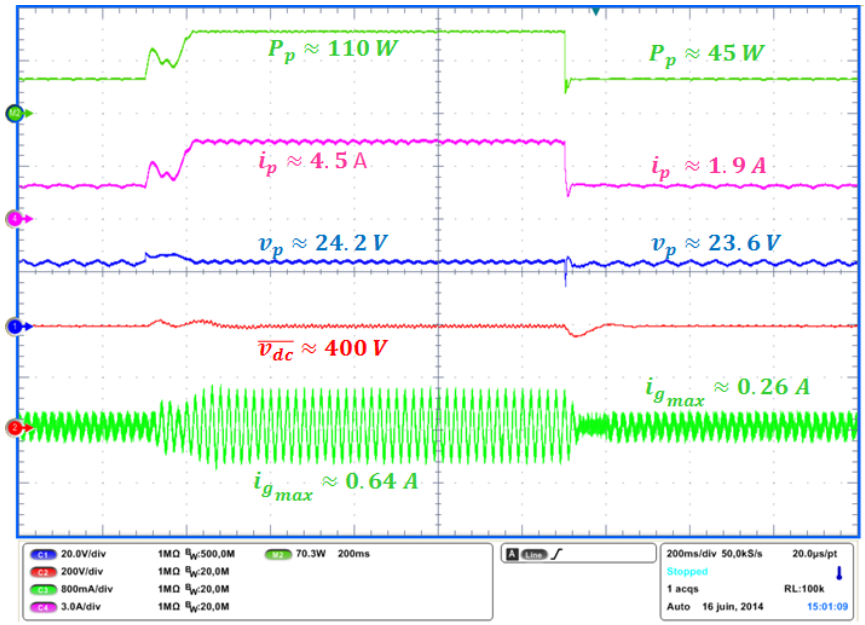

Fig. 5.20. Experimental results for sudden changes of 55 W in the maximum power of the PV module

5.4.4. Start-up of the microinverter system

The start-up of the microinverter has been captured in figure 5.21 in order to illustrate the transient behavior from the initial condition of the DC-DC stage control (supposed at test) to the steady- state working at a maximum power point. The inverter is turned on, having the output of the voltage regulator at zero because of the absence of power in the DC-DC stage. The start command is given to the MPPT system which reaches the steady- state in 300 ms approximately. The voltage of the DC bus reaches the value of reference but have an overshoot of less than 40 V (10 % of the nominal voltage) which is controlled 100 ms after reaching the maximum power point.

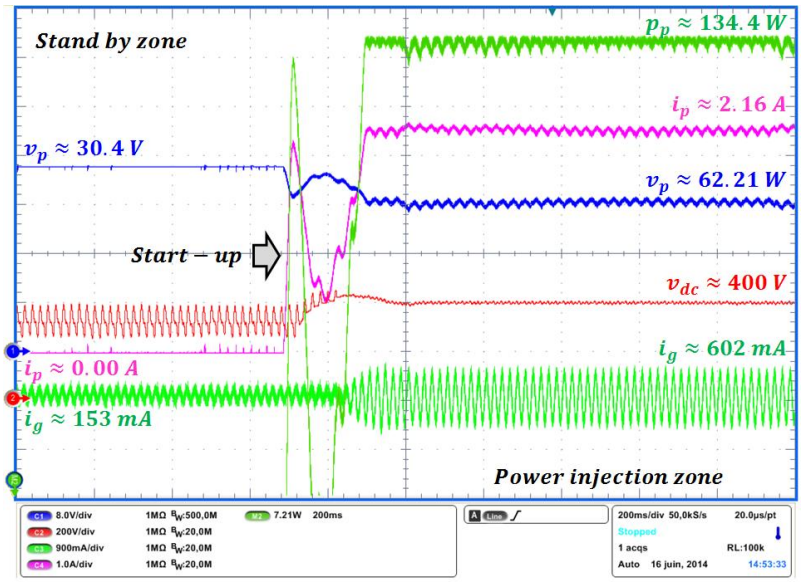

Fig. 5.21. Detail of the microinverter variables during the start-up.

5.5. CONCLUSIONS

In this chapter, the study of an entirely-sliding-mode-controlled transformer-less single-phase dual-stage grid-connected microinverter has been presented. The coupling of the building blocks has been done studying the cascade connection of the DC-DC and DC-AC conversions with the MPPT algorithm. A global linear model has been derived for the cascade connection of the DC-DC and the DC-AC stages and its stability has been numerically evaluated showing that the chain DC-DC-AC is asymptotically stable in the overall range of the operational conditions. The operation of the overall system has been tested using simulation and experimental results confirming the initial hypothesis of the compatibility of the proposed independent control laws and the feasibility of a microinverter satisfying all the desired control objectives.

5.6. REFERENCES

Module Integrated Converter

[1] Y. Zhou, L. Liu, H. Li, "A High-Performance Photovoltaic Module-Integrated Converter (MIC) Based on Cascaded Quasi-Z-Source Inverters (qZSI) Using eGaN FETs," *IEEE Trans. Ind. Electron.,* vol. 28, no. 6, pp. 2727-2738, Jun. 2013.

[2] F.F. Edwin, X. Weidong, V. Khadkikar, "Dynamic Modeling and Control of Interleaved Flyback Module-Integrated Converter for PV Power Applications," *IEEE Trans. Ind. Electron.,* vol. 61, no. 3, pp. 1377-1388, Mar. 2014.

[3] B. Sahan, A.N. Vergara, N. Henze, A. Engler, P. Zacharias, "A Single-Stage PV Module Integrated Converter Based on a Low-Power Current-Source Inverter," *IEEE Trans. Ind. Electron.,* vol. 55, no. 7, pp. 2602-2609, Jul. 2008.

[4] Q. Li; P. Wolfs, "A Review of the Single Phase Photovoltaic Module Integrated Converter Topologies With Three Different DC Link Configurations," *IEEE Trans. Power Electron.,* vol. 23, no. 3, pp. 1320-1333, May. 2008.

Microinverters

[5] H. A. Sher, K.E. Addoweesh, "Micro-inverters - Promising Solutions in Solar Photovoltaics," *Energy for Sustainable Development*, vol. 16, pp. 389-400, Dec. 2012.

[6] C.L. Trujillo, D. Velasco, E. Figueres, G. Garcerá, R. Ortega, "Modeling and control of a push–pull converter for photovoltaic microinverters operating in island mode," *Applied Energy,* vol. 88, pp. 2824-2834, Aug. 2011.

[7] A. Amirahmadi, L. Chen, U. Somani, H. Hu, N. Kutkut, I. Bartarseh, "High Efficiency Dual-Mode Current Modulation Method for Low-Power DC/AC Inverters," *IEEE Trans. Power Electron.,* vol. 29, no. 6, pp. 2638-2642, Jun. 2014.

[8] D.R. Nayanasiri, D.M. Vilathgamuwa, D.L. Maskell, "Half-Wave Cycloconverter-Based Photovoltaic Microinverter Topology With Phase-Shift Power Modulation," *IEEE Trans. Power Electron.,* vol. 28, no. 6, pp. 2700-2710, Jun. 2013.

[9] N. Sukesh, M. Pahlevaninezhad, P.K. Jain, "Analysis and Implementation of a Single-Stage Flyback PV Microinverter With Soft Switching," *IEEE Trans. Ind. Electron.,* vol. 61, no. 4, pp. 1819-1833, Apr. 2014.

[10] Z. Zhang; X.-F. He; Y.-F. Liu, "An Optimal Control Method for Photovoltaic Grid-Tied-Interleaved Flyback Microinverters to Achieve High Efficiency in Wide Load Range," *IEEE Trans. Power Electron.,* vol. 28, no. 11, pp. 5074-5087, Nov. 2013.

AC module

[11] D. Meneses, F. Blaabjerg, O. García, J.A. Cobos, "Review and Comparison of Step-Up Transformerless Topologies for Photovoltaic AC-Module Application," *IEEE Trans. Power Electron.,* vol. 28, no. 6, pp. 2649-2663, Jun. 2013.

[12] M. Kusakawa, H. Nagayoshi, K. Kamisako, K. Kurokawa, "Further Improvement of a Transformerless, Voltage-Boosting Inverter for AC Modules," *Solar Energy Materials and Solar Cells*, Volume 67, Mar. 2001, Pages 379-387.

Our proposal

[13] O. Lopez-Santos, L. Martinez-Salamero, G. Garcia, H. Valderrama-Blavi, "Sliding-mode control of a transformer-less dual-stage grid-connected photovoltaic micro-inverter," in Proc. 10th Int. Multi-Conf. on Systems, Signals & Devices (SSD), 2013, pp. 1-6.

Quadratic boost converter

[14] O. Lopez-Santos, L. Martinez-Salamero, G. Garcia, H. Valderrama-Blavi, T. Sierra-Polanco, "Robust Sliding-Mode Control Design for a Voltage Regulated Quadratic Boost Converter," *IEEE Trans. Power Electron.,* vol. 30, no. 4, pp. 2313-2327, Apr. 2015.

[15] O. Lopez-Santos, L. Martinez-Salamero, G. Garcia, H. Valderrama-Blavi and D.O. Mercuri, "Efficiency analysis of a sliding-mode controlled quadratic boost converter," *IET Power Electron.,* vol. 6, no. 2, pp. 364-373, Feb. 2013.

LFR-Concept

[16] A. Cid-Pastor, L. Martinez-Salamero, A. El Aroudi, R. Giral, J. Calvente, R. Leyva, "Synthesis of loss-free-resistors based on sliding-mode control and its applications in power processing," Control Engineering Practice, vol. 21 no. 5 pp. 689-699. May. 2013.

Conclusions and perspectives

This dissertation has summarized the theoretical analysis, discussions, simulation and experimental results of our study about the control problems associated with a low power photovoltaic generator. Using a dual-stage grid-connected topology of module oriented converter or microinverter as it is also called, it has been possible to study the problem of the maximum power point tracking, the problem of input impedance matching of a high-gain DC-DC converter, and the problem of the grid-connection of a DC-AC converter, all from the perspective of the sliding mode control theory. We have proposed and analyzed in detail a new MPPT algorithm which is performant and is compatible with the control of the DC-DC stage through the input conductance. In the DC-DC stage, we have intensively studied the quadratic boost converter and its operational modes using the Loss-Free-Resistor concept. The DC-AC converter has been controlled to ensure the stability of the power flow in the microinverter regulating the voltage in the DC bus and injecting real power to the grid with a high power quality level. The control of both converters has been obtained using current control loops based on simple hysteresis comparators which ensure the sliding motion giving simplicity and robustness to the system. Finally, the three constitutive elements (MPPT, DC-DC and DC-AC) have been studied together deriving a global linear mode of the microinverter which allows understanding the dynamic of the entire system. Therefore, it has been demonstrated that the proposed control laws are feasible and reliable, compatible with a real application with microinverters.

The development of this thesis has also generated research questions related with the aspects listed below and which concentrate our future efforts:

- Complement the study and comparison of the quadratic boost converter topologies and operational modes concluding about the best obtained performance.
- Optimize the overall system applying appropriate assembling techniques and layout optimization to minimize the size of the prototype close to the commercial products.
- Integrate the implementation of the entire control system into a single digital device studying the effect of discretization in the performance and stability of the system.
- Extend the results of the MPPT algorithm to multivariable systems and give its properties to work in mismatched conditions.

Appendix 1:
DC-DC converter design criteria

This appendix presents the main criteria to select the values of the passive components of the CCSS-QB converter (Cascaded Connected Single Switch Quadratic Boost) which is shown in figure A1.1. As it can be observed, this converter has two inductors (L_1 and L_2) and two capacitors (C_1 and C_2). The output voltage of the converter is the same voltage of the capacitor C_2 defining the DC bus. The DC bus voltage fed the DC-AC stage maintaining a regulated voltage level to ensure the equilibrium of the power in the system.

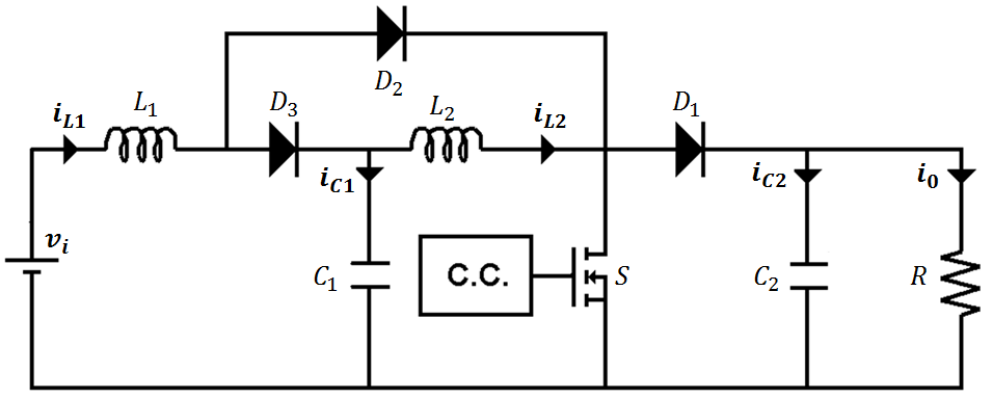

Fig. A1.1. Circuit diagram of the CCSS-QB converter.

To design the values of the passive components, it is necessary to define the power and voltage levels of the converter. Considering that the output voltage of the DC-DC converter is the same DC bus voltage, the value of the capacitor C_2 will be obtained from the analysis of the DC-AC stage assuming the voltage at this point as constant. The figure A1.2 shows the waveforms of the current on inductors L_1 and L_2, and also the voltage on the capacitor C_1.

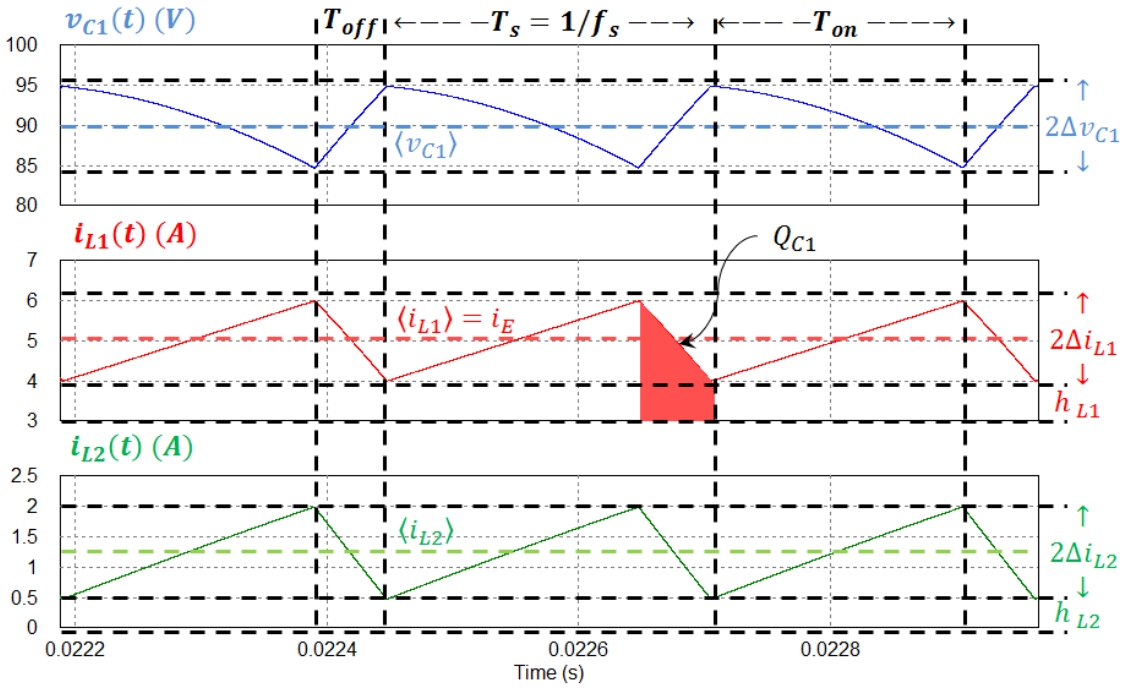

Fig. A1.2. Current and voltage waveforms of the quadratic boost converter.

The current and voltage waveforms at stationary state are composed of a continuous component (average) and an oscillatory component (ripple) which has a fundamental frequency equal to the switching frequency f_s. The amplitude of these ripples defines one of the main criteria to the converter parameters design.

A1.1. Inductor L_1

To ensure the sliding motion of the converter, the input current (current on inductor L_1) must work always in continuous conduction. Therefore, the hysteresis band which defines the current ripple must be always positive. However, although this condition is sufficient to stabilize the converter, our work concentrates on continuous conduction mode (CCM) operation which implies that the other inductor current is also always positive. For the inductor L_1, it is required to accomplish the condition:

$$i_{L1}|_{P=P_{min};\, v_{in}=v_{in_{max}}} > \frac{\Delta i_{L1}}{2} + h_{L1} \tag{A1.1}$$

Where h_{L1} (represented in figure A1.2) is a security term to avoid the discontinuous conduction mode during the transient regimes and also to avoid unexpected commutation due to the measurement noise. Using this consideration, the expressions (3.6) to (3.9) relate the mean values of the converter variables.

Using the above analysis, the value of the inductor L_1 can be selected using the switching frequency, the input and output voltages, and the width of the hysteresis band $2\Delta_{i_{L1}}$. Then, the expression (3.119) can be solved for determining L_1 and leads to:

$$L_1 = \frac{V_{C2}}{2f_s\Delta_{i_{L1}}}\left(\frac{m-1}{m^3}\right) \tag{A1.2}$$

being $m = \frac{V_{C2}}{V_{C1}} = \frac{V_{C1}}{V_i}$ and $V_{C2}$the regulated voltage of the DC bus.

A1.1. Inductor L_2

Using the same criteria for the inductor L_1, the continuous conduction mode is ensured by:

$$i_{L2}|_{P=P_{min};\, v_{in}=v_{in_{max}}} > \frac{\Delta i_{L2}}{2} + h_{L2} \tag{A1.3}$$

It is important to mention that the dynamic behavior of the inductor current i_{L2} is in fact a result of the ideal sliding dynamic induced through the inductor current i_{L1}. Besides, the transient response on the inductor current i_{L2} can exhibit deviations with respect to the equilibrium point during changes of the reference or disturbances. Therefore selection of h_{L2} is a key design aspect. The value of the inductor can be selected by satisfying:

$$L_2 > \frac{V_{C2}}{2f_s\Delta_{i_{L2}}}\left(\frac{m-1}{m}\right) \tag{A1.4}$$

A1.2. Capacitor C_1.

The design of the capacitor C_1 must be done to satisfy the stability condition (3.117). That expression can be rewritten as:

$$C_1 < 2C_2m^2 \tag{A1.5}$$

Further, the value of C_1 must ensure a low ripple in order to satisfy the approximations introduced by the use of the equivalent control for analyzing the sliding motion. Using definition of Q_{C1} in figure A1.2 after simple mathematical manipulations, the following expression is obtained:

$$C_1 > \frac{\overline{i_{L1}}m}{2f_s\Delta_{V_{C1}}} \tag{A1.6}$$

Appendix 2:

DC-AC converter design criteria

This appendix presents the main criteria to select the value of the inductor and the capacitor of the full bridge converter shown in figure A2.1 using bipolar commutation. As it can be observed, the inductor is the main element of the grid connection and the capacitor is the coupling element which connects the DC-AC stage to its power source (DC-DC converter operating as SM-LFR).

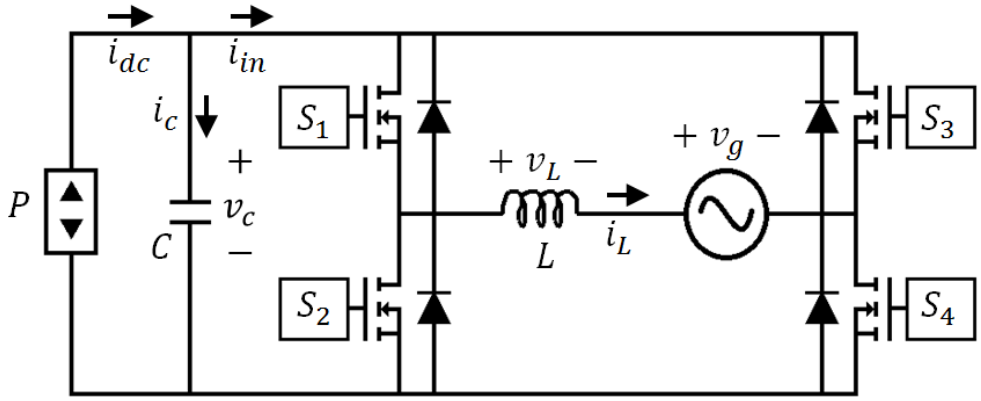

Fig. A2.1. Circuit diagram of the full-bridge grid-connected converter

The value of the inductance is constrained by the attainability condition (4.20). This expression can be used for designing L an the following upper limit is deduced:

$$L < \frac{\sqrt{{V_c}^2 - {V_{max}}^2}}{\omega I_{max}} \tag{A2.1}$$

By satisfying this condition for the maximum value of I_{max} (Maximum operational power) and considering a constant hysteresis band, the value of the inductance will define the switching frequency range of the inverter.

It is worth to highlight that the variation of the switching frequency is not only produced by a change of the operational point of the inverter but also by the time-varying characteristics of the reference. It is possible to observe in figure A2.2 that the switching frequency varies between a lower limit established at the maximum of the waveform and an upper limit deduced at the zero crossing (see expressions 4.107 and 4.108).

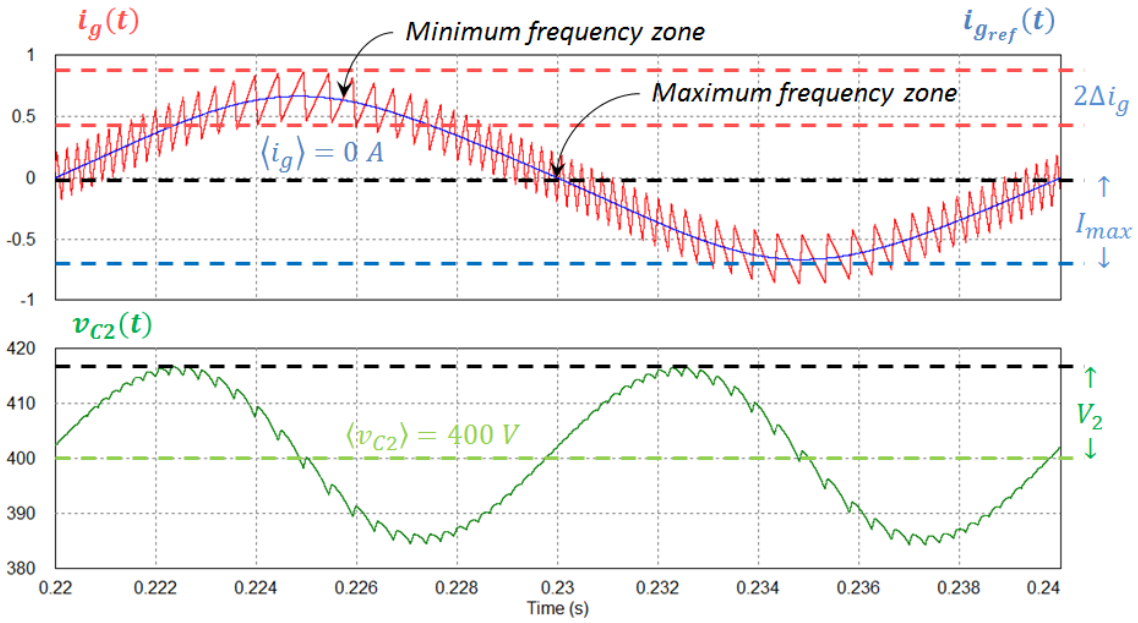

Fig. A2.2. Grid current and DC bus voltage waveforms of the power source inverter.

After defining the value of the inductor, it is then possible to determine a value for the capacitor considering a maximum allowable voltage ripple at the DC bus. For this, the expression (4.86) is solved for C as follows:

$$C > \frac{\sqrt{\left(\omega L {I_{max}}^2\right)^2 + (V_{max} I_{max})^2}}{4\omega V_{dc} V_2} \tag{A2.2}$$

being V_{dc} the regulated value of the voltage V_{C2} of the quadratic boost converter. It is important to recall that at this point the condition (3.117) must also be verified.

List of publications

Journal papers

- O. Lopez-Santos, L. Martinez-Salamero, G. Garcia, H. Valderrama-Blavi, T. Sierra-Polanco, "Robust Sliding-Mode Control Design for a Voltage Regulated Quadratic Boost Converter," *IEEE Trans. Power Electron.*, vol. 30, no. 4, pp. 2313-2327, Apr. 2015.
- O. Lopez-Santos, L. Martinez-Salamero, G. Garcia, H. Valderrama-Blavi, D. Mercury, "Efficiency Analysis of a Sliding-Mode Controlled Quadratic Boots Converter," *IET Power Electron*., vol. 6, no. 2, pp. 364-373, Feb. 2013.

Conference papers

- O. Lopez-Santos, L. Martinez-Salamero, G. Garcia, H. Valderrama-Blavi, "Control de Potencia en un Microinversor Fotovoltaico Conectado a la Red Eléctrica," *in Proc. 21th Seminario Anual de Automática, Electrónica Industrial e Instrumentación (SAAEI)*, 2014, pp. 1-4.
- O. Lopez-Santos, L. Martinez-Salamero, G. Garcia, H. Valderrama-Blavi, T. Sierra-Polanco, "Comparison of the Quadratic Boost Topologies Operating under Sliding-Mode Control," *in Proc. Brazilian Power Electron. Conf. (COBEP),* 2013, pp. 66-71.
- O. Lopez-Santos, L. Martinez-Salamero, G. Garcia, H. Valderrama-Blavi, "Sliding-Mode Control of a Transformer-Less Dual-Stage Grid-Connected Photovoltaic Micro-inverter," *in Proc. 10th Int. Multi-Conf. Systems, Signals & Devices,* 2013, pp. 1-6.

- O. Lopez-Santos, L. Martinez-Salamero, G. Garcia, H. Valderrama-Blavi, "Regulación PI y Control en Modo Deslizante en un Convertidor Elevador Cuadrático," *in Proc. 20th Seminario Anual de Automática, Electrónica Industrial e Instrumentación (SAAEI)*, 2013, pp. 1-4.
- O. Lopez-Santos, L. Martinez-Salamero, G. Garcia, H. Valderrama-Blavi, "Sliding-Mode Indirect Control of the Quadratic Boost Converter Operating in Continuous Conduction Mode or Discontinuous Conduction Mode," *in Proc. IEEE 4th Colombian Workshop on Circuits and Systems (CWCAS),* 2012, pp. 1-6.

Working papers

- O. Lopez-Santos, G. Garcia, L. Martinez-Salamero, J.C. Avila-Martinez, L. Seguier, "Non-Linear Control of the Output Stage of a Solar Micro-Inverter," (In review: *International Journal of Control)*
- O. Lopez-Santos, L. Martinez-Salamero, G. Garcia, H. Valderrama-Blavi, D. Zambrano-Prada, "The Inductor Conduction Modes of the Quadratic Boost Converter," *(Working paper).*
- O. Lopez-Santos, G. Garcia, L. Martinez-Salamero, "A Complete Sliding-Mode Control Approach of a Two-Stage Photovoltaic Micro-inverter System," (In review – *Energy Conversion Conf. & Expo.)*